UCLA
UCLA Electronic Theses and Dissertations

Title
Voltage Control of Perpendicular Magnetization in Multiferroics

Permalink
https://escholarship.org/uc/item/1ff7j91q

Author
Wang, Qianchang

Publication Date
2018

Peer reviewed|Thesis/dissertation

eScholarship.org Powered by the California Digital Library
University of California

UNIVERSITY OF CALIFORNIA

Los Angeles

Voltage Control of Perpendicular Magnetization in Multiferroics

A dissertation submitted in partial satisfaction of the

requirements for the degree Doctor of Philosophy

in Mechanical Engineering

by

Qianchang Wang

2018

© Copyright by

Qianchang Wang

2018

ABSTRACT OF THE DISSERTATION

Voltage Control of Perpendicular Magnetization in Multiferroics

by

Qianchang Wang

Doctor of Philosophy in Mechanical Engineering

University of California, Los Angeles, 2018

Professor Gregory P. Carman, Chair

Magnetic memory has attracted substantial interest due to its non-volatility and zero power dissipation in stand-by mode. The key of magnetic memory is deterministic control of magnetic bits, especially those with perpendicular magnetic anisotropy (PMA), which have higher thermal stability and smaller footprint compared to in-plane memory bits. Among all the magnetization control mechanism, the strain-mediated multiferroics has surprisingly high energy efficiency (1-3 orders of magnitude better) compared to the other mechanisms using nanoscale magnetization control. The strain-mediated multiferroic control employs a piezoelectric/magnetoelastic heterostructure. To write the magnetic memory, a voltage pulse is applied to the piezoelectric substrate and the induced mechanical strain is transferred to a magnetic element attached to the piezoelectric substrate causing magnetization rotation due to the magnetoelastic effect. The

magnetization change can be read out using a magnetic tunnel junction (MTJ). Using strain-mediated multiferroics to control in-plane magnetization has been successfully demonstrated both numerically and experimentally. However, there is little work on using strain-mediated multiferroics to control perpendicular magnetization.

In this dissertation, we provide a thorough study on strain-mediated perpendicular magnetization control, including modeling, experiments, and several new device concepts that extend beyond the traditional memory applications. In Chapter 1, we briefly introduce the memory hierarchy and present non-volatile memory technologies, including magnetic memory. We compare the strain-mediated multiferroic magnetization control with other popular control mechanisms. We also describe the simulation basics, micro-fabrication processes, and characterization techniques for the strain-mediated multiferroics. In Chapter 2, we focus on the simulation of strain-mediated perpendicular magnetization control. Three systems are investigated: 1) single nanodot with constant voltage actuation, 2) multiple nanodots coupled by dipole interaction, 3) single nanodot with AC voltage actuation. In Chapter 3, we focus on the experimental investigation of strain-mediated perpendicular magnetization control. Micro-scale magnetic devices are fabricated with two kinds of piezoelectric substrate: PMN-PT bulk and PZT thin film. By analyzing the test results, the challenge and limitation of multiferroic control of perpendicular magnetization are identified. Empirical experiences are summarized to help guide future multiferroic device design. In Chapter 4, we examine a hybrid strain and spin-orbit torque control mechanism. Two models are developed to simulate the hybrid system and surprisingly interesting phenomena are observed. Using the simulation capabilities developed, we propose several new devices that are go beyond standard memory applications. Finally the last chapter summarizes the contents of this dissertation.

This dissertation of Qianchang Wang is approved.

Kang L. Wang

Robert N. Candler

Pei-Yu Chiou

Gregory P. Carman, Committee Chair

University of California, Los Angeles

2018

To my family

Table of Contents

Chapter 1. Introduction 1

1.1 Motivation 1

1.1.1 Memory hierarchy and non-volatile memory 2

1.1.2 Magnetic memory 4

1.1.3 Multiferroic magnetization control 8

1.1.4 Perpendicular magnetic memory 11

1.2 Micromagnetic simulation basics 13

1.3 Micro-fabrication basics 17

1.3.1 Lithography 17

1.3.2 Deposition 22

1.3.3 Etch 23

1.4 Characterization 25

1.4.1 Magnetic characterization 25

1.4.2 Piezoelectric characterization 28

Chapter 2. Strain-mediated perpendicular magnetization control: simulation 33

2.1 Recent progress of simulations 33

2.2 Strain-mediated 180° perpendicular magnetic switching 37

2.2.1 Motivation 37

2.2.2 Simulation setup 39

2.2.3 Results and analysis 42

2.3 Strain-mediated perpendicular Bennett clocking 48

2.3.1 Literature review and motivation 49

2.3.2 Simulation setup 52

2.3.3 Results and analysis 55

2.4 Pure voltage controlled magnetic oscillation 61

2.4.1 Simulation setup 62

2.4.2 Results and analysis 64

Chapter 3. Strain-mediated perpendicular magnetization control: experiment 72

3.1 Recent progress of experiments ... **72**
3.2 PMN-PT device ... **79**
3.2.1 Material ... 80
3.2.2 Electrode design: a parametric study ... 83
3.2.3 Device on PMN-PT (generation 1) ... 94
3.2.4 Device on PMN-PT (generation 2) ... 101
3.2.5 Device on PMN-PT (generation 3) ... 102
3.3 Device on PZT thin film ... **105**
3.3.1 PZT characterization ... 105
3.3.2 Fabrication ... 109
3.3.3 Characterization ... 112
3.3.4 Analysis ... 115
3.4 Chapter summary ... **119**

Chapter 4. Hybrid strain and SOT control of perpendicular magnetization ... **122**
4.1 Recent progress of hybrid magnetization control mechanisms ... **122**
4.2 Simulation of hybrid strain-mediated and spin-orbit torque system ... **126**
4.2.1 Finite element model ... 126
4.2.2 Macrospin model ... 129
4.3 Deterministic bi-directional perpendicular switching ... **130**
4.3.1 Results ... 130
4.3.2 Vector analysis ... 133
4.3.3 Mathematical derivation ... 139
4.4 Strain-mediated spin torque nano-oscillator (STNO) ... **141**
4.4.1 Introduction: how STNO works ... 142
4.4.2 Simulation setup ... 146
4.4.3 Results and the role of strain ... 148
4.4.4 Mathematical derivation ... 153
4.4.5 Applications ... 157
4.5 Deterministic directional perpendicular switching for memory application ... **160**
4.5.1 Background: perpendicular magnetic switching by SOT ... 161
4.5.2 Simulated structure ... 163

4.5.3 Simulation results and analysis 164
4.5.4 Memory device design 173
4.5.5 Supplemental information 175
4.6 Chapter summary 187

Chapter 5. Conclusion and outlook 189

References 192

List of Figures

Figure 1-1. Prediction of data supply and demand, reference: [1].. 1

Figure 1-2. Computer memory hierarchy, reference: [2]–[4]. Note MRAM is not in current computer memory hierarchy and is added only for comparison.. 2

Figure 1-3. Comparison between the emerging and established memories, reference: [5]. 3

Figure 1-4. Comparison between different types of memories, reference: [6]. 4

Figure 1-5. Spin-transfer torque switching of magnetic tunnel junction, reference: [7]. 5

Figure 1-6. Comparison between STT-MRAM and SOT-MRAM, reference: [9]. 6

Figure 1-7. Comparison between STT and SOT switching in terms of switching speed and energy, reference: [10]. 7

Figure 1-8. Magnetic switching by voltage-controlled magnetic anisotropy, reference: [10]....... 8

Figure 1-9. Coupling between electrics, magnetics and mechanics, reference: [12]. 9

Figure 1-10. Magnetoelectric effect achieved in multiferroic heterostructure by combining a piezoelectric layer and a magnetostrictive layer. (a)-(c) reference: [12], (d) reference: [14]. 9

Figure 1-11. Purely electric field driven magnetic switching using strain-mediated multiferroic structure, reference: [15]. 11

Figure 1-12. Magnetic switching with in-plane and perpendicular anisotropies, reference: [6]. 12

Figure 1-13. Illustration of the vector terms in LLG equation. 13

Figure 1-14. Comparison between photo lithography using negative resist and positive resist... 18

Figure 1-15. Deposition techniques: (a) E-beam evaporation, reference: [27]. (b) DC plasma sputter, reference: [28]. 22

Figure 1-16. Working principle of reactive ion etching. Reference: [29]. 24

Figure 1-17. Magneto-optic Kerr effect. (a) Polar, longitudinal and transversal MOKE. (b) Optical setup for MOKE. Reference: [30]. 26

Figure 1-18. Vibrating sample magnetometer. Reference: [31]. 27

Figure 1-19. Anomalous Hall effect. Reference: [32]. 28

Figure 1-20. Ferroelectric characterization. (a) P-E loop example, reference: [33]. (b) Sawyer-Tower circuit for polarization measurement, reference: [34]. 29

Figure 1-21. Working principle of strain gauge. Reference: [35] 30

Figure 1-22. Piezoresponse force microscopy principle. Reference: [35]. 32

Figure 1-23. Piezoresponse force microscopy with ramp voltage mode. (a) Measurement under coercive voltage. (b) Measurement above coercive voltage. Reference: [37]. 32

Figure 2-1. The coercivity field Hc change by biaxial strain $\varepsilon yy - \varepsilon xx$. Reference: [45]. 35

Figure 2-2. Finite element model simulation results of strain-mediated in-plane magnetization control. Reference: [46]. 36

Figure 2-3. (a) Model setup illustration. (b) Schematics of 180° precessional magnetization switching. 41

Figure 2-4. Simulation results of 180° perpendicular switching of CoFeB. 43

Figure 2-5. Consecutive 180° perpendicular switching of CoFeB. 45

Figure 2-6. Strain-mediated perpendicular switching of crystalline Terfenol-D. 46

Figure 2-7. (a) 3D illustration of the Bennett clocking system simulated in the model. (b) Information flow of Bennett clocking process. 54

Figure 2-8. Simulation results for Bennett clocking of Ni system. 56

Figure 2-9. Simulation results for Bennett clocking of CoFeB system. 57

Figure 2-10. Simulation results for Bennett clocking of Terfenol-D system. 59

Figure 2-11. (a) 3D illustration of the simulated structure (unit: nm). Trajectory of magnetic precession (b) without voltage, (c) with voltage. 63

Figure 2-12. (a)-(d) Temporal evolution of perpendicular magnetization m_z under alternate applied voltage with different amplitudes and frequencies. (e) Summary of simulation results of steady oscillation cases and theoretical fitting line derived from Kittel equation. 65

Figure 2-13. Magnetic oscillation for magnets with different thicknesses. 68

Figure 2-14. Magnetic oscillation with symmetric and asymmetric voltage application. 69

Figure 2-15. Magnetic precession for different voltage waveforms. 70

Figure 3-1. Schematic of the experimental setup and results. Reference: [118]. 73

Figure 3-2. Left: Scheme of the sample and experimental configuration. Right: The repeatable high/low magnetization states (open circle) switched by pulsed electric fields (blue line). Reference: [121] 74

Figure 3-3. Left: Schematic of the device. Right: A representative MOKE data showing magnetic rotation under electric field application. Reference: [36]. 75

Figure 3-4. Device illustration and representative results in reference [18]. 76

Figure 3-5. Ring structure and MFM image of magnetization rotation in reference [128]. 78

Figure 3-6. Device illustration (left) and results (right) showing modulation of perpendicular magnetic anisotropy by electric field in reference [133]. 79

Figure 3-7. Microscope images of PMN-PT surfaces. 80

Figure 3-8. AFM images of PMN-PT surfaces. 81

Figure 3-9. Definition of surface roughness parameters Ra and Rq. (Reference: Wikipedia "surface roughness") 81

Figure 3-10. Crystal orientation of [011] and [001] PMN-PT. 82

Figure 3-11. Strain-gauge measurement of [011] PMN-PT for both x-direction and y-direction.82

Figure 3-12. PMN-PT poling setup. 83

Figure 3-13. Data sheet for [001] PMN-PT (available on TRS website). 84

Figure 3-14. Data sheet for [011] PMN-PT (available on TRS website). 84

Figure 3-15. Comparison of strain response between simulation (a) and experimental results (b) for [011] PMN-PT. 85

Figure 3-16. Impact of distance between patterned electrodes on strain distribution for [011] PMN-PT substrate. The two electrodes are aligned along x-direction (a), y-direction (b), with ±45° rotation (c,d). The shadowed region is where the value $\varepsilon eff = \max \varepsilon ip - \varepsilon 33$ is maximized. 87

Figure 3-17. Impact of distance between patterned electrodes on strain distribution for [001] PMN-PT substrate. The shadowed region is where the value $\varepsilon eff = \max \varepsilon ip - \varepsilon 33$ is maximized. 88

Figure 3-18. xz cut planes for d = 20, 500, 1500 um in the (defined in Fig. 3-17). The arrow shows electric field, the color shows $\varepsilon 11$, and the deformation shows mechanical displacement. 89

Figure 3-19. Impact of electrode size on strain distribution for [001] PMN-PT substrate. 90

Figure 3-20. Impact of electrode size on strain distribution for PZT-5H substrate. 91

Figure 3-21. Impact of device's thickness on strain generated by patterned electrodes on [001] PMN-PT. 92

Figure 3-22. Impact of Young's modulus on strain transfer. 93

Figure 3-23. Illustration of gen1 device on [011] PMN-PT. 94

Figure 3-24. Poling of PMN-PT without the existence of continuous top electrode. 96

Figure 3-25. Fabrication process flow of gen1 device on PMN-PT. Unit: nm. 97

Figure 3-26. Test setup for the gen1 device using the probe station with in-situ applied voltage. 98

Figure 3-27. Perpendicular magnetic switching of the Hall bar (left) by anomalous Hall resistance measurement and continuous film (right) by MOKE measurement. 98

Figure 3-28. SOT switching test of gen1 device on [011] PMN-PT. 99

Figure 3-29. The impact of applied voltage on SOT switching. 100

Figure 3-30. The impact of Joule heating on the magnetic switching. 100

Figure 3-31. Device illustration and coercive field shift test for gen2 device on [011] PMN-PT. 102

Figure 3-32. Device illustration and coercive field shift test for gen1 device on [011] PMN-PT. 102

Figure 3-33. Fabrication process flow of devices on PMN-PT with continuous top electrode. The unit of the numbers is nm. 103

Figure 3-34. Fabrication process flow of devices on PMN-PT with continuous top electrode. The unit of the numbers is nm. 104

Figure 3-35. AFM image of the PZT thin film. 105

Figure 3-36. XRD of the PZT thin film and the data from reference [137] for comparison. 106

Figure 3-37. PE loop for the 200 nm PZT. (a) Top to bottom measurement. (b) Bottom to top measurement. 107

Figure 3-38. PFM measurement for the 200 nm PZT. (a) In-phase. (b) PR amplitude. 107

Figure 3-39. Sensitivity deflection calibration for the PFM tip. 108

Figure 3-40. Different planarization plans for PZT thin film the AFM images showing surface roughness after planarization. 109

Figure 3-41. 3D illustration of the device on PZT thin film. (Unit: nm) 110

Figure 3-42. Process flow of fabricating Hall bar on PZT film. (a) Pattern the e-beam resist for magnetic pillar. (b) Ion mill magnetic pillar and lift-off resist. (c) Pattern the e-beam resist

for Hall bar. (d) Ion mill Hall bar and lift-off resist. (e) Pattern photo resist for leads and contact pads, deposit Au and lift-off resist. 111

Figure 3-43. Process flow of replacing the gating pads. (a) Cross section of the device before the process. (b) Process flow. (c) Cross section of the device after the process....................... 112

Figure 3-44. VSM (blue) and Hall resistance (orange) measurement of the magnetic film. (a) Out-of-plane field switching. (b) In-plane field switching. 113

Figure 3-45. Perpendicular coercive field measured by anomalous Hall effect. (a) Test setup. (b)(c) Illustration of the two devices. (d)(e) Coercive field with different applied voltage to the bottom electrode of PZT for the two devices shown in (b) and (c), respectively. 114

Figure 3-46. COMSOL simulation of the two devices with 10 V applied to the bottom electrode. (a)(b)(c) Device cross-section, perpendicular electric field, strain along x axis for the device with gating pads sitting on HSQ layer. (d)(e)(f) Device cross-section, perpendicular electric field, strain along x axis for the device with gating pads sitting on PZT surface. 115

Figure 3-47. Mumax simulation results. 117

Figure 3-48. Comparison between current design (left) and the optimized design (right). 118

Figure 3-49. Voltage-induced strain measured by XMCD-PEEM. Reference: [141]. 121

Figure 4-1. Hybrid strain + STT control. Left: strain is generated from surface acoustic wave, reference: [143]. Right: strain is generated from PZT substrate, reference: [144]. 123

Figure 4-2. Hybrid STT + VCMA control. Reference: [146]. 123

Figure 4-3. A memory architecture based on hybrid SOT + VCMA control. Reference: [148]. 124

Figure 4-4. Three-terminal magnetic memory based on STT + SOT hybrid control. Left: reference [149]. Right: reference [150]. 125

Figure 4-5. A two-terminal magnetic memory based on STT + SOT hybrid control. (a) Device illustration. (b) SEM image of the MTJ pillar. Reference: [151]. 126

Figure 4-6. Illustration of simulated structure in Section 4.3. 131

Figure 4-7. Representative simulation results. 131

Figure 4-8. Simulation results when the voltage is applied before current. 132

Figure 4-9. Vector diagram for the hybrid SOT + strain system. The three main terms, i.e., spin-orbit torque, PMA, and magnetoelastic field are drawn out for magnetic spin in four quadrants, respectively. 134

Figure 4-10. Explanation of deterministic bi-directional switching for positive applied current. 135

Figure 4-11. Explanation of deterministic bi-directional switching for negative applied current. 136

Figure 4-12. Comparison between switching from ‘up’ to ‘down’ under different current directions. Vector diagram and three magnetization components vs. time for switching by (a)(b): positive current, and (c)(d): negative current. 137

Figure 4-13. Explanation of the behavior when the voltage is applied ahead of current. 138

Figure 4-14. Switching when the current is reversed while the voltage is kept unchanged. 138

Figure 4-15. (a) Visualization of equation 4-10. (b) Parametric study done using macrospin simulation with varying the applied strain and current. 140

Figure 4-16. Device and vector analysis of a conventional spin-torque nano-oscillator (STNO). 142

Figure 4-17. Radiation of a STNO with external bias field. Left: device illustration. Right: radiation signal with different applied current. Reference: [158]. 143

Figure 4-18. Different ways of achieving field-free STNO. (a) The fixed layer has perpendicular easy axis, reference: [159]. (b) The fixed layer has a canted magnetization, reference:s [107]. (c) The MTJ stack has two fixed layer with in-plane and perpendicular easy axis, respectively, reference: [160] 144

Figure 4-19. Device and vector analysis for the field-free STNO. 145

Figure 4-20. Comparison between STT-based and SOT based STNO. 146

Figure 4-21. Simulation setup and the strain distribution for -1.5 V applied voltage. 147

Figure 4-22. Comparison between the finite element model and the macrospin model............ 148

Figure 4-23. Simulation results of the strain-mediated STNO. (a) Perpendicular magnetization vs. time in a 4-ns simulation. (b) FFT of the plot in (a). 148

Figure 4-24. (a) Illustration of the total effective field in *yz*-plane. (b) 3D vector analysis showing how the spin-orbit torque cancels with the Gilbert damping torque. 149

Figure 4-25. Self-adjustable property of the strain-mediated STNO. 151

Figure 4-26. Phase diagram of the parametric study for the strain-mediated STNO with varying input strain and current. Gilbert damping is $\alpha = 0.5$. 152

Figure 4-27. Phase diagram of the parametric study for the strain-mediated STNO with varying input strain and current. Gilbert damping is $\alpha = 0.01$. 153

Figure 4-28. Comparison between the analytical solution and numerical simulation. A slice of the phase diagram with constant current and varying strain is examined.......................... 156

Figure 4-29. Comparison between the analytical solution and numerical simulation. A slice of the phase diagram with constant strain and varying current is examined.......................... 157

Figure 4-30. Using an array of strain-mediated STNO as a radiator....................................... 158

Figure 4-31. Using strain-mediated STNO as a frequency mixer. 159

Figure 4-32. Magnetic oscillation with AC current input... 160

Figure 4-33. (a) Schematic illustration of the simulated structure. (b) The top view of the simulated structure. (c) Temporal change of biaxial strain induced by the −0.5 V applied voltage. (d) Temporal evolution of the perpendicular magnetization in the free CoFeB layer. (e) Vector diagrams of the magnetization distribution. 163

Figure 4-34. Finite element model results of strain-mediated SOT switching for different voltage polarities (positive or negative) and initial states (‘up’ or ‘down’). 166

Figure 4-35. Switching phase diagrams for strain-mediated SOT switching. 168

Figure 4-36. Symmetry analysis of strain-mediated SOT switching....................................... 171

Figure 4-37. Schematics of MeSOT-RAM based on strain-mediated SOT switching mechanism. 174

Figure 4-38. Simulation results of finite element model and macrospin model for the same structure shown in Fig. 4-33(a). (a)(b)(c) show the plot for m_z, m_x, m_y values, respectively. 175

Figure 4-39. Vector diagram of finite element model and macrospin model. 176

Figure 4-40. Temporal change of volume-averaged perpendicular magnetization m_z for different initial states and different relative angles under +0.5V and −0.5V applied voltages using the macrospin model. 177

Figure 4-41. Macrospin results of varying current and voltage for fixed angle θ = 45°. The dashed vertical lines indicate the fastest switching case for each plot. 178

Figure 4-42. Mirror symmetry rules for (a) ordinary vector and (b) pseudovector/axial vector. 179

Figure 4-43. Mirror symmetry analysis with respect to *x-z* plane. (a) Pure SOT system. (b) Adding magnetic bias field to SOT system breaks in-plane symmetry. 180

Figure 4-44. Illustration of divergence of total torque in stable and unstable equilibriums. 183

Figure 4-45. Four types of magnetization state after application of strain/current. 187

List of Figures

Table 1. Parameters for CoFeB and Terfenol-D used in the model... 42

Table 2. Parameters for Ni, CoFeB and Terfenol-D used in the Bennett clocking model. 53

ACKNOWLEDGEMENTS

First I would like Prof. Greg Carman for his time and efforts being my PhD supervisor. I was admitted to UCLA in 2014 as a master student and Prof. Carman was assigned as my initial academic advisor. Unlike normal academic advisors who only meet their assigned mentees once a year, Prof. Carman generously gave me the opportunity to meet with him weekly, which was truly valuable to me. Encouraged by Prof. Carman, I decided to stay as a PhD student after the first year. I feel extremely grateful to Prof. Carman for giving me the great freedom to work on various research projects, as well as educating me both professionally and personally. His guidance, patience, trust, constant encouragement and compliments also help me build confidence and motivate me to continuously work on challenging projects.

I also want to express my gratitude to Prof. Kang Wang for encouraging me and driving me forward whenever I considered giving up. His passion about science and his philosophy of setting high standards inspired me to work harder and never give up on any challenges I may be faced with in the future. I feel sincerely grateful for his insights in my research as well as his advice on my prospective career path. I also had the chance to discuss with Prof. Chris Lynch and Prof. Abdon Sepulveda about my research and I appreciate their suggestions very much. Moreover, I would like to thank Prof. Candler and Prof. Chiou for serving in my PhD committee.

I always feel very lucky that I spent my PhD career in an extremely warm and friendly lab. As an international student, it was tough to fit into the culture here. So I feel very grateful to my ‘local’ labmates, Tony Barra, Auni Kundu (although not officially from Prof. Carman’s lab), Andres Chaves, and Devin Schneider. Thank you for engaging me in your daily meaningless chat, explaining American culture and slang words to me, taking me to the gym, sharing gossip,

pranking each other, etc. I am also constantly impressed by your (especially Tony's) creative, fantastic and sometimes ridiculous ideas. Interacting with you has allowed me to be able to think out of the box. Thanks to John Domann for showing me how to be a rigorous researcher. Thank you Cheng-Yen Liang, Cai Chen, and Jin-Zhao Hu for teaching me about finite element simulations. I also got numerous valuable advice from senior AML members in the beginning of my PhD career, including Scott Strutner, Wei Sun, and Paul Nordeen. Thanks to all the lovely lab members and Yu-Ching Hsiao, my PhD journey was full of fun and I have never regretted pursing a PhD degree at UCLA.

I also would like to thank the students and collaborators outside our lab. Thank you Hao Wu for your continuous help with film deposition and for teaching me to do the Hall resistance measurements. Thanks Guoqiang Yu, Xiang Li and Qiming Shao for fruitful discussions about spintronics. Thank you Jizhai Cui for sharing your experiences of doing research and also being a successful graduate student. More importantly, your childlike curiosity about everything encouraged me to actively learn new knowledge and explore the unknowns. Thank you Xu Li and Zhi (Jackie) Yao for all your theoretical support. Thanks you Sidhant for being able to answer all the questions about micro-fabrication. Thank you Kevin Fitzell and Zhuyun (Maggie) Xiao for the help with experimental measurements.

Working collaboratively and being able to ask all the experienced students for instant advice saved me a lot of time and allowed me to rapidly gain new knowledge. These all contribute to the collaborative environment created by Translational Applications of Nanoscale Multiferroic Systems (TANMS) Center, a National Science Foundation (NSF) Nanosystems Engineering Research Center. I would like to thank TANMS for allowing me to cooperate with people with

diverse backgrounds, for helping me build leadership skills through mentoring undergrads, and for financially supporting my PhD. I also want to thank the staff from Integrated Systems Nanofabrication Cleanroom (ISNC), Nano & Pico Characterization Lab (NPC), UCLA Nanoelectronics Research Facility, and Center of High Frequency Electronics (CHFE), for their technical support and for being so accommodating.

The experimental work with PZT thin film discussed in Chapter 3 was conducted in Western Digital while I was a research summer intern. I would like to thank Jordan Katine at Western Digital for providing me with such a valuable opportunity of carrying on the challenging project in a free and resourceful environment. This also allowed me to experience working life in a company and helped me make the decision to pursue an industrial career after graduation. I would like to give special thanks to my mentor Jeff Lille. Thank you for your technical guidance, sincere suggestions, constant encouragement and trust. I also appreciate the opportunity to interact with several intelligent engineers in Western Digital. Thank you Patrick Braganca, Alexei Bogdanov, Lei Wan and all technicians for the technical education and for sharing your personal experiences with me. It never ceased to amaze me how knowledgeable an engineer can be after dedicating more than ten years in a field. You certainly set a good example to me for my future career as an engineer.

Finally, I would like to express my gratitude to my parents, for your strict requirements in my childhood, for giving me great freedom after I grew up and entered college, and for the endless love and unconditional support at all times. Also, your positive attitudes towards life have had and will continue to have a great impact on me.

VITA

Education

2014 – 2016	M.S. in Mechanical Engineering University of California, Los Angeles
2010 – 2014	B.S. in Physics University of Science and Technology of China, Hefei, China

Employment history

2016 – 2018	Graduate Student Researcher Department of Mechanical and Aerospace Engineering University of California, Los Angeles
2018	Research Summer Intern Western Digital Corporation, San Jose, USA
2015 – 2016	Teaching Assistant Department of Mathematics University of California, Los Angeles

Publications

1) **Q. Wang**, J. Domann, G. Yu, A. Barra, K. L. Wang, and G. P. Carman. "Strain-Mediated Spin-Orbit-Torque Switching for Magnetic Memory", *Physical Review Applied* 10, no. 3 (2018): 034052.

2) **Q. Wang**, X. Li, C. Y. Liang, A. Barra, J. Domann, C. Lynch, A. Sepulveda, and G. Carman. "Strain-mediated 180 switching in CoFeB and Terfenol-D nanodots with perpendicular magnetic anisotropy", *Applied Physics Letters* 110.10 (2017): 102903.

3) **Q. Wang**, J. Z. Hu, C. Y. Liang, A. Sepulveda, and G. Carman. "Voltage-induced strain clocking of nanomagnets with perpendicular magnetic anisotropies", submitted, 2018. Available on arXiv: https://arxiv.org/abs/1812.02268.

4) **Q. Wang**, Y. Li, A. Chaves, J. D. Schneider, J. Z. Hu, and G. Carman. "Pure voltage controlled perpendicular magnetic oscillation", submitted, 2018. Available on arXiv: https://arxiv.org/abs/1812.02264.

Presentations

1) **Q. Wang**, J. Domann, Z. Yao, J. D. Schneider, J. Z. Hu, Y. Wang, and G. P. Carman. "Broadband antenna using strain-mediated spin Hall nano-oscillator", *invited talk* at International Magnetic Conference, Singapore (2018 April).

2) **Q. Wang**, C. Y. Liang, and G. P. Carman. "Voltage induced strain-mediated perpendicular magnetization control for in-memory computing device", poster presentation at International Magnetic Conference, Singapore (2018 April).

3) **Q. Wang**, J. Domann, G. Yu, A. Barra, K. L. Wang, and G. P. Carman. "A hybrid magnetic random-access memory using spin-orbit torque and multiferroics", oral presentation at APS March Meeting, Los Angeles, USA (2018 March).

4) **Q. Wang**, J. Domann, G. Yu, A. Barra, K. L. Wang, and G. P. Carman. "Strain Assisted Field-Free Deterministic Switching of Perpendicular Magnetization by Spin-Orbit Torque", oral presentation at 62nd Annual Conference on Magnetism and Magnetic Materials, Pittsburgh, USA (2017 November).

5) **Q. Wang** and G. P. Carman. "Dynamic Response of Strain-Mediated Perpendicular Magnetic Switching for Memory and Logic Devices", paper and oral presentation on TECHCON conference, Austin, USA (2017 September).

6) **Q. Wang**, C. Y. Liang, X. Li, and G. P. Carman. "Dynamic Response of Strain-mediated Perpendicular Magnetic Tunnel Junction", poster presentation at 61st Annual Conference on Magnetism and Magnetic Materials, New Orleans, USA (2016 November).

7) **Q. Wang**, C. Y. Liang, and G. Carman. "Simulation of Strain-mediated Perpendicular Clocking for Nanomagnetic Logic", oral presentation at XXV International Materials Research Congress, Cancun, Mexico (2016 August).

Chapter 1. Introduction

1.1 Motivation

The past few years have witnessed a rapid growth in demand for data storage. On one hand, this creates huge opportunities for the data storage industry as a shortage of data storage supply is predicted to occur in a few years, as shown in Fig. 1-1. On the other hand, driven by the expansion of Internet of Things (IoT) and the evolution in artificial intelligence and big data learning, there is an increasing demand for a new type of memory that has large storage capability (i.e., small cell size), fast read/write time, long endurance, and low power consumption.

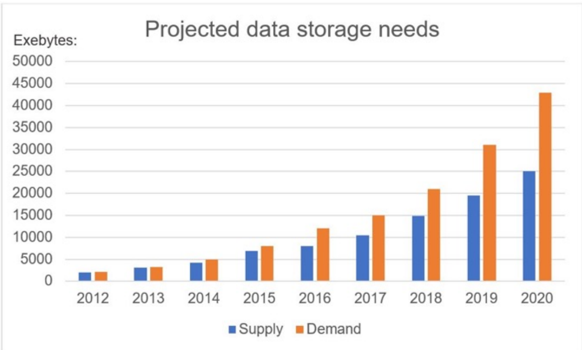

Figure 1-1. Prediction of data supply and demand, reference: [1].

All of these demands impose enormous challenges to be successful with currently available memory technologies hence increasing efforts have been devoted to develop/explore next-generation memory technologies. The specific topic of magnetic memory represents one of the

faster emerging non-volatile memories that could meet high density, high read/write speed and high endurance requirements and thus is the focus of this dissertation.

1.1.1 Memory hierarchy and non-volatile memory

A von-Neumann computing architecture consists of separate computing and memory modules, and the computation relies on data shuttling back and forth between the logic gates and memory parts. In this architecture, there does not exist a single type of memory that is sufficiently fast for computational purpose, while having sufficient storage capability required for long-term memory. Therefore, computer memory has a complex multi-level structure and each level serves a specific purpose with different performance metrics and requirements including speed, power, density, storage capability, etc. The complex memory structure is also known as memory hierarchy as shown in Fig. 1-1.

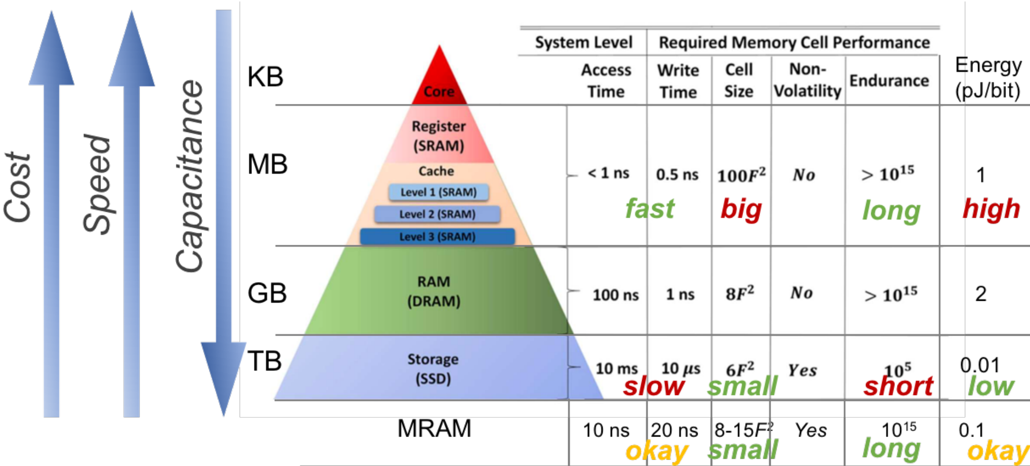

Figure 1-2. Computer memory hierarchy, reference: [2]–[4]. Note MRAM is not in current computer memory hierarchy and is added only for comparison.

The working memories, SRAM/DRAM (Static/Dynamic Random Access Memory), are located close to the central processing unit (CPU) and are designed to allow fast data accessibility during computation. But these memories are volatile and require frequent information refreshing, therefore, they have extensive stand-by power consumption. In addition, their density and storage capability are relatively low. The main origin of volatility is the leakage current for SRAM and charge refresh for DRAM. The information stored in volatile memory is temporal and will be lost when power is turned off. Non-volatile memories, i.e., Flash and HDD (hard disk drive), are used for long-term data storage. These later memories are fairly dense and have large storage capabilities, but the data access speed is considered slow compared to the previous memories.

Type of Memories

	Emerging Memories				Established Memories	
	FeRAM *(or FRAM)*	MRAM	ReRAM *(or RRAM)*	PCRAM *(or PRAM, PCM)*	DRAM	Flash NAND
Nonvolatile	YES	YES	YES	YES	NO	YES
Endurance	High (10^{12})	High (10^{15})	Medium (10^{8})	Medium (10^{8})	High (10^{15})	Low (10^{5})
2012 latest technological node produced (nm)	130 nm	130 nm	R&D	45 nm	30 nm	20 nm
Cell Size (cell size in F^2)	Large (15-20)	Large/Medium (6-40)	Medium (6-12)	Medium (6-12)	Small (6-10)	Very small (4)
Write speed	Medium (100ns)	High (10 ns)	Medium (75 ns)	Medium (75 ns)	High (10ns)	Low (10 000 ns)
Power Consumption	Low	High/Low	Low	Low	Low	Very High
Cost ($/Gb)	High ($ 10 000/Gb)	High ($ 1000 – 100 /Gb)	R&D	Medium (few $/ Gb)	Low ($1/Gb)	Very Low ($ 0.1/Gb)

Figure 1-3. Comparison between the emerging and established memories, reference: [5].

There are several types of emerging non-volatile memory technologies and significant progress has been made especially in the last decade. The main four categories are FeRAM (ferroelectric RAM), MRAM (magnetoresistive RAM), ReRAM (resistive change RAM), and PCRAM (phase change RAM). The comparison between these four types of emerging NVMs and the established memories (DRAM ad Flash) are represented in Fig. 1-3.

Compared to other emerging NVMs, MRAM is surprisingly superior in term of speed and endurance, making it a promising candidate for replacing existing memories (SRAM/DRAM) as shown in Fig. 1-4. In addition, these MTJ based memories have promise for radiation immunity and is compatible with CMOS devices.

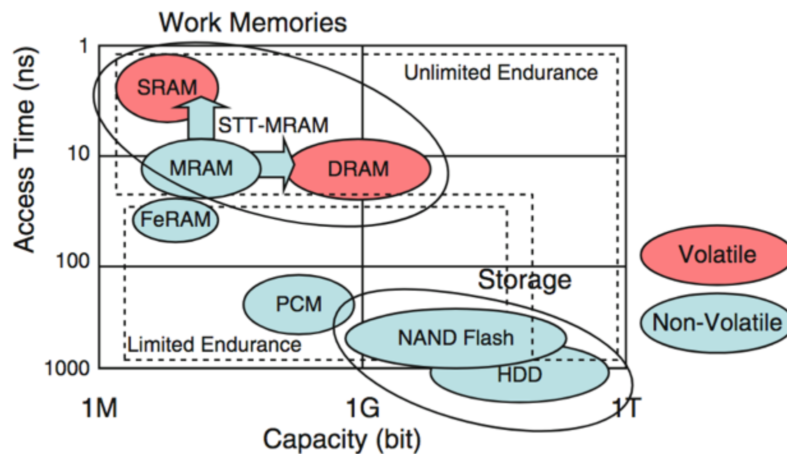

Figure 1-4. Comparison between different types of memories, reference: [6].

1.1.2 Magnetic memory

The magnetic memory area has several different sub-classes depending on the magnetic switching mechanism employed. In most cases, MRAM specifically refers to STT-MRAM, which uses spin-transfer torque (STT) for magnetic switching and represents the most mature

technology amongst available magnetic memories. The key element of STT-MRAM is the magnetic tunnel junction (MTJ) and its working principle is illustrated in Fig. 1-5. MTJ is a sandwiched structure consisting of two ferromagnetic layers (also known as free layer and pinned layer, respectively) and an insulating tunnel barrier in between. The free layer magnetization can be switched to parallel or anti-parallel states relative to the pinned layer, depending on the STT current direction in the MTJ stack. The pinned layer has a large magnetic coercivity field, therefore its magnetization remains constant during the switching process. The resistance of the MTJ stack is probed by passing a small tunneling current, which does not disturb the free layer's magnetization state. The resistance measured with this tunneling current is low for a parallel and high for anti-parallel state configurations, which are encoded as either '0' and '1' for memory application. The tunnel magnetoresistance ratio (TMR), which is defined as TMR = $(R_{AP}-R_P)/R_P$, is used to evaluate the MTJ's sensitivity.

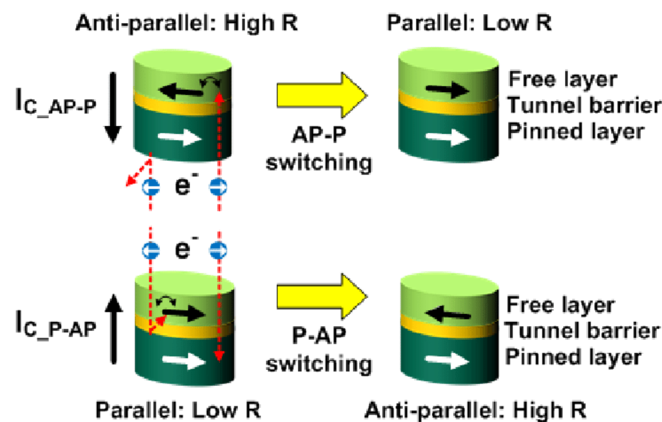

Figure 1-5. Spin-transfer torque switching of magnetic tunnel junction, reference: [7].

SOT-MRAM, which relies on spin-orbit torque magnetic switching, is another type of magnetic memory being investigated. Spin-orbit torque is induced by applying current through a heavy metal that is adjacent to the free layer of the MTJ stack due to spin Hall effect, and the

magnetization of the free layer can be changed depending on the SOT current's direction. As shown in Fig. 1-6, unlike STT switching mechanism, the switching current in SOT devices does not tunnel through the oxide layer of the MTJ stack, which represents the main degradation mechanism in STT-MRAM. Therefore, the SOT-MRAM appears to have better endurance than STT-MRAM. Another bottleneck of STT switching mechanism is its relatively long incubation time, due to the small initial torque when the magnetization is parallel/antiparallel to the spin polarization.[8] However, this is not a problem for SOT switching because the initial torque is relatively large (the magnetization is perpendicular to the polarization).

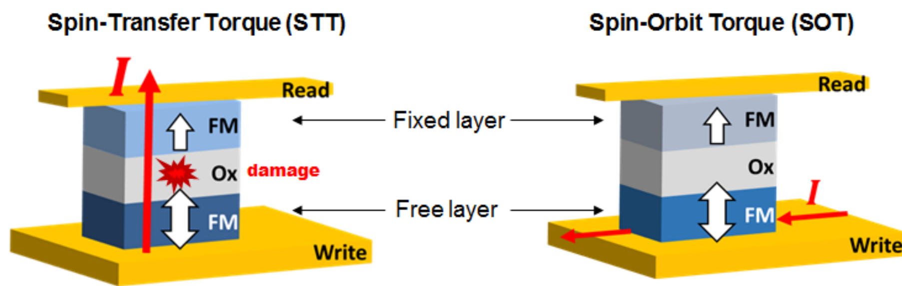

Figure 1-6. Comparison between STT-MRAM and SOT-MRAM, reference: [9].

SOT switching has higher spin current injection efficiency than STT switching. In addition, it has been demonstrated that the switching current could be lowered by 2-3 orders of magnitude by using topological insulator rather than the heavy metal layer used in conventional SOT devices. Therefore, SOT switching is potentially more energy efficient that STT switching. SOT switching is also faster than STT switching with similar energy dissipation as shown in Fig. 1-7.

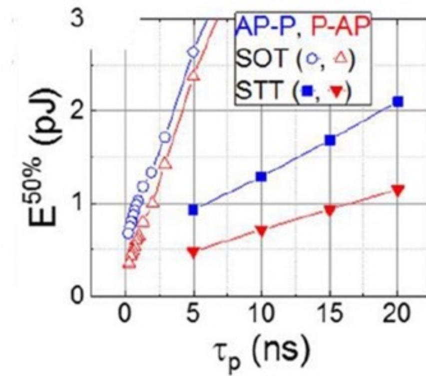

Figure 1-7. Comparison between STT and SOT switching in terms of switching speed and energy, reference: [10].

Another type of magnetic memory, magnetoelectric RAM (MeRAM), relies on voltage-controlled magnetic anisotropy (VCMA) effect, as demonstrated in Fig. 1-8. The applied electric field to the MTJ increases or decreases the energy barrier between the two stable states, depending on the electric field direction. Magnetic switching happens when the energy barrier is sufficiently low to overcome the energy barrier defined by thermal fluctuation. This type of VCMA switching requires accurate timing of the applied voltage pulse, so VCMA switching is non-deterministic. In addition, the switching is not directional. In other words, by applying the same voltage pulse, the magnetization can switch both from up to down, and down to up, i.e. non-deterministic. Despite those shortcomings, researchers have shown that MeRAM is superior to STT-MRAM in terms of speed and energy dissipation for both writing and reading. [11]

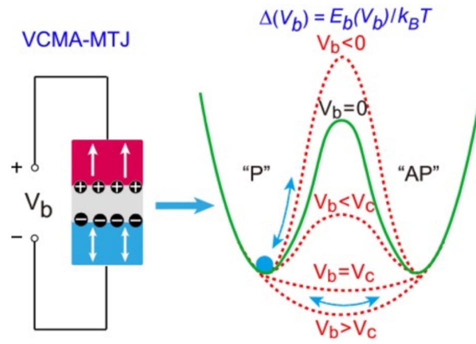

Figure 1-8. Magnetic switching by voltage-controlled magnetic anisotropy, reference: [10].

1.1.3 Multiferroic magnetization control

Using multiferroic composites is another approach to efficiently control magnetization. Multiferroic composites generally refer to the materials that exhibit more than one primary ferroic coupling as illustrated in Fig. 1-9. However most researchers refer to the magnetoeletric coupling present in multiferroics that translates electrics to magnetics or the opposite way rather than the more general energy transfer between a wide range of states.

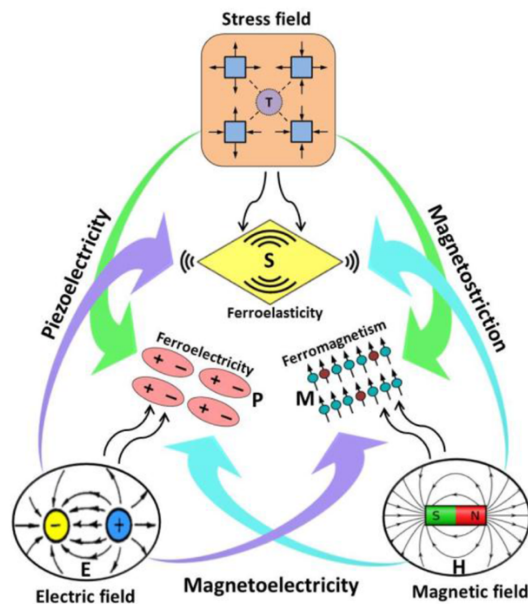

Figure 1-9. Coupling between electrics, magnetics and mechanics, reference: [12].

Some materials, for example BiFeO3, have an intrinsic magnetoelectric effect. However, the number of single phase multiferroics that have been discovered is limited and the magnetoelectric coupling is usually considered to be relatively small. [13] The other route to achieve magnetoelectric effect is by using a laminated heterostructure that combines a piezoelectric substrate and a magnetostrictive layer. As shown in Fig. 1-9, piezoelectric materials translate energy between electrics and mechanics, while magnetostrictive (also known as magnetoelastic) materials translate energy between mechanics and magnetics.

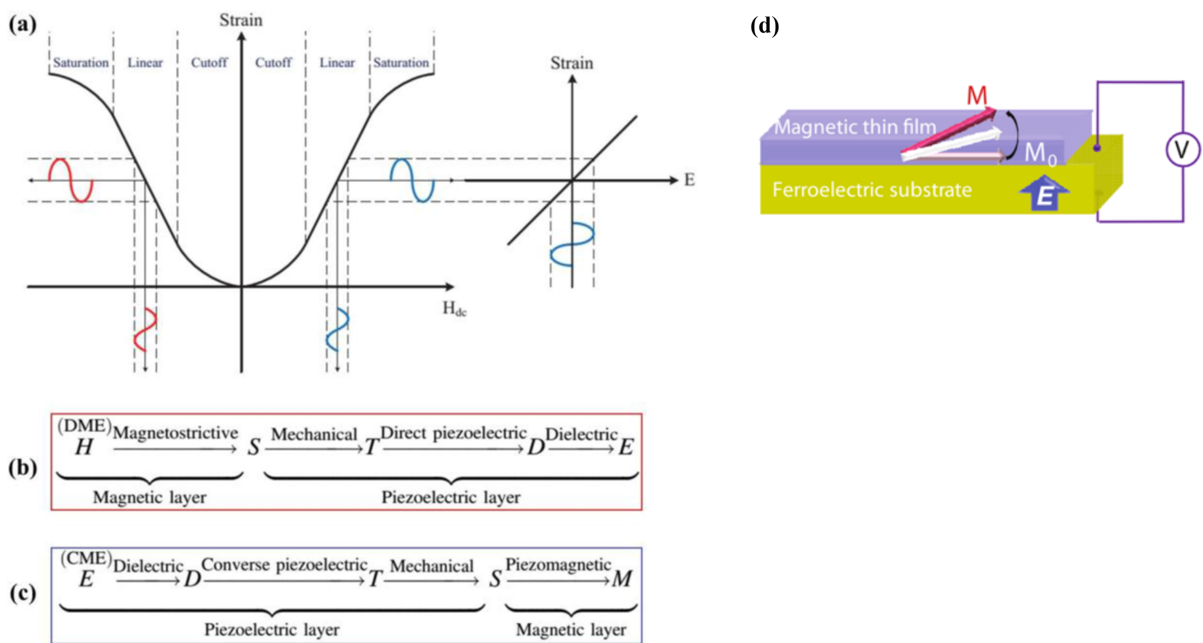

Figure 1-10. Magnetoelectric effect achieved in multiferroic heterostructure by combining a piezoelectric layer and a magnetostrictive layer. (a)-(c) reference: [12], (d) reference: [14].

In a multiferroic heterostructure as shown in Fig. 1-10(d), a voltage is applied to the piezoelectric substrate and induces mechanical strain, which is then transferred to the attached

magnetostrictive layer and lead to magnetization switching or magnetic domain reorientation. More specifically, the direct magnetoelectric (DME) effect converts an applied magnetic field to polarization change in piezoelectric layer as shown in Fig. 1-10(b), while the converse magnetoelectric (CME) converts an applied electric field to the magnetization change as shown in Fig. 1-10(c). The magnetization control mechanism using CME is also known as strain-mediated magnetization control (i.e. strain mediated multiferroic).

If the magnetic layer in a multiferroic heterostructure is patterned into elements with bi-stable magnetic states, the strain-mediated magnetization control can be used for magnetic memory application. Fig. 1-11 shows potential memory designs with strain-mediated multiferroic structure. [15] Fig. 1-11(a) illustrates a MTJ stack fabricated on a ferroelectric substrate, whose free layer is controlled by applying electric field to the substrate. The electric field induced strain is modifying the magnetic energy profile of the free layer. As shown in Fig. 1-11(c), without a strain, the easy axis is along the perpendicular direction producing two stable magnetic states. When the applied strain is sufficiently large (-0.08%, or 800 ppm), the easy axis changes to in-plane ($\theta = 0°$) from out of plane. Therefore, the magnetization rotates from out-of-plane to in-plane under applied strain, and by accurately timing the applied voltage pulse, the magnetization can switch 180° ending up in a magnetic orientation opposite state to the original state. This switching process is also referred to as ballistic switching or precessional switching in the community. Similar to VCMA, the strain induced magnetic switching is non-deterministic and non-directional.

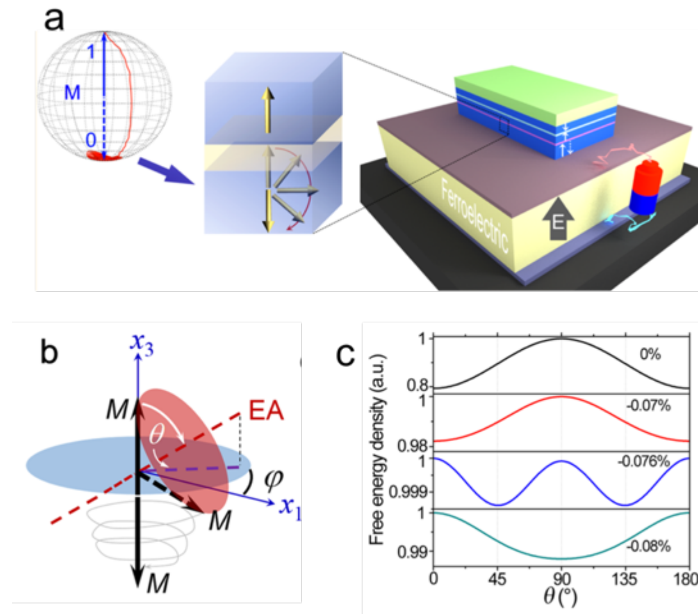

Figure 1-11. Purely electric field driven magnetic switching using strain-mediated multiferroic structure, reference: [15].

Summarizing, the strain-mediated multiferroic control compared to the magnetic switching mechanism mentioned in previous section (i.e., STT, SOT and VCMA) are 1-3 orders of magnitude more energy efficient and thus represents an interesting technology. Some simulation work has predicted that the energy dissipation using strain-mediated multiferroic control is 0.01~0.1 fJ per bit per flip [16]–[19], while it is 10~100 fJ for STT and 1fJ for VCMA [20].

1.1.4 Perpendicular magnetic memory

The memory bit with perpendicular magnetic anisotropy (PMA) has relatively smaller footprint compared to in-plane magnetic memory bit. [21], [22] This is because the in-plane anisotropy depends on the lateral shape of the in-plane memory bit. To accurately fabricate the desired in-plane shapes becomes challenging, especially in sub-100 nm range, which hinders the scaling down of in-plane magnetic memory bit. In contrast, the memory bit with PMA has a

better tolerance of the lateral shape, and sub-20 nm MTJ with PMA has been successfully demonstrated in 2011. [23]

It is also shown that perpendicular magnetic memory bit requires less switching current than in-plane memory bit (reference: page 118 in [6]). For in-plane magnetic memory elements, the energy barrier to avoid random thermal switching (i.e., 60 k_BT, where k_B is Boltamann constant, and T is the temperature) is defined by the energy difference between easy axis and hard axis, which are both in-plane directions. However, because the switching between the two in-plane states consists of out-of-plane precession, the actual energy barrier that needs to be overcome is the energy difference between the in-plane state and out-of-plane state, which is much higher than 60 k_BT. In contrast, switching magnetic memory with PMA only needs to overcome the 60 k_BT energy barrier. Although the argument presented is primarily specific to STT switching, the argument also is valid for other switching mechanisms as well, since in-plane magnetic switching by SOT, VCMA or strain also consists of out-of-plane magnetic precession. Therefore, switching PMA memory bit is theoretically more energy efficient than switching in-plane memory bit.

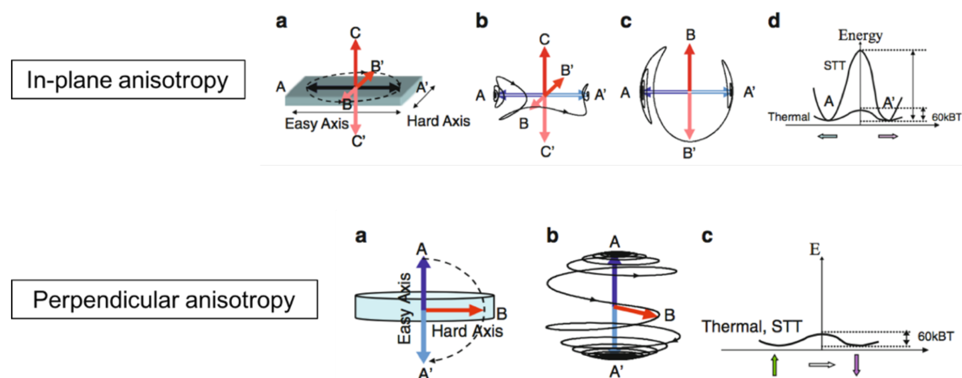

Figure 1-12. Magnetic switching with in-plane and perpendicular anisotropies, reference: [6].

1.2 Micromagnetic simulation basics

In 1935, Landau and Lifshitz [33] proposed a phenomenological equation to describe the dynamics of magnetization. Gilbert [34] modified the Landau-Lifshitz equation such that large damping was taken into account and proposed Landau-Lifshitz-Gilbert (LLG) equation:

$$\frac{\partial \boldsymbol{m}}{\partial t} = -\mu_0 \gamma \left(\boldsymbol{m} \times \boldsymbol{H}_{eff}\right) + \alpha \left(\boldsymbol{m} \times \frac{\partial \boldsymbol{m}}{\partial t}\right) \quad \text{Eq. 1-1}$$

where $\boldsymbol{m}$ is the normalized magnetization, μ_0 is the vacuum permittivity, γ is the gyromagnetic ratio and α is the Gilbert damping factor. LLG equation describes the precessional motion of magnetic spin under effective field. Fig 2.13 shows the directions for precession and damping term, and the dotted spiral shows the trajectory of magnetization under the assumption that the effective field is constant.

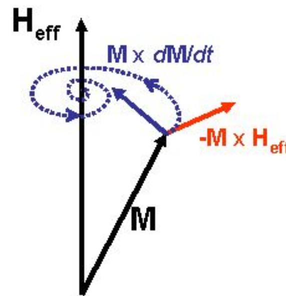

Figure 1-13. Illustration of the vector terms in LLG equation.

In general case, the effective field in LLG equation consists of five terms:

$$\boldsymbol{H}_{eff} = \boldsymbol{H}_{MCA} + \boldsymbol{H}_{ext} + \boldsymbol{H}_{ex} + \boldsymbol{H}_{Demag} + \boldsymbol{H}_{ME} + \boldsymbol{H}_{a} \quad \text{Eq. 1-2}$$

where H_{MCA} is magneto-crystalline anisotropy (MCA) field, H_{ext} is external field, H_{ex} is exchange field, H_{demag} is demagnetization field, H_{me} is magneto-elastic field and H_a is a generic other anisotropy term that can be added to accommodate other effects such as PMA.

Magnetocrystalline anisotropy (MCA)

MCA primarily arises from spin-orbital coupling between the orbital motion of electrons and crystal electric field. It is easier to magnetize along specific directions in a crystalline structure as compared with other directions. A general formula that describes this magnetocrystalline anisotropy behavior is given by: [24]

$$E_{MCA} = K_0 + K_0(m_1^2 m_2^2 + m_2^2 m_3^2 + m_3^2 m_1^2) + K_0(m_1^2 m_2^2 m_3^2) + \cdots \quad \text{Eq. 1-2}$$

where K_i ($i = 0,1,2 \ldots$) are MCA constants determined by the material and temperature. The MCA field is calculated as:

$$\boldsymbol{H}_{MCA} = -\frac{1}{\mu_0 M_S}\frac{\partial E_{MCA}}{\partial \boldsymbol{m}} \quad \text{Eq. 1-3}$$

The MCA field is zero on average for polycrystalline, which is the case for most common magnetic materials. Therefore, the MCA field is commonly considered negligible in many micromagnetic simulations.

Exchange anisotropy

Exchange energy arises from the exchange effect between the atom and its nearest neighbors. It is a quantum mechanical effect due to the wave function of indistinguishable particles being

subject to exchange symmetry. Exchange energy depends on the relative orientation of spins of two electrons, which is given by:

$$E_{ex} = -2A_{ex}\boldsymbol{S}_i \cdot \boldsymbol{S}_j = -2A_{ex}S_iS_j cos\phi \qquad \text{Eq. 1-4}$$

where A_{ex} is the exchange constant, and ϕ is the angle between the spins. A_{ex} is positive for ferromagnetic material and is negative for antiferromagnetic material. In a continuous model, the exchange energy density can be written as:

$$E_{ex} = A_{ex}(\nabla \boldsymbol{m})^2 \qquad \text{Eq. 1-5}$$

where ***m*** is the normalized magnetization vector. The exchange field is defined as:

$$\boldsymbol{H}_{ex} = -\frac{1}{\mu_0 M_S}\frac{\partial E_{ex}}{\partial \boldsymbol{m}} \qquad \text{Eq. 1-6}$$

Demagnetization anisotropy

Demagnetization energy describes the dependence of magnetization on the shape, which is a long-range term, compared to localized exchange energy and MCA energy. Demagnetization field is expressed as the gradient of magnetic potential ϕ:

$$\boldsymbol{H}_{demag} = -\nabla\phi \qquad \text{Eq. 1-7}$$

The demagnetization energy is given by

$$E_{ex} = -\frac{1}{2}\mu_0 M_S \boldsymbol{m} \cdot \boldsymbol{H}_{demag} \qquad \text{Eq. 1-8}$$

Demagnetization energy can also be expressed using a macroscopic parameter:

$$E_{ex} = -\frac{1}{2}\mu_0 M_S^2 N_d \quad \text{Eq. 1-9}$$

where N_d is the demagnetization factor depending on the specific shape. For commonly used shapes, the demagnetization factor can be found in reference [25].

<u>Magnetoelastic anisotropy</u>

The magnetoelastic field $\boldsymbol{H}_{ME}$ can be represented by the following equation [24]:

$$H_{ME}(m,\varepsilon) = -\frac{1}{\mu_0 M_S}\frac{\partial}{\partial m}\{B_1[\varepsilon_{xx}\left(m_x^2 - \frac{1}{3}\right) + \varepsilon_{yy}\left(m_y^2 - \frac{1}{3}\right)$$
$$+\varepsilon_{zz}\left(m_z^2 - \frac{1}{3}\right)] + 2B_2(\varepsilon_{xy}m_x m_y + \varepsilon_{yz}m_y m_z + \varepsilon_{zx}m_z m_x)\} \quad \text{Eq. 1-10}$$

where m_x, m_y and m_z are components of normalized magnetization along *x, y* and *z* axis, B_1 and B_2 are first and second order magnetoelastic coupling coefficients. B_1 and B_2 are calculated using the equation: $B_1 = B_2 = \frac{3E\lambda_S}{2(1+\nu)}$, where E is the Young's modulus and λ_S is the saturation magnetostriction coefficient of the magnetic material. In the formula of $\boldsymbol{H}_{ME}$, $\boldsymbol{\varepsilon}$ is the total strain that consists two parts: $\boldsymbol{\varepsilon} = \boldsymbol{\varepsilon}_p + \boldsymbol{\varepsilon}^{\boldsymbol{m}}$, where ε_p is the piezostrain can be determined from linear piezoelectric constitutive relations, and $\boldsymbol{\varepsilon}_{ij}^{\boldsymbol{m}} = 1.5\,\lambda_s(m_i m_j - \delta_{ij}/3)$ is the strain contribution due to isotropic magnetostriction, and δ_{ij} is Kronecker function [24]. It is also important to realize that the magnetization also influences the strain through $\boldsymbol{\varepsilon}^{\boldsymbol{m}}$, and the strain influences the magnetization through $\boldsymbol{H}_{ME}$ term in Eq. 1-2, i.e. two way coupling. It has been shown that the two-way coupled model is more accurate than the one-way coupled model, i.e., no feedback from magnetization to mechanical strain.[26]

1.3 Micro-fabrication basics

Microscale and nanoscale devices can be made through a series of micro-fabrication steps. In this section, we introduce some micro-fabrication techniques that were used in the work presented in Chapter 3.

1.3.1 Lithography

Lithography represents one of the more important microfabrication processes, which can transfer a pattern from a mask to a photoresist layer that is light-sensitive on substrate. The pattern is then used for deposition or etching step that is discussed later. Generally, the lithography process consists of the following steps: spin coat, exposure, and development. Depending on the light source, the lithography can be roughly divided into photo lithography and e-beam lithography.

In photo lithography, the light source is normally in ultraviolet (UV) range generated from mercury lamps and three common used wavelengths include: g-line (436 nm), h-line (405 nm) and i-line (365 nm). In a projection system, the minimum feature size is limited by light diffraction and the critical dimension is defined as: $\mathrm{CD} = \frac{k\lambda}{NA}$, where k is a constant depending on the process, λ is the wavelength of the incident light, and NA is the numerical aperture of the lens. To enhance the pattern resolution, one can decrease the wavelength. For example, the state-of-art photo lithography tool uses deep UV light that has wavelengths of 248 nm and 193 nm.

Except the wavelength, one can also increase the NA by filling the gap between the lens and the wafer with a liquid medium like water. This technology is also known as immersion lithography.

The optical aligner that was used in the work presented in Chapter 3 uses i-line light source, hence we focus on introducing the normal photo lithography in this section. Two photoresists were used in the work: AZ 5214 (positive photoresist) and nLOF 2020 (negative photoresist). The resist is called positive or negative if the resist becomes soluble or insoluble in the developer. Fig. 1-14 compares the photo lithography process using positive and negative resist.

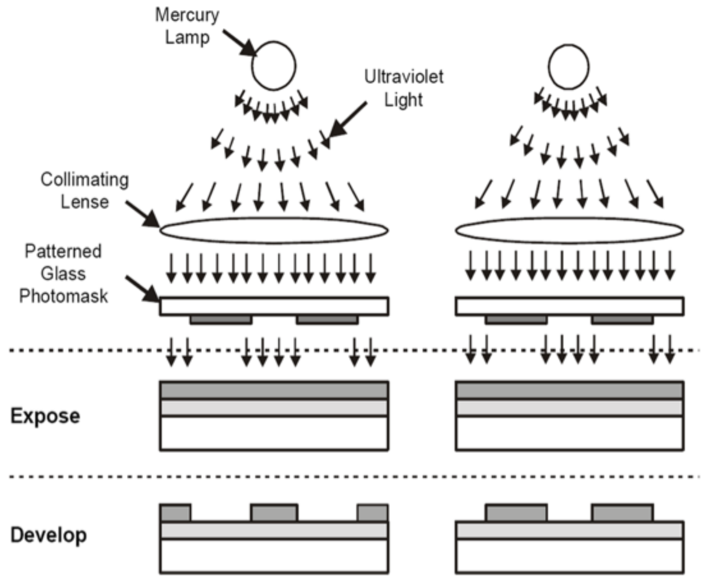

Figure 1-14. Comparison between photo lithography using negative resist and positive resist.

The pattern resolution does not depend on the polarity of the resist, and theoretically any lithography can be done using both positive and negative resist. However, due to light diffraction and absorption, the side wall of the exposed area is never perfectly vertical, but usually contains some modest slopes. For negative resist, it makes the bottom edge of an open area more into the resist body than the top edge. In other words, the exposed area has a negative slope (also known

as undercut), which makes the following deposition and lift-off process easier. Therefore, the negative resist is preferred compared to the positive resist. Below are the recipes for nLOF 2020 and AZ 5214. Also, negative resist is usually more thermally stable and physically robust than positive resist, making it more suitable as an etching mask. The positive resist can be also used to generate undercut with image reversal process, however, the extra step of flood exposure makes it less convenient to use than directly using negative photoresist.

nLOF 2020

1) Solvent clean: acetone, methanol, IPA, N2 dry.
2) Oxygen plasma clean 1min @ 50°C (tool = Matrix 150 Downstream Asher, pressure = 3.75 Torr, power = 80 W)
3) [optional] Dehydration: 5min @100°C (both time and temperature are not critical). Cool down (i.e., leave it in the plastic holder) for 5min.
4) [optional] Spin coat HMDS to enhance the adhesion:
    a. ramp = 500 rpm/s, speed = 500 rpm, 5s;
    b. ramp = 500 rpm/s, speed = 3000 rpm, 60s; (increase speed to 3500 rpm for sample smaller than 1cm×1cm)
    c. ramp = 500 rpm/s, speed = 0 rpm, 0s.
5) Immediately after HMDS, spin coat AZ nLOF2020 using the same program as above.
6) [optional] Grab a q tip to clean the edges. (Because resist may accumulate at edges.)

7) Soft bake: 1min @110°C

8) Exposure: 68 mJ/cm^2 (need to adjust slightly depending on the substrate and lamp power, I have used 7.5s with mercury lamp power 8.5mW/cm^2, and 5.5s with mercury lamp power 12mW/cm^2), hard contact mode, gap=30um

9) Post exposure baking: 1min @110°C

10) Develop: 60s in AZ300MIF, rinse in water. Check the patterns after the 60s, and if necessary, add some time for development.

11) Rinse in DI water (NO acetone, NO methanol, NO IPA) and N2 dry.

12) Descum: oxygen plasma 1min @ 50°C (tool = Matrix 150 Downstream Asher, pressure = 3.75 Torr, power = 80 W)

AZ 5214

All the steps above except step 7-10 are applicable for other kind of photoresists as well. When using AZ 5214, the step 7-10 should be changed as:

7) Soft bake: 1min @100°C

8) Exposure: 10s with mercury lamp power 8.5mW/cm^2, hard contact mode, gap=30um

9) No post-exposure bake.

10) Develop: 45s in diluted AZ400K (AZ400K:DI water = 1:4), rinse in water.

AZ 5214 with image reversal

AZ 5214 can be used as negative resist by adding a flood exposure step. The step 7-10 in the recipe for nLOF 2020 should be changed in to following steps:

7) Soft bake: 1min @100°C

8) Exposure: 6s with mercury lamp power 8.5mW/cm^2, hard contact mode, gap=30um

9) Flood exposure 180s

10) Develop: 30s in diluted AZ400K (AZ400K:DI water = 1:4), rinse in water.

Some tips

In our experiment, we usually process with small (~1cm^2) piezoelectric substrate. One should note that for these small substrates, after spin coating the photoresist, the resist may accumulate at the substrate's edge. This accumulated resist adds a gap between the photomask and the sample or makes the interface region uneven, which in turn reduces the exposure resolution. Therefore, one approach to improve the photo lithography resolution is to wipe the edge of the sample following the spin coat step using a q tip, i.e., edge removal. Another important suggestion is that sparking discharge may happen in the piezoelectric sample during the baking process. More specifically, abrupt temperature increases may result in the piezoelectric's polarization undergoing a sudden reorientation that induces an unwanted electrical arc, and in the worst case, may shatter the sample. I have seen this happened in poled PMN-PT with size of 1cm × 1cm when the sample is put on a 150°C hot plate. I tested a few other samples and it turned out that un-poled PMN-PT (regardless of size), or poled PMN-PT with size around 5mm × 5mm, are both safe when putting on a hot plate with temperature up to 250°C. In other words, the thermal discharge is primarily an issue for poled PMN-PT with relatively large sizes. To avoid this

problem of electrical arcing , one can slowly ramp the hot plate, however, this may request to re-calibrate the baking time in the photo lithography process.

1.3.2 Deposition

There are mainly two deposition techniques that were used in the experiments presented in Chapter 3: e-beam evaporation and sputtering. Fig. 1-15 illustrates the working principles for both techniques.

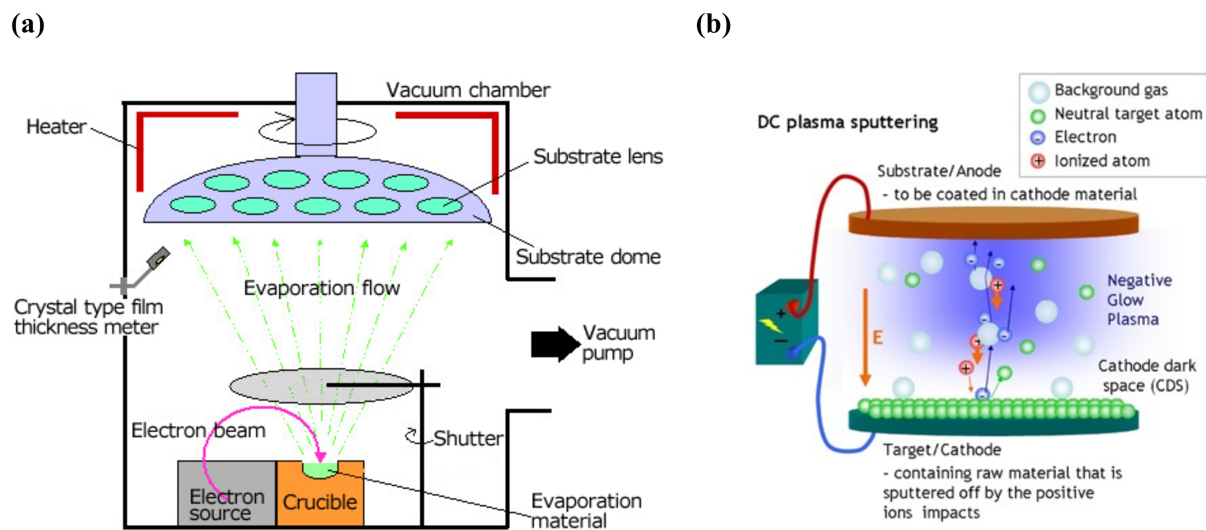

Figure 1-15. Deposition techniques: (a) E-beam evaporation, reference: [27]. (b) DC plasma sputter, reference: [28].

In e-beam evaporation, electron beam is generated and accelerated from an electron source, and then the beam is deflected by electromagnetic coil to shoot toward the target. When the electrons with high kinetic energy hits the target, the target material is heated up rapidly and the temperature is sufficiently high to melt and vapor the material. The vapor is then coated onto the substrate.

In sputtering, a plasma is generated by DC or AC voltage, and the charged ions in the plasma are accelerated and physically bombard the target surface. Usually Ar gas is used because Ar does not react with other materials. When the bombarding has sufficient energy, the target atoms are knocked off and diffuse towards the substrate.

The e-beam evaporation is a highly directional deposition process, which is good for lift-off process, but may be bad if one wants a conformal film or good step coverage. In addition, the rapid cooling down when the material vapor reaches the substrate surface, which is usually at room temperature, this may cause residual stress inside the deposited film due to thermal mismatch. The ions in sputtering have higher kinetic energy than the electrons in e-beam evaporation, therefore, the film deposited by sputtering is denser and has better adhesion to the substrate. Specifically, for dioxide like SiO2, sputtering usually gives a film with less pinholes hence less electrical leakage issues.

1.3.3 Etch

The etching process in general can be divided into chemical etching and physical etching, or dry etching and wet etching. Fig. 1-16 shows the working principles for two dry etching techniques that I used the most, including one chemical etching (reactive ion etching, or RIE) and one physical etching (ion mill).

In reactive ion etching, the sample is placed is treated by reactive gas (for example, O2 and CF4 gases are used in Fig. 1-16) with plasma activation. The gases are ionized by plasma generated by RF power, and react with the etched target, forming volatile byproducts with low

vapor pressure. In ion milling, Argon gas is used instead of reactive gases, and the etching is achieved by physical bombardment of the accelerated Argon ions onto the target surface.

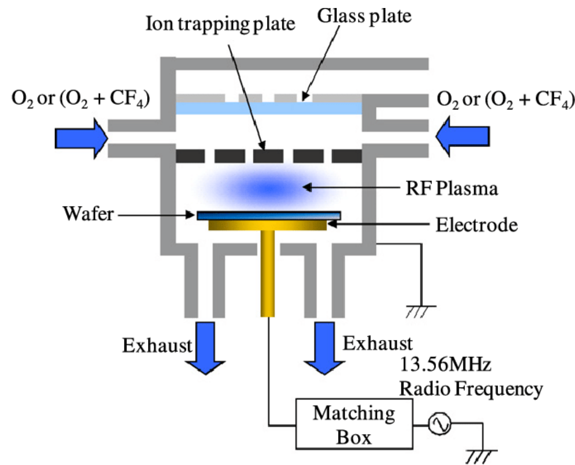

Figure 1-16. Working principle of reactive ion etching. Reference: [29].

As a chemical etching technique, the RIE is selective and fast etching process. Because of its selectivity, it is easier to control the vertical etch accuracy as each etching gas targets specific material. However, it is not as directional as physical etching, but rather has an isotropic in-plane etching profile. A more advanced technique, deep RIE, can be used to improve the aspect ratio of the etching profile by alternately etching and depositing a passive polymer layer on sidewalls. Another weakness of RIE is that the etching gas has limited choices and not all target material has a selective etching gas with a volatile byproduct. In contrast, physical etching is not selective and can attack almost all materials to some degree. The etching rate is dependent on the DC bias that accelerates the Argon ions, therefore, the etched structure usually has more vertical sidewalls. Accurate ion milling can be achieved with secondary ion mass spectrometer (SIMS)

endpoint detection system. The SIMS system can provide the information of the material currently being etched.

1.4 Characterization

Characterization of a strain-mediated multiferroic device consists of two parts: magnetic characterization and piezoelectric characterization. We will discuss several characterization techniques in this section, particularly focusing on the techniques that were used in the work presented in Chapter 3.

1.4.1 Magnetic characterization

Magneto-optic Kerr effect (MOKE) refers to the effect that light changes its polarization and intensity following reflection from a magnetized surface. As shown in Fig. 1-17, depending on the relative orientation between the surface's magnetization and the incident light, there are three types of MOKE setup. The polar MOKE is used to measure the out-of-plane magnetization, while the longitudinal MOKE is used to measure the in-plane magnetization. Fig. 1-17(b) illustrates a simplified optical setup for MOKE measurement. The spatial resolution of the MOKE is restricted by the size of the incident laser spot, which is usually 0.1~1 mm^2. The detector provides an absolute readout value influenced by the optical property of the sample surface, the size of the laser spot, the attenuation by the optical polarizers/filters, and the sensitivity of the photodiode detector, etc. Therefore, the MOKE signal is typically presented as a normalized quantity. MOKE represents a relatively easy characterization method to determine whether a magnetic film has in-plane or perpendicular anisotropy as well as provides information regarding the magnetic film's coercivity and anisotropy field. However, quantifying the film's

magnetization such as remanent or saturation magnetization is challenging with the MOKE setup.

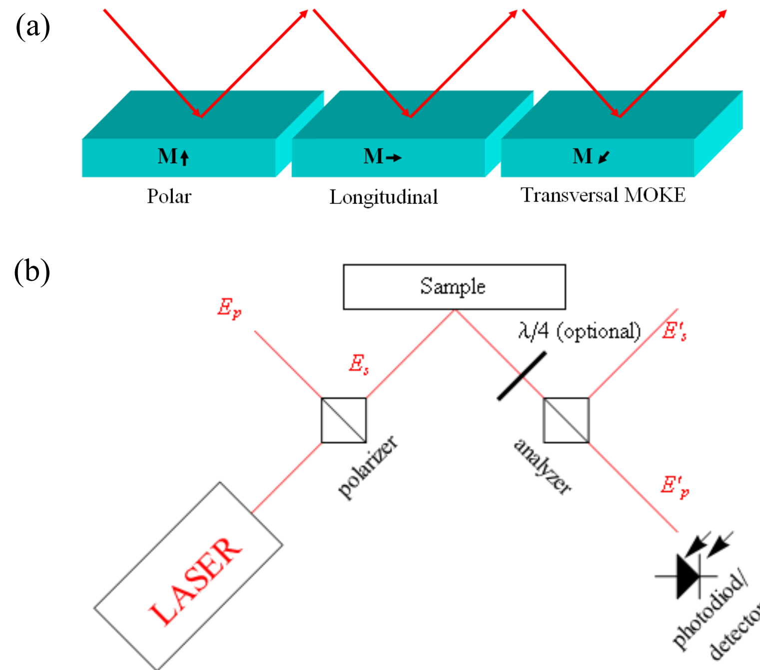

Figure 1-17. Magneto-optic Kerr effect. (a) Polar, longitudinal and transversal MOKE. (b) Optical setup for MOKE. Reference: [30].

Vibrating sample magnetometer (VSM) is one of the techniques for quantifying the remanent or saturation magnetization. Fig. 1-18 shows VSM measurement setup. The sample is mounted onto a rod holder that is sinusoidally mechanically vibrated between two pickup coils. Following Faraday's law of induction, the voltage generated in the pickup coil is proportional to the magnetic moment of the sample. Depending on the sample surface's orientation with respect to the magnetic field direction, the VSM can characterize the in-plane or out-of-plane magnetization with quantified magnetic information, i.e., VSM gives values for remanent and saturation magnetization.

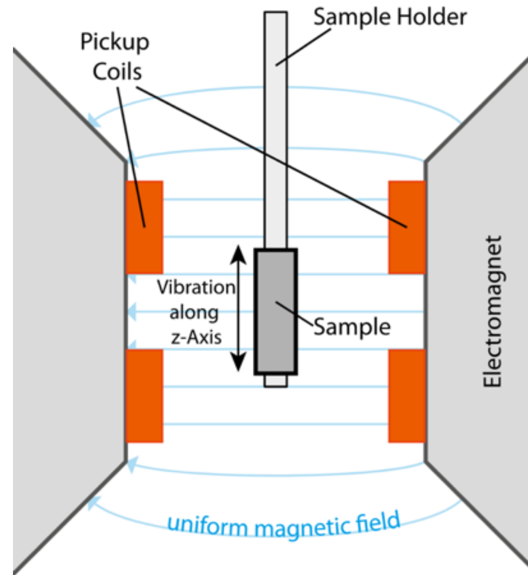

Figure 1-18. Vibrating sample magnetometer. Reference: [31].

Both MOKE and VSM measure the total magnetic moment of the magnetic sample being detected by the laser spot or put inside the sample holder, and cannot be used to characterize the magnetization of microscale or nanoscale devices. For these smaller geometries, a Hall bar defined by a cross shape structure can be used to characterize magnetization at the device-level. Generally, a current is applied to one arm of the cross while the voltage is measured in the other arm that is perpendicular to the applied current, and the Hall resistance is defined as the measured voltage divided by the applied current. Depending on different Hall effects, the Hall resistance can be used to characterize some of the magnetic properties. For example, the ordinary Hall effect refers to moving electrons deflecting under external magnetic field due to Lorentz force, leading to a potential difference across the conductor. The ordinary Hall resistance is proportional to the external field, hence it is used in Hall sensor to measure the magnetic field.

There are other types of Hall effects, including anomalous Hall effect, planar Hall effect, spin Hall effect, quantum Hall effect, etc.

In this work, we mainly use anomalous Hall effect in order to measure perpendicular magnetization of the magnetic device. As shown in Fig. 1-19, when an ordinary current passes near the ferromagnetic material, depending on the perpendicular magnetization of the ferromagnetic material, a voltage difference may be generated perpendicular to the current direction. We use anomalous Hall effect to characterize the PMA effect of the magnetic layer as well as perpendicular magnetic switching.

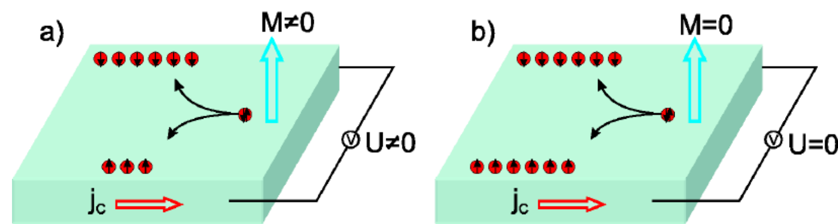

Figure 1-19. Anomalous Hall effect. Reference: [32].

1.4.2 Piezoelectric characterization

The ferroelectric property is characterized by measuring the P-E (polarization-electric field) hysteresis loop, which is usually done through Sawyer-Tower circuit. Fig. 1-20 (a) shows a normal P-E loop and the definition of saturation and remanent polarization, as well as coercivity electric field. Fig. 1-20 (b) illustrates a simplified Sawyer-Tower circuit for polarization measurement. The ferroelectric material is connected with a reference capacitor (or shunt capacitor C_{shunt}) in series. An alternate voltage is used as the input signal, and an oscilloscope is used to measure the voltage across the shunt capacitor V_{shunt}. The shunt capacitance is designed to be much higher than the ferroelectric sample capacitance, hence most of the voltage drop

happens in the ferroelectric sample. The charge across the ferroelectric film can be estimated by the charge accumulated on the shunt capacitor, which can be easily calculated as $Q = C_{shunt} \times V_{shunt}$ if the shunt capacitor has high quality and low leakage.

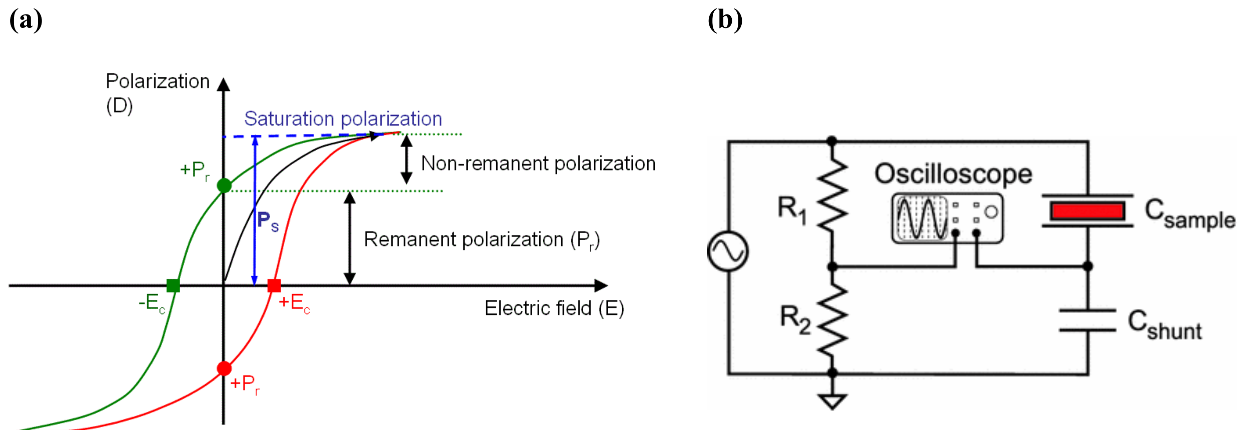

Figure 1-20. Ferroelectric characterization. (a) P-E loop example, reference: [33]. (b) Sawyer-Tower circuit for polarization measurement, reference: [34].

The piezo-strain can be directly measured using commercialized strain gauge. The working principle is illustrated in Fig. 1-21.

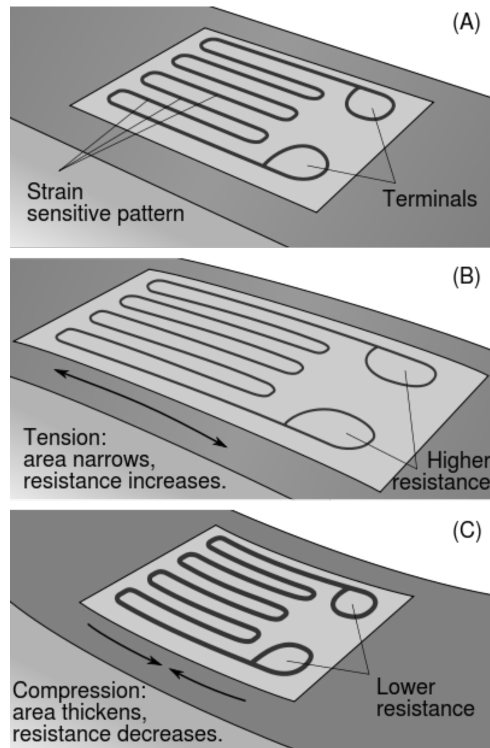

Figure 1-21. Working principle of strain gauge. Reference: [35].

A strain gauge typically has a zig-zag wire pattern, and the wires get elongated with resistance increased under tensile strain along the parallel wire direction. In contrast, the resistance decreases under compression along the parallel wire direction. The strain gauge is an easy way to directly measure the strain response for bulk piezoelectric material within the range 100 ~ 3000 ppm. A continuous top and bottom electrodes need to be deposited onto the bulk piezoelectric material, and the strain gauge is then glued on the top electrode. Note the strain gauge only measures the in-plane uniaxial strain components, and the measured strain is the surface average of the area covered by the strain gauge, e.g. typically millimeters. Biaxial in-plane strain can be measured using two strain gauge with wires arranged perpendicular with each other.

For piezoelectric thin films, it is challenging to directly measure the strain response using strain gauge because the in-plane strain generated by continuous electrode is relatively small (~10 ppm) due in part to substrate clamping. To overcome substrate clamping patterned electrodes are used for the piezoelectric PZT thin film generating reasonable localized strain (~1000 ppm).[36] One approach to further characterize piezoelectric property of thin films is to use piezoresponse force microscopy (PFM).

PFM is an advanced measurement mode in atomic force microscopy (AFM) using a special probe tip coated by metal layer. Fig. 1-22 demonstrates the working principle of PFM. An alternate electric field is applied by applying voltage to the metalized tip that sits directly onto the piezoelectric sample surface. The sample deformation is detected in a similar fashion to AFM, i.e., a laser spot is reflected by the probe cantilever and the vertical movement of the cantilever can be measured by a photodiode detector. The output signal's phase provides polarization information of the piezoelectric sample. Using PFM to do x-y plane scanning provides the information of the domain structure of the ferroelectric film.

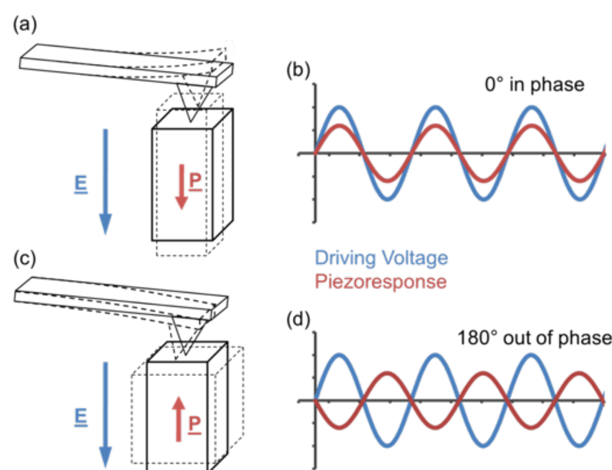

Figure 1-22. Piezoresponse force microscopy principle. Reference: [35].

Another way to operate PFM is to probe the deformation while ramping the voltage. This can provide the information of piezoelectric coefficient of the substrate. Fig. 1-23 shows the theoretical vertical deformation of the sample surface as a function of applied voltage under and above the electrical coercive voltage. When the applied voltage is smaller than the coercive voltage, the deformation should have a linear response and the slope of the z-V curve represents a good estimation for piezoelectric coefficient d33. When the applied voltage is above coercive voltage, a butterfly loop arises due to polarization reversal at coercive voltage.

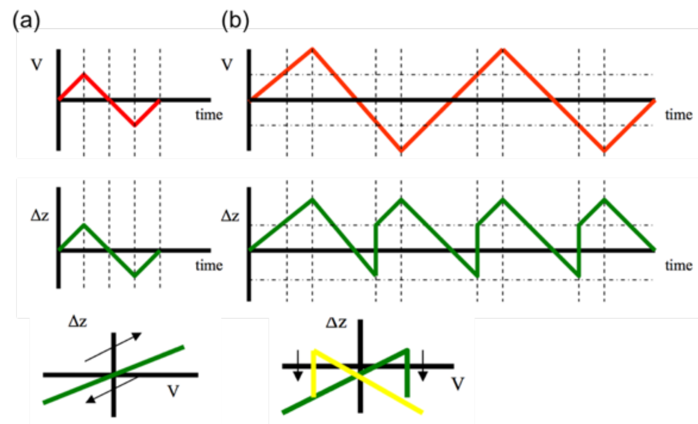

Figure 1-23. Piezoresponse force microscopy with ramp voltage mode. (a) Measurement under coercive voltage. (b) Measurement above coercive voltage. Reference: [37].

Chapter 2. Strain-mediated perpendicular magnetization control: simulation

2.1 Recent progress of simulations

Quasi-static model

Stoner-Wohlfarth model (SW model) is a quasi-static model that predicts equilibrium states for the magnetic system. The method is based on minimization of the system's free energy assuming single domain and coherent magnetization behaviors. Using SW model, Chiba et al (2010) simulated quasi-static magnetic switching controlled by electric field. [38] Atulasimha et al (2010) [39] used a single spin model to simulate strain-mediated multiferroic Bennett clocking. The energy terms are expressed as:

$$E_{total} = E_{dipole} + E_{shape} + E_{stress} \qquad \text{Eq. 2-1}$$

where E_{dipole} is the dipole-dipole interaction energy between nearest neighbors, E_{shape} is the shape anisotropy energy, and E_{stress} is the energy caused by the voltage induced stress. Specifically, the stress-induced anisotropy is expressed as:

$$E_{stress} = -\frac{3}{2}[\lambda_S \sigma V] sin^2\theta \qquad \text{Eq. 2-2}$$

where λ_S is the saturation magnetostriction, σ is the applied stress, V is the volume of the Nickel nanomagnet, and θ is the angle between the magnetization and the applied stress.

LLG equation – macrospin model

The SW model cannot provide dynamic information of the magnetic switching, thus it is not a useful tool to evaluate switching speed or switching incoherency. To obtain temporal information of magnetization change, a more complete set of LLG equations needs to be solved for dynamic simulation.

One approach to simulate magnetic switching with LLG equation is a macrospin model, where the whole magnetic element is treated as a single spin. Therefore, the exchange anisotropy is ignored and the demagnetization anisotropy (or shape anisotropy) is calculated using demagnetization factors. The equation used for magnetoelastic anisotropy induced by strain can be found in Eq. 1-10 in Chapter 1. Roy et al (2012) simulated an in-plane multiferroic nanomagnetic by solving a stochastic LLG equation with thermal fluctuations added. [40] The energy efficiency of strain-mediated multiferroic control was predicted to be 2aJ at room temperature. The impact of voltage ramp rate was also investigated. The PZT response time was estimated to be below 1 ps using a simple resistance-capacitance (RC) circuit assumption.

LLG equation – micromagnetic simulation

Micromagnetic simulations also use a mesh to represent regions of the magnetic material by dividing it into small unit cells. In each unit cell the assumption is that the magnetization is representative of a single spin. This assumption holds when the size of the unit cell is much smaller than the single-domain limit of the magnetic material, which is usually 1~10 nm. The strain is usually considered as a constant input in micromagnetic. An open source framework, object-oriented micromagnetic framework (OOMMF) is readily available to implement the micromagnetic simulation with that the strain is uniform in the magnetic regions. There are several researches on using micromagnetic simulation to study magnetoelastic coupling and a

few are highlighted here. Aimon et al [41] studied the magnetic response of CFO/BFO multiferroic composite. Yahagi et al [42] studied the dynamics of nanomagnetic periodic arrays triggered by acoustic wave through magneto-elastic coupling. Gilbert et al [43] investigated the strain-mediated magnetization reorientation in nanoscale Ni disks on PMN-PT substrate. Zhao et al [18] examined the strain effect on the magnetization of both free layer and fixed layer of the in-plane MTJ stack patterned on PMN-PT substrate. Chavez et al [44] simulated the dipole coupling between two Ni nanodots and showed the strain induced magnetoelastic anisotropy can be used to tune the dipole coupling.

LLG equation – micromagnetics with elastodynamics

Liang et al [45] developed a finite element model for analytically solving LLG equation, and simulated strain-mediated magnetization control of a single domain Ni structure on PZT thin layer. The weak forms of the coupled PDEs that govern electrostatics, elastodynamics, micromagnetics are solved by finite element analysis, giving the all transient states during the switching process. The M-H hysteresis loop of a nanoscale Ni structure with in-plane magnetic anisotropy was simulated using the finite element model, and the results was compared to previous models.

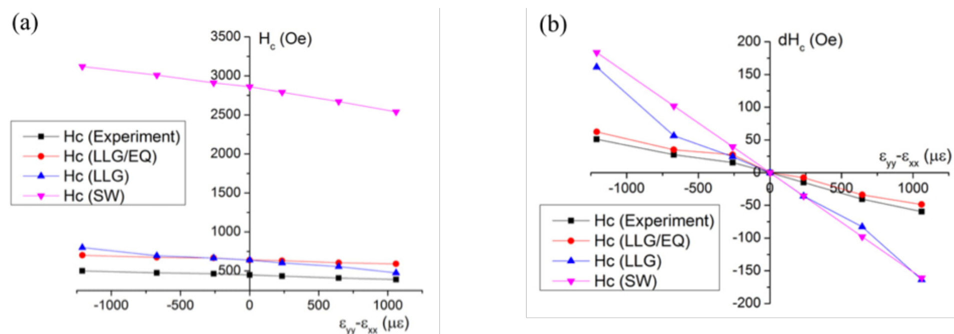

Figure 2-1. The coercivity field Hc change by biaxial strain $\varepsilon_{yy} - \varepsilon_{xx}$. Reference: [45].

As shown in Fig. 2-1, the model proposed by Liang (LLG/EQ) is superior to SW model and pure LLG model that does not take elastodynamics into consideration during the computation, and the simulation matches well with experimental data. It should be emphasized that the converse magnetoelastic effect (i.e., the change of magnetization affects strain distribution) is also taken into consideration in this FEM coupled simulation.

Later on, Liang et al added piezoelectric constitutive equations into the simulation and simulated a nanoscale Ni disk controlled by patterned electrodes on PZT substrate. The representative results are shown in Fig. 2-2. In that study, they demonstrated that the in-plane magnetization of Ni can be rotated 90° by applying voltage to different pair of electrodes.

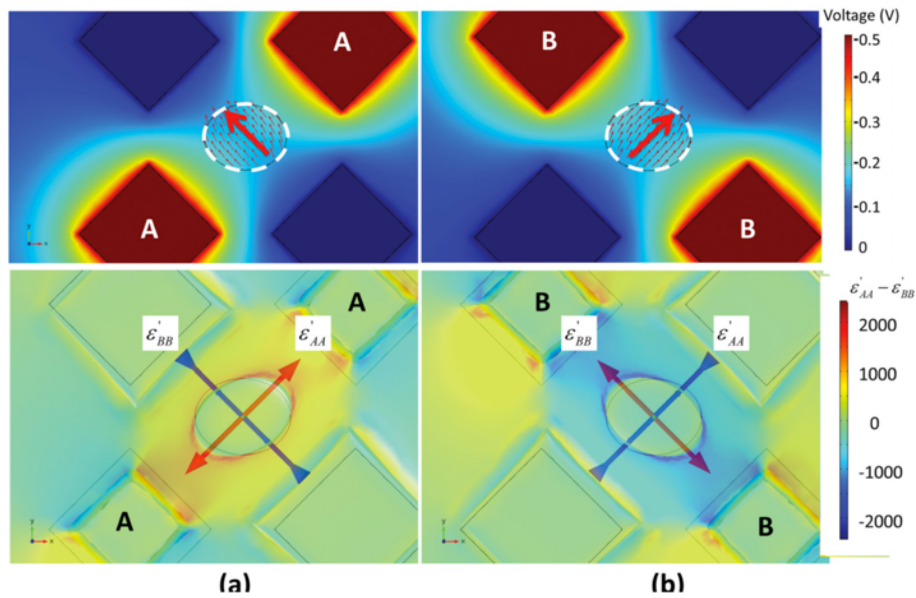

Figure 2-2. Finite element model simulation results of strain-mediated in-plane magnetization control. Reference: [46].

2.2 Strain-mediated 180° perpendicular magnetic switching

2.2.1 Motivation

Magnetic memory has attracted substantial attention due to its promise of high energy efficiency combined with non-volatility. In this context, magnetization is conventionally controlled using spin-transfer torque (STT).[47], [48] More recently, spin-orbit torque (SOT)[49]–[51] has been considered as a more efficient mechanism to control magnetization, but SOT, like STT, relies on switching via an applied electrical current. Such nanoscale current-based switching methods produce substantial ohmic heating losses resulting in inefficiencies. As a result, considerable effort is being directed toward voltage-control of magnetism to eliminate the need for high switching currents and thereby reduce the ohmic losses.[52]–[55] One promising voltage control method is strain-mediated multiferroics (composites between magnetostrictive and piezoelectric thin films)[56], [57] which provide ultra-high energy efficiency[20]. However, few studies exist to analyze the more interesting multiferroic materials, like CoFeB and Terfenol-D, with perpendicular magnetic anisotropy (PMA) where 180° out-of-plane (OOP) magnetization reversal is possible.

Previous strain-mediated multiferroic studies have demonstrated 90° in-plane magnetic switching both experimentally[18], [36] and theoretically[46]. Complete 180° magnetic reversal in-plane has been analytically demonstrated using either four-fold symmetric shape anisotropy[58], [59] or precessional switching[15], [60], [61]. Similarly, 180° strain-mediated in-plane precessional switching of CoFeB has been computationally demonstrated[62]. However, attention to in-plane magnetic memory elements has decreased because the element sizes needed for thermal stability are sufficiently large to cause multi-domain formation that leads to

inefficient and complicated switching dynamics.[63] This problem can be avoided by using nanopatterned memory elements that exhibit PMA, which have higher thermal stability at comparably smaller length scales.[22], [64] In addition, many previous strain-mediated switching simulations consider only one-way coupling from mechanics to magnetics.[58], [59], [61] In contrast, our model reflects the bi-directional influence including magnetization changes on strain distribution. The two-way coupling makes a noticeable difference in magnetoelastic materials.[43] Some other papers use fully coupled model to simulate strain-mediated perpendicular switching based on Ni system,[15], [60] however, these studies did not model multiferroic materials that are interesting to memory application, i.e. CoFeB and Terfenol with PMA effects. As a result, a study is needed to investigate out of plane OOP strain-mediated switching in memory relevant materials which considers the full magnetostriction coupling to more accurately predict energy and switching requirements.

In this study, we develop a numerical finite element model which incorporates micromagnetics and elastodynamics to evaluate the temporal response of a magnetoelastic nanodot exhibiting PMA. In particular, our study compares OOP switching of CoFeB, which is widely used in proposed MRAM (magnetoresistive random-access memory) applications, and Terfenol-D ($Tb_{0.7}Dy_{0.3}Fe_2$), which is well known for its giant magnetostriction at room temperature. This comparison is intended to highlight the differences in switching dynamics between the two materials and suggest using Terfenol-D as a benchmark for energy efficient switching with realistic geometries for strain-mediated multiferroic composites.

2.2.2 Simulation setup

The model assumes linear elasticity, linear piezoelectricity, and electrostatics. Thermal fluctuations, which can lead to switching errors, are not considered in this model as they would require a stochastic approach as used by others.[65], [66] The mechanical loss of PZT substrate is assumed negligible due to the relatively low damping of linear PZT formulations.[67] The behavior of the piezoelectric thin film follows linear piezoelectricity:

$$\boldsymbol{\varepsilon} = s_E : \boldsymbol{\sigma} + d^t \cdot \boldsymbol{E} \qquad \text{Eq. 2-3}$$

$$\mathbf{D} = d : \boldsymbol{\sigma} + e_\sigma \cdot \boldsymbol{E} \qquad \text{Eq. 2-4}$$

where $\boldsymbol{\varepsilon}$ is strain, $\boldsymbol{\sigma}$ is stress, $\mathbf{D}$ is electric displacement, $\mathbf{E}$ is electric field, s_E is the piezoelectric compliance matrix under constant electric field, d and d^t are the piezoelectric coupling matrix and its transpose, and e_σ is electric permittivity matrix measured under constant stress. The magnetic state of equilibrium is determined by the minimum of the total energy density:

$$E_{total} = E_{me} + E_{exch} + E_{demag} + E_{perp} \qquad \text{Eq. 2-5}$$

where E_{exch} is the exchange energy density[46], E_{demag} is the demagnetization energy density[46], E_{perp} is the perpendicular anisotropy (PMA) energy density, and E_{me} is the magnetoelastic energy density[24] and has the following form for cubic materials:

$$E_{me} = B_1[\varepsilon_{xx}\left(m_x^2 - \frac{1}{3}\right) + \varepsilon_{yy}\left(m_y^2 - \frac{1}{3}\right) + \varepsilon_{zz}\left(m_z^2 - \frac{1}{3}\right)] + B_2[\varepsilon_{xy} m_x m_y + \varepsilon_{yz} m_y m_z + \varepsilon_{zx} m_z m_x] \qquad \text{Eq. 2-6}$$

where m_x, m_y and m_z are components of normalized magnetization along $\hat{x}$, $\hat{y}$ and $\hat{z}$, B_1 and B_2 are first and second order magnetoelastic coupling coefficients. The electric field induced strain in the piezoelectric layer (Eq. 2-3) couples with the magnetization in the magnetoelastic nanodots through E_{me}. The definition of E_{total} in Eq. 2-5 assumes that the magnet's grain size is

smaller than a magnetic exchange length, which results in a magnetocrystalline anisotropy energy density that is negligibly small. The PMA energy density is formulated using a phenomenological PMA coefficient, K, which can account for interfacial effects as well as residual stress:

$$E_{perp} = Km_z^2 \qquad \text{Eq. 2-7}$$

The precessional magnetic dynamics are governed by the Landau-Lifshitz-Gilbert (LLG) equation:

$$\frac{\partial \boldsymbol{m}}{\partial t} = -\mu_0 \gamma \left(\boldsymbol{m} \times \boldsymbol{H}_{eff}\right) + \alpha \left(\boldsymbol{m} \times \frac{\partial \boldsymbol{m}}{\partial t}\right) \qquad \text{Eq. 2-8}$$

where $\boldsymbol{m}$ is the normalized magnetization, μ_0 is the vacuum permittivity, γ is the gyromagnetic ratio and α is the Gilbert damping parameter. $\boldsymbol{H}_{eff}$ is the effective magnetic field that is obtained by taking the derivative of total energy density (Eq. 2-5) with respect to the magnetization $\boldsymbol{m}$. The magnetization and displacement variables can be computed simultaneously in time domain by solving the coupled partial differential equations in weak form using the finite element method. This approach and solution process follows the work of Liang et al[45], [46] and is therefore not repeated. The coupled solutions yielded by this process contain 3 displacement components, 3 components of magnetization, scaler magnetic potential, and the electric potential. To be specific, the approach solves simultaneously the coupled magnetization and displacement variables to develop an accurate solution.

The multiferroic system analyzed with this model is illustrated in Fig. 2-3(a). The system consists of a ferromagnetic element (of 50nm diameter) on the top surface of a PZT thin film, which has a poling direction along the out of plane $\hat{z}$. The PZT layer is 600nm×600nm×100nm,

and both the bottom surface and side boundaries of the PZT layer are considered mechanically fixed, i.e. continuous PZT attached onto a thick silicon substrate. Two 50 nm×50 nm conducting top electrodes are located along $\hat{x}$, 20nm away from the outside edge of the magnetic nanodot. The bottom side of the PZT, which is adjacent to the Si substrate, is electrically grounded.

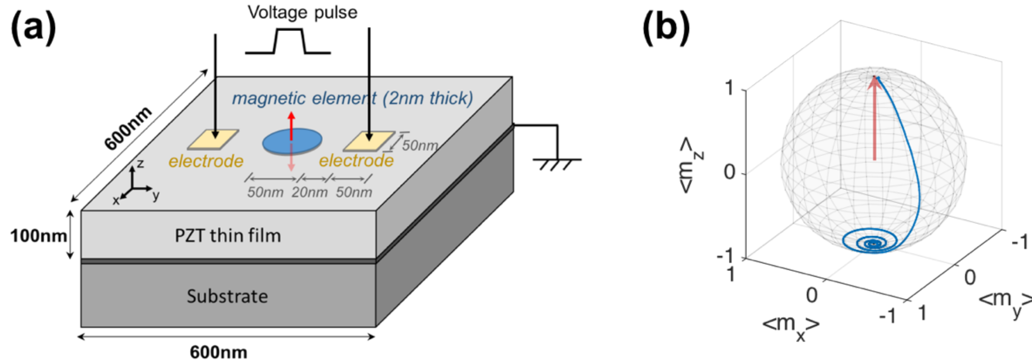

Figure 2-3. (a) Model setup illustration. (b) Schematics of 180° precessional magnetization switching.

A positive voltage is applied to both top electrodes to induce an anisotropic strain with compression along $\hat{y}$ and tension along $\hat{x}$.[36] The magnetic materials (CoFeB and Terfenol-D) have a positive λ_s so the magnetization tends to re-align in-plane along the tensile axis $\hat{x}$ when voltage is applied. By accurately timing the voltage pulse, 180° magnetic switching can be achieved. This is commonly referred to as precessional switching and has been described in several papers.[15], [60], [61] The thickness of the CoFeB element exhibiting PMA was 1.6nm to ensure thermal stability. In other words, the energy barrier is sufficiently large to prohibit spontaneous magnetic switching at room temperature: $\Delta E_b > 40k_BT \approx 0.2aJ$. For crystalline Terfenol-D, the thickness was 2nm due to the PMA mechanism being used and is discussed in the following paragraph. The material parameters for CoFeB[22], [68]–[70] and Terfenol-D[71]–[73] used in the model are provided in Table I.

The PMA effects in CoFeB and Terfenol-D are known to differ in strength and cause. The PMA effect in CoFeB originates from interfacial effects.[22] In this case, the coefficient K in the E_{perp} term in Eq. 2-7 is inversely proportional to the CoFeB thickness, $\mathrm{K} = -K_i/t_{CoFeB}$, where K_i is the interfacial anisotropy coefficient K_i = 1.3mJ/m^2.[22] For amorphous Terfenol-D and crystalline Ni, it has been experimentally demonstrated that PMA is produced during deposition by stresses generated from thermal coefficient and/or lattice mismatches between the film and substrate.[74], [75] In this work, the PMA is produced in Terfenol-D by deposition induced in-plane residual stress in thicknesses similar to those reported for Ni (2nm)[76] and ensure an energy barrier >$40k_BT$. The PMA coefficient can be estimated from $E_{perp} = Km_z^2 = \frac{3}{2}\lambda_s\sigma$ as $K = -3.4\times10^5\ J/m^3$.

Table 1. Parameters for CoFeB and Terfenol-D used in the model.

Parameter	Description	Units	CoFeB	Terfenol-D
M_s	Saturation magnetization	A/m	1.2×10^6	8×10^5
α	Gilbert damping factor	-	0.01	0.06
A_{ex}	Exchange stiffness	J/m	2×10^{-11}	9×10^{-12}
λ_s	Saturation magnetostriction coefficient	ppm	50	1200
E	Young's modulus	GPa	160	80
ρ	Density	kg/m^3	7700	9210
ν	Poisson's ratio	-	0.3	0.3

2.2.3 Results and analysis

Fig. 2-4(a) shows the volume averaged magnetization components for a CoFeB element as a function of time when released from a canted direction (1,1,1). The plot illustrates the

normalized magnetization components m_x, m_y and m_z as the spin preccesses toward $+\hat{z}$. The inset in the figure shows the 3D trajectory of the magnetization precession. Fig. 2-4(b) plots m_z as a function of time as three different voltages are applied to the two side electrodes shown in Fig. 2-3(a). These voltages are applied after the magnetization reaches equilibrium, as illustrated in Fig. 2-4(a). The magnetization undergoes 180° reorientation (from $+\hat{z}$ to $-\hat{z}$) for all applied voltages here. A reduction in switching time is observed as the magnitude of the exciting voltage pulse is increased from 2.8V to 4V. Compared to this, a smaller reduction is observed when voltages are increased even further (from 6V to 8V). This trend shows that, in general, larger voltages produce shorter flipping times but that this effect reaches a limit at high voltages.

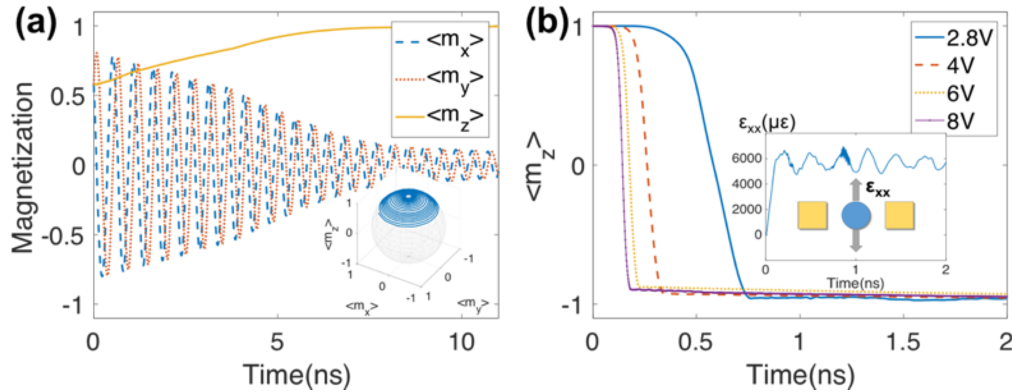

Figure 2-4. Simulation results of 180° perpendicular switching of CoFeB.

The minimum voltage required to achieve 180° flipping in CoFeB is 2.8V (corresponding to an electric field of 28MV/m). The associated dissipation energy: $E = \frac{1}{2}QV = 29.6fJ$, where Q is the total charge on the two electrodes and V is the voltage applied to the electrodes. This energy can be substantially lowered by changing the memory bit geometry or by selecting more aggressive estimates for the magnetostrictive properties of CoFeB which have been reported.[77] The inset of Fig. 2-4(b) plots the volume averaged strain along $\hat{x}$, ε_{xx}, inside the CoFeB nanodot

as a function of time for an applied 2.8V. The data shows strain increases with voltage ramping to the targeted level, and then oscillates around this equilibrated level.

For CoFeB, the exchange length is $L_{ex} = \sqrt{\frac{2A_{ex}}{\mu_0 M_s^2}} = 4.70$ nm. This metric can be used to approximate the single-domain limit of CoFeB as: $L_{SD} \approx 10L_{ex} = 47nm$; a size which is similar to the CoFeB element studied here (50nm diameter). As a result, one would predict a risk of incoherent magnetization reversal given the nanodot size, but our model predicts incoherency only when the applied voltages and ramp speeds become much higher than those considered here (e.g. when 20V is applied in 0.1ns). Such incoherent switching at high voltage is attributable to the generation of strain gradients or non-uniformity inside the magnetic element. Similarly, if the frequency content of the strain ramping function is higher than ferromagnetic resonance (FMR), non-uniform magnetic excitations, like spin wave modes, may be generated which can also lead to incoherent flipping. As a consequence, we suggest that incoherent switching can be avoided by lowering either the applied voltage or increasing the ramp time, although both methods will adversely affect switching speed. The trade-off between high voltage, fast ramp time, and incoherent flipping defines a temporal bound on switching speed in a multiferroic memory bit.

Fig. 2-5(a) shows magnetization versus time for a single CoFeB element subjected to the 2.8V voltage pulses presented in Fig. 2-5(b). The pulse durations required for the three flips in Fig. 2-5(a) are 0.65ns, 0.2ns and 0.26ns, which are much longer than relaxation time RC of PZT substrate (resistance-capacity product RC $\approx$ 0.2ps).[78] A simple calculation shows that, the required time for the mechanical wave to propagate from the electrodes to the magnetic nanodot is around 4.4ps (wave speed $v = \sqrt{E/\rho} \approx 4558 \mathrm{m/s}$, distance 20nm), which is 1~2 orders faster than the pulse duration needed for 180° switching. Consequently, even though mechanical

damping of PZT substrate may influence the acoustic wave propagation characteristics, the impact on switching timing is believed to be negligible.

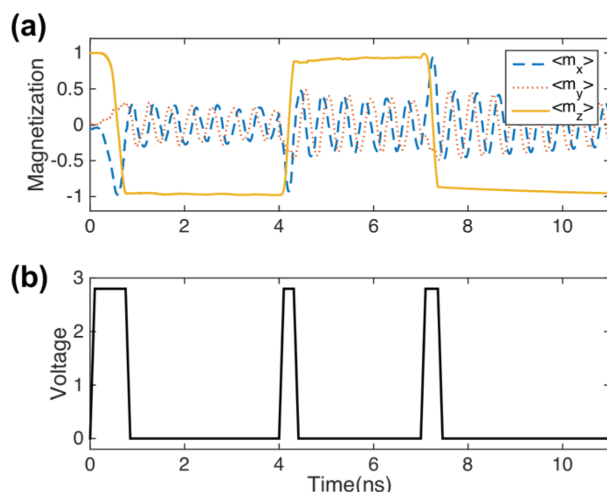

Figure 2-5. Consecutive 180° perpendicular switching of CoFeB.

Fig. 2-5 shows that the second and third voltage pulses are initiated prior to the magnetization reaching equilibrated state, i.e. while m_x and m_y are still oscillating. These pulses applied to a non-equilibrium state produce 180° switching times three times faster than if only an initial pulse is applied to an equilibrium state. This suggests that successive memory writing steps can proceed without waiting for complete magnetic relaxation. As a result, magnetic switching can be repeated at frequencies higher than $1/t_{relax}$, where t_{relax}>10ns from Fig. 2-4(a).

Figure 2-6(a) shows the magnetization precession of Terfenol-D under similar conditions as described in Fig. 2-4(a) for CoFeB. However, Terfenol-D's oscillation decays more rapidly than CoFeB's due to Terfenol-D's higher Gilbert damping parameter (α_{TD}= 0.06 whereas α_{CoFeB}= 0.01).

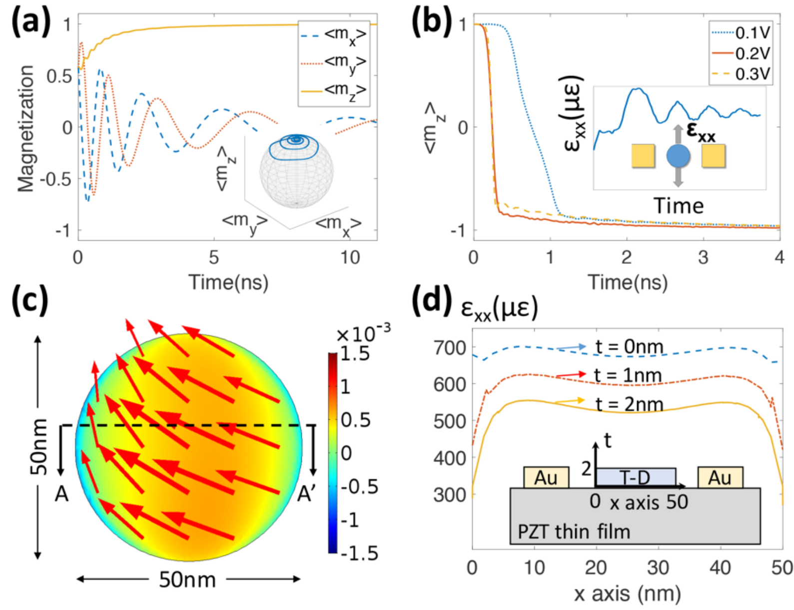

Figure 2-6. Strain-mediated perpendicular switching of crystalline Terfenol-D.

Figure 2-6(b) shows the magnetic response of Terfenol-D when 0.1V, 0.2V and 0.3V voltage pulses are applied at the PZT's top surface electrodes. The inset of Fig. 2-6(b) shows the volume averaged strain oscillations when 0.1V is applied to the electrodes. Results show that 0.2V (i.e. 2MV/m) produces a fastest switching time in Terfenol-D of 0.31ns, a time that is comparable CoFeB's fastest switching (0.2 ns). The minimum voltage required to flip Terfenol-D is 0.1V (an electric field of 1MV/m). This corresponds to an energy dissipation of 22aJ, three orders of magnitude less than is needed to switch CoFeB (29.6fJ) due to Terfenol-D's substantially larger λ_s (see Table 1).

While Terfenol-D requires less voltage and energy than CoFeB to magnetically switch, it does so at the expense of decreased coherency. It can be seen from Fig. 2-6(b) that switching speed for the 0.3V and 0.2V Terfenol-D cases are similar. This is because the incoherent behavior in Terfenol-D begins to appear at lower voltages, near 0.3V (for CoFeB, this occurs

near 20V). This difference is unrelated to exchange effects, as Terfenol-D's exchange length is similar to CoFeB's ($L_{ex}(TD) = 4.73nm$). Instead, Fig. 2-6(c)-(d) shows that the low voltage incoherence is due to the larger magnetoelastic coupling present in Terfenol-D, which causes the spin states to couple more strongly with any non-uniform strain distribution inside the nanodot. The high magnetoelasticity also produces additional mechanical non-uniformities due to substrate clamping and shear lag, which will be discussed later.

Fig. 2-6(c) shows a contour plot of ε_{xx} as the magnetization reaches a steady state in-plane configuration under an applied 0.3V excitation, where incoherence begins to occur. The color bar shows that the strain varies as a function position with all strain magnitudes below $1000\mu\varepsilon$. The red arrows in Fig. 2-6(c) indicate an instantaneous snapshot of the in-plane magnetization components in the Terfenol-D nanodot as the spins rotate in-plane. The direction and amplitude of the arrows highlight the incoherence across the diameter of the dot. To quantify the strain non-uniformity inside the dot, ε_{xx} distribution along the cross section AA' in Fig. 2-6(c) is plotted. In Fig. 2-6(d), ε_{xx} is displayed as a function of position (in both the lateral and vertical directions) for the 0.3V case. The strain decreases $\sim 150\mu\varepsilon$ from the Terfenol-D/PZT interface to Terfenol-D's free top surface, and from the center to the edges of the Terfenol-D along the radial direction. The Terfenol-D/PZT interface exhibits more uniform strain than Terfenol-D's free top surface due to the clamping of Terfenol-D by the PZT surface. This is the classical shear lag problem described previously by Liang et al. for magnetoelastic elements.[46] While similar strain non-uniformity is also present in the CoFeB dot, the spin coupling to these mechanical states is weaker, and the magnetic state is instead dominated by the shape and exchange anisotropies. Thus, the CoFeB magnetic orientation rotates more coherently than Terfenol-D's

for similar geometric and excitation conditions. This indicates that there is a trade-off between energy efficiency and coherence of switching in multiferroic memory devices.

In conclusion, the simulation results presented here demonstrate energy efficient 180° OOP switching in CoFeB and Terfenol-D nanodots through voltage-induced strain. A fully coupled micromagnetic and elastodynamic model is used to capture the incoherent multiferroic switching behavior of CoFeB and Terfenol-D in extreme cases of high and low, and fast and slow, voltage excitation. The model also clarifies the influence of magnetostrictive properties to couple with non-uniform strain states. A trade-off exists between energy efficient switching and coherence of magnetic rotation. In particular, high magnetoelastic coefficients contribute to high energy efficiency but simultaneously may cause incoherent switching in the presence of non-uniform strains. Results show that 180° OOP magnetic bit flips can be both ultrafast (<0.5ns) and energy efficient (29.6fJ for CoFeB and 22aJ for Terfenol-D). This work validates the feasibility and efficiency of strain-mediated perpendicular magnetic memory, which will prove crucial for next generation ultralow power magnetic memory and logic devices. The electrode/bit design in this work focused on structures that can be easily fabricated. However, additional work is needed on electrode designs to increase strain mediated multiferroic memory bit density in the future.

2.3 Strain-mediated perpendicular Bennett clocking

Nanomagnetic logic (NML) has attracted attention during the last two decades due to its promise of high energy efficiency combined with non-volatility. Data transmission in NML relies on Bennett clocking through dipole interaction between neighboring nanomagnetic bits. This dissertation uses a fully coupled finite element model to simulate Bennett clocking based on strain-mediated multiferroic system for Ni, CoFeB and Terfenol-D with perpendicular magnetic

anisotropies. Simulation results demonstrate that Terfenol-D system has the highest energy efficiency, which is 2 orders of magnitude more efficient than Ni and CoFeB. However, the high efficiency is associated with switching incoherency due to its large magnetostriction coefficient. It is also suggested that the CoFeB clocking system is slower and has lower bit-density than in Ni or Terfenol-D systems due to its large dipole coupling. Moreover, we demonstrate that the precessional perpendicular switching and the Bennett clocking can be achieved using the same strain-mediated multiferroic architecture with different voltage pulsing. This study opens new possibilities to an all-spin in-memory computing system.

2.3.1 Literature review and motivation

In modern electronics based on CMOS, levels of electric charge are encoded as binary bits '0' or '1'. Since charge is a scalar value, we can only change the magnitude of charge. For example, we define more change as logic bit 0, and less charge represent bit 1. Switching between the two states requires changing the magnitude of charge, which involves current flow thus has unavoidable Joule dissipation I^2R. In nanomagnetics, we encode the magnetization direction of nanomagnet as bit '0' or '1'. Switching magnetization is actually flipping electron spins. There is no need for macroscopic movement of electrons hence promises ultra-low energy dissipation.[78]–[80] The information is transferred using unidirectional magnetization propagation with dipole interaction between neighboring bits referred to as Bennett clocking.[39], [78], [81]

The concept of using electronic spin to represent binary bits can track its history back to 1980s. It is predicted that the spin based quantum computing can reach Landauer-Shannon limit of kTln(1/p), where p is the error probability.[81] In 1994, Bandyopadhyay et al translated this

concept into practice.[82] He pointed out that antiferromagnetism is the basis of computing paradigm. Also, it is reasonable to assume that only take into account nearest-neighbor interaction, because spin-spin coupling is short range and decays exponentially with distance. Bandyopadhyay proposed designs for NOT, AND, and NAND gates, which lay the foundation for later NML design.

In 1999, Amlani et al proposed an interesting configuration called magnetic quantum celluar automata (MQCA) and showed its ability to perform logic operations. However, the device required extremely low temperature (~1K) owing to small charging energies achievable with the fabrication technique.[83] The name ‘quantum’ is because it used quantum mechanical tunneling of charge between neighboring dots to switch logic state.

In 2005, a group from University of Notre Dame experimentally demonstrated the magnetic switching of MQCA wires using the external magnetic field, also known as clocking field.[84] The clocking field helped to align magnetization of all dots along hard axis. After it was removed, the dots can release into their favorable states by forming antiferromagnetic ordering. This process is later called Bennett clocking. This is the first time that experimentally shows magnetic interactions between nanomagnets are strong enough to allow room-temperature operation. In 2006, the same group realized majority logic gates using MQCA system with assistance of external magnetic field.[85] The state of the central nanomagnet is determined by the majority vote of its three input neighbors. Due to shape anisotropy, the easy axis is along the long axis of the ellipse. The neighbors along long axis vote for ferromagnetic ordering while the neighbor along short axis votes for antiferromagnetic ordering. The three input can be determined by applying horizontally external clocking field. It can be shown that this device can

function as either NAND or NOR gate by changing the first-input bit value. This is the first experimental demonstration of using Bennett clocking for Boolean logic operation. However, the three inputs are not independent, i.e., they cannot be controlled individually, which limits the device's application potential.

The key to realize Bennett clocking is the generation of the clocking field. The common way to generate clocking fields is with an oscillating magnetic field either from external application[84], [86] or on-chip generation by current through a wire[87]. Researchers have also experimentally demonstrated Bennett clocking using spin Hall effect.[88] However, both methods require high energy input (~100 fJ per flip[78]), thus sacrificing the intended advantage of NML, i.e. low energy dissipation. An alternative approach uses a strain-mediated multiferroic system representing an energy efficient technique to control nano-scale magnetic anisotropies.[18]–[20], [36] Strain-mediated Bennett clocking has been demonstrated by both simulation[17], [78], [89]–[92] and experiment[93]. While the energy efficiency (~100 aJ per flip[78], [93]) of strain-mediated Bennett clocking has been demonstrated, these studies are limited to in-plane magnetic system and analysis uses an oversimplified uncoupled macrospin model to understand the process. Compared to in-plane bits, nanomagnets with perpendicular magnetic anisotropy (PMA) are more promising due to the smaller bit size producing higher information density.[22], [64] Furthermore, the dipolar interaction between PMA dots is less susceptible to shape variation, which is suggested to significantly impact device behaviors for in-plane Bennett clocking[84], [94]–[96]. Therefore, theoretical examinations of perpendicular Bennett clocking system are needed to assess this concept and guide future NML design.

2.3.2 Simulation setup

In this work, we study a four-bit Bennett clocking system for different materials (Ni, CoFeB, and Terfenol-D) with perpendicular magnetic anisotropies. A 3D finite element model that couples micromagnetics, electrostatics, and elastodynamics are used to simulate the strain mediated Bennet clocking. The model assumes linear elasticity, linear piezoelectricity, and electrostatics. Thermal fluctuations are not considered in this model. Previous research has shown that the presence of thermal fluctuation at room temperature will increase switching error rate, which could be compensated by increasing the applied strain level.[65], [90]

Three different magnetoelastic materials with perpendicular magnetic anisotropy are investigated, i.e. Ni, CoFeB and Terfenol-D. For each material system, an array of four disks along the x axis is simulated. All magnetoelastic disks have a 50 nm diameter, and their bottom surfaces are perfectly adhered to the PZT thin film. The thicknesses of the magnetoelastic disks depend upon the material modeled, as shown in Table I. The thickness values are chosen to ensure the magnetic state is thermally stable with a thermal energy barrier $\Delta E_b > 40k_BT \approx 0.2aJ$, for each material system studied. Each magnetoelastic disk is surrounded (along y axis) by a pair of square electrodes with 30 nm side lengths. For each electrode pair, voltage is always applied or removed simultaneously while the bottom electrode is held grounded. The edge-to-edge distance from each magnetic disk and its control electrode is 20 nm. The edge-to-edge distance between neighboring magnetic disks (i.e., $d_{E\text{-}E}$ in Fig. 2-7(a)) depends on the material system, as shown in Table 2. The $d_{E\text{-}E}$ is selected so that the dipole coupling between neighboring disks is sufficient for clocking while the magnetic interactions from other disks is negligible. The material parameters for Ni[24], [45], [60], [97], CoFeB[22], [68]–[70] and

Terfenol-D[71]–[73] are provided in Table I. The Gilbert damping α for all materials are set to be 0.5 to improve numerical stability. The actual damping factors are: α(Ni) = 0.038[24], α(CoFeB) = 0.01[22], α(Terfenol-D) = 0.06[71], which are smaller than the damping used in the simulation. Therefore, the actual clocking speed is expected to be slower as it will take longer to stabilize at the transient in-plane state when the strain is turned on.

Table 2. Parameters for Ni, CoFeB and Terfenol-D used in the Bennett clocking model.

Parameter	Description	Units	Ni	CoFeB	Terfenol-D
t	Thickness	nm	2	1.6	2
M_s	Saturation magnetization	A/m	4.8×10^5	1.2×10^6	8×10^5
A_{ex}	Exchange stiffness	J/m	1.05×10^{-11}	2×10^{-11}	9×10^{-12}
L_{ex}	Exchange length	nm	8.52	4.70	4.73
λ_s	Saturation magnetostriction coefficient	ppm	-34	50	1200
E	Young's modulus	GPa	180	160	80
ρ	Density	kg/m^3	8900	7700	9210
K_{PMA}	PMA coefficient	J/m^3	-1.3×10^5	-8.1×10^5	-3.4×10^5
V	Applied voltage	V	3	3.5	-0.3
Δt_p	Pulse duration	ns	2	2.5	2
d_{E-E}	Edge-to-edge distance between neighboring disks	nm	50	70	60
E_{flip}	Energy per flip	fJ	11.1	14.5	0.11

Figure 2-7(a) illustrates the simulated multiferroic structure consisting of a piezoelectric thin film on a substrate, magnetoelastic disks, and ground/surface electrodes. The piezoelectric material is PZT-5H[98] poled along the *z* direction with 1000 nm × 1000 nm lateral *x-y*

dimension and a 100 nm thickness. The PZT film's four sides and bottom surfaces are mechanically fixed while the bottom surface is electrically grounded.

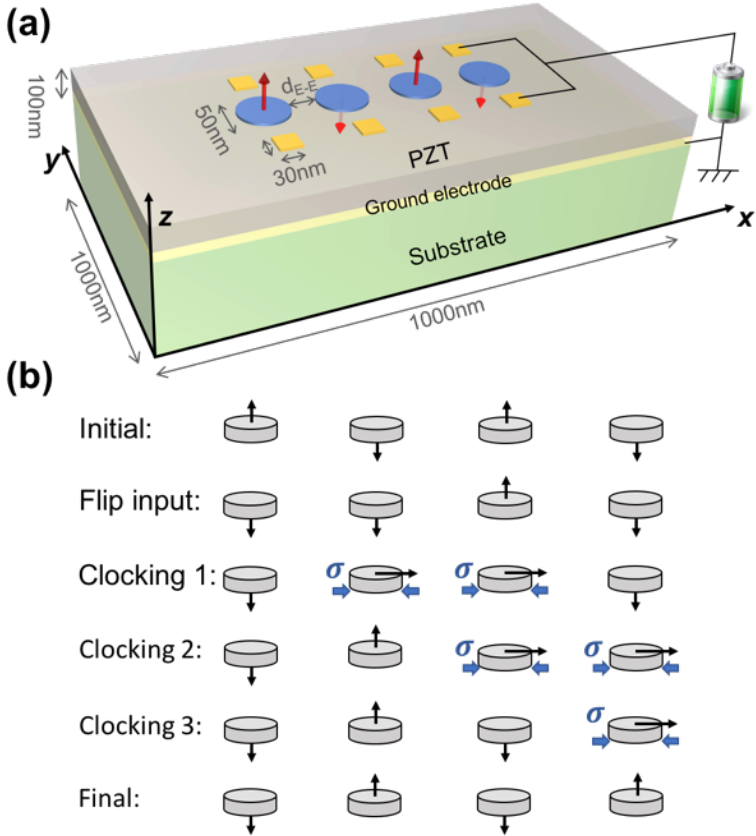

Figure 2-7. (a) 3D illustration of the Bennett clocking system simulated in the model. (b) Information flow of Bennett clocking process.

Fig 2-7(b) is the schematic of information flow for a four-bit nanomagnetic logic (NML) system. The information is encoded as the perpendicular magnetization m_z, which is illustrated by the arrow attached to each disk. Assume the four memory bits start as an anti-parallel magnetic state "↑↓↑↓" as shown in the first row in Fig 2-7(b). Initially new information is written in disk 1, and its magnetization is switched from up to down using a short (~< 1 ns) voltage pulse[19], [60], as shown in the second row in Fig 2-7(b). When disk 1 changes its state, disk 2

does not spontaneously update its state because dipole coupling is insufficient to overcome the energy barrier of disk 2. Therefore, an additional clocking field is needed which is achieved by applying the same voltage to disk 2 and disk 3 (see the third row in Fig 2-7(b)). The voltage-induced strain produces a localized clocking field that rotates the disks' easy axes to in-plane. Then removing the voltage from disk 2 produces an unstable in-plane magnetic state susceptible to external dipole fields. However, disk 3 is still mechanically strained and its in-plane magnetization has a much smaller impact on disk 2 compared to disk 1. Therefore, the magnetization of disk 2 preferably aligns anti-parallel to the disk 1, which is "↑" as shown in the fourth row in Fig. 2-7(b). In other words, the magnetic state or information in disk 1 is now propagated to disk 2. The process is subsequently executed on the remaining magnetic bits (see the last two rows in Fig. 2-7(b)). This causes information from the input bit to cascade along the information line uni-directionally with the end-system exhibiting the opposite state "↓↑↓↑" to the initial state.

2.3.3 Results and analysis

Figure 2-8 shows simulation results for the Bennett clocking process in a four Ni disk system with an edge-to-edge distance between neighboring disks $d_{E\text{-}E}$ of 50 nm and an initial perpendicular magnetic state represented as "↑↓↑↓". Fig. 2-8(a) plots the normalized average perpendicular magnetization m_z (solid line) as well as the applied voltage (orange dashed line) as a function of time for each disk. A 3V (30 MV/m) is applied to disk 1 with 0.8 ns duration, which includes 0.1 ns ramping time for both voltage application/removal steps. The voltage-induced strain is tensile along x axis and compressive along y axis, producing an effective field $\boldsymbol{H_{ME}}$ along the y axis due to the negative λ_S for Ni. The magnetization starts to rotate towards in-

plane, and the voltage is removed when the magnetization crosses the *x-y* plane (corresponding to $m_z = 0$). Then magnetization continues to precess to its new perpendicular equilibrium state $m_z = -1$, i.e. disk 1 undergoes 180° perpendicular switching.

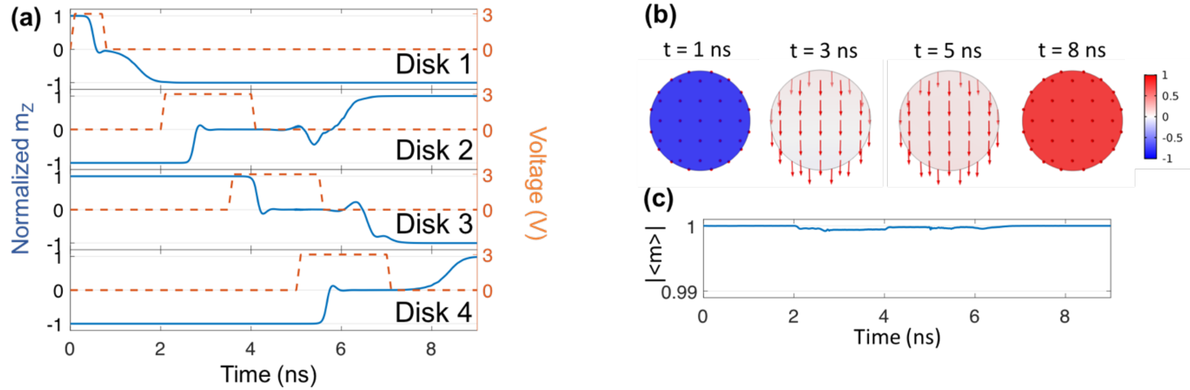

Figure 2-8. Simulation results for Bennett clocking of Ni system.

After disk 1 has stabilized at t = 2 ns, a voltage pulse (3V) is consecutively applied to disks 2, 3, and 4, for t = 2~4 ns, 3.5~5.5 ns, 5~7 ns, respectively. These 2 ns clocking voltage pulses are sufficiently long to stabilize the magnetization in-plane. It is worth noting that in real Bennett clocking system, longer pulses are needed for magnetization to stabilize in-plane, because the actual Gilbert damping is smaller than that is used in the simulation. Upon removal of the clocking voltage (t= 4, 5.5, 7 ns), each disk (2,3, and 4) flips to a new state that is anti-parallel to the preceding disks orientation due to the dipolar field as illustrated in Fig. 2-7(b). At t = 9 ns, the 4-disk system reaches a new equilibrium state with each disk having an opposite magnetic state to its initial state, and strain-mediated Bennet clocking is finished.

Figure 2-8(b) provides the magnetic spin configurations for disk 2 at four distinct times (t = 1, 3, 5, 8 ns) during its 180° switching. The red arrows represent the direction and amplitude of the in-plane magnetization components while the color contour quantifies the m_z component's

magnitude. The switching process is predominantly coherent, as shown by the uniformity of both contour color and arrow directions. The switching coherency is quantitively examined in Fig. 2-8(c) by plotting the temporal evolution of averaged magnetization amplitude for disk 2, which is defined as:

$$|<\mathrm{m}>| = \sqrt{<m_x>^2+<m_y>^2+<m_z>^2} \qquad \text{Eq. 2-9}$$

where $<m_x>$, $<m_y>$, $<m_z>$ denote the volume averaged magnetization in *x, y, z* directions, respectively. The |<m>| = 1 corresponds to complete coherent switching, where all the spins point in the same direction throughout the switching process. |<m>| = 0 represents a completely random spin switching process, where $<m_x>$, $<m_y>$, $<m_z>$ magnitudes are all zeros. As shown in Fig. 2-8(c), the Bennett clocking process for disk 2 (as well as the other disks) is very coherent during the whole Bennett clocking process.

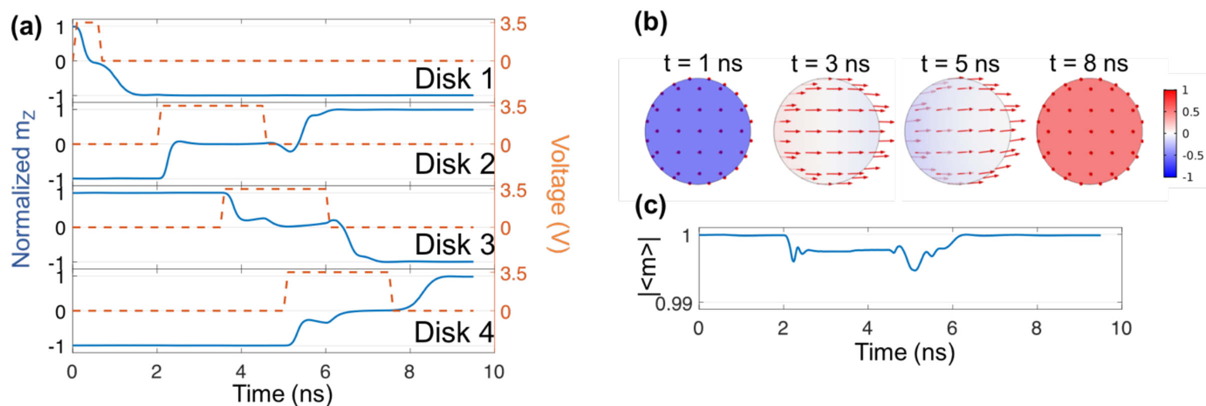

Figure 2-9. Simulation results for Bennett clocking of CoFeB system.

Figure 2-9 shows Bennet clocking results for a CoFeB system with a thickness of 1.6 nm and $d_{E\text{-}E}$ of 70 nm. The larger $d_{E\text{-}E}$ relative to Ni is related to the substantially larger CoFeB Ms

producing larger dipolar fields. Additionally, since CoFeB has a positive λ_S, the applied voltage produces an effective $\boldsymbol{H_{ME}}$ along x axis.

As shown in Fig. 2-9(a), the 3.5 V used is similar to Ni because their magnetostriction coefficients are of similar magnitude. The initial voltage pulse duration applied to disk 1 is 0.7 ns to produce 180° precessional switching. This is followed by consecutive voltage pulse widths of 2.5 ns duration applied to disks 2, 3, and 4 at t = 2~4.5 ns, 3.5~6 ns, 5~7.5 ns, respectively. The pulse duration is longer than Ni and the reason is explained as follows. At t = 4 ns, disk 2 and 3 have experienced 2 ns and 0.5 ns voltage/strain, respectively. Disk 2's magnetization has stabilized in-plane and is ready for voltage removal, however, disk 3 still has small precession near its temporal equilibrium state. If the voltage applied to disk 2 is removed at t = 4 ns, the small perturbation of disk 3 may cause a flipping error in disk 2. To avoid this, the voltage to disk 2 is applied until 4.5 ns when disk 3 is completely stabilized. This issue is not present in Ni system due to weaker dipole coupling making it less susceptible to small spin perturbations compared to CoFeB. In addition, taking into consideration the actual Gilbert damping of CoFeB (0.01) is smaller than that of Ni (0.038), the Bennett clocking process for CoFeB is expected to be slower than that for Ni system.

Figure 2-9(b) provides representative spin configurations for disk 2 at t = 1, 3, 5, 8 ns in the Bennett clocking process for CoFeB system. Similar to Ni system, the voltage-induced strain is tensile along the x axis and compressive along the y axis. However, the effective field $\boldsymbol{H_{ME}}$ is now along the x axis due to the positive λ_S for CoFeB. Therefore, the spins are aligned along x axis at t = 3 ns and 5 ns. The color non-uniformity present at t = 5 ns indicates the switching process possesses some incoherency relative to Ni.

As shown by |<m>| for disk 2 in Fig. 2-9(c), slight incoherency is observed in CoFeB system, which is attributable to the relatively smaller exchange length of CoFeB compared to Ni (see Table 2). The incoherency is initially observed during voltage application and becomes larger upon removal of the voltage. This can be explained as follows. The dominating effective fields in the beginning and the end of the clocking, when m_z is large, are both PMA field since $\boldsymbol{H_{PMA}} \propto m_z$. $\boldsymbol{H_{PMA}}$ is uniform throughout the disk, so the switching is highly coherent. During voltage application, the dominating field becomes $\boldsymbol{H_{ME}}$, but $\boldsymbol{H_{ME}}$ has a spatial distribution caused by a non-uniform strain generated from the patterned electrodes. This non-uniform strain leads to a spatial distribution of spins inside the disk. After removing the voltage (i.e. strain) applied to disk 2, the dominating effective field becomes the dipolar field but there is still the presence of an $\boldsymbol{H_{ME}}$ due to strain generated from disk 3. Both $\boldsymbol{H_{ME}}$ and dipolar field are spatially variant and thus, they both contribute to the magnetic incoherency. Therefore, the incoherency becomes even larger after voltage removal due to this combined effect, i.e. non-uniform dipolar fields and $\boldsymbol{H_{ME}}$.

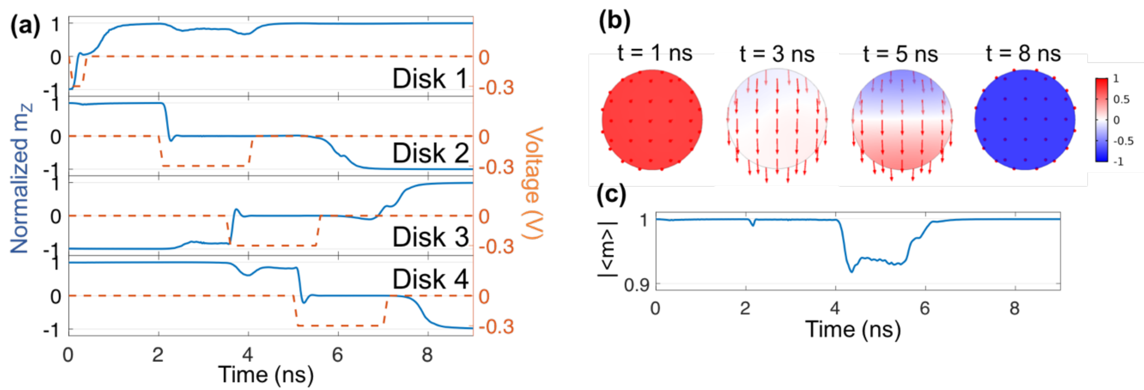

Figure 2-10. Simulation results for Bennett clocking of Terfenol-D system.

Figure 2-10 shows the Bennett clocking results for Terfenol-D system with a thickness of 2 nm and a $d_{E\text{-}E}$ distance of 60 nm. As shown in Fig. 2-10(a), the applied voltage for this system of

disks is only is -0.3 V, which is an order of magnitude smaller compared to either Ni or CoFeB. This is directly attributed to the fact that Terfenol-D has the largest λ_S amongst these three materials and represents the largest value available at room temperature in a soft magnetic material system. Initially a short -0.3 V pulse with duration of 0.4 ns is applied to disk 1 to achieve the precessional switching. This is followed by consecutive voltage pulses of 2 ns duration applied to the disks 2, 3, and 4 at t = 2~4 ns, 3.5~5.5 ns, 5~7 ns, respectively. This timing sequence is the same as Ni system and is attributed to similar magnitudes of dipolar coupling.

Figure 2-10(b) and 2-10(c) show the representative spin configurations and temporal evolution of |<m>| for disk 2 during the Bennett clocking process. The negative applied voltage induces compressive strain along *x* axis and tensile strain along *y* axis leading to an effective magnetoelastic field $\boldsymbol{H_{ME}}$ along the *y* axis due to the positive λ_S for Terfenol-D. It is important to note that the vertical temporal axis in Fig. 2-10(c) has a much larger range compared to the |<m>| plots for both Ni and CoFeB. Therefore, incoherency present in the Terfenol-D system is considerably larger than Ni and CoFeB. This is attributed to the much larger λ_S thus stronger coupling to the non-uniform strain distribution as discussed in previous research.[19] Similar to CoFeB, the switching is incoherent when the voltage is applied disk 2, and becomes larger upon voltage removal.

In conclusion, strain-mediated Bennett clocking has been successfully performed in three popular magnetoelastic material systems. Ni has the most coherent clocking process. CoFeB encounters slightly incoherent switching, mainly due to its small exchange length. Terfenol-D exhibits larger incoherency due to large λ_S. This also suggests that λ_S has a more important

impact on magnetic coherency than exchange length. As a trade-off for incoherency, the Terfenol-D requires smaller voltage for clocking, producing 2 orders higher efficiency than either Ni and CoFeB systems, as shown in Table 2. The energy dissipation per bit per flip is calculated as $E = \frac{1}{2}QV$, where Q is the total charge on the pair of electric pads during voltage application, and V is the applied voltage. While CoFeB is the most mature ferromagnetic metal in magnetic memory because of large readout signal in magnetic tunnel junctions, the large Ms of CoFeB requires increased distances between disks to avoid magnetic perturbation of adjacent disks. This sacrifices the memory density in CoFeB system. In contrast, Ni system has the potential to provide highest memory density. However, the on-chip readout mechanism for Ni or Terfenol-D is less mature than CoFeB. This study clearly reveals the strengths and shortcomings of different material systems in Bennett clocking for NML devices. Additional studies on hybrid NML combining different materials may be able to utilize advantages from each material system.

2.4 Pure voltage controlled magnetic oscillation

Nanomagnetic oscillator has been used for many applications including nano-scale RF signal generator[99]–[101], microwave-assisted recording, nano-scale magnetic field sensor[102], and neuromorphic computing hardware[103]. In a conventional nanomagnetic oscillator, steady magnetic oscillation is achieved when the spin torque induced by the applied current cancels with the Gilbert damping.[102]–[108] However, the current-driven magnetic oscillation can be significantly power-consuming at nanoscale due to Joule heating. In contrast, voltage-driven magnetic oscillation can be potentially more energy efficient due to negligible Joule heating. The strain-mediated multiferroics is one of the voltage-based magnetization control mechanism. Static magnetization control by multiferroics has been demonstrated both numerically and

experimentally.[18], [19], [36], [45] There are also some work on using multiferroics for dynamic magnetization control, such as spin wave generation[109], [110] and ferromagnetic resonance driven by surface acoustic wave on piezoelectric substrate[111], [112]. However, there is few research on voltage-driven nanomagnetic oscillators.

One preliminary work on using strain-mediated multiferroics to drive magnetic oscillation simulates an ellipse magnet with in-plane anisotropy.[113] The magnetic oscillation is drive by a pair of off-axis electrodes on the piezoelectric substrate. The cone angle of the in-plane oscillation amplitude, however, is only 90 degree, which is limited by its mechanism of oscillating between easy and hard axes. There is lack of frequency modulation mechanism, which is one of the most important features of nanomagnetic oscillators. Therefore, a more systematic simulation is desired to develop a voltage-driven nanomagnetic oscillators with large oscillation amplitude and wide tunable frequency range.

In this study, a nano-scale Ni disk with perpendicular magnetic anisotropy (PMA) is studied as the oscillator. It is shown that the perpendicular oscillator can have large oscillation amplitude (magnetization oscillates between two easy axes $m_z = +1$ and $m_z = -1$) and wide frequency tunability.

2.4.1 Simulation setup

Figure 2-11(a) illustrates the simulated multiferroic structure. A PZT-5H (simplified as PZT below) substrate is used as the piezoelectric material with lateral size of 1500 nm × 1500 nm and 800 nm thickness. The PZT's top surface is mechanically free, and its bottom surface is fixed (i.e. mechanically clamped on a thick substrate) and low-reflecting boundary conditions are

applied to the four lateral sides. A Nickel magnetic disk with a diameter of 50 nm and a height of 2 nm is perfectly adhered in the center of the PZT top surface. Two 50 nm × 50 nm square electrodes are placed symmetrically adjacent to the Ni disk along *y* axis. The edge-to-edge distance between the electrode and the magnetic disk is 20 nm. Voltage pulses are always applied to or removed from the two electrodes simultaneously, while the bottom surface of PZT is electrically grounded.

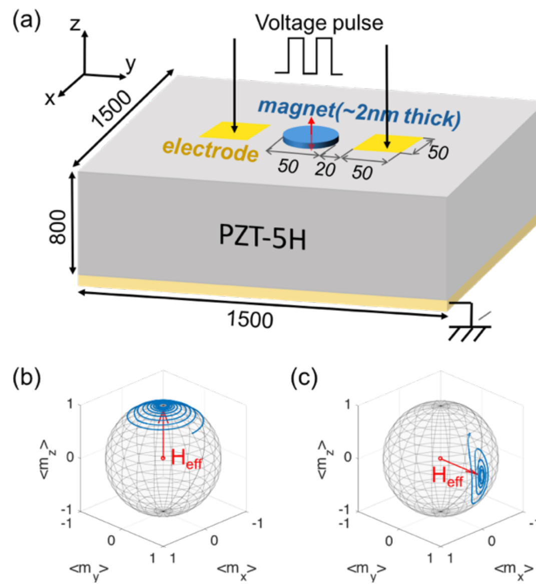

Figure 2-11. (a) 3D illustration of the simulated structure (unit: nm). Trajectory of magnetic precession (b) without voltage, (c) with voltage.

Figure 2-11(b) and (c) provide the results of magnetic precession for the Ni disk without and with applied voltage, respectively. In both figures, the magnetization is released from a canted direction $\boldsymbol{m} = (0, 1, 1)/\sqrt{2}$. Fig. 2-11(b) illustrates the 3D trajectory for a 5-ns magnetic precession without applied voltage. In this result the magnetic anisotropy is dominated by PMA with the effective field $\boldsymbol{H_{eff}}$ along the *z* direction. In contrast, Fig. 2-11(c) presents the results with an applied 1.8 V to the electrodes. The voltage induces a compressive strain along the *y* axis

and a tensile strain along *x* axis between the two top electrodes. This strain combined with the negative magnetostrictive of Ni produces a dominating magnetoelastic field along the *y* axis. Without applied voltage, there are two stable states $m_z = +1$ and $m_z = -1$. Applying voltage brings the magnetization to an intermediate state, i.e., in-plane. By accurately timing the voltage application, it is possible to oscillate the magnetization perpendicularly between $m_z = +1$ and $m_z = -1$.

2.4.2 Results and analysis

Figure 2-12(a)-(d) present simulation results for four different voltage input conditions. In the figures the blue dashed line represents the applied voltage while the solid black line represents the Ni disk's volume averaged perpendicular magnetization component m_z as a function of time. All four voltage inputs are square waves with minimum value 0 and maximum value V_0. The initial voltage at t = 0 is $V_0/2$ and ramps towards V_0. All ramps occur in 0.1 ns for 1.1 GHz voltage and the portion of the ramp within a period is kept the same for voltages applied at other frequencies. This is to eliminate the effect of voltage ramp on the magnetic dynamics.

Figure 2-12(a)(b)(c) show the results of the cases with voltage amplitude 1.8V at different frequencies of 0.8 GHz, 1.1 GHz and 1.6 GHz, respectively. Steady magnetic oscillation is achieved in the 1.1 GHz case in Fig. 2-12(b) while the magnetic dynamics is disordered in other two cases. The explanation is as follows. The magnetic oscillation consists of two stages. The first stage is 180° perpendicular switching when voltage is turned on. This stage requires accurate timing, i.e., the frequency of applied voltage should match ferromagnetic resonance (FMR). Turning off the voltage too late or too early leads to over- or under-shooting of $m_z = -1$, hence disrupt the magnetic oscillation, as shown in Fig. 2-12(a) and (c), respectively. The second

stage is small perturbation near $m_z = \pm 1$ during voltage-off half period. This stage does not require accurate timing and the voltage is designed to be symmetric for simplicity, i.e., the voltage-off and voltage-on periods have the same length in Fig. 2-12.

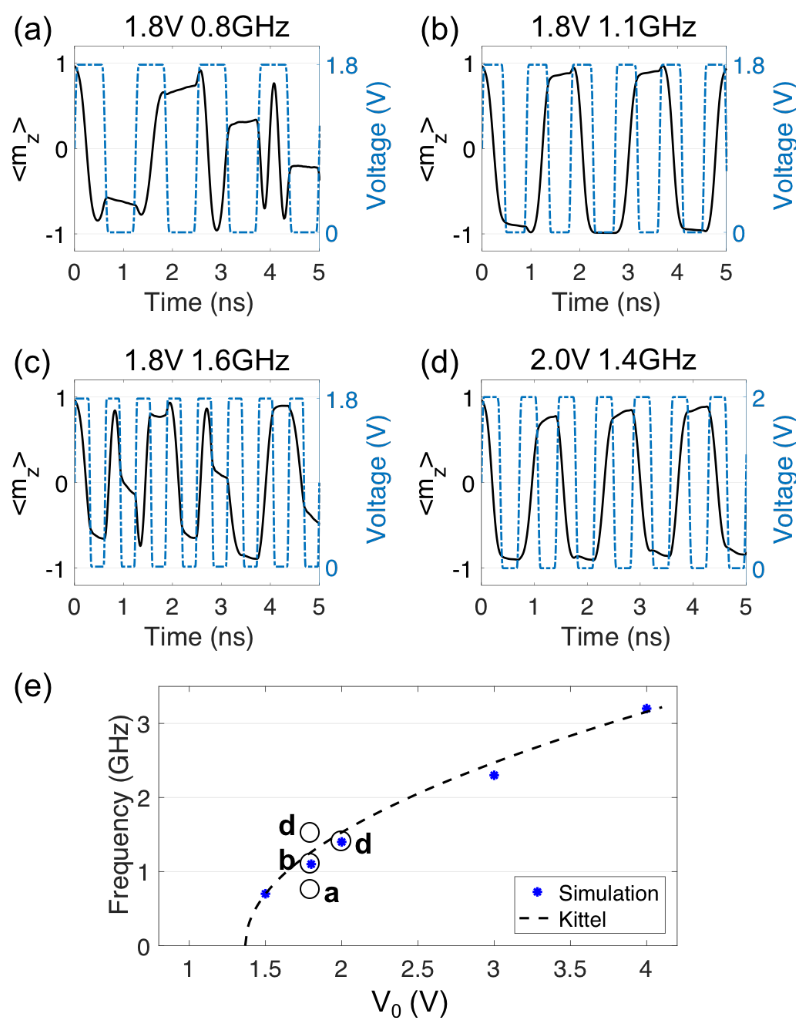

Figure 2-12. (a)-(d) Temporal evolution of perpendicular magnetization m_z under alternate applied voltage with different amplitudes and frequencies. (e) Summary of simulation results of steady oscillation cases and theoretical fitting line derived from Kittel equation.

The oscillation frequency is tunable as shown by another oscillation case with applied voltage 2 V at 1.4 GHz in Fig. 2-12(d). This is because increasing the voltage amplitude

increases the FMR of the magnetic disk. It can be inferred that the upper limit of the frequency of the magnetic oscillator is mainly restricted by the breakdown field of the PZT substrate, and the lower limit is determined by the minimum voltage required to overcome PMA and initiate the oscillation.

To better understand the frequency shift caused by voltage amplitude, Fig. 2-12(e) summarizes five steady oscillation cases (marked by blue stars) with a theoretical fitting curve derived from Kittel equation. The four cases discussed in Fig. 2-12(a)-(d) are also marked on Fig. 2-12(e) by black circles. There is a good agreement between the Kittel equation and the steady oscillation cases. This confirms that the key of tuning frequency of the magnetic oscillator is shifting FMR of the magnetic disk by applied voltage.

The derivation of the theoretical fitting line in Fig. 2-12(e) is shown below. For a thin disk as simulated in this work, the demagnetization factors are approximately $N_x = N_y = 1$, $N_z = 0$,[25] and the coordinate is defined in Fig. 2-11. Then the Kittel equation is simplified as:[114]

$$f = \frac{\gamma \mu_0}{2\pi} \sqrt{H_{eff}(H_{eff} + M_S)} \qquad \text{Eq. 2-10}$$

Assume the strain along *y* axis ε_{yy} as the main contributing component to the magnetoelastic field because other strain components are either tensile or negligibly small, the magnetoelastic can be expressed as:

$$H_{me} = -\frac{2}{\mu_0 M_S} B_1 m_y \varepsilon_{yy} \qquad \text{Eq. 2-11}$$

Then the total effective field can be written as:

$$H_{eff} = -\frac{2}{\mu_0 M_S} B_1 m_y(\varepsilon_{yy} + 2\times10^{-3}) \qquad \text{Eq. 2-12}$$

Here the PMA effect is taken into consideration as a preset 2000 ppm strain given the fact that $\varepsilon_{yy} \approx -2000\ ppm$ is the minimum required strain to overcome PMA. To further simplify the calculation, we take $m_y = 0.2$ instead of a temporally variant value.

Plugging equation 2-12 into 2-10 results in an equation of the frequency as a function of ε_{yy}. Then ε_{yy} and voltage amplitude are related by a linear equation: $\varepsilon_{yy} = -1463\times V_0\ (ppm)$. This is obtained from a stationary simulation that calculates the strain component ε_{yy} inside the Ni disk with varying applied voltage V to the top electrodes in the structure shown in Fig. 2-11. The analytical expression of frequency as a function of voltage amplitude is drawn as the dashed line in Fig. 2-12(e).

Except for changing voltage amplitude, another way to shift the FMR of the magnetic disk is by changing its geometry. Fig. 2-13 compares the results of the multiferroic magnetic oscillators with 2 nm and 1.8 nm thicknesses. Fig. 2-13(a) shows that the 4 V at 3.2 GHz can excite steady magnetic oscillation, however, the same voltage application does not work when the thickness is decreased to 1.8 nm, as shown in Fig. 2-13(b). As shown in Fig. 2-13(c), the steady oscillation occurs again for the 1.8 nm thick disk when the applied voltage is increased to 4.3 V. The explanation is as follows. The PMA is inversely proportional to the magnet's thickness, so the 1.8 nm oscillator has stronger PMA hence requires higher voltage to overcome the PMA. This means the FMR curve for the 1.8 nm oscillator will shift towards right compared to the 2 nm oscillator (shown in Fig. 2-12(e)), as the intersection point of the FMR curve on *x* axis

corresponds to the minimum voltage required to overcome PMA. Therefore, the 1.8 nm oscillator requires higher voltage to achieve a steady magnetic oscillation at the same frequency.

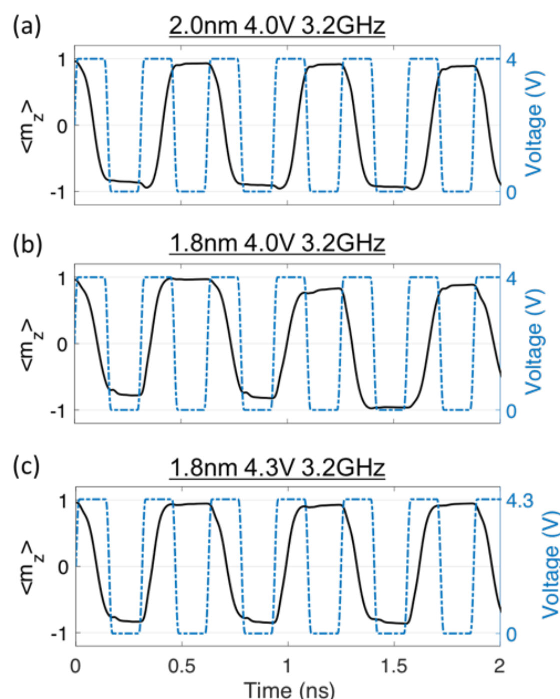

Figure 2-13. Magnetic oscillation for magnets with different thicknesses.

All the cases discussed above have symmetric applied voltage profile, i.e., the voltage-on and voltage-off have the same temporal length within each period of voltage profile. As discussed previously, the voltage-on stage requires accurate timing and should match the FMR. In contrast, the length of voltage-off stage has more flexibility and can be tuned to achieve an arbitrary overall oscillation frequency. Fig. 2-14(a) and (b) compare the 1.8 V applied voltage at 0.55 GHz with symmetric and asymmetric profile, respectively. No steady magnetic oscillation is achieved in Fig. 2-14(a) because the frequency of the voltage does not match the FMR of the magnetic disk, which is 1.1 GHz at 1.8 V. In contrast, the voltage-on portion in Fig. 2-14(b) is designed to matches the FMR of 1.1 GHz, but the voltage-off portion is purposely extended.

Consequently, a steady magnetic oscillation with an overall much lower frequency (i.e., 0.55 GHz) is achieved by using the asymmetric voltage profile.

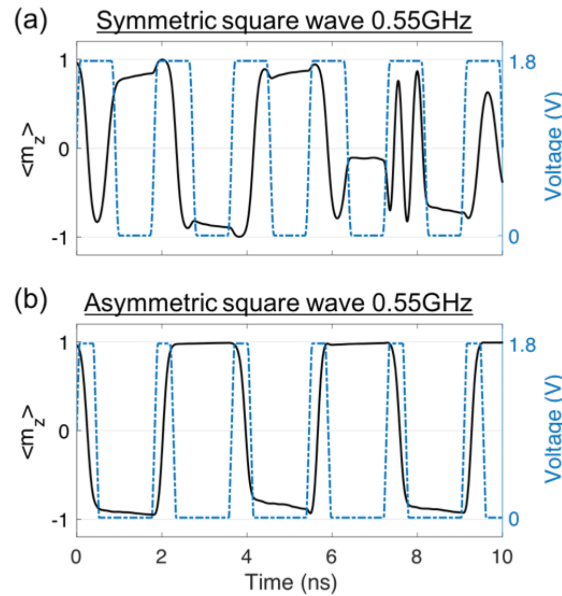

Figure 2-14. Magnetic oscillation with symmetric and asymmetric voltage application.

Figure 2-15 examines the impact of voltage waveforms for a purely voltage driven magnetic oscillator. Fig. 2-15(a) has the simple square wave with 1.8 V amplitude and steady oscillation is achieved when the voltage has 1.1 GHz frequency. As shown in Fig. 2-15(b), simply changing the square wave to a sinusoidal wave with the same amplitude $\mathrm{V} = 0.9 + 0.9\sin{(2\pi f_0 t)}$ (f_0 = 1.1 GHz) does not result in a similar magnetic response. Instead, we take the zeroth- and first-order components of the Fourier series expansion of the square wave to build the wave $\mathrm{V} = 0.9 + \frac{4}{\pi}\times 0.9\sin{(2\pi f_0 t)}$, and a steady magnetic oscillation is achieved as shown in Fig. 2-15(c). In other words, the sinusoidal wave built in this way is equivalent to the square wave in exciting magnetic oscillation. Since sinusoidal waves are easier to generate by source meters than square

waves, this provides a potentially easier way to achieve the purely voltage driven magnetic oscillations.

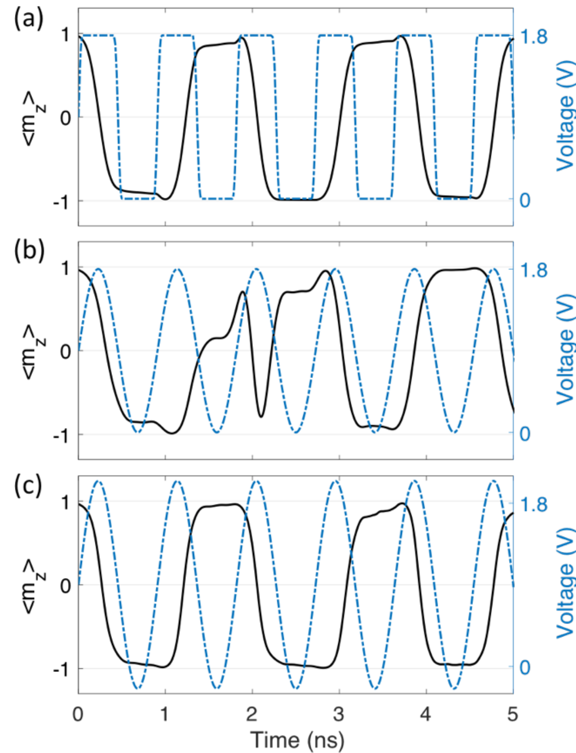

Figure 2-15. Magnetic precession for different voltage waveforms.

In conclusion, a new magnetic oscillator mechanism is proposed and an alternate voltage applied to the piezoelectric substrate can excite steady magnetic oscillation. The oscillation frequency can be tuned by changing the FMR of the magnet, either by changing the amplitude of the alternate voltage or by changing the thickness of the magnet. The frequency range achieved in this study is from 275 MHz to 1.6 GHz (note the magnetic oscillation frequency is half of the voltage frequency). Using an asymmetric voltage profile adds more tunability the system and further extends the lower bound of the oscillation frequency. A simplified analytical equation is derived to link the oscillation frequency and the voltage amplitude. This helps understand the

working principle of the purely voltage driven magnetic oscillator and guide future design of the oscillator with specified frequency range.

Chapter 3. Strain-mediated perpendicular magnetization control: experiment

3.1 Recent progress of experiments

Pure external stress induced magnetization switching was investigated by several groups. Bootsmann et al (2005) switched arrays of magnetostrictive microdots using external applied strains.[115] The micro-scale magnetic dots were fabricated on Si3N4 membrane, which covers a mini vacuum chamber. Changing the pressure inside the vacuum chamber creates a stress/strain on the magnetic membrane. The 90 degree switching was observed by magnetic force microscopy (MFM) imaging under 0.04% (i.e., 400 ppm) applied strain. Ozkaya et al (2008) showed magnetization of Co and Ni thin films could be controlled by directly applying uniaxial stress. [116] Using a flexible polyimide substrate, they were able to apply very large strain 1% (i.e., 10,000 ppm). When the stress/strain was applied to Co/Cu/Ni stack, the magnetization inside Co and Ni layer rotates to different directions, because Co has positive magnetostriction and Ni has negative magnetostriction. The magnetization change can be detected by giant magnetoresistance (GMR) effect of the Co/Cu/Ni stack.

Although researchers showed successful magnetization control by applying external stress/strain, the complexity of generating strain (which need external facilities) makes the devices less appealing in practical application. Therefore, researchers tried to use piezoelectric material to generate strain, and the ferromagnetic/piezoelectric laminated structure was investigated. Using this heterostructure, an applied voltage to the piezoelectric substrate, strain is

generated and is transferred to the attached ferromagnetic material. This in-situ voltage controlled strain generation method makes the approach defined by strain-mediated magnetization more technologically interesting.

Wan et al (2006) reported strain-mediated magnetization control in the hybrid structures of Pb(Zr0.52Ti0.48)O3 (PZT) and Tb0.30Dy0.7Fe2 (Terfenol-D).[117] Weiler et al (2009) demonstrated reversible 90 degrees magnetization switching of Ni thin film by applying voltage to piezoelectric layer.[118] The experimental setup is shown in Fig. 3-1. The magnetization change was measured by both ferromagnetic resonance spectroscopy and SQUID.

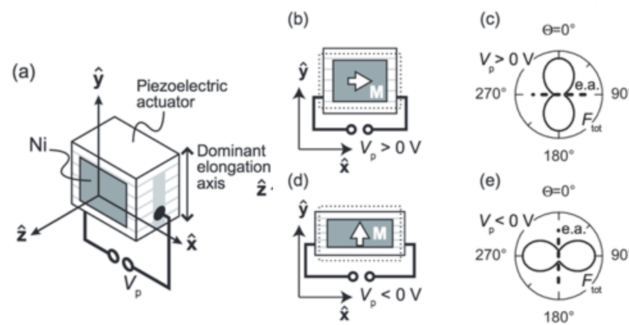

Figure 3-1. Schematic of the experimental setup and results. Reference: [118].

Other material systems were also used to successfully demonstrate strain-mediated magnetization control. For example, Liu et al (2009) reported the magnetization control of Fe3O4 on PMN-PT, PZT, and PZN-PT substrates.[119] However, the magnetization change is transient since when the voltage is turned off the magnetic state returns to its original orientation. Wu et al (2011) reported reversible and permanent magnetization control of Ni on PMN-PT substrate.[120] After rotating the magnetic state with applying electric field to PMN-PT substrate, the magnetization was found to be stable at room temperature, i.e. due to remanenat

strains. Zhang et al (2012) reported repeatable bi-directional switching of CoFeB thin film by applying positive or negative voltage to the PMN-PT substrate.[121] The experimental setup and results are shown in Fig. 3-2. Those achievements of reversible bi-directional magnetic switching open the door of using strain-mediated magnetic control mechanism as a magnetic memory application.

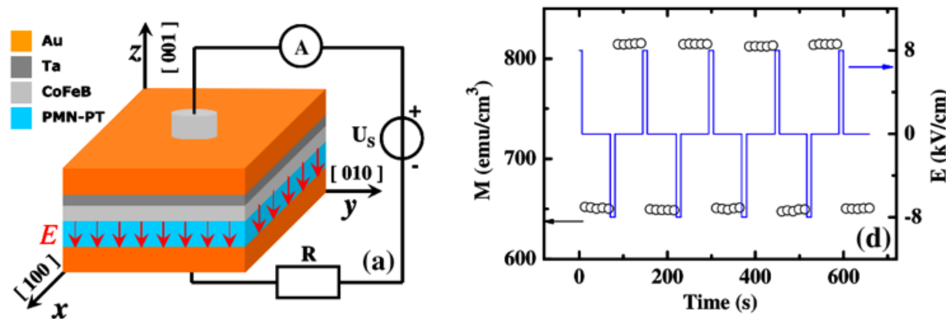

Figure 3-2. Left: Scheme of the sample and experimental configuration. Right: The repeatable high/low magnetization states (open circle) switched by pulsed electric fields (blue line). Reference: [121].

Note all the ferromagnetic/piezoelectric systems mentioned above have used *bulk* piezoelectric substrates, and *continuous* ferromagnetic thin film. Instead of controlling continuous ferromagnetic film, the same scheme can also be used for magnetization control of nanomagnetic dots as demonstrated by Buzzi et al (2013).[122] The magnetization of the nanoscale Ni disks was rotated 90 degree by applying voltage to the PMN-PT substrate. The magnetic rotation was imaged using x-ray magnetic circular dichroism (XMCD). This is the first experimental demonstration of using strain-mediated method to control nanomagnetic dots. However, in this work, the strain is applied to all nanomagnetic islands at the same time. For

more practical memory application, a method is needed to control individual magnetic element with strain.

Cui et al (2013) suggested use patterned electrode to individually rotate magnetic disks using a bulk piezoelectric substrate.[36] Device illustration and results are shown in Fig. 3-3. Two pairs of electrodes are deposited around the Ni square element with 0.5mm length. When positive voltage is applied to electrodes AA with the bottom surface of PZT grounded, the Ni element undergoes tensile strain along AA and compressive strain along BB. The bi-axial strain induces a magnetoelastic anisotropy and rotates the in-plane magnetization as shown by the M-H curve measured by MOKE (the right plot in Fig. 3-3).

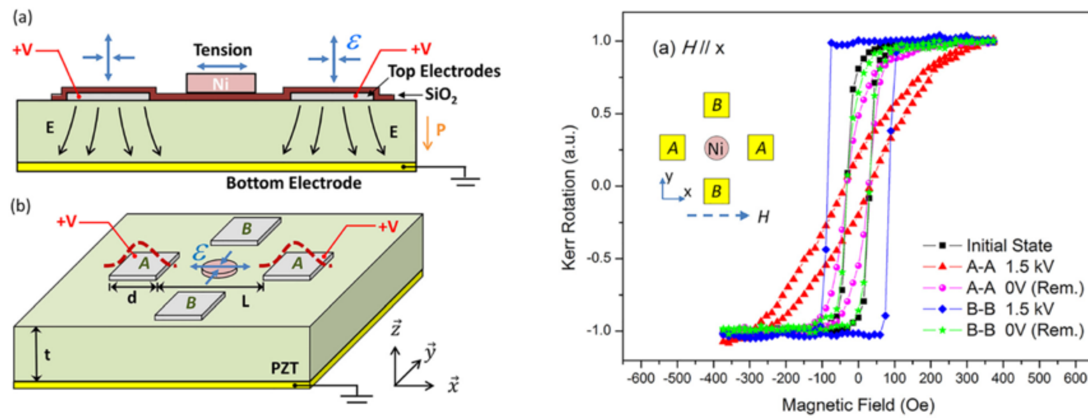

Figure 3-3. Left: Schematic of the device. Right: A representative MOKE data showing magnetic rotation under electric field application. Reference: [36].

Cui [36] also quantified the magnetoelastic effect by correlating the strain and the change of anisotropy field H_a, which is defined as the saturation field along hard axis. The relationship is quantified using the equation: $\varepsilon_{xx} - \varepsilon_{yy} = \frac{-\Delta H_a M_S(1+\nu)}{3\lambda_S E}$. The thickness of the PZT is 0.5 mm, and the piezoelectric coefficients are d_{33} = 690 pC/N and d_{31} = 340 pC/N. When the distance between the pair of electrodes is 1 mm, simulation results show that the 1.5 kV applied voltage generates

a biaxial strain ($\varepsilon_{xx} - \varepsilon_{yy}$) as 1100 ppm. This corresponds to approximately 350 Oe change of H_a, which matches with the experimental results. The simplified equation provides a quantitive way to correlate the strain level and the M-H curve change, and it is used to characterize our device in the following sections.

Both Buzzi and Cui used external facilities (XMCD or MOKE) to measure the magnetization change. For a memory device, an on-chip reading mechanism must be present that is compatible with the strain-mediated magnetization writing mechanism. Li et al (2014) built a micro-scale magnetic tunnel junction (MTJ) stack with in-plane magnetic anisotropy on [011] PMN-PT.[123] They demonstrated that the TMR of the MTJ can be modulated by applying voltage to a continuous top and bottom electrodes on PMN-PT substrate.

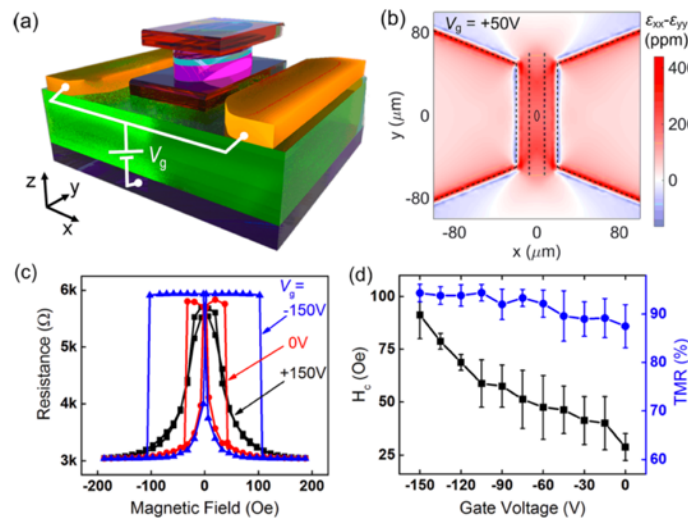

Figure 3-4. Device illustration and representative results in reference [18].

Later on, Zhao et al (2016) also built a micro-scale MTJ on PMN-PT substrate.[18] The difference from Li's work is that Zhao used patterned electrodes to actuate the [001] PMN-PT substrate, which represents one step closer towards a scalable strain-mediated magnetic memory

device. Fig. 3-4 summarize the device structure, strain simulation and the testing results. They numerically showed that 50 V applied voltage to the 0.5 mm thick PMN-PT substrate generates a biaxial strain ($\varepsilon_{xx} - \varepsilon_{yy}$) of 270 ppm. A simplified calculation, which was similar to Cui's calculation [36], was used to correlate the ~60 Oe coercivity field H_c change with ~1000 ppm biaxial strain generated by +150 V applied voltage. The author assumed the coercivity field is proportional to the anisotropy field.

It is interesting to note that the strain exerted on free layer and reference layer inside the MTJ is similar, as suggested in reference [18] with both simulation and experimental data. The magnetization in both layers rotated under the applied strain. As discussed in [18], the low resistance state of MTJ was achieved under applied strain as a result of multi-domain switching assisted by dipole coupling between the free layer and the reference layer. Although the MTJ can toggle between high and low resistance states using strain-mediated approaches, the 'switching' mechanism may not work for nano-scale MTJ device, where the switching becomes single-domain and the dipole coupling is much weaker. This posits a challenge to strain-mediated magnetization control, and further efforts are needed to develop an efficient readout method for strain-mediated magnetization control.

While researchers are making considerably progress on controlling patterned magnetic element, on the other hand, there are a few works trying to replace the bulk piezoelectric substrate with piezoelectric thin films (< 5 um thickness). Some test dats suggests that the piezoelectric coefficient reduces by ~70% due to substrate clamping effect.[124] In addition, the in-plane residual stress from the PZT thin film deposition makes it difficult to polarize in-plane, which also contributes to the reduction of piezoelectric coefficient in PZT thin films.[125], [126]

Overall, one should expect an 80%~90% reduction of piezoelectric coefficient in PZT thin film compared to bulk PZT with the same composition. The strain reduction can be mitigated by applying larger electric fields but once again this does represent a challenge.

Chung et al (2009) demonstrated using PZT thin film to rotate magnetization of a Ni nanobar.[127] The PZT thin film in this work was actuated using a continuous electrodes. Later, Cui et al (2015) used patterned electrodes on 1 um thick PZT thin film to control magnetization of an individual nano-scale Ni ring.[128] As shown in Fig. 3-5, the in-plane magnetization inside the nano-scale Ni ring was rotated by a small angle by applying 25 V to the electrode pairs. It was suggested in this work that the roughness of the PZT thin film and the defects of the nano-scale magnetic structures made the strain-mediated magnetization control extremely challenging in nano-scale.

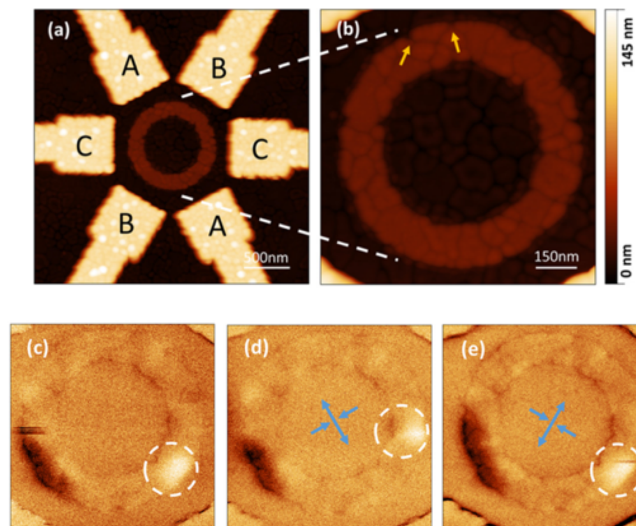

Figure 3-5. Ring structure and MFM image of magnetization rotation in reference [128].

As mentioned in the introduction chapter, magnetic element with perpendicular magnetic anisotropy (PMA) is more appealing for memory application, because it has a smaller footprint

and higher thermal stability compared to in-plane magnetic element. However, there are limited efforts on strain-mediated modulation of perpendicular magnetic anisotropy. Different PMA material systems were investigated, including CoPd (2010)[129], FePd (2013)[130], CoPd (2013),[131] [Co/Pd]n/CoFeB (2013)[132], Ta/CoFeB/MgO/Ta (2015)[133]. All the ferromagnetic materials are continuous thin film grown on bulk PMN-PT substrate.

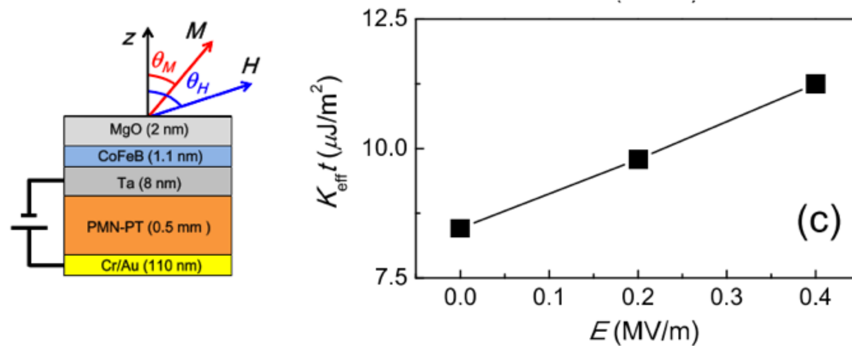

Figure 3-6. Device illustration (left) and results (right) showing modulation of perpendicular magnetic anisotropy by electric field in reference [133].

The following of the chapter will focus on developing strain-mediated control of perpendicular magnetization on both bulk PMN-PT substrate and PZT thin films.

3.2 PMN-PT device

$Pb(Mg_{1/3}Nb_{2/3})O_3]_{1-x}$-$(PbTiO_3)_x$[x = 0.28~0.32] (also known as PMN-PT) single crystal is a commonly used bulk piezoelectric material used in strain-mediated magnetic devices due to its relatively larger strains as well as the potentially smoother surfaces associated with single crystals. Although the thickness (0.5 mm) makes the material less technologically interesting (i.e., difficult to incorporate with CMOS transistor systems), the material has mature growth process and very high piezoelectric coefficient. Commercialized PMN-PT products are readily

available with relatively smooth surfaces (~1 nm). All the PMN-PT substrates used in this work were from TRS technology, and they all have the size of 1cm × 2cm × 0.5 mm (thickness).

3.2.1 Material

First, the surface roughness and appearance vary from batch to batch. Fig. 3-7 shows some microscope images of the PMN-PT surfaces. Some surface had the appearance of black dots or obvious domain structures, as shown in Fig. 3-7 (a) and (b), respectively. It is unclear how the appearance relates to the material property.

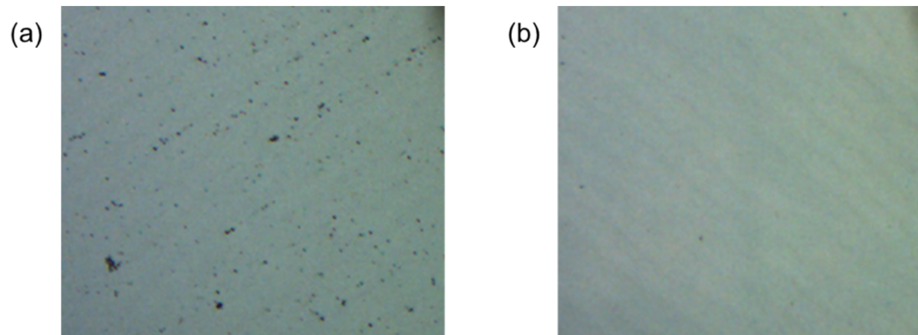

Figure 3-7. Microscope images of PMN-PT surfaces.

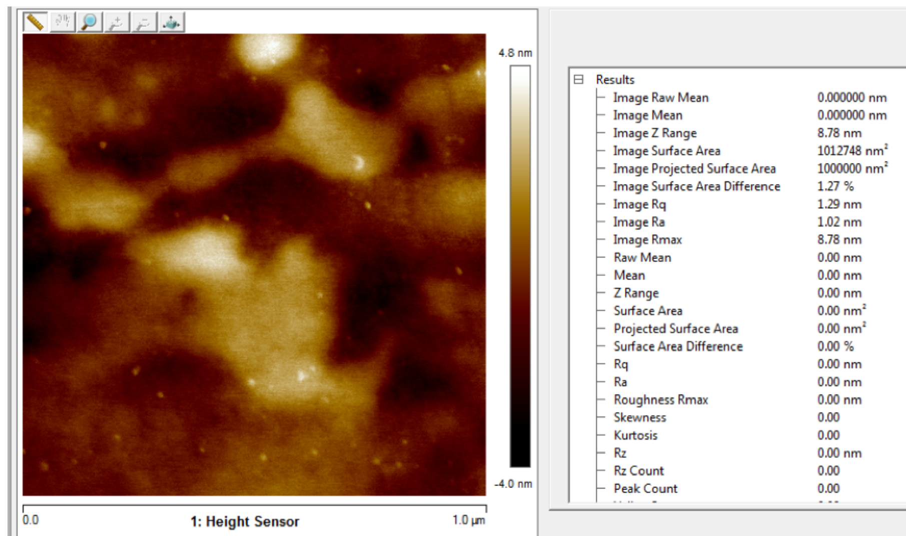

Figure 3-8. AFM images of PMN-PT surfaces.

Figure 3-8 shows a representative AFM images of the PMN-PT surface. The domain is usually large (>1 um). Therefore, small region scan (1 um) looks relatively smooth, the surface roughness parameters Ra and Rq (defined in Fig. 3-9) are approximately equal or less than 1 nm. However, large region scans reveal a better indication of surface roughness. Generally, a smooth PMN-PT can have Ra, Rq = 0.6~0.7 nm, while a rough PMN-PT surface can have Ra, Rq > 2nm.

Parameter	Description	Formula
R_a,[8] R_{aa}, R_{yni}	arithmetical mean deviation of the assessed profile	$R_a = \frac{1}{n}\sum_{i=1}^{n}\lvert y_i\rvert$ [8]
R_q, R_{RMS}[8]	root mean squared	$R_q = \sqrt{\frac{1}{n}\sum_{i=1}^{n} y_i^2}$ [8]

Figure 3-9. Definition of surface roughness parameters Ra and Rq. (Reference: Wikipedia "surface roughness")

As shown in Fig. 3-10, there are two types of PMN-PT: [011] cut and [001] cut, and the direction refers to the out-of-plane crystalline direction. Fig. 3-11 provides strain gauge measurement of the piezoelectric response of the [011] cut PMN-PT. Similar results can be found in literatures [120], [134]. Generally, applying 400 V to the 0.5 mm thick [011] PMN-PT (i.e., 0.8 MV/m) generates approximately -1000 ppm in x direction and +500 ppm in y direction (i.e., anisotropic). For [001] cut PMN-PT (results not shown here), with the same applied electric field, the strain is approximately -500 ppm in both x and y directions (i.e., isotropic). As shown in Fig. 3-11, there are two peaks at +100 V and -100 V respectively. At those voltages, the substrate gets re-poled to the opposite direction and there is a sudden reversal of polarization, leading to an electrical spike signal. Re-poling the piezoelectric substrate may cause cracks

especially PMN-PT, which is single-crystal. Therefore, one should avoid doing this frequently during the testing.

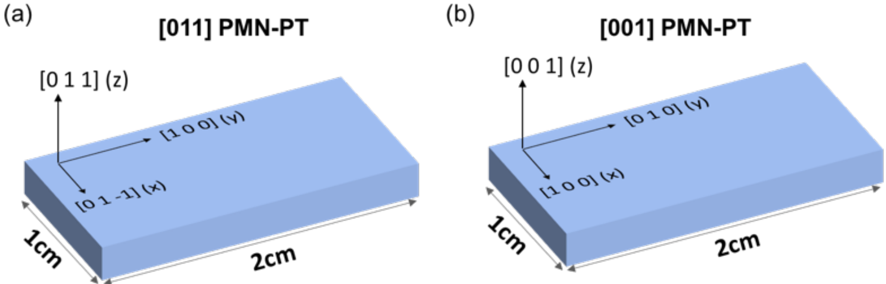

Figure 3-10. Crystal orientation of [011] and [001] PMN-PT.

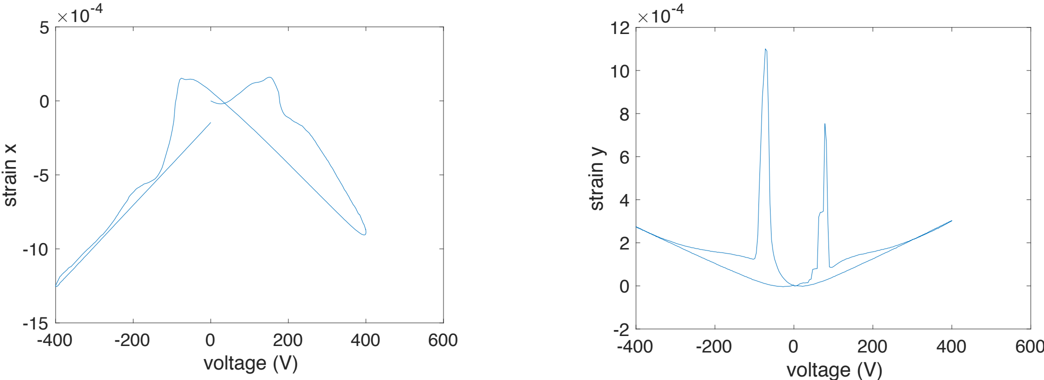

Figure 3-11. Strain-gauge measurement of [011] PMN-PT for both x-direction and y-direction.

Figure 3-12 shows the poling setup. A 400 V is applied to the PMN-PT by using a power supply (GW Instek GPS-3030DD) and an amplifier (Trek Model 50/750, ×150 amplification). A voltmeter is also connected to the output of the amplifier, in order to monitor the applied voltage in real time. A simple clamping fixture is made based on copper board. The PMN-PT has metal deposited on both sides. Usually the poling process needs to be done prior to magnetic film deposition, because poling PMN-PT after magnetic film deposition typically produces residual stress inside the magnetic film. The magnetic film deposition may require high temperature

annealing process, which is above the Curie temperature of the PMN-PT (160 C). In other words, the PMN-PT may become de-poled during the magnetic film deposition and annealing process. However, it is still suggested to pole the PMN-PT before the magnetic film deposition, and pole again after the magnetic film deposition. Empirically this helps reduce the residual stress inside the magnetic thin film and there is ancillary information suggesting it may be eliminated.

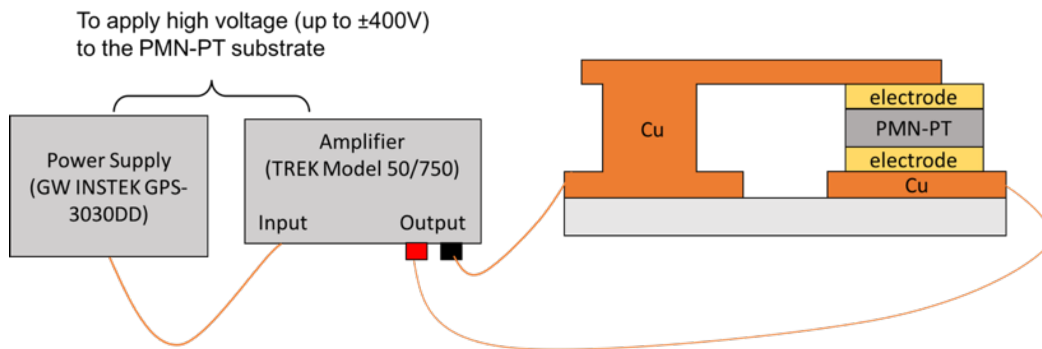

Figure 3-12. PMN-PT poling setup.

3.2.2 Electrode design: a parametric study

Although there are a few publications that have experimentally demonstrated the strain-mediated multiferroic control of magnetization, there is lack of a general rule that can guide future multiferroic system design. In this section, we discuss the influence of the strain inside the controlled magnetic device: distance between patterned electrodes, size and orientation of the electrodes, and the thickness of the device on the operational principles.

Figure 3-13 and figure 3-14 are data sheets for [001] and [011] PMN-PT, respectively, from TRS technology's website.

MEASURED AND DERIVED ELASTIC COMPLIANCE CONSTANTS, s_{ij} (10^{-12} m^2/N), AND ELASTIC STIFFNESS CONSTANTS, c_{ij} (10^{10} N/m^2), FOR TRS X2B

Material	s_{11}^E	s_{12}^E	s_{13}^E	s_{33}^E	s_{44}^E	s_{66}^E	s_{11}^D	s_{12}^D	s_{13}^D	s_{33}^D	s_{44}^D	s_{66}^D
TRS X2B	52.1	-24.6	-26.4	59.9	16.0	28.3	41.8	-34.8	-3.9	10.3	14.0	28.3

Material	c_{11}^E	c_{12}^E	c_{13}^E	c_{33}^E	c_{44}^E	c_{66}^E	c_{11}^D	c_{12}^D	c_{13}^D	c_{33}^D	c_{44}^D	c_{66}^D
TRS X2B	12.4	11.1	10.4	10.8	6.3	3.5	12.6	11.3	9.3	16.8	7.1	3.5

TABLE II. Piezoelectric Coefficients, d_{ij} (pC/N), e_{ij} (C/m^2), g_{ij} (10^{-3}Vm/N), h_{ij} (10^8V/m), and Electromechanical Coupling Factors, k_{ij}, For TRS X2B

Material	d_{33}	d_{31}	d_{15}	e_{33}	e_{31}	e_{15}
TRS X2B	1540	-699	164	22.3	-3.9	10.3

Material	g_{33}	g_{31}	g_{15}	h_{33}	h_{31}	h_{15}
TRS X2B	32.2	-14.6	11.9	27.7	-4.8	8.7

Material	k_{33}	k_{31}	k_{15}	k_t	k_{31} (45°C)
TRS X2B	0.91	0.44	0.35	0.60	0.81

Dielectric Constants, ε_{ij} (e_0), and Dielectric Impermeability Constants, β ($10^{-4}/e_0$), For TRS X2B

Material	ε_{33}^T	ε_{11}^T	ε_{33}^S	ε_{11}^S	β_{33}^T	β_{11}^T	β_{33}^S	β_{11}^S
TRS X2B	5400	1560	910	1340	1.85	6.41	10.99	7.46

*** Ec: 1.8-3kv/cm, Trt: 80-100°C**

Figure 3-13. Data sheet for [001] PMN-PT (available on TRS website).

$$s^E = \begin{bmatrix} 19.84 & -37.58 & 23.81 & 0 & 0 & 0 \\ -37.58 & 96.06 & -62.03 & 0 & 0 & 0 \\ 23.81 & -62.03 & 46.88 & 0 & 0 & 0 \\ 0 & 0 & 0 & 15.82 & 0 & 0 \\ 0 & 0 & 0 & 0 & 182.86 & 0 \\ 0 & 0 & 0 & 0 & 0 & 24.77 \end{bmatrix} \times 10^{-12} m^2/N$$

$$c^E = \begin{bmatrix} 19.58 & 8.51 & 1.31 & 0 & 0 & 0 \\ 8.51 & 10.85 & 10.03 & 0 & 0 & 0 \\ 1.31 & 10.03 & 14.74 & 0 & 0 & 0 \\ 0 & 0 & 0 & 6.70 & 0 & 0 \\ 0 & 0 & 0 & 0 & 0.73 & 0 \\ 0 & 0 & 0 & 0 & 0 & 4.64 \end{bmatrix} \times 10^{10} N/m^2$$

$$e = \begin{bmatrix} 0 & 0 & 0 & 0 & 17.76 & 0 \\ 0 & 0 & 0 & 7.78 & 0 & 0 \\ 3.91 & -10.31 & 19.43 & 0 & 0 & 0 \end{bmatrix} C/m^2$$

$$d = \begin{bmatrix} 0 & 0 & 0 & 0 & 2736.6 & 0 \\ 0 & 0 & 0 & 183.1 & 0 & 0 \\ 771.4 & -1147 & 1454.6 & 0 & 0 & 0 \end{bmatrix} \times 10^{-12} C/N$$

$$\varepsilon^T = \begin{bmatrix} 6032 & 0 & 0 \\ 0 & 1680.5 & 0 \\ 0 & 0 & 5880 \end{bmatrix}$$

$$\varepsilon^S = \begin{bmatrix} 941.6 & 0 & 0 \\ 0 & 1572.3 & 0 \\ 0 & 0 & 660 \end{bmatrix}, \quad \varepsilon_0 = 8.85 \times 10^{-12} \text{ (F/m)}$$

Figure 3-14. Data sheet for [011] PMN-PT (available on TRS website).

These material parameters are used as input to the finite element model using COMSOL. The PMN-PT has dimension of 5 mm × 5mm × 0.5 mm. The mechanical boundary conditions are as follows: one corner of the PMN-PT bottom surface is fixed, and its adjacent two side planes and the bottom surface are on rollers. Note the xyz-coordinates are defined as shown in Fig. 3-10, and the default poling direction is +z direction. Fig. 3-15 compares the simulation results of [011] PMN-PT and the measurement data. The simulation matches the experiment very well. Since the model assumes linear elastics and linear piezoelectrics, the response in the simulation is linear and the phase change at high electric field is absent in this model.

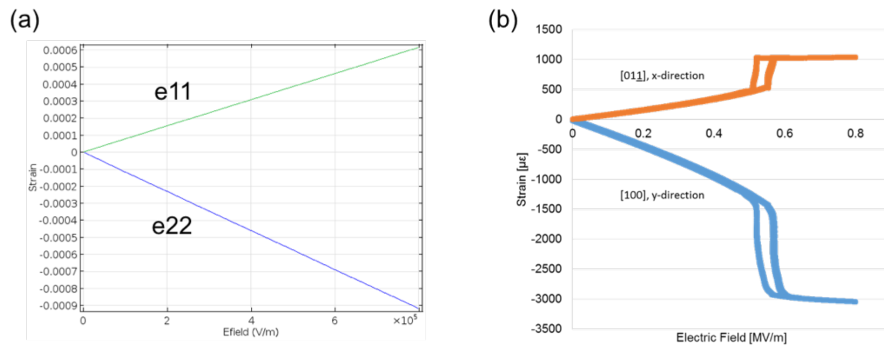

Figure 3-15. Comparison of strain response between simulation (a) and experimental results (b) for [011] PMN-PT.

We have also used the model to understand the influence of electrode configurations. First, we keep the size of the electrodes fixed, and vary the distance between the electrodes. The simulated configurations and results are shown in Fig. 3-16 and Fig. 3-17. This design of electrodes follows previous work by Cui.[135] The top two patterned electrodes (200um × 800 um) are electrically grounded, and a +400 V is applied to the bottom of PMN-PT. The principle strain components along x, y, z directions (i.e., e11, e22, e33) are probed inside the 10um × 10

um Au disk in the center. The disk has 1 um thickness and the surface average strains for the bottom surface of the disk is calculated.

The strain affects perpendicular magnetic anisotropy by the following equation:

$$E_{strain} = -\frac{3}{2}\lambda_S \sigma = -\frac{3}{2}\lambda_S Y \varepsilon_{eff} \quad \text{Eq. 3-1}$$

where Y is Young's modulus, λ_S is the saturation magnetostrictive coefficient. We define effective strain as:

$$\varepsilon_{eff} = \max(\varepsilon_{ip}) - \varepsilon_{33} \quad \text{Eq. 3-2}$$

This can be understood in the following way. For a positive magnetostrictive (i.e., $\lambda_S > 0$) material like CoFeB, a tensile strain in perpendicular direction (i.e., $\varepsilon_{33} > 0$) increases the PMA, therefore the strain's contribution to PMA is a positive value. On the contrary, an in-plane tensile strain (i.e., $\varepsilon_{ip} > 0$) increases the in-plane anisotropy along the strain direction, which in turn decrease PMA. And if the in-plane anisotropy overcomes PMA along any in-plane direction, the magnet does not retain PMA anymore. In other words, it is the maximum value of all in-plane strain components that matters the most. Therefore, we use the value $\varepsilon_{eff} = \max(\varepsilon_{ip}) - \varepsilon_{33}$ to represent how strain influences the PMA.

Results for [011] PMN-PT are presented in Fig. 3-16. There are four electrode configurations examined. In reality, the [011] PMN-PT actuation primarily comes from continuous top and bottom electrodes. Because the anisotropic strain response in-plane, having patterned electrodes (which adds asymmetry to the system) makes the strain distribution more complex and in many cases not intuitive to understand or predict.

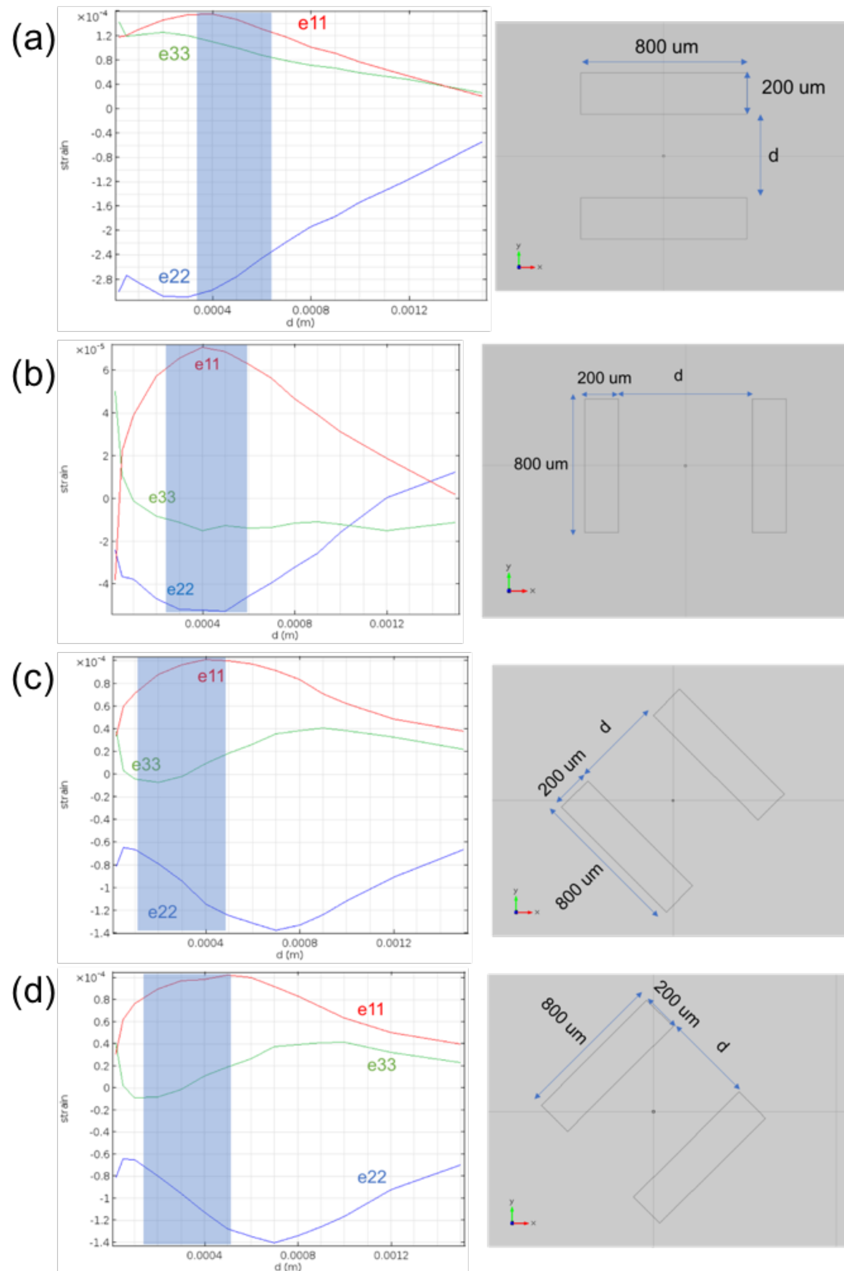

Figure 3-16. Impact of distance between patterned electrodes on strain distribution for [011] PMN-PT substrate. The two electrodes are aligned along x-direction (a), y-direction (b), with ±45° rotation (c,d). The shadowed region is where the value $\varepsilon_{eff} = \max(\varepsilon_{ip}) - \varepsilon_{33}$ is maximized.

There are some interesting observations. For example, the configuration in Fig. 3-16 (a), where the electrodes are along x-direction, is a poor choice for strain-mediated PMA control for positive magnetostrictive material like CoFeB. This is because the e11 and e33 are nearly equally positive, this means the positive e11 tries to rotate the magnetization in-plane, however, at the same time, the equally strong e33 tries to further stabilize the perpendicular magnetization. In contrast, the configuration shown in Fig. 3-16(b) is superior because it's maximum effective strain (approximately 80 ppm) among all the four configurations. In addition, it can be seen that the effective strain is maximized when the distance is 200~600 um.

Figure 3-17 presents the parametric study results for [001] PMN-PT by varying the distance between the patterned electrodes. Since [001] PMN-PT is isotropic in-plane, there is no need to check different electrode orientations. Therefore, only one electrode layout is examined. The effective strain is also maximized when the distance is 200~600 um, and the maximum effective strain here is $\varepsilon_{eff} = \varepsilon_{11} - \varepsilon_{33} = +90$ ppm.

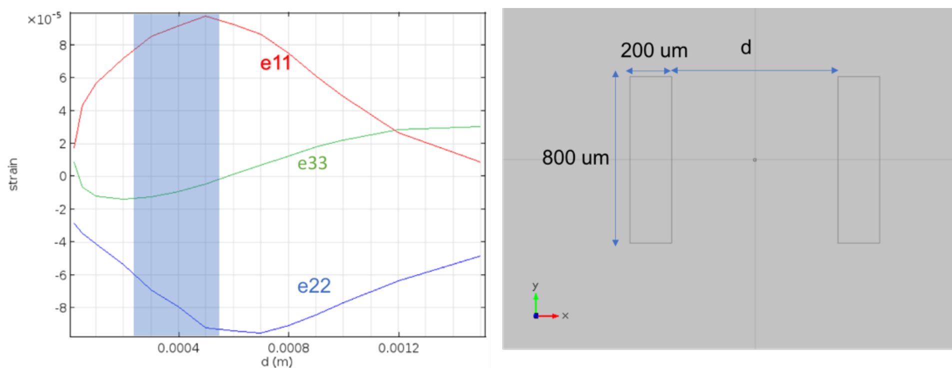

Figure 3-17. Impact of distance between patterned electrodes on strain distribution for [001] PMN-PT substrate. The shadowed region is where the value $\varepsilon_{eff} = \max(\varepsilon_{ip}) - \varepsilon_{33}$ is maximized.

As suggested by both Fig. 3-16 and Fig. 3-17, the distance between patterned electrodes needs to be approximately same and similar to the thickness of the piezoelectric substrate. That is, these are rules of thumb to effectively generate localized strain when applying perpendicular electric field. To better intuitively understand this we examine the details of the parametric study shown in Fig. 3-17 for [001] PMN-PT.

Figure 3-18 shows the xz cut planes for d = 20, 500, 1500 um cases, respectively, for the parametric study presented in Fig. 3-17. The substrate is [001] PMN-PT, and the two top electrodes are grounded while a +400V is applied to the bottom. In the xz cut planes, the red arrow represents the electric field direction and amplitude, the color represents the principle strain along x-direction ε_{11}, and the mechanical deformation is also drawn with a scale factor of 300 for all three cases.

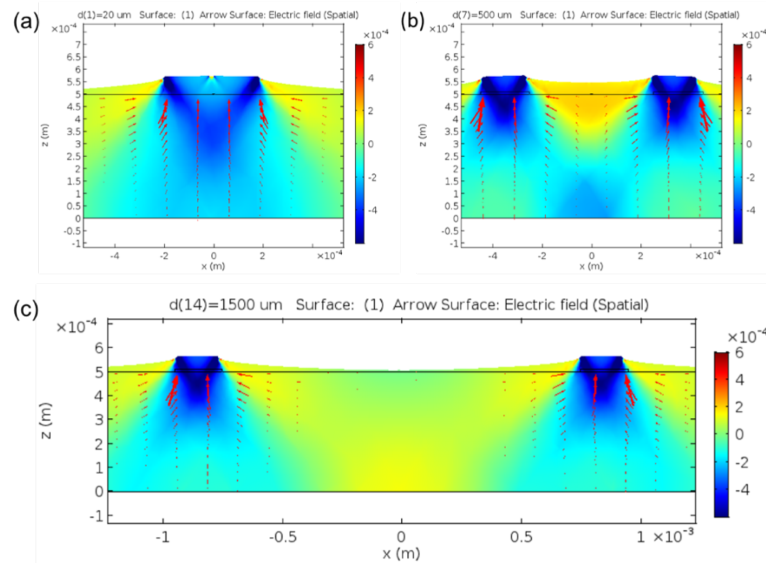

Figure 3-18. xz cut planes for d = 20, 500, 1500 um in the (defined in Fig. 3-17). The arrow shows electric field, the color shows ε_{11}, and the deformation shows mechanical displacement.

It can be seen that, when the distance between two electrodes is too close (Fig. 3-18(a)), the whole region between the two electrodes rises and the in-plane strain caused by the rising-up of the patterned electrodes is small. When the distance between two electrodes is too large (Fig. 3-18(c)), the device in the center (too tiny to be seen in the image) is too far away from the patterned electrodes, the strain effect does not propagate efficiently from the electrode to the central device and thus once again is small. There is naturally an optimized range for the distance between these two extremes, which is suggested to be approximately equal to the thickness of the substrate (Fig. 3-18(b)).

Since [011] PMN-PT does not have any advantage over the isotropic [001] PMN-PT substrate in terms of the strain amplitude, and the strain generated by patterned electrodes on [011] PMN-PT has complex distribution, we only focus on studying [001] PMN-PT in the following simulations.

Next we examine how the electrode size influences the strain on [001] PMN-PT. Fig. 3-19 shows the results for varying the width (w) and height (h) of the electrode, while keeping the distance between the two electrodes fixed at 500 um.

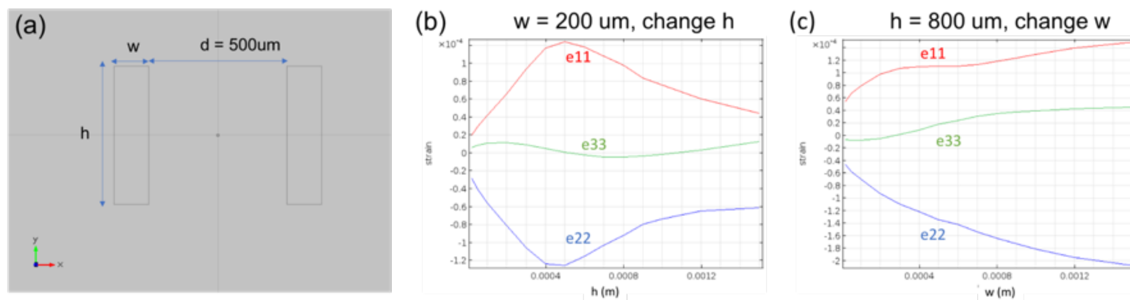

Figure 3-19. Impact of electrode size on strain distribution for [001] PMN-PT substrate.

It can be seen from Fig. 3-19 that the height has an optimized value, which approximately equals to the thickness of the piezoelectric substrate (i.e., 500 um). On the other hand, the conclusion regardin the width of the electrode is different, i.e. the larger the better. This is a good thing because in an actual device, the electrode leads usually increase the effective width, which increases the strain generated in the center.

As a side note, bulk PZT was also simulated as a comparison to the [001] PMN-PT. The PZT-5H is used with the same dimension as PMN-PT (i.e., 5 mm × 5mm × 0.5 mm), and the same mechanical boundary condition is applied (i.e., one corner of the PMN-PT bottom surface is fixed, and its adjacent two side planes and the bottom surface have roller connections). The top electrodes are grounded, and a +400 V is applied to the bottom. The results are shown in Fig. 3-20.

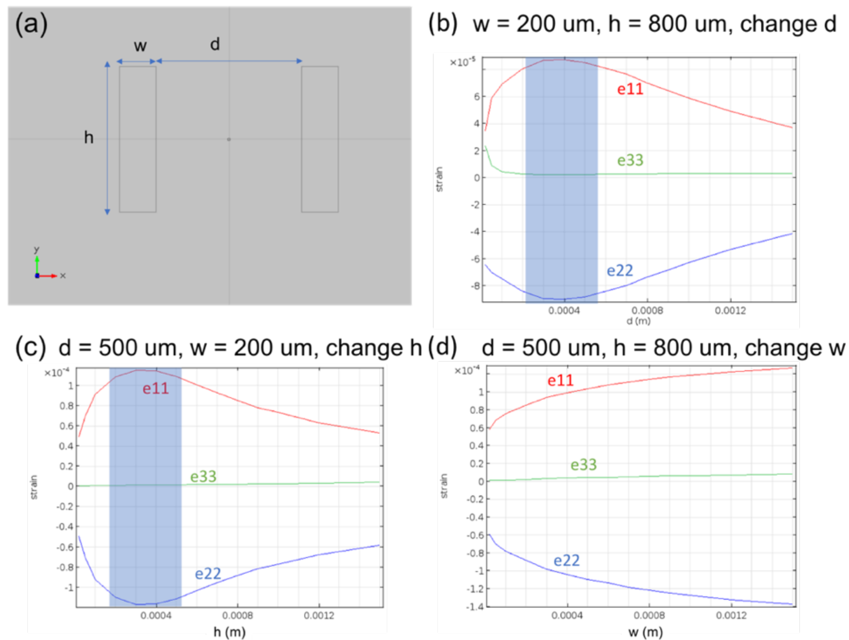

Figure 3-20. Impact of electrode size on strain distribution for PZT-5H substrate.

Basically, a similar conclusion can be drawn: the distance between electrodes and the height of the electrode should be 200 ~ 600 um, the width of the electrode should be as large as possible. The maximum in-plane bi-axial strain $\varepsilon_{11} - \varepsilon_{22}$ is about 200 ppm, which seems to be too low compared to the 1200 ppm achieved in Cui's bulk PZT experiment.[36] However, it should be noted that Cui applied 1.5 kV to the PZT (which is about 4 times larger than what we applied here), and the PZT coefficient of his PZT is about 1.5 times higher than PZT-5H in COMSOL. Taking into those factors, our simulation agrees with his experiment.

Last, we studied how the device's thickness impact the strain for [001] PMN-PT. The results are shown in Fig. 3-21. The device is simplified as a gold block with lateral dimension of 10 um × 10 um. The thickness t is varied from 200 nm to 1 um. The surface average of the principle strains along three axes are calculated for both top and bottom surface of the device, and the results are plotted in Fig. 3-21(b).

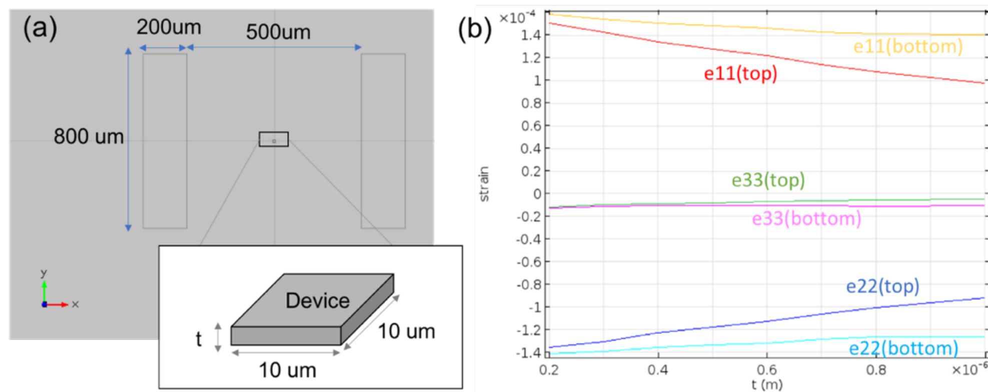

Figure 3-21. Impact of device's thickness on strain generated by patterned electrodes on [001] PMN-PT.

By looking at the three bottom strain components, it can be seen that the thickness has an influence on the localized strain, however, the impact is small and plateaus after 800 nm. By comparing the same strain component for top and bottom surface, it can be seen that the

percentage of strain that is transferred from bottom to the top also drops as the thickness increases. The drop is linear and does not plateau within the thickness range studied.

With a similar model setup as shown in Fig. 3-21, we also manually changed the Young's modulus of the device material (Y[Au] = 70 GPa), and studied how the Young's modulus affects the strain transfer. Fig. 3-22 shows the results for different Young's modulus. It can be seen that for soft material (Y = 10 GPa), the thickness has negligible impact on the bottom strain, while for hard material (Y = 200 GPa), the bottom strain drops much faster as thickness increases. Also, the percentage of strain that is transferred from bottom to top is small for materials with high Young's modulus. In actual devices, the thickness of the device is usually less than 200 nm, at which over 95% strain is transferred from the bottom to the top regardless of the Young's modulus. In other words, the impact of device thickness or device material is small in actual devices.

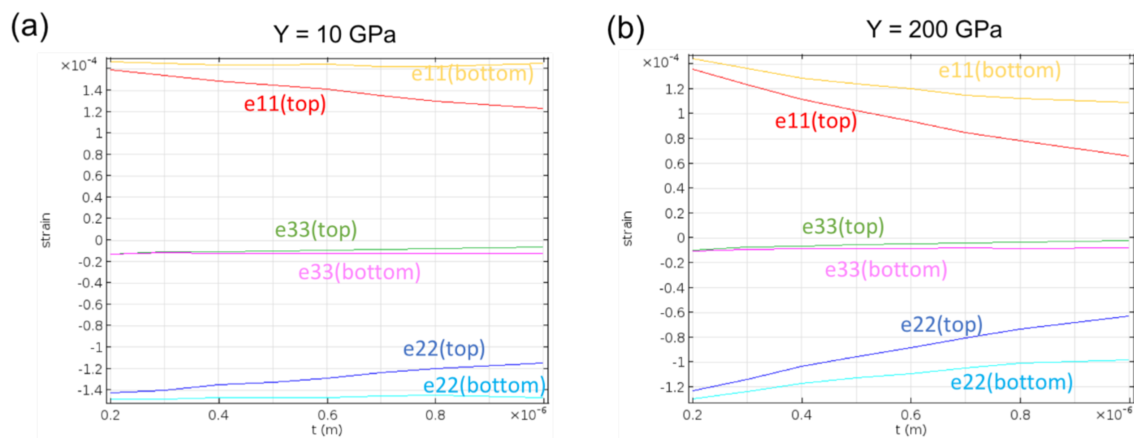

Figure 3-22. Impact of Young's modulus on strain transfer.

3.2.3 Device on PMN-PT (generation 1)

Before we consider the fabrication and testing portions, it should be emphasized that the devices in this section (i.e., on PMN-PT with patterned electrodes) were built before the parametric study in section 3.2.2 was conducted. In this section, we mistakenly used [011] PMN-PT to fabricate the devices, although it is shown in section 3.2.2 that [011] PMN-PT is less optimal choice for generating strains with patterned electrodes.

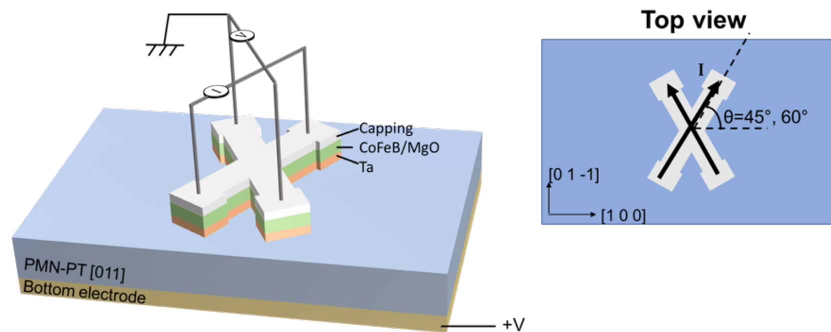

Figure 3-23. Illustration of gen1 device on [011] PMN-PT.

In the first generation (gen1) device, there is no separate electrodes to apply voltage to, but rather we use the device itself as the ground, and apply +400 V to the bottom. The device structure is shown in Fig. 3-23. It is worth mentioning that, we poled the PMN-PT before the magnetic film deposition step, otherwise the poling step causes residual stress inside the magnetic thin film. Normally there is a separate top metal deposition step when fabricating on PMN-PT, and one can always take advantage of that metal layer and pole the PMN-PT before the magnetic material deposition. However, in our PMA system, the magnetic layer is so thin (~1 nm) that its magnetic property is very sensitive to the surface roughness. So we prefered to deposit the whole stack (Ta/CoFeB/MgO/Ta) at the same time without breaking vacuum between

depositions. In other words, we do not have a continuous metal layer to pole PMN-PT at any time point.

First we tried two ways to pole the PMN-PT with the bare top surface. The first method is to use a spin coat photoresist layer and deposit gold (using the Denton sputtering machine at ISNC in UCLA) on top. Then we use the gold as top electrode to pole the PMN-PT. After poling, the gold can be removed by doing lift-off. However, this does not work well because the photoresist layer has a low dielectric constant and hence low capacitance. When applying voltage to the double dielectric layer (i.e., photoresist and piezoelectric substrate), over 90% voltage drop happens inside the photoresist layer. The effective voltage across the PMN-PT substrate is insufficient to electrically pole the sample. The other method is to use a piece of Aluminum foil as a temporal top electrode. However, the small gap between the foil sheet and the PMN-PT surface may also lead to inefficient poling.

Then we considered another poling method without an existing continuous top electrode on PMN-PT for poling, as shown in Fig. 3-24. It should be emphasized that in step 4, we observed that weird patterns appeared on top of the PMN-PT surface after etching without protecting the bottom Pt. Therefore, even though Pt is not attacked by the gold etchant [136], it is still suggested to protect the bottom electrode using photoresist.

1. Deposit bottom electrode Ti(10nm)/Pt(100nm)

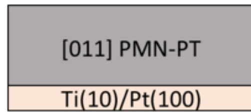

2. Deposit top electrode Au(40nm)

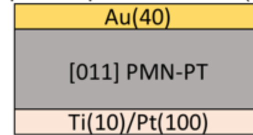

3. Pole the PMN-PT using the clamping fixture on copper board.

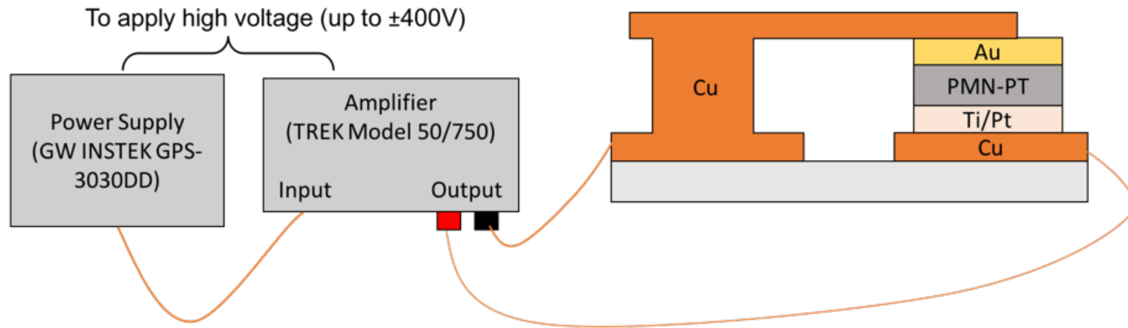

4. Spin coat a photoresist layer to protect bottom electrode. Etch away the top Au electrode using diluted gold etchant TFA (TFA:water=1:4, 1min).

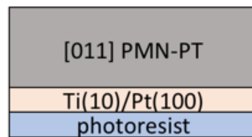

5. Strip photoresist using Acetone.

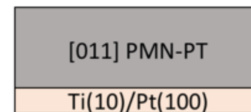

Figure 3-24. Poling of PMN-PT without the existence of continuous top electrode.

Following this step, we fabricated the device on both [011] PMN-PT and Si/SiO2 substrate. Fig. 3-25 shows the process flow. The thickness of CoFeB layer is 1 nm here. Note the detailed photo lithography steps can be found in Chapter 1.

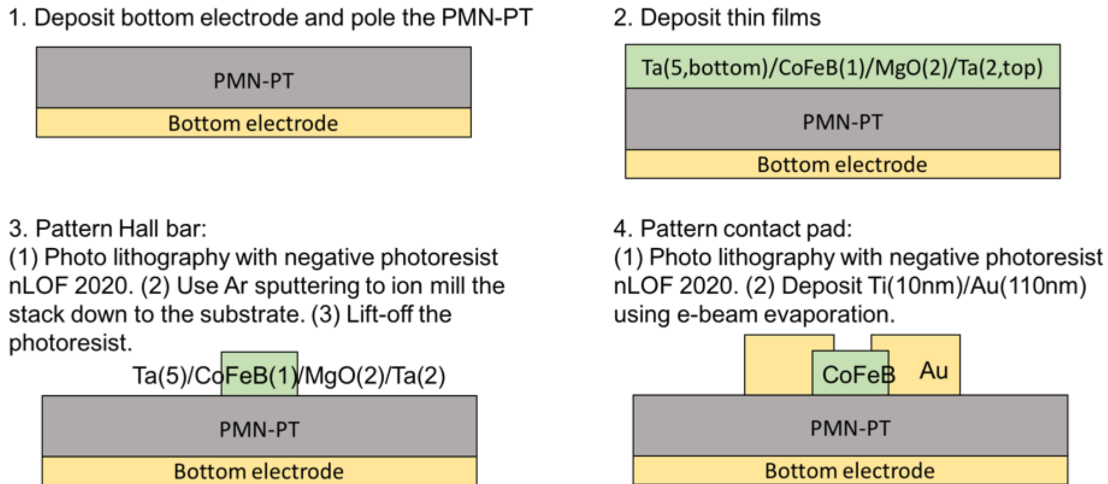

Figure 3-25. Fabrication process flow of gen1 device on PMN-PT. Unit: nm.

After fabrication, we tested the devices using a four probe station with the ability to apply in-plane or out-of-plane magnetic field by an electromagnet. Fig. 3-26 shows the testing setup for gen1 device. The four probes are used to measure the anomalous Hall resistance with Keithley 2612A sourcemeter (details of anomalous Hall resistance measurement can be found in Chapter 1). The PMN-PT device is placed on a piece of Si wafer with 200 nm Au deposited on top. The Si piece is taped onto the electromagnet, and the output cable from the voltage amplifier (used to generate 400 V) is connected to the Si piece. The voltage amplifier and the four probes have a common ground.

Figure 3-27 presents the testing results of switching under perpendicular external magnetic field. The results show that the CoFeB film has good PMA (Hc ~ 35 Oe)however an applied voltage of 100 V and 200 V applied to the bottom of PMN-PT does not obviously modify the PMA.

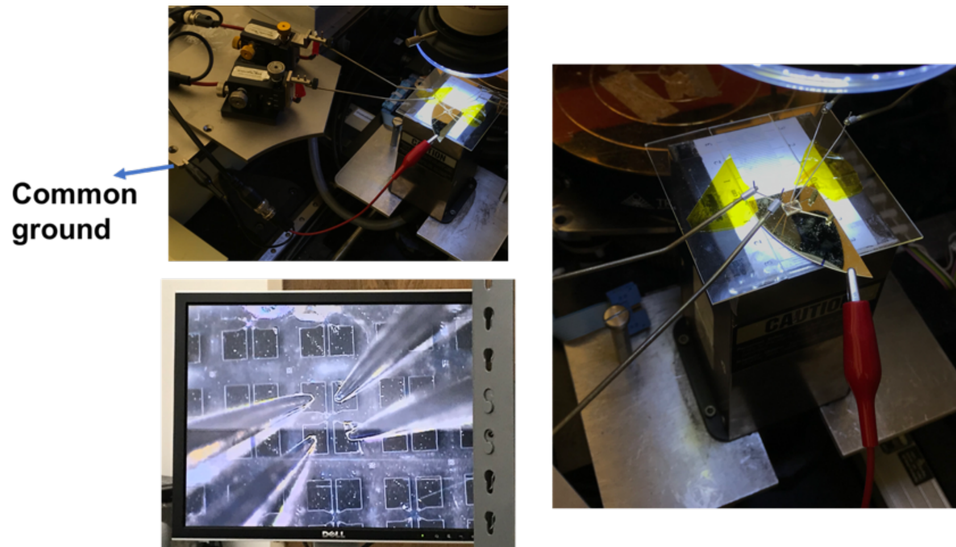

Figure 3-26. Test setup for the gen1 device using the probe station with in-situ applied voltage.

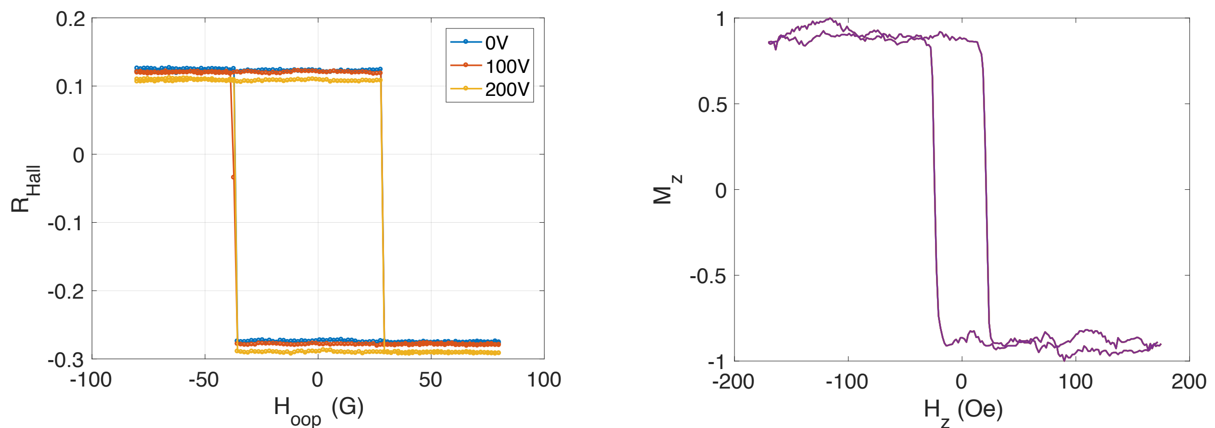

Figure 3-27. Perpendicular magnetic switching of the Hall bar (left) by anomalous Hall resistance measurement and continuous film (right) by MOKE measurement.

Figure 3-28 presents the spin-orbit torque (SOT) switching results under in-plane bias field. The bias field is swept from 200 G to 0, and then swept from 0 towards the negative direction until -200 G. The results are presented in two plots, respectively. The device showed good SOT switching behavior: (1) switching reverses direction when the bias field reverses direction; (2)

threshold switching current is smaller for larger bias magnetics field. It should be emphasized here that the 'field-free' switching that occurs at zero magnetic field is due to the remanent field inside the electromagnet. In other words, there is a 10~20 Oe field existing even when we cut off the power of the electromagnet. Because the remanent field is not a fixed value, it is hard to compensate or eliminate.

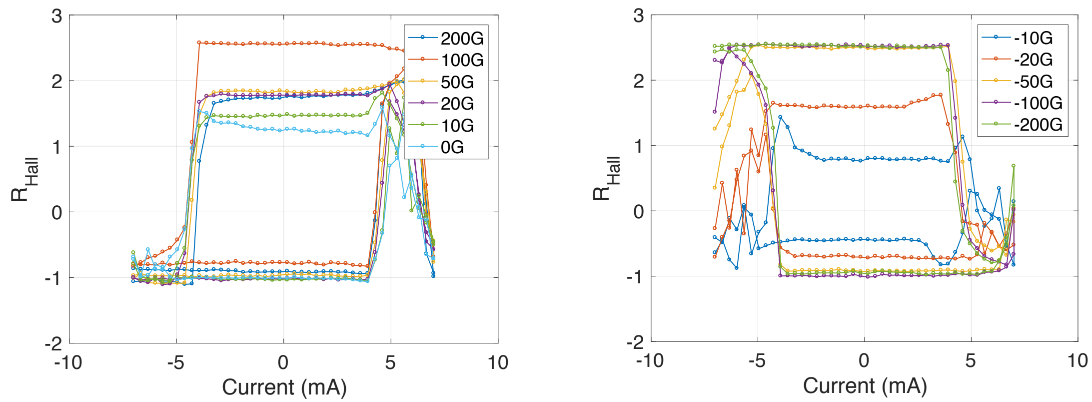

Figure 3-28. SOT switching test of gen1 device on [011] PMN-PT.

Figure 3-29 presents the spin-orbit torque (SOT) switching with different applied voltage to the bottom of PMN-PT. The in-plane bias field is fixed to be 100 Oe. There is no change of threshold switching current under different applied voltages.

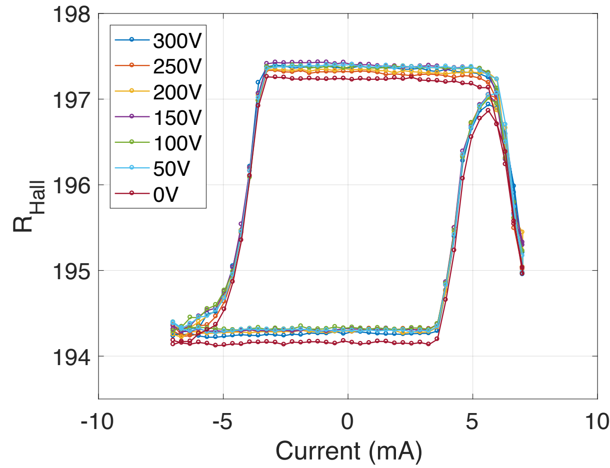

Figure 3-29. The impact of applied voltage on SOT switching.

Figure 3-30 presents the magnetic switching curves with different applied current for anomalous Hall resistance measurement. The heating effect of the 3 mA current is non-negligible as the coercivity field of the magnetic material becomes much smaller.

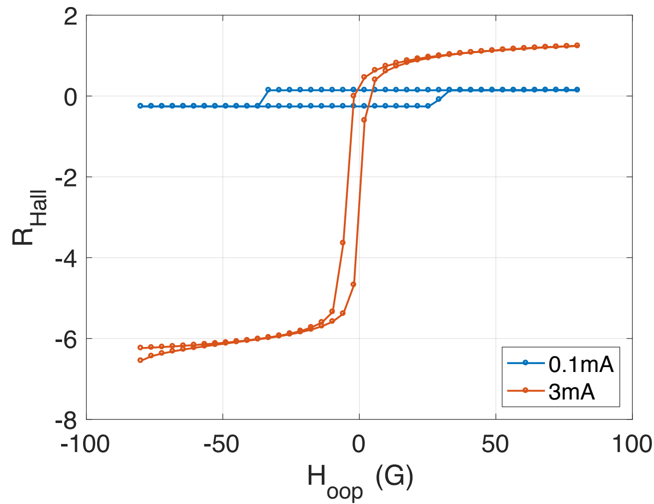

Figure 3-30. The impact of Joule heating on the magnetic switching.

3.2.4 Device on PMN-PT (generation 2)

Instead of using the Hall bar itself as a terminal for straining the substrate, we redesigned the device and patterned big electrodes on top of the PMN-PT as the terminal to apply voltage to the PMN-PT substrate. This is the 2nd generation (or gen2) device. The device illustration and the results are shown in Fig. 3-31. Four big gold pads are patterned on top of the substrate and the spacing between adjacent pads is 1 um. The bottom of PMN-PT is grounded, while a +400 V is applied to all the top electrodes at the same time. Simulation shows that the strain generated to the center of the Hall bar are $\varepsilon_{xx} = 45\ ppm$, $\varepsilon_{yy} = -90\ ppm$, $\varepsilon_{zz} = 25\ ppm$ for 400 V applied voltage. Fig. 3-31(b) shows the perpendicular coercive field changing with applied voltage for both positive and negative switching field. The data point and error bar show the average and standard deviation of coercivity field for 20 sweeps, respectively. The dashed red line is the linear fitting of the data points. The slope of the fitting line is -0.2 Oe / 100 V for the positive Hc side, and +0.1 Oe / 100 V for the negative Hc side. The effective strain for +400 V applied voltage is 20 ppm as defined in Eq. 3-2.

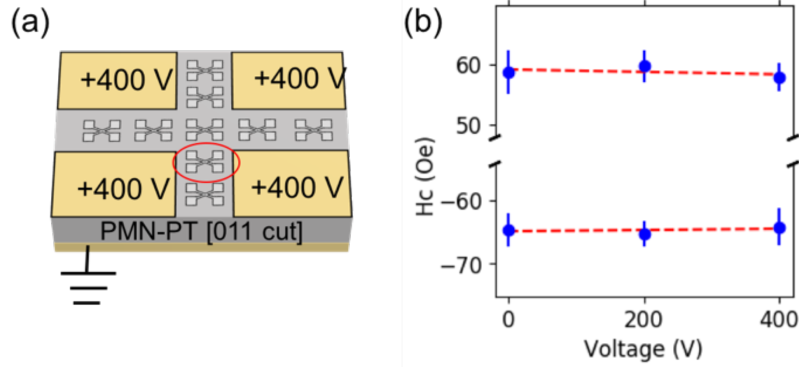

Figure 3-31. Device illustration and coercive field shift test for gen2 device on [011] PMN-PT.

As a comparison, similar test is also performed to the first generation device and the results are shown in Fig. 3-32. Simulation shows that the strain generated at the center of the Hall bar are $\varepsilon_{xx} = 150\ ppm$, $\varepsilon_{yy} = -140\ ppm$, $\varepsilon_{zz} = -8\ ppm$ for -400 V voltage applied to the bottom electrode.

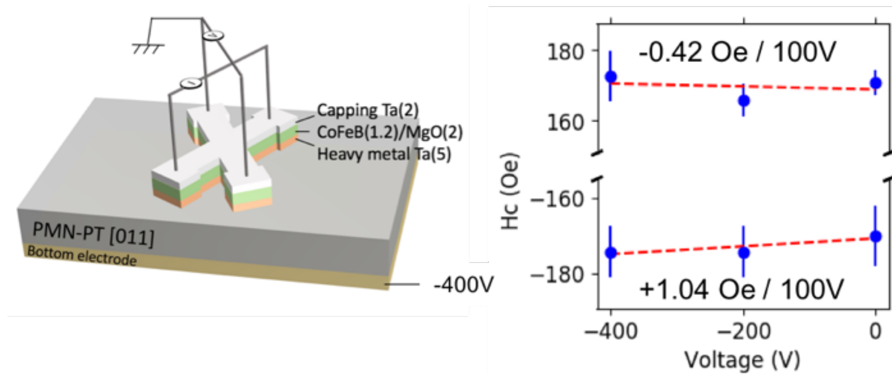

Figure 3-32. Device illustration and coercive field shift test for gen1 device on [011] PMN-PT.

3.2.5 Device on PMN-PT (generation 3)

Both simulation and experiment suggest that using patterned electrodes to perform strain-mediated perpendicular switching is not a good choice, because the effective strain is too small. To get a larger strain effect, it is better to use a continuous top electrode to actuate the PMN-PT.

We added an insulating layer to isolate the device and the top electrode. The process flow is shown in Fig. 3-33. All the top films are deposited in the same deposition run, and the MgO and Alumina are deposited using RF sputtering while the metals are deposited using DC sputtering.

1. Deposit bottom electrode and pole the PMN-PT

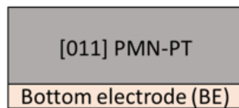

2. Deposit thin films.

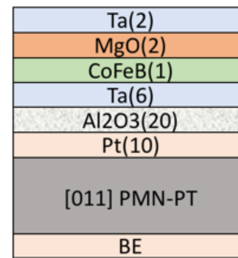

3. Pattern Hall bar:
(1) Photo lithography with negative photoresist nLOF 2020. (2) Use Ar sputtering to ion mill the stack down to Ta layer. (3) Lift-off the photoresist.

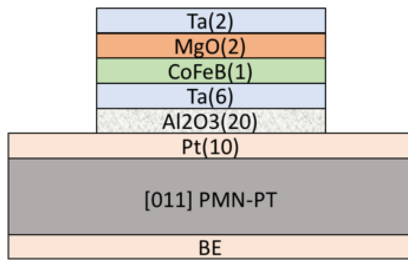

4. Pattern contact pad:
(1) Photo lithography with negative photoresist nLOF 2020. (2) Deposit Ti(10nm)/Au(110nm) using e-beam evaporation.

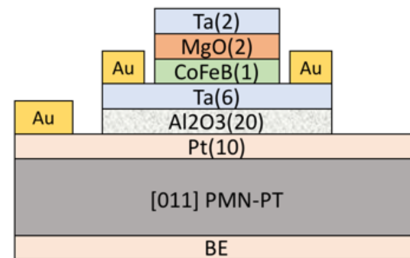

Figure 3-33. Fabrication process flow of devices on PMN-PT with continuous top electrode. The unit of the numbers is nm.

Figure 3-34(a) shows the completed device, and Fig. 3-34(b) shows an example anomalous Hall resistance measurement of the device. The Hall resistance readout is small because the 20 nm Alumina layer is not a good insulating layer. Due to the pinholes in the Alumina layer and relatively large Hall bar structure (20 um), the Hall bar turns out to be electrically connected to the top Pt electrode right on top of the PMN-PT substrate. The current applied to the Hall bar leaks through the Pt layer, causing the small Hall resistance signal.

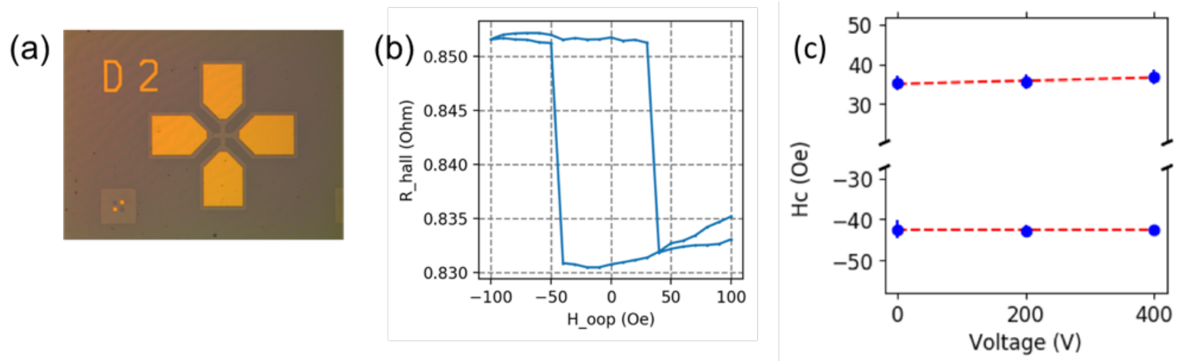

Figure 3-34. Fabrication process flow of devices on PMN-PT with continuous top electrode. The unit of the numbers is nm.

Although the Alumina layer failed in insulating the Hall bar and the top electrode of the PMN-PT substrate, we were still able to observe perpendicular magnetic switching using the anomalous Hall measurement and the coercive field can be extracted from the switching curve. Fig. 3-34(c) shows the testing results for multiple sweeps under different applied voltage. Simulation shows that the strain generated to the center of the Hall bar are $\varepsilon_{xx} = 500\ ppm$, $\varepsilon_{yy} = -700\ ppm$, $\varepsilon_{zz} = 160\ ppm$ for 400 V voltage applied to PMN-PT substrate. However, under such high strain, there is an absence of obvious shifts in the coersive field.

3.3 Device on PZT thin film

Pb(Zr,Ti)O3 is another common used piezoelectric material, and the ratio of Ti and Zr components varies in different PZT composites. The PZT film used in this work is 200 nm thick 20/80 PZT thin film with 10 nm Pt bottom electrode on 4-inch Si/SiO2 wafer from Radiant Technologies.

3.3.1 PZT characterization

First we characterized the PZT film. Fig. 3-35 shows the AFM image of the PZT surface. The Rq and Ra (defined in Fig. 3-9) are 3.7 nm and 3.0 nm, respectively. It is shown that the PZT has rough surface and a planarization process is needed before magnetic thin film deposition, otherwise, the roughness (~10 nm) may endanger the perpendicular magnetic anisotropy of CoFeB thin film (~1 nm). Generally the Rq and Ra need to be less than 1 nm to ensure good PMA of the CoFeB thin film.

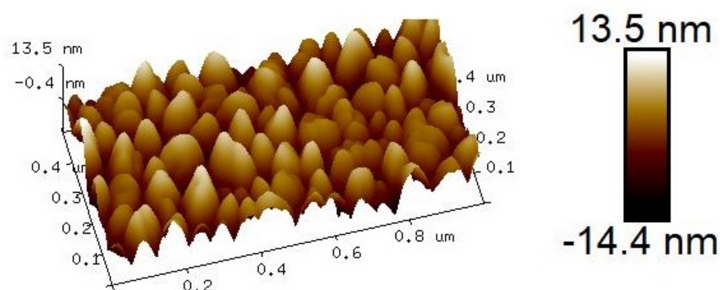

Figure 3-35. AFM image of the PZT thin film.

The X-ray powder diffraction (XRD) data shown in Fig. 3-36 shows that the PZT has good crystalline structure. Note the Pt peak at around 40 degree comes from the bottom Pt electrode.

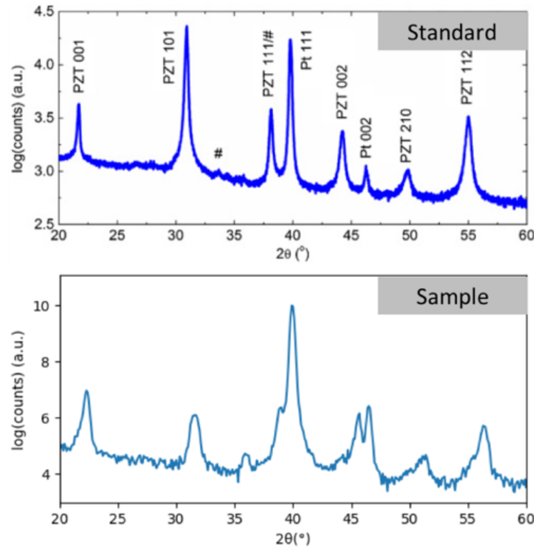

Figure 3-36. XRD of the PZT thin film and the data from reference [137] for comparison.

Figure 3-37 shows the polarization – electric field hysteresis loop. The working principle of PE loop measurement can be found in Section 1.4.2. Fig. 3-37(a) shows the PZT has good ferroelectric property with coercive field around 12 MV/m and coercive voltage around 2.5 V. The asymmetry of the PE loop comes from the asymmetry of the top (100nm thick Pt, circle with diameter 0.5 mm) and bottom (10nm Pt, continuous film) electrodes. This is confirmed by Fig. 3-37(b) where we switched the top and bottom electrode contacts and the asymmetry was reversed.

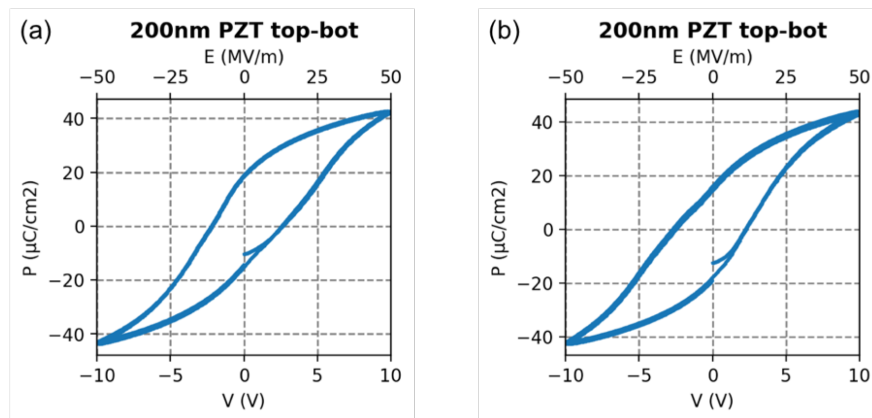

Figure 3-37. PE loop for the 200 nm PZT. (a) Top to bottom measurement. (b) Bottom to top measurement.

Note the PE loops shown in Fig. 3-37 were measured at a speed that the complete sweep was done in 10 ms. When the speed was increased to 5 ms per loop, the similar PE hysteresis loop was obtained. However, when the speed was further increased to 1 ms per loop, no PE hysteresis loop observed. This is because the voltage sweep speed is too fast to charge the PZT.

We also did piezoresponse force microscope (PFM) for the PZT thin film. Fig. 3-38 shows the PR in-phase and amplitude signals in the PFM measurement. The amplitude is defined as: PR amplitude = $\sqrt{(PR\ in-phase)^2+(PR\ quadrant)^2}$. A good linear response was observed regardless of the direction of the voltage sweep. We were not able to see the butterfly hysteresis loop because the PFM tip is actuated at a frequency (15 kHz) that is too high to fully charge the PZT. The slope of the in-phase signal shows the piezoresponse is approximately 10 mV for 1 V applied voltage. Similar PFM data was obtained whether the PFM tip is landed on bare PZT surface, or a circular electrode (0.5 mm diameter) sitting right on top of PZT, or an electrode sitting on HSQ planarization layer on PZT.

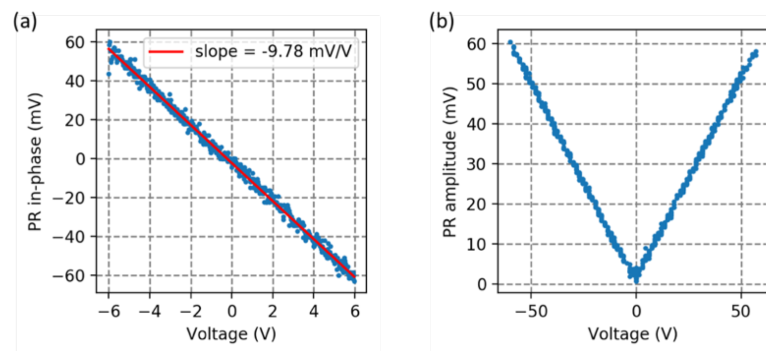

Figure 3-38. PFM measurement for the 200 nm PZT. (a) In-phase. (b) PR amplitude.

The sensitivity deflection is calibrated to be 184 nm/V as shown in Fig. 3-39. The PFM measurement is used to calculate the piezoelectric response as follows:

= Signal (in mV) × deflection sensitivity (in nm/mV)/[deflection gain × applied AC bias (in V)]

= 10 (mV) × 183 (nm/mV) / [16 × 2 (V)]

= 57 (pm/V)

This means for 1 V applied voltage by the PFM tip to the PZT substrate, the localized vertical deflection is 57 pm. However, 57 pm/V is not the real d33 of the PZT substrate as the PZT thin film is mechanically clamped. To extract the d33 from the piezoelectric response, we simulated in COMSOL a 200 nm PZT with bottom and sides mechanically fixed. We actuated the PZT using a small top electrode, while keeping the bottom continuous electrode grounded. It is shown that the 57 pm local deflection corresponds to a d33 coefficient of 73 pm/V. It is known that a normal d33 for PZT continuous thin film on Si substrate is ~50 pm/V. [138] Therefore, our measurement and calculation for the PZT thin film appears to be reasonable.

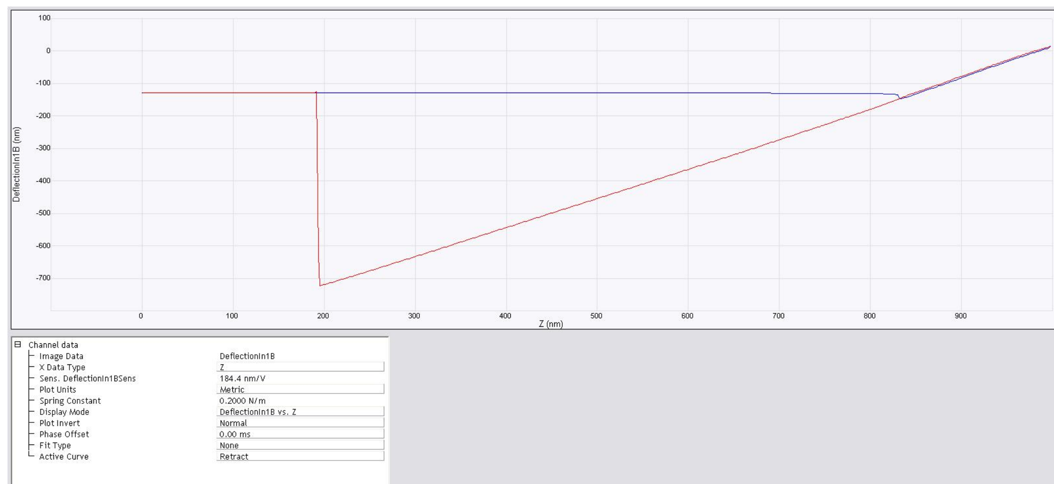

Figure 3-39. Sensitivity deflection calibration for the PFM tip.

3.3.2 Fabrication

As mentioned in the previous section, we need to planarize the PZT film. Fig. 3-39 showed different planarization plans and the AFM images after planarization. Plan A is to direct ion mill the PZT surface at high angle (70 degree) for 15 min. Plan B is to first deposit 10 nm Alumina (the Young's modulus of Alumina is 200~400 GPa) and then ion mill until PZT surface. Both Plan A and B only slightly improved the surface roughness. Plan C is to first spin coat 6% HSQ and then dry etch HSQ. The etching is well time-controlled such that the residual HSQ has a thickness of 20~30 nm. Plan C provides a smooth enough surface for the following fabrication step. The Rq and Ra of the PZT surface after Plan C are both approximately 0.8 nm.

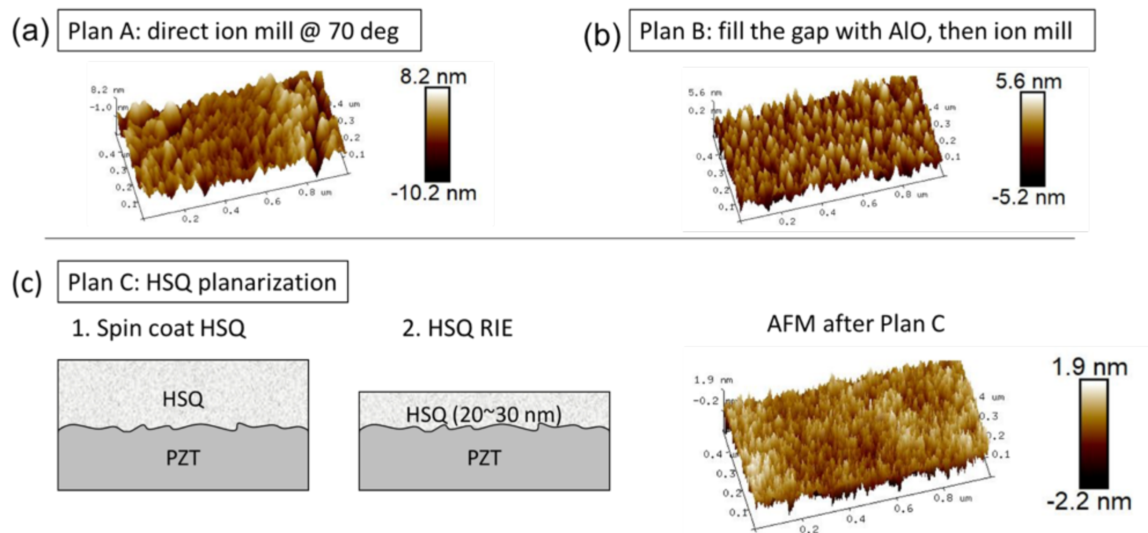

Figure 3-40. Different planarization plans for PZT thin film the AFM images showing surface roughness after planarization.

The device is illustrated in Fig. 3-41. A Hall bar is patterned to measure anomalous Hall resistance and get the information for perpendicular magnetization of the central magnetic pillar. The magnetic pillar is CoFeB(1.2nm)/MgO(2nm)/Ta(2nm) and its diameter is 350 nm. The

width of the Hall bar is 400 nm for both the current wire and the voltage readout arm. There are four gating pads where we can apply voltage to. A via is etched to get access to the bottom electrode (not shown here). The distances between gating pads is 800 nm. The size of the gating pad (not including the lead) is 1.5 um by 1.5 um.

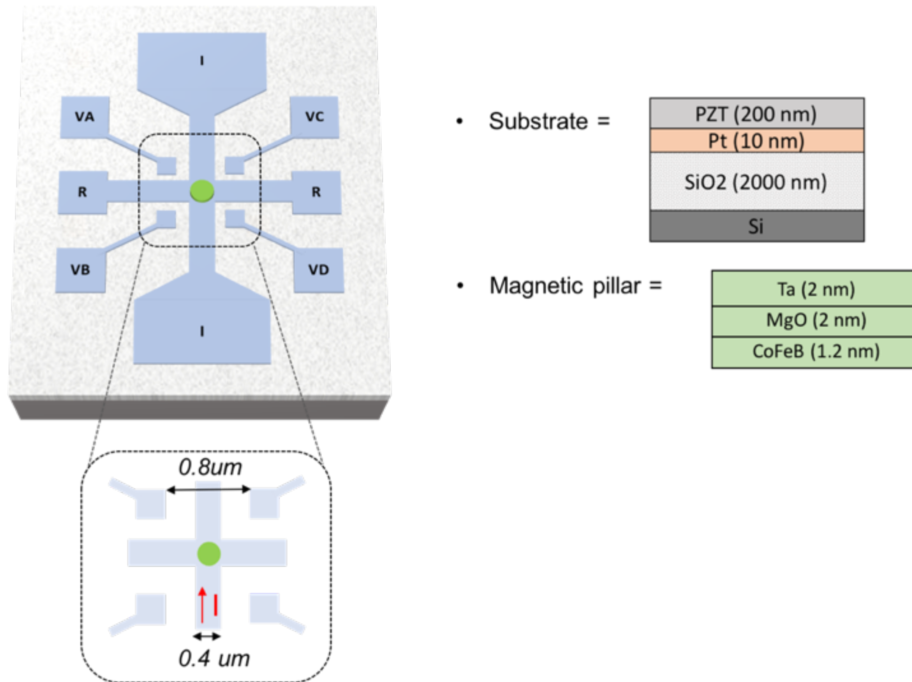

Figure 3-41. 3D illustration of the device on PZT thin film. (Unit: nm)

The device is fabricated using the process flow shown in Fig. 3-42. There are two e-beam lithography steps, two ion mill steps, and one photo lithography step. Note the gating pads are patterned in the same step with the Hall bar, i.e., after fabrication, the gating pads sit on top of the HSQ planarization layer not on top of PZT surface.

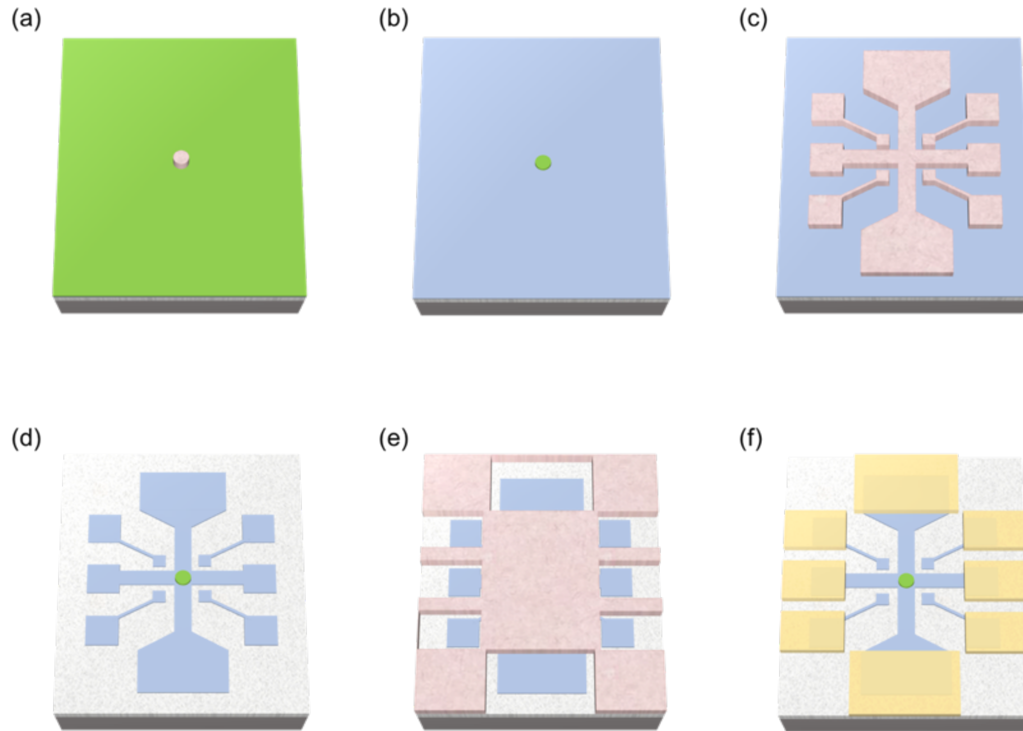

Figure 3-42. Process flow of fabricating Hall bar on PZT film. (a) Pattern the e-beam resist for magnetic pillar. (b) Ion mill magnetic pillar and lift-off resist. (c) Pattern the e-beam resist for Hall bar. (d) Ion mill Hall bar and lift-off resist. (e) Pattern photo resist for leads and contact pads, deposit Au and lift-off resist.

In another device, we replaced the Ta gating pads with Au gating pads using the process shown in Fig. 3-43. As illustrated in Fig. 3-43(b), the e-beam resist is patterned that cover the four gating pads, and then the original Ta pads and the HSQ planarization layer were etched. After that a thin gold layer was deposited. Fig. 3-43(c) shows the cross section of the device after the replacement. The main difference is that the gating pads are sitting on PZT surface and can be used to apply electric field directly to the PZT.

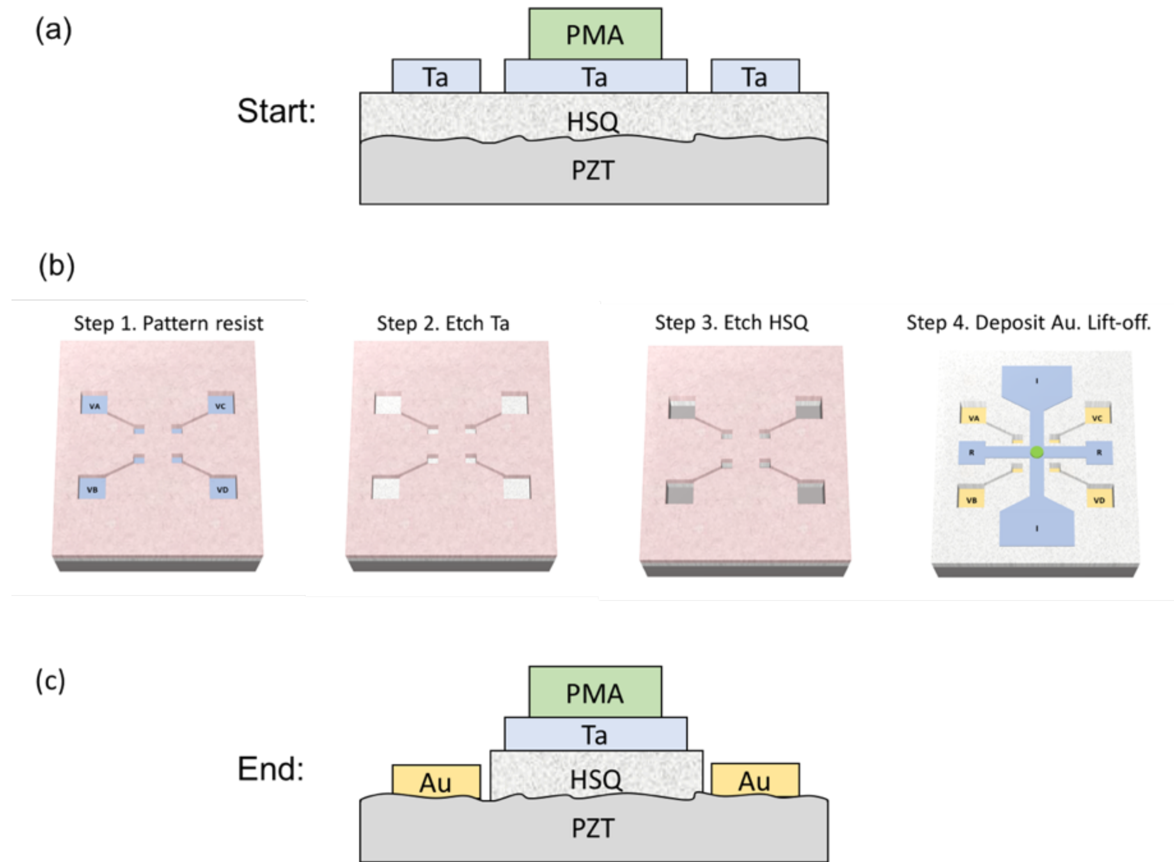

Figure 3-43. Process flow of replacing the gating pads. (a) Cross section of the device before the process. (b) Process flow. (c) Cross section of the device after the process.

3.3.3 Characterization

Figure 3-44 shows the characterization of the magnetic film using VSM and anomalous Hall resistance measurement for the continuous magnetic film (blue curves) and the patterned magnetic pillar (orange curves), respectively. The working principle of VSM is explained in Section 1.4.1. It is shown that the film has good perpendicular magnetic anisotropy before and after patterning. The perpendicular coercive field is ~10 Oe before patterning and is increased to ~250 Oe after patterning. In contrast the in-plane anisotropy field is decreased after patterning.

This is partially because the in-plane shape anisotropy of the magnetic film is decreased after patterning into nano-scale pillar.

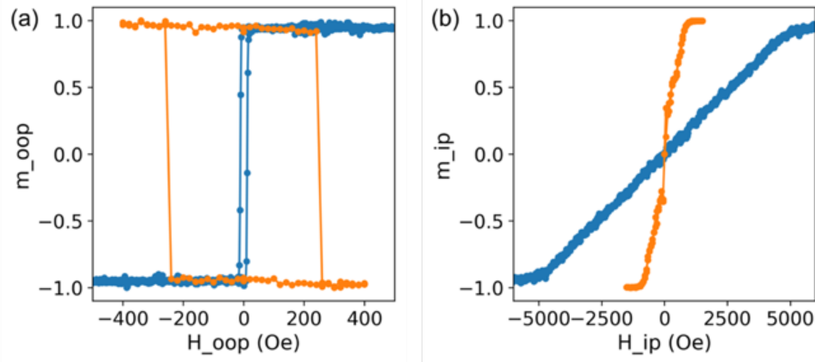

Figure 3-44. VSM (blue) and Hall resistance (orange) measurement of the magnetic film. (a) Out-of-plane field switching. (b) In-plane field switching.

Figure 3-45 shows the testing data with gating pads sitting on PZT and HSQ surface, respectively. As shown in Fig. 3-45(a), the top four gating electrodes are grounded, while a voltage is applied to the bottom electrode. Fig. 3-45 (d)(e) shows the coercive field measurements with different applied voltage for the two devices shown in Fig. 3-45 (b) and (c), respectively. Each data point is the average of 50 sweeps and the error bar shows the standard deviation of the coercive field, indicating the variance of the coercive field due to thermal fluctuation.

A clearly linear relationship between the applied voltage and coercive field is observed in the device with gating pads on PZT surface as shown in Fig. 3-45(d). The slope is ~3.5 Oe / V and a ±20 Oe shift is achieved with ±6 V applied voltage. In contrast, no coercive field shift is observed in the device with gating pads on HSQ layer as shown in Fig. 3-45(e). Note the Hc shift shown in Fig. 3-45(d) does not have a butterfly-shape hysteresis, which might be because the

gating pads are too small (square shape with 1.5 um width) to reverse the polarization of the local PZT area.

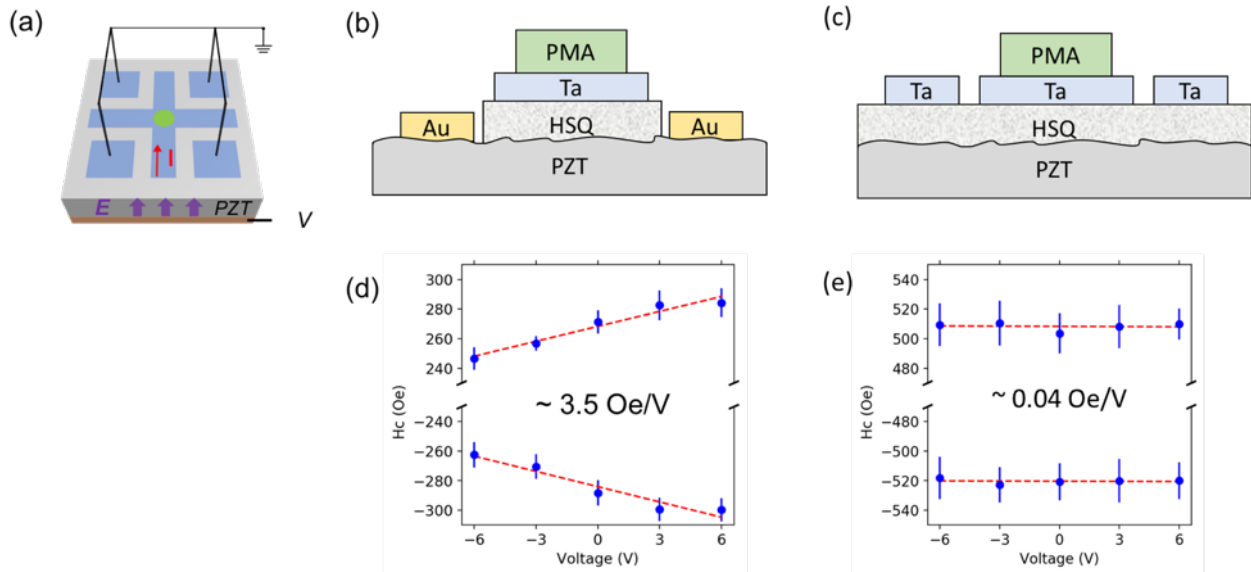

Figure 3-45. Perpendicular coercive field measured by anomalous Hall effect. (a) Test setup. (b)(c) Illustration of the two devices. (d)(e) Coercive field with different applied voltage to the bottom electrode of PZT for the two devices shown in (b) and (c), respectively.

To better understand the difference between the two devices, a COMSOL simulation is performed to examine the electric field and strain distribution for the two devices with +10 V voltage applied to the bottom electrode. A 30 nm HSQ layer is added on top of PZT, and is simulated using the property of SiO2 as the HSQ is Si-O based compounds after curing. The arrows in Fig. 3-46 (b) and (e) show the electric field and the equipotential lines are also illustrated. The color demonstrates the amplitude of the *z* component of the electric field. It is shown that for the device shown in Fig. 3-46(a), the electric field concentrates in the HSQ layer. There is negligible electric field in PZT substrate and therefore negligible strain is generated as shown in Fig. 3-46(c). This is because the huge dielectric constant between the HSQ and PZT

($\varepsilon_{HSQ} = 3$, $\varepsilon_{PZT} = 1700$). As a result, the capacitance of the HSQ layer is much smaller than the PZT layer. The device can be simplified as two capacitors in series, and a quick calculation shows that more than 90% electrical potential drop happens in the HSQ layer. In contrast, when the gating pads are directly on PZT surface, decent amount of electric field and strain are generated in the PZT layer as shown in Fig. 3-46 (e)(f).

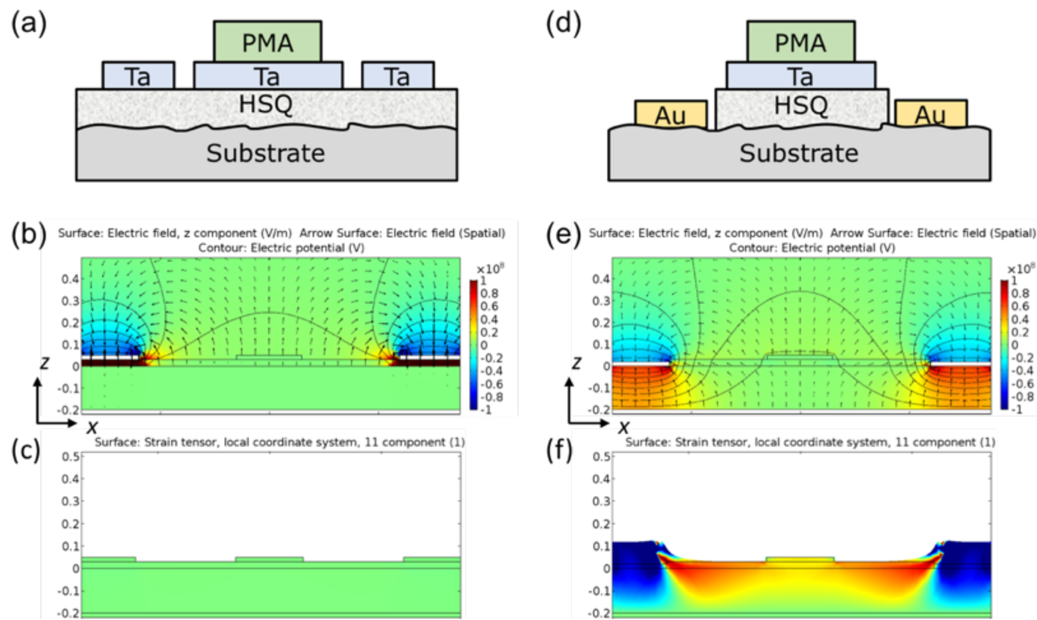

Figure 3-46. COMSOL simulation of the two devices with 10 V applied to the bottom electrode. (a)(b)(c) Device cross-section, perpendicular electric field, strain along *x* axis for the device with gating pads sitting on HSQ layer. (d)(e)(f) Device cross-section, perpendicular electric field, strain along *x* axis for the device with gating pads sitting on PZT surface.

3.3.4 Analysis

It is shown by simulation that the averaged strain inside the magnetic pillar is approximately 100 times different in the two tested devices. As shown in Fig. 3-45, the coercive field shift is

also about 100 times different for the two devices. Therefore, it is reasonable to contribute the Hc shift to the strain. Other effects, such as special interface effect or VCMA, can be also ruled out because the two devices have the same interface for the magnetic pillar, i.e., the magnetic layer both sit on HSQ layer. The testing results show ±20 Oe shift is achieved with ±6 V applied to the PZT substrate. To validate the effect, we did mathematical and numerical analysis in this section.

First the perpendicular magnetic energy density can be expressed as:[55], [139]

$$E_{perp} = M_S \int H dm = \frac{M_S}{R_{Hall,max}} \int H dR_{Hall} \approx M_S H_c \qquad \text{Eq. 3-3}$$

assuming the R_{Hall}-H curve from the anomalous Hall measurement is perfect rectangular. Here M_S is the saturation magnetization, and Hc is the coercive field. And the magnetoelastic energy density in terms of strain is:[36], [132], [140]

$$E_{me} = \frac{3}{2}\lambda_S \sigma = \frac{3}{2}\lambda_S Y \varepsilon \qquad \text{Eq. 3-4}$$

where σ is stress, ε is strain, Y is the Young's modulus of the magnet, and λ_S is the saturation magnetoelastic coefficient. Assuming the magnetoelastic energy converts into perpendicular magnetic energy:

$$M_S \times \Delta H_c = \frac{3}{2} \times \lambda_S \times Y \times \varepsilon \qquad \text{Eq. 3-5}$$

The parameters for CoFeB are: Y = 160 Gpa = 160×10^9 N/m^2, λ_S = 35 ppm = 35×10^{-6}, Ms = 850 emu/cc = $4\pi\times850\times10^{-4}$ T, ΔH_c = 20 Oe = 20×79.6 A/m. Plug the parameters into equation 3-5, we get:

$$4\pi \times 850 \times 10^{-4} (Tesla) \times 20 \times 79.6 (A/m) = \frac{3}{2} \times 35 \times 10^{-6} \times 160 \times 10^{9} (N/m^2) \times \varepsilon \quad \text{Eq. 3-6}$$

Note the units on both sides are J/m^3, i.e., energy density. From equation 3-6, we can get $\varepsilon = 2.02 \times 10^{-4} = 202\ ppm$. This means the 20 Oe Hc shift mathematically corresponds to ~200 ppm strain. We define the effective strain as $\varepsilon_{eff} = \varepsilon_{zz} - \varepsilon_{ip}$, which can be understood in this way: any positive in-plane strain decreases the perpendicular magnetic anisotropy while positive strain along z direction increases the perpendicular magnetic anisotropy.

Using the piezoelectric coefficient measured using PFM (d33 = 73 pm/V and other d coefficients are adjusted proportionally from the values for bulk PZT), it can be shown that 6 V applied voltage generates a volume averaged strain inside the magnetic pillar as: ε_{xx}=ε_{yy}= -113 ppm, ε_{zz}= +108 ppm. In other words, both mathematical calculation and COMSOL simulation show that there is a 200 ppm effective strain generated. A Mumax simulation is conducted to further confirm the Hc shift is caused by strain through magnetoelastic field. As shown in Fig. 3-47, the 200 ppm strain causes approximately 20 Oe coercive field shift.

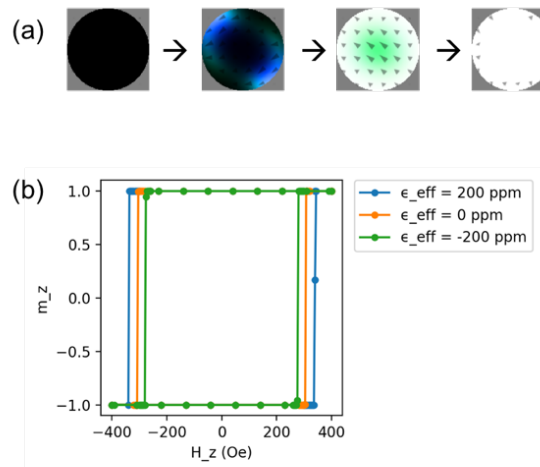

Figure 3-47. Mumax simulation results.

The goal of the device on PZT thin film is to use voltage-induced strain to switch perpendicular magnetization, which requires the coercive field shift to be larger than the coercive field itself. Therefore, after validating the testing results with mathematical calculation and numerical simulation, we investigated the limit of using strain to shift the coercive field. An optimization is performed by varying the thickness of the PZT substrate and the distance between the gate electrodes, while keeping the width of the Hall bar unchanged (400 nm). It is found that by using a 1 um thick PZT with 1.2 um distance between gating pads, the effective strain (i.e., the subtraction between in-plane strain and out-of-plane strain) can be increased from 200 ppm to 1000 ppm. Fig. 3-48 compares the current design (left) and the optimized design (right). According to the previous calculation, 1000 ppm strain will give us approximately 100 Oe Hc shift. This may be more technologically interesting if the coercive field of the magnetic pillar at zero field could be reduced to less than 100 Oe by optimizing the fabrication process.

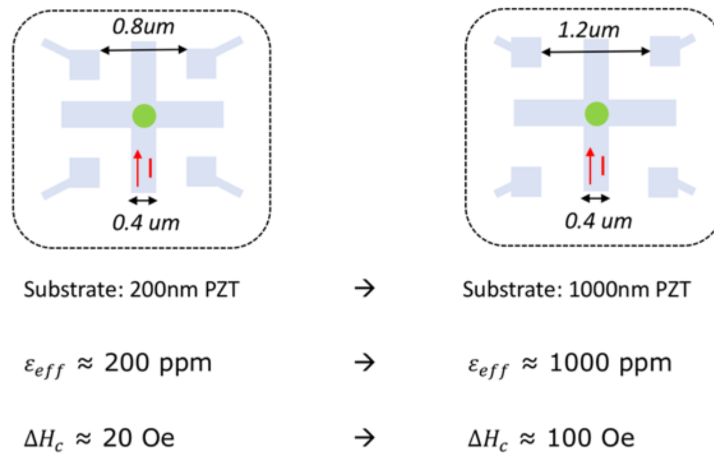

Figure 3-48. Comparison between current design (left) and the optimized design (right).

3.4 Chapter summary

Take home message 1: how to design patterned electrode in multiferroic control

In this chapter, we have discussed how to design the device for strain-mediated magnetization control with patterned electrodes on piezoelectric substrate. Some general rules one should keep in mind in order to get a decent amount of strain are: (1) spacing between electrodes should be 1-3 times of the thickness; (2) the size of the electrodes should be at least same with the thickness. The mechanical property of the magnetic material has a small impact on the strain distribution.

Take home message 2: Re-define the biaxial strain

We have showed that for perpendicular magnetization control, what matters is the subtraction between the in-plane strain and out-of-plane strain components $\varepsilon_{eff} = \varepsilon_{zz} - \varepsilon_{ip}$, instead of the biaxial strain $\varepsilon_{bi} = \varepsilon_{xx} - \varepsilon_{yy}$ that are focused in in-plane magnetization control by multiferroics. Especially, the strain along *z* direction is of great importance, which is always ignored in in-plane magnetization control.

Take home message 3: PMN-PT is not good for perpendicular magnetization control

We also demonstrated that PMN-PT is not a good candidate for perpendicular magnetization control because:

(1) The strain generated in [001] cut PMN-PT tend to have compression in plane and tension out of plane, i.e., $\varepsilon_{zz} > 0$. In this case, the perpendicular magnetization anisotropy is enhanced. The results presented in Yu's work in 2015 also confirms this.[133]

(2) Although the [011] cut PMN-PT is great for generating large in-plane biaxial strain ($\varepsilon_{bi} = \varepsilon_{xx} - \varepsilon_{yy}$ can usually achieve 1500 ppm), the difference sign of *x* component and *y* component (i.e., one is tension and the other is compression) makes it not suitable for perpendicular magnetization control. The tensile in-plane strain tends to decrease PMA and bring the magnetization in-plane, however, the compressive in-plane strain has the opposite effect. As a result, there is competing magnetoelastic effect along different axes. It has been shown by Roberto et al (2018) that the strain generated in the bulk PMN-PT is non-uniform even the PMN-PT is actuated using the continuous electrode.[141] As shown in Fig. 3-49, the strain distribution is non-uniform with domain size 2~5 um. The magnetic element has the size of 20 um in the device fabricated on PMN-PT substrate. Note the CoFeB is not patterned into pillar in the device fabricated on PMN-PT. It can be inferred that within the CoFeB layer of the Hall bar, the strain is spatially variant. And the CoFeB is polycrystalline and has its own domain structure as well. All these together (i.e., competing strain along *x* and *y* axes, non-uniform strain in PMN-PT, polycrystalline structure of CoFeB) may lead to the cancellation of magnetoelastic effect inside the CoFeB element. We consider this being the reason why we did not see obvious strain-mediated magnetization change in the device fabricated on [011] PMN-PT.

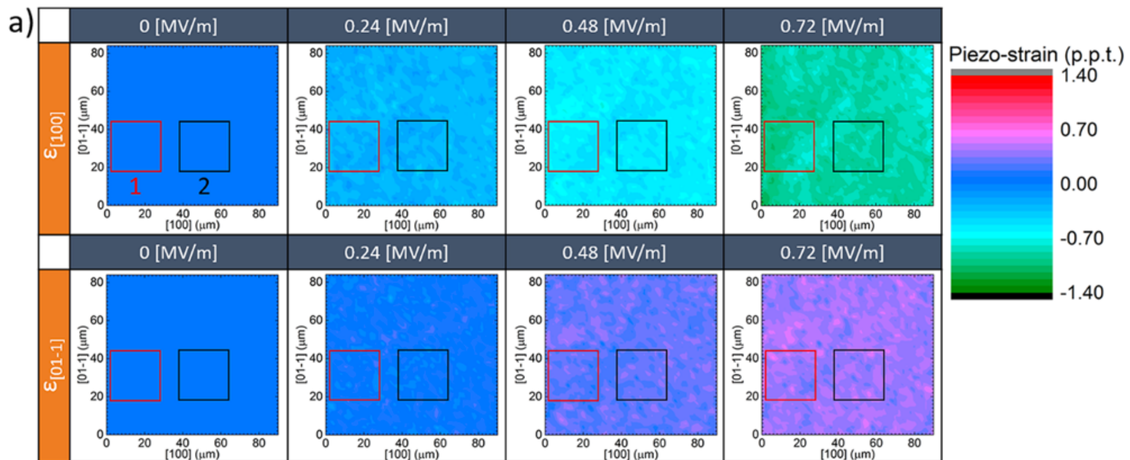

Figure 3-49. Voltage-induced strain measured by XMCD-PEEM. Reference: [141].

Take home message 4: PZT thin film is better for perpendicular magnetization control, but its effect is limited.

We observed an evident perpendicular coercive field shift in the device fabricated on PZT thin film, indicating the perpendicular magnetic anisotropy can be tuned by strain. However, the shift is too small to achieve pure strain-mediated perpendicular magnetic switching. We demonstrated that by optimizing the device geometry, the strain effect may be increased by 5 times, and the coercive field shift can achieve 100 Oe. This may not be technologically interesting either, unless a clear pathway was figured out to reduce the coercive field of the magnetic pillar to be less than 100 Oe. Using strain to control perpendicular magnetization is mainly restricted by the material properties, especially the amount of effective strain that can be generated by the piezoelectric substrate. There are some other ways to further push the potential the PZT substrate. For example, it is shown that the d33 can be increased by 3 times by etching PZT thin film into discrete island since the substrate clamping effect is reduced.[142] In addition, more efforts need to be devoted to developing a reading mechanism because it has been shown that the strain may also affect the fixed layer in MTJ, which makes the readout tricky.[18]

Chapter 4. Hybrid strain and SOT control of perpendicular magnetization

4.1 Recent progress of hybrid magnetization control mechanisms

As introduced in Chapter 1, there are four major mechanisms of magnetic memory: spin-transfer torque (STT), spin-orbit torque (SOT), voltage controlled magnetic anisotropy (VCMA), and strain-mediated multiferroics. Each individual control mechanism has its advantages and shortcomings. In recent years, there has been extensive researches on hybrid magnetization control using two or more of the above-mentioned mechanisms. In this section, some examples of hybrid control will be discussed.

Strain + STT

Biswas et al (2013) demonstrated a hybrid nanomagnetization control method using spin transfer torque assisted by surface acoustic wave (SAW).[143] As shown in Fig. 4-1, SAW generates a propagating strain and rotates the magnetization of the nanomagnet 90º to hard axis, then STT is used to switch it 180º. A similar idea is also implemented in another work by Khan et al (2014).[144] Instead of using strain generated by SAW, in Khan's work, the strain is generated by applying voltage to the PZT substrate as shown in Fig. 4-1. A CoFe square disk with 58 nm width and 1.2 nm thickness is simulated. The magnetic disk has perpendicular magnetic anisotropy and the thermal fluctuation is taken into consideration in the simulation as a noise field. An in-plane biaxial strain is applied to reduce the energy barrier thus only a tiny STT

current is sufficient to switch the magnetization 180º perpendicularly. It is estimated that the switching energy efficiency is ~50 times larger than pure STT control method.

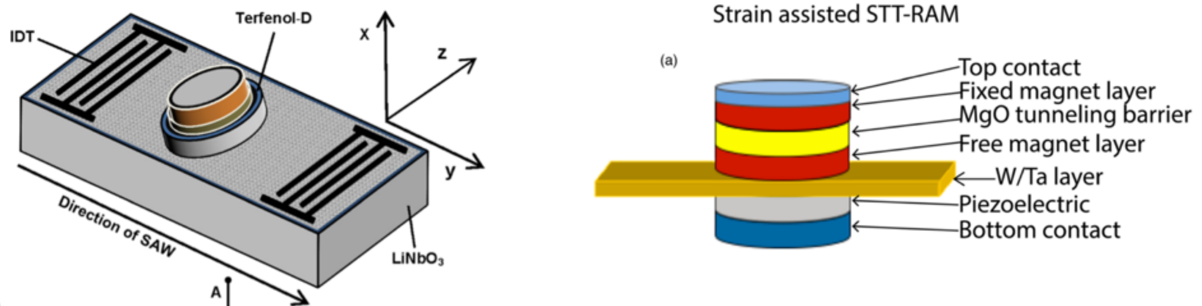

Figure 4-1. Hybrid strain + STT control. Left: strain is generated from surface acoustic wave, reference: [143]. Right: strain is generated from PZT substrate, reference: [144].

STT/SOT + VCMA

In 2012 and 2013, Prof. Wang's group explored hybrid STT + VCMA control to achieve a bi-directional switching using a unipolar voltage.[145], [146] The writing mechanism is shown in Fig. 4-2. During writing, an external bias field is applied. When a relatively small voltage Vc1 is applied, the VCMA effect dominates and the coercive field decreases and becomes smaller than the applied bias field. Therefore, the Rap state is more favored. When the applied voltage exceeds a threshold voltage where STT begins to play a role, the hysteresis loop shifts and the Rp state becomes favorable.

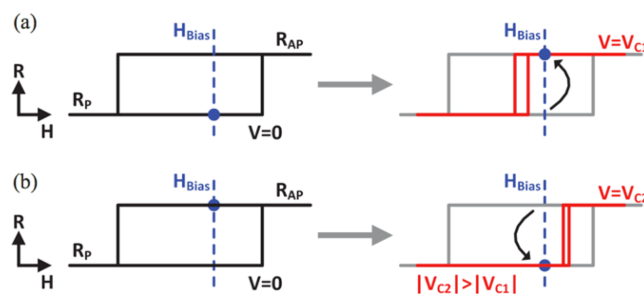

Figure 4-2. Hybrid STT + VCMA control. Reference: [146].

Kang et al (2016) simulated the magnetic switching of perpendicular MTJ by VCMA effect assisted by STT and SOT, respectively.[147] In this work, the VCMA is used to decrease the energy barrier and thus reduce the threshold current by STT/SOT switching. It is demonstrated the switching with the hybrid STT/SOT + VCMA can be faster and more energy efficient than pure STT/SOT based magnetic memory.

Yoda et al (2016) experimentally demonstrated a memory architecture based on hybrid SOT + VCMA effects.[148] As shown in Fig. 4-3, the writing voltage is applied to the bit-line to reduce the switching energy barrier of the memory bits to be written. A uniform current is applied to the word line, and only the bits with reduced energy barrier by VCMA effect can be written, while other bits remain unchanged.

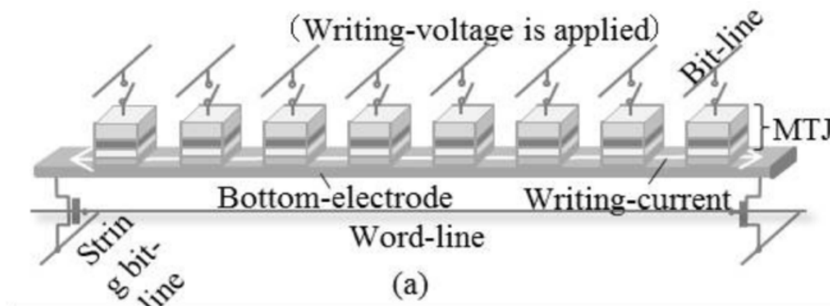

Figure 4-3. A memory architecture based on hybrid SOT + VCMA control. Reference: [148].

STT + SOT

The memory device based on spin-orbit torque is usually a 3-terminal device: two terminals are used to apply SOT current to the heavy metal strip for writing, two terminals are used to measure TMR through MTJ stack for reading, and one terminal is shared for writing and reading. The hybrid STT + SOT control for magnetic memory device also usually has 3 terminals, as proposed by van den Brink et al (2014) [149] or Wang et al (2015) [150]. Their devices are

shown in Fig. 4-4. They both simulated a perpendicular MTJ with both STT and SOT currents applied. For perpendicular magnetic switching by pure SOT, it usually requires an external in-plane field for symmetry breaking. This will be further discussed in section 4.4 in this chapter. In van den Brink and Wang's work, they used STT to replace the bias field for symmetry breaking.

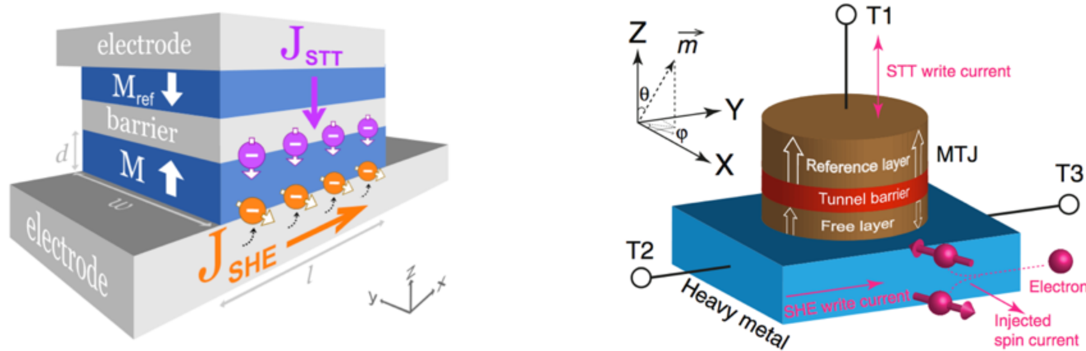

Figure 4-4. Three-terminal magnetic memory based on STT + SOT hybrid control. Left: reference [149]. Right: reference [150].

Recently, Sata et al (2018) demonstrated a two-terminal memory device based on hybrid SOT + STT control mechanism.[151] When a voltage is applied, there will be both in-plane current generated in the Ta wire and an out-of-plane current flowing through the MTJ stack, contributing to the ultrathin Ta strip. It is shown that the dominating switching current is from SOT, while the STT breaks the symmetry and helps achieve deterministic and directional perpendicular switching.

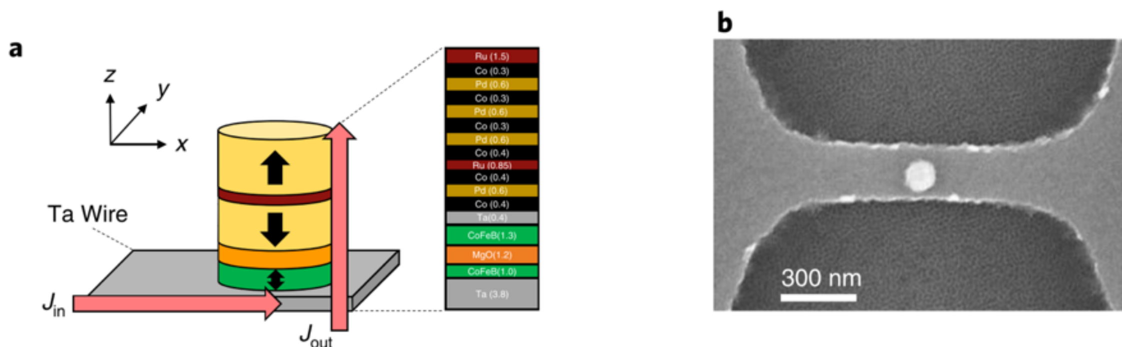

Figure 4-5. A two-terminal magnetic memory based on STT + SOT hybrid control. (a) Device illustration. (b) SEM image of the MTJ pillar. Reference: [151].

4.2 Simulation of hybrid strain-mediated and spin-orbit torque system

To my knowledge, there is no published study on hybrid strain + SOT control yet, except for the work that will be discussed in the following sections.

4.2.1 Finite element model

A fully coupled micromagnetic and elastodynamic finite element model is developed using multiphysics software to simulate the strain-mediated SOT switching. The precessional magnetic dynamics are governed by the Landau-Lifshitz-Gilbert (LLG) equation with SOT terms[50], [152], [153]:

$$\frac{\partial \boldsymbol{m}}{\partial t} = -\mu_0\gamma\left(\boldsymbol{m}\times\boldsymbol{H}_{eff}\right) + \alpha\left(\boldsymbol{m}\times\frac{\partial \boldsymbol{m}}{\partial t}\right) - \frac{\gamma\hbar}{2e}\frac{J_C}{M_S t_F}\xi_{DL}\boldsymbol{m}\times(\boldsymbol{m}\times\widehat{\boldsymbol{\sigma}}) \qquad \text{Eq. 4-1}$$

where $\boldsymbol{m}$ is the normalized magnetization, μ_0 the vacuum permittivity, γ the gyromagnetic ratio, $\hbar$ the reduced Planck constant, *e* the elementary charge, J_C the current density, $\widehat{\boldsymbol{\sigma}}$ the polarized spin accumulation, α the Gilbert damping factor, t_F the thickness of the free magnetic layer, M_S the saturation magnetization, and ξ_{DL} is the damping-like spin Hall angle. Note the field-like term is not considered in the calculation since it is believed to have no deterministic effect on the magnetization switching[154]. Additionally, $\boldsymbol{H}_{eff}$ is the effective field and consists of four components: $\boldsymbol{H}_{eff} = \boldsymbol{H}_{ex} + \boldsymbol{H}_{Demag} + \boldsymbol{H}_{PMA} + \boldsymbol{H}_{ME}$, where $\boldsymbol{H}_{ex}$ is the exchange field, $\boldsymbol{H}_{Demag}$ the demagnetization field, $\boldsymbol{H}_{PMA}$ the effective PMA field, and $\boldsymbol{H}_{ME}$ the magnetoelastic field. The

PMA field is generalized in the following equation using a phenomenological PMA coefficient K_{PMA}: $\boldsymbol{H}_{PMA} = -\frac{2}{\mu_0 M_S} K_{PMA} m_z \hat{\boldsymbol{z}}$[19], [60]. Specifically, for materials where the PMA originates from interfacial effects (e.g., CoFeB), the PMA coefficient is written as $K_{PMA} = -K_i/t_F$, where K_i = 1.3 mJ/m^2 for CoFeB and t_F is the free layer thickness[22]. The magnetoelastic field $\boldsymbol{H}_{ME}$ is obtained by taking the derivative of magnetoelastic energy density with respect to the magnetization $\boldsymbol{m}$[24]:

$$\boldsymbol{H}_{ME}(\boldsymbol{m}, \boldsymbol{\varepsilon}) = -\frac{1}{\mu_0 M_S}\frac{\partial E_{ME}}{\partial \boldsymbol{m}} = -\frac{1}{\mu_0 M_S}\frac{\partial}{\partial \boldsymbol{m}}\{B_1[\varepsilon_{xx}\left(m_x^2 - \frac{1}{3}\right) + \varepsilon_{yy}\left(m_y^2 - \frac{1}{3}\right)$$
$$+\varepsilon_{zz}\left(m_z^2 - \frac{1}{3}\right)] + 2B_2(\varepsilon_{xy} m_x m_y + \varepsilon_{yz} m_y m_z + \varepsilon_{zx} m_z m_x)\} \quad \text{Eq. 4-2}$$

where m_x, m_y and m_z are components of normalized magnetization along *x, y* and *z* axis, B_1 and B_2 are first and second order magnetoelastic coupling coefficients. The magnetic material is assumed to be polycrystalline allowing magnetocrystalline anisotropy to be neglected. The formula for calculating demagnetization and exchange field is given by Liang *et al*[46] thus not repeated here. Thermal fluctuations are neglected in all calculations.

Assuming linear elasticity and piezoelectricity, the behavior of the piezoelectric thin film follows:

$$\boldsymbol{\varepsilon}_p = s_E : \boldsymbol{\sigma} + d^t \cdot \boldsymbol{E} \quad \text{Eq. 4-3}$$

$$\boldsymbol{D} = d : \boldsymbol{\sigma} + e_\sigma \cdot \boldsymbol{E} \quad \text{Eq. 4-4}$$

where $\boldsymbol{\varepsilon}_p$ is strain contribution from piezoelectric effect, $\boldsymbol{\sigma}$ is stress, $\boldsymbol{D}$ is electric displacement, $\boldsymbol{E}$ is electric field, s_E is the piezoelectric compliance matrix under constant electric field, d and d^t

are the piezoelectric coupling matrix and its transpose, and e_σ is electric permittivity matrix measured under constant stress. The total strain is expressed as $\boldsymbol{\varepsilon} = \boldsymbol{\varepsilon}_p + \boldsymbol{\varepsilon}^{\boldsymbol{m}}$, where $\boldsymbol{\varepsilon}_{ij}^{\boldsymbol{m}} = 1.5\,\lambda_s(m_i m_j - \delta_{ij}/3)$ represents the strain contribution due to isotropic magnetostriction, δ_{ij} is Kronecker function, and λ_s is saturation magnetostriction coefficient[24].

The magnetization and displacement are simultaneously computed by numerically solving the coupled LLG equation, electrostatic equation, and elastodynamic equation in time domain using finite element method. The strain transferred from the piezoelectric layer to magnetic layer influences the magnetization through $\boldsymbol{H}_{ME}$, and conversely the magnetization change influences the strain through $\boldsymbol{\varepsilon}^{\boldsymbol{m}}$. In other word, the mechanics and magnetics in the finite element model are fully coupled and the coupling is bidirectional. It has been shown that the two-way coupled simulation predicts more accurately than one-way coupled simulation[26], [45].

The piezoelectric substrate simulated in this work is $Pb(Zr,Ti)O_3$ (PZT) poled along the $\hat{z}$ direction. The bottom surface of the PZT is mechanically fixed and electrically grounded while the top surface is traction free. The CoFeB material parameters are: $\alpha = 0.01$, $M_s = 1.2\times10^6$ A/m, $B_1 = B_2 = -2.77\times10^7$ N/m^2, exchange stiffness $A_{ex} = 2\times10^{-11}$ J/m (used in $\boldsymbol{H}_{ex}$), $\lambda_s = 150$ ppm, Young's modulus E = 160 GPa, density $\rho = 7700$ kg/m^3, Poisson's ratio $\nu = 0.3$ and spin Hall angle ξ_{DL} = 1[22], [68]–[70], [155], [156]. Note the heavy metal is sufficiently thin that the impact of the heavy metal on the CoFeB strain distribution is neglected in the mechanical analysis. Also, the voltage (~1 mV) required to generate the SOT current is trivially small compared to the PZT (~0.5 V) and is thus neglected in electrostatics calculation. To avoid divergence, the magnetization is always initialized from a slightly canted direction (m_x, m_y, m_z)

= (0.1, 0.1, ±0.99). And a 1 ns temporal evolution is performed before any application of current/voltage to allow the magnetization to settle down.

4.2.2 Macrospin model

A simplified macrospin model is developed for faster simulation. In the macrospin model, a single spin is used to represent the magnetization of the entire disk. The strain is assumed uniform and constant throughout the magnetic element and does not vary spatially as in the finite element model. Although the macrospin model does not take into consideration the non-uniform strain distribution or the converse magnetoelastic coupling, it is beneficial because the computation time for each temporal evolution is only ~1/1000 of the time consumed in the fully coupled model. The LLG equation is the same as used in the finite element model. However, the total effective field for the macrospin model only consists of three components: $\boldsymbol{H}_{eff} = \boldsymbol{H}_{Demag} + \boldsymbol{H}_{PMA} + \boldsymbol{H}_{ME}$. The exchange field $\boldsymbol{H}_{ex}$ is absent due to the assumption of uniform magnetization, which is reasonable for small structures such as the 50 nm diameter CoFeB disk modeled in this work. In addition, the demagnetization field is simplified to $\boldsymbol{H}_{Demag} = -\boldsymbol{N}M_s\boldsymbol{m}$, where $\boldsymbol{N}$ is the demagnetization tensor for an oblate spheroid[25]. The PMA and magnetoelastic effective fields, as well as all material parameters used in macrospin model are the same with those used in the finite element model. Similar to the finite element model, to avoid singularity solution, the magnetization is always initialized from a slightly canted direction (m_x, m_y, m_z) = (0.1, 0.1, ±0.99) in the macrospin model.

4.3 Deterministic bi-directional perpendicular switching

In this section, we present a structure with hybrid SOT + strain control. When the polarization from the SOT current is parallel to the uniaxial applied strain, and with certain combination of current and strain, a deterministic switching is observed. However, the switching is bi-directional. In other words, for the same given current and strain, the perpendicular magnetization always switch by 180º and the final state depends on the initial state. The model setup and results will be demonstrated in this section, followed by a theoretical analysis.

4.3.1 Results

Figure 4-6 shows the magnetoelastic/heavy metal/piezoelectric heterostructure simulated in the finite element model. The magnetic element is a CoFeB disk with a 50 nm diameter and a 1.5 nm thickness, which has perpendicular easy axis. The SOT effect was considered as a constant spin polarization along *x* axis as $\hat{\boldsymbol{\sigma}} = (1,0,0)$. The CoFeB disk is attached to a 100 nm-thick $Pb[Zr_xTi_{1-x}]O_3$ (PZT) substrate poled along the *z* axis. Two 50 nm × 50 nm electrodes are placed on PZT top surface and are 20 nm away from the CoFeB edge along the *y* direction, while the bottom of the PZT is electrically grounded. The bottom and four sides of the PZT is mechanically fixed. Note the Gilbert damping factor in all the simulations presented in Section 4.3 is 0.5, i.e. artificially high to improve numerical stability.

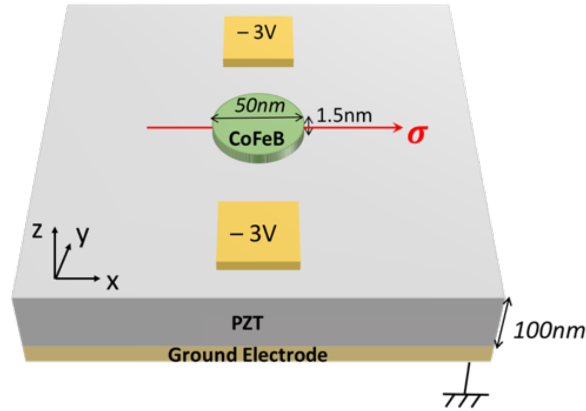

Figure 4-6. Illustration of simulated structure in Section 4.3.

A voltage V_0 = -3 V is applied to the two top electrodes, and a current density of $I_0 = 2\times10^8$ A/cm^2 is applied simultaneously, inducing a spin-orbit torque following Equation 4-1. The magnetization of the CoFeB is initialized as either 'up' (m_z = +1) or 'down' (m_z = -1). A 1-ns simulation is conducted using the finite element model in COMSOL. The results are presented in Fig. 4-7.

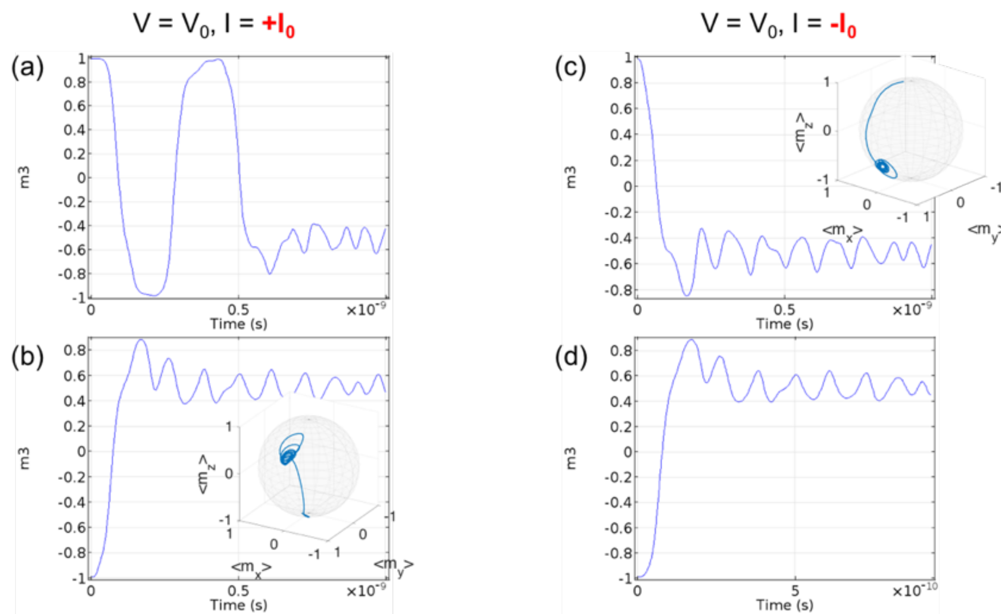

Figure 4-7. Representative simulation results.

Figure 4-7 (a) and (b) shows the results for positive applied current, i.e., polarization $\hat{\boldsymbol{\sigma}}$ = (+1,0,0). The magnetization is initialized as 'up' in (a) and 'down' in (b). The y axis presents the volume averaged perpendicular magnetization of the CoFeB disk. It can be seen that the magnetization both undergoes 180º switching regardless of the initial state. The inset plot in Fig. 4-7(b) shows the 3D trajectory of the magnetic precession for the case simulated in Fig. 4-7(b). Then the current direction is reversed, i.e., polarization $\hat{\boldsymbol{\sigma}}$ = (-1,0,0), and the simulation results are presented in Fig. 4-7 (c) and (d) for 'up' and 'down' initial magnetization, respectively. It can be seen that the current direction does not make a difference here. In either of the cases shown in Fig. 4-7, the switching can be completed if the applied voltage/current are removed after 0.5 ns. In other words, the switching is deterministic, i.e., no accurate timing of the applied voltage/current pulse is required. However, the switching is not directional, i.e., final state depends on the initial state.

More simulation results are presented in Fig. 4-8. The voltage -3 V is applied first at t = 0 ns, and the current is applied at t = 0.5 ns. Interestingly, under this situation, the final state depends on the direction of the applied current. The results seem to be contradictory with the results shown in Fig. 4-7, where it was shown that the current direction does not matter. An explanation will be given in the section 4.3.2.

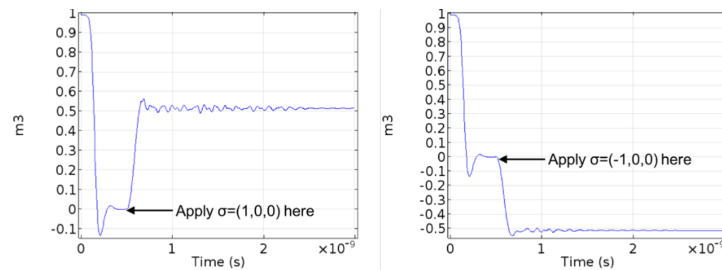

Figure 4-8. Simulation results when the voltage is applied before current.

4.3.2 Vector analysis

In this system, three major terms in the magnetic dynamics are: perpendicular magnetic anisotropy (PMA) field H_{PMA}, magnetoelastic field H_{ME}, and spin-orbit torque field H_{SOT}. The PMA field is along z direction and is proportional to the perpendicular magnetization: $H_{PMA} \propto m_z\hat{\boldsymbol{z}}$. The spin-orbit torque field is $H_{SOT} \propto \boldsymbol{\sigma}\times\boldsymbol{m}$. Note this is the damping-like torque term and the field-like torque is ignored.

The three components of magnetoelastic field are as follows:

$$H_{ME,x} = -\frac{2}{\mu_0 M_S}[B_1\varepsilon_{xx}m_x + B_2(\varepsilon_{xy}m_y + \varepsilon_{xz}m_z] \quad \text{Eq. 4-5}$$

$$H_{ME,y} = -\frac{2}{\mu_0 M_S}[B_1\varepsilon_{yy}m_y + B_2(\varepsilon_{yx}m_x + \varepsilon_{yz}m_z] \quad \text{Eq. 4-6}$$

$$H_{ME,z} = -\frac{2}{\mu_0 M_S}[B_1\varepsilon_{zz}m_z + B_2(\varepsilon_{xz}m_x + \varepsilon_{yz}m_y] \quad \text{Eq. 4-7}$$

The COMSOL simulation shows that the main strain component is a tensile strain along y axis. Therefore, the magnetoelastic field is along y direction and is proportional to the m_y: $H_{ME} \propto m_y\hat{\boldsymbol{y}}$. A vector diagram is presented in Fig. 4-9 with all three vectors are drawn out for magnetization lying in the four quadrants in *yz*-plane. The spin polarization from SOT current is assumed to be $\hat{\boldsymbol{\sigma}}$ = (1,0,0). Whether the spin state is stable depends on the summation of the projection of the three vectors onto the tangential direction (drawn as the dashed line). Generally, the first and the third quadrants are symmetric. In other words, if the spin state in the first quadrant is stable (three field vectors cancel with each other along the tangential direction), there must be a corresponding stable state in the third quadrant. The same is true for the second and the fourth quadrants. Whether the first/third or the second/fourth quadrants have stable states

depend on the relative strength of the H_{ME} and H_{PMA}. In our simulation, the pure strain is strong enough to overcome the PMA and bring the magnetization in-plane without the existence of spin-orbit torque. This means the H_{ME} is stronger than H_{PMA}, and the first and third quadrants (the regions in shadow in Fig. 4-9) have stable spin states. This argument originates from the paper by Fan et al (2014). [157] It can be inferred that, when the SOT current reverses its direction, the H_{SOT} reverses the direction in all four quadrants, then the stable states will exist in the second and the fourth quadrants.

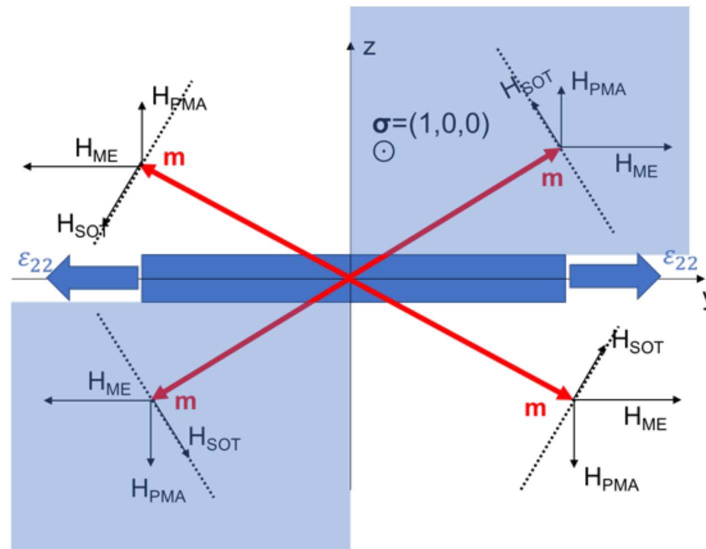

Figure 4-9. Vector diagram for the hybrid SOT + strain system. The three main terms, i.e., spin-orbit torque, PMA, and magnetoelastic field are drawn out for magnetic spin in four quadrants, respectively.

As discussed above, for positive applied current, i.e., $\hat{\boldsymbol{\sigma}} = (+1,0,0)$, there are two stable states in the first and the third quadrants. As shown in Fig. 4-10, when the magnetization is initialized as 'up', H_{PMA} is pointing along $+z$ direction, H_{SOT} is along $-y$ direction, and H_{ME} is zero due to $m_y = 0$. Therefore, under applied voltage and current, the magnetization will precess counterclockwise and reach the stable state in the third quadrant first. In contrast, when the

magnetization is initialized as 'down', H_{PMA} is pointing along $-z$ direction, H_{SOT} is along $+y$ direction, and H_{ME} is zero again due to $m_y = 0$. Similarly, the magnetization will precess counterclockwise and this time the stable state in the first quadrant is found first. This explains why the magnetization always switch to the opposite perpendicular direction regardless of the initial state as shown in Fig. 4-7 (a)(b).

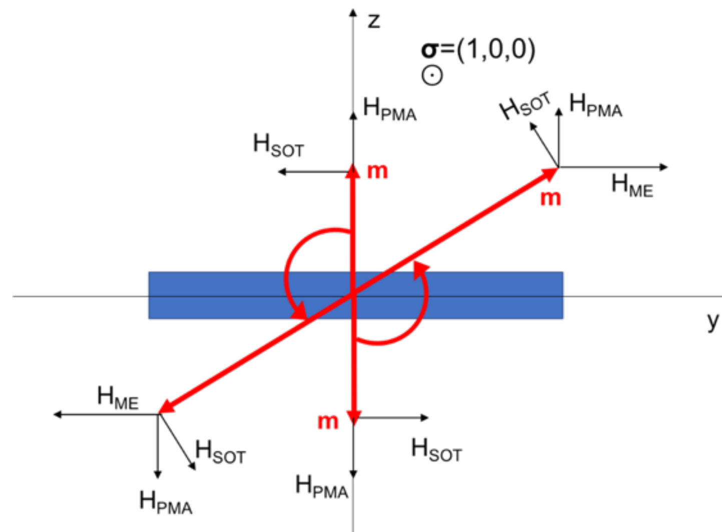

Figure 4-10. Explanation of deterministic bi-directional switching for positive applied current.

Figure 4-11 presents the analysis for negative applied current. Compared to Fig. 4-10, the only difference here is the polarization is reversed to be $\hat{\boldsymbol{\sigma}} = (-1,0,0)$. The H_{SOT} reverses its direction in all quadrants, while other terms are kept unchanged. In this situation, the magnetization always precess clockwise. When initialized from 'up', the stable state in the fourth quadrant is achieved first, while for initial state as 'down', the stable state in the second quadrant is reached first. Eventually, the magnetization always switch to the opposite vertical direction regardless of the initial state. This explains the simulation results presented in Fig. 4-7 (c)(d). In summary, the direction of the applied current affects the switching direction (either clockwise or

counterclockwise). However, the final state is always the opposite to the initial state regardless of the current direction.

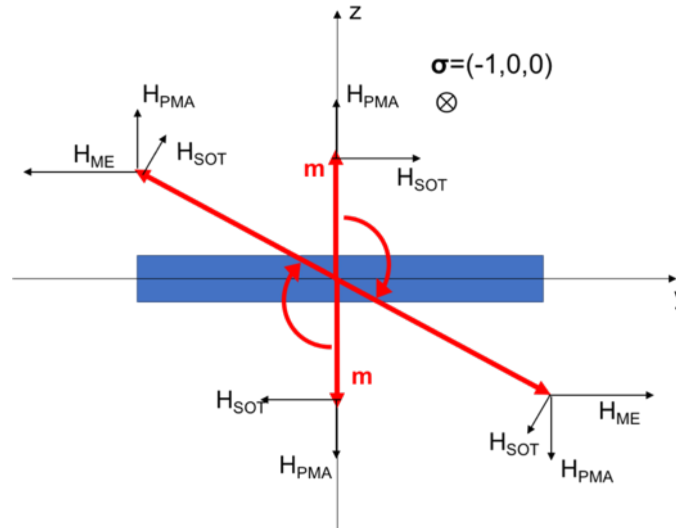

Figure 4-11. Explanation of deterministic bi-directional switching for negative applied current.

Although the final states are both ‘downward’ when the initial state is ‘up’ for both positive and negative applied current, the final states have a slight difference, i.e., the *y* component of the final magnetization. We can examine the *y* component to confirm our analysis. As shown in Fig. 4-12(a), for negative applied current, the magnetization precesses clockwise and reaches the stable state in the fourth state. Then the final state should have a positive m_y. This is confirmed by the simulation results presented in Fig. 4-12(b). For positive applied current as shown in Fig. 12(c), the magnetization precesses counterclockwise and the stable state lies in the third quadrant. Therefore, the final magnetic state should have a negative m_y, which is confirmed in the simulation results shown in Fig. 4-12(d).

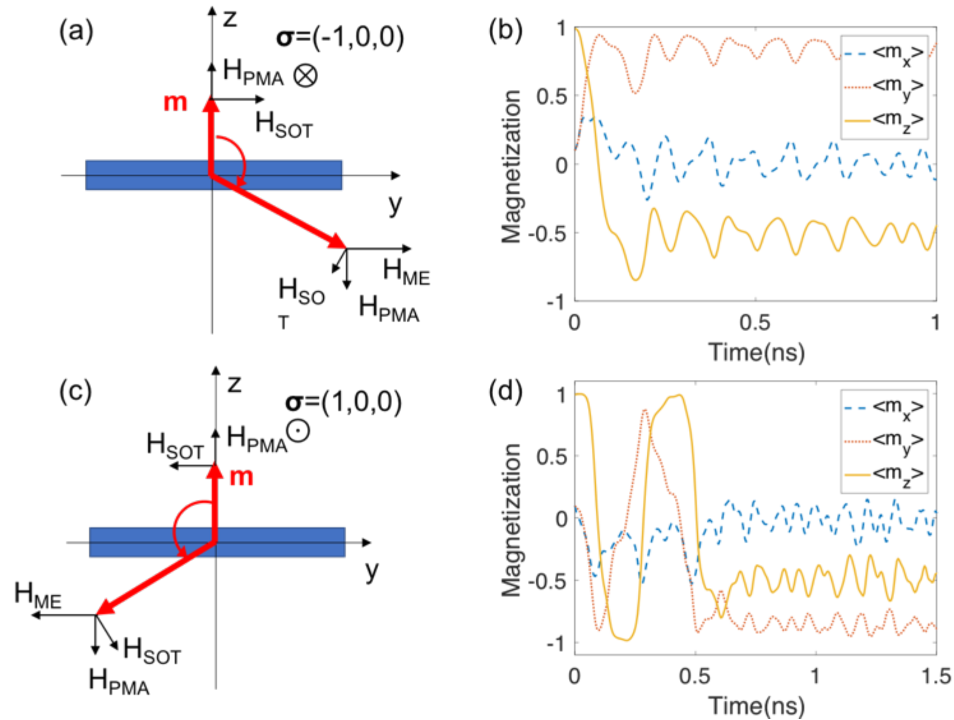

Figure 4-12. Comparison between switching from 'up' to 'down' under different current directions. Vector diagram and three magnetization components vs. time for switching by (a)(b): positive current, and (c)(d): negative current.

After confirming our vector analysis by comparing with the simulation results, we can then explain the 'paradox' raised in Fig. 4-8. When the voltage is first applied for certin time period, the magnetization is brought into in-plane as the H_{ME} overcomes H_{PMA}. At this time point, $H_{PMA} = 0$ as $m_z = 0$. Applying positive current will lead to the magnetization precessing counterclockwise and the stable state in the first quadrant is achieved first. So the final state is 'upward'. In contrast, applying negative current will lead to the magnetization precessing clockwise and the stable state in the fourth quadrant is achieved first. So the final state is 'downward'. In summary, if the voltage is applied first, the final state (either upward or downward) does depend on the current direction.

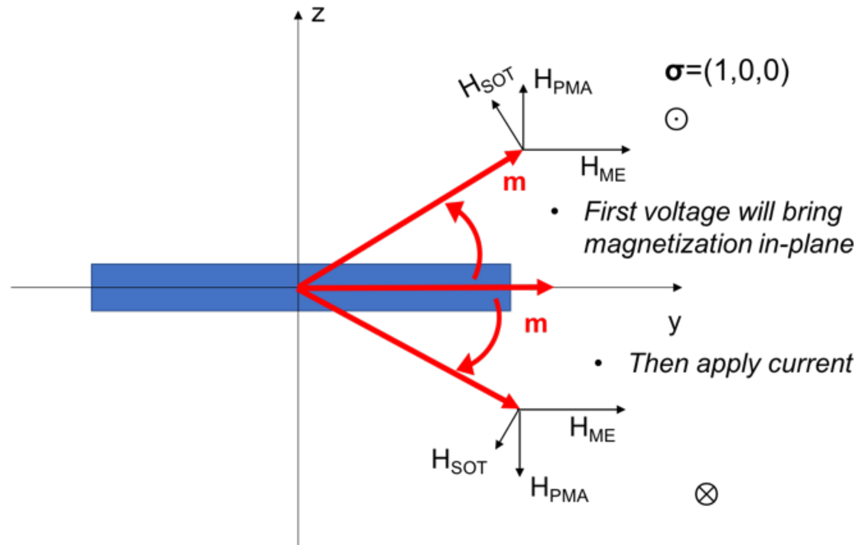

Figure 4-13. Explanation of the behavior when the voltage is applied ahead of current.

Figure 4-14 investigates another interesting case: after applying the voltage and current at the same time, we reverse the current direction while keeping the voltage unchanged. The simulation result is shown in Fig. 4-14 (a). The current and voltage are applied for 1 ns with positive current applied, and the current is reversed at t = 1 ns. The magnetization also reverses the direction after reversing the current direction.

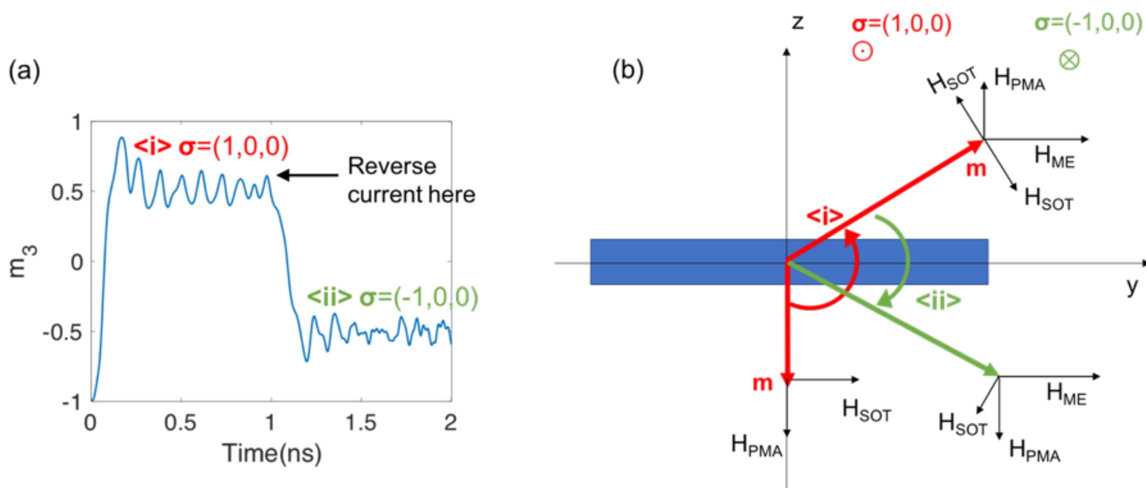

Figure 4-14. Switching when the current is reversed while the voltage is kept unchanged.

This can be explained in Fig. 4-14 (b) using the vector analysis. When the positive current is applied first, as shown by the magnetization vectors in red, the magnetization switches from 'down' counterclockwise to 'upward' state in the first quadrant. Then a negative current is applied, and the magnetic precession is shown in green in Fig. 4-14 (b). The magnetization rotates clockwise under negative applied current and reaches the stable state in the fourth quadrant.

4.3.3 Mathematical derivation

The stable state is mathematically determined by the LLG equation (equation 4-1) with $\frac{\partial \boldsymbol{m}}{\partial t} =$ 0:

$$\left(\boldsymbol{m}\times\boldsymbol{H}_{eff}\right) = -C\boldsymbol{m}\times(\boldsymbol{m}\times\widehat{\boldsymbol{\sigma}}) \quad \text{Eq. 4-8}$$

where the parameters associated with spin-orbit torque current is simplified as *C*. For positive applied current, the spin polarization is $\widehat{\boldsymbol{\sigma}}$ = (1,0,0). The effective field consists of PMA and magnetoelastic fields:

$$\boldsymbol{H}_{eff} = \boldsymbol{H}_{PMA} + \boldsymbol{H}_{ME} = Am_z\widehat{\boldsymbol{z}} + Bm_y\widehat{\boldsymbol{y}} \quad \text{Eq. 4-9}$$

where the parameters associated with PMA is included in coefficient *A*, and the parameters associated with magnetoelastic effect is included in coefficient *B*. Plug the H_{eff} and $\widehat{\boldsymbol{\sigma}}$ into equation 4-8, we get three equations in *x, y* and *z* direction, respectively:

$$(A - B)m_y m_z = C(m_y^2 + m_z^2) \quad \text{Eq. 4-10}$$

$$-Am_x m_z = -Cm_x m_y \quad \text{Eq. 4-11}$$

$$Bm_xm_y = -Cm_xm_z \quad \text{Eq. 4-12}$$

Another equation that governs the magnetization is the uniformity equation:

$$m_x^2 + m_y^2 + m_z^2 = 1 \quad \text{Eq. 4-13}$$

Equation 4-11 and 4-12 are correlated with each other, and two trivial solutions are $m_y = m_z = 0$, $m_x = \pm 1$. The non-trivial solution of m_x, m_y and m_z exists when $m_x = 0$. In this case, equation 4-10 can be re-written as:

$$\frac{A-B}{C} m_y m_z = m_y^2 + m_z^2 = 1 \quad \text{Eq. 4-14}$$

The second equal sign originates from the uniformity equation. The solution to equation 4-10 relies on the intersection points of the two curves: a circle defined by $m_y^2 + m_z^2 = 1$ and an inversely proportional curve defined by $m_y m_z = \frac{C}{A-B}$.

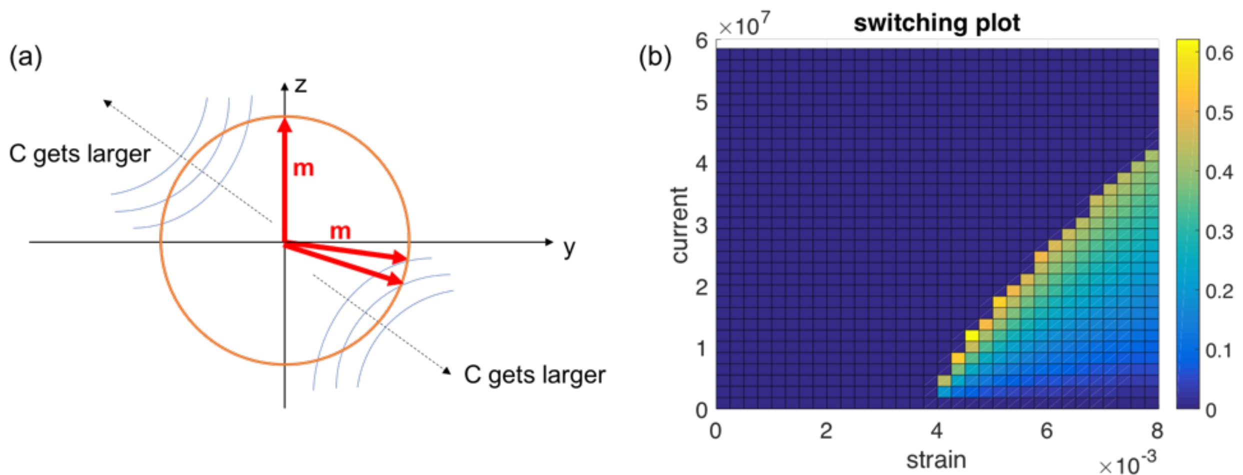

Figure 4-15. (a) Visualization of equation 4-10. (b) Parametric study done using macrospin simulation with varying the applied strain and current.

The two curves are drawn in Fig. 4-14. Note the coefficient A and B corresponds to PMA and magnetoelastic effect, respectively. In our case A < B since the magnetoelastic field overcomes PMA. Therefore, the inversely proportional curves exist in the second and the fourth quadrant.

Because the derivation comes from a static analysis, the dynamic magnetic precession cannot be revealed from the mathematical derivation. However, Fig. 4-15 (a) helps visualize the solution to the equation 4-10. The solution of m_y and m_z are determined by the intersecting points between the orange circle with radius 1 and the blue curves. Some conclusions can be drawn: (1) there are always a pair of stable states, if there is any; (2) the final state has a larger m_z component for larger applied current; (3) there may not be any stable state, i.e., switching does not happen, when the current is too large. The conclusion (1) matches the conclusion from the vector analysis in Fig. 4-9. The conclusion (2) and (3) are confirmed by a parametric study done by macrospin simulation as shown in Fig. 4-15 (b). Each small box represents a case simulated in the macrospin model, and the color represents the perpendicular magnetization of the final stable magnetic state. Another interesting point is that from Fig. 4-15 (a), the maximum m_z after switching is when the blue curve is tangent to the circle, i.e. max(m_z) = $1/\sqrt{2} \approx 0.7$. This is approximately the maximum value achieved in the parametric study shown in Fig. 4-15 (b).

4.4 Strain-mediated spin torque nano-oscillator (STNO)

In the previous section, we have shown that certain combination of current and strain can result in deterministic switching in a strain + SOT system when the spin polarization (along *x* axis) is perpendicular to the strain direction (along *y* axis). In this section, we will show that when the current is higher than a certain threshold level, a steady magnetic oscillation can be

induced. A new type of spin torque nano-oscillator (STNO) is proposed using the hybrid strain + SOT control.

4.4.1 Introduction: how STNO works

Figure 4-16 demonstrates a conventional STNO. As shown in Fig. 4-16 (a), a conventional STNO is based on a magnetic tunnel junction (MTJ) with the free layer and fixed layer having in-plane easy axes. An in-plane external magnetic field is applied along +*x* axis.

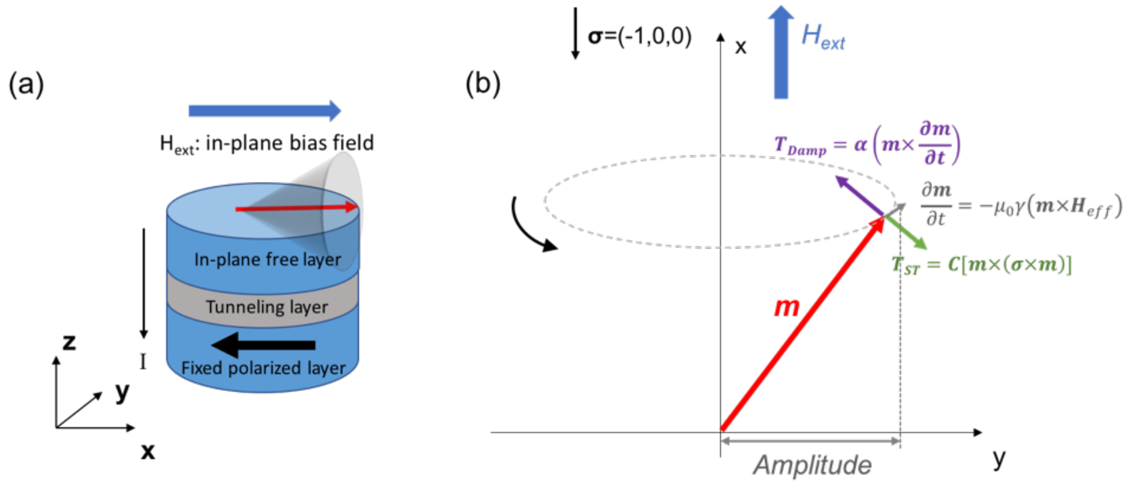

Figure 4-16. Device and vector analysis of a conventional spin-torque nano-oscillator (STNO).

A current is applied through the MTJ stack and becomes polarized as with spin polarization **σ**=(-1,0,0) due to spin-transfer torque effect. This exerts a torque on the magnetization in the free layer $\boldsymbol{T}_{ST} = C[\boldsymbol{m}\times(\boldsymbol{\sigma}\times\boldsymbol{m})]$, where C is a coefficient associated with the applied current. The magnetic precession is governed by the LLG equation:

$$\frac{\partial \boldsymbol{m}}{\partial t} = -\mu_0\gamma(\boldsymbol{m}\times\boldsymbol{H}_{eff}) + \alpha\left(\boldsymbol{m}\times\frac{\partial \boldsymbol{m}}{\partial t}\right) + C[\boldsymbol{m}\times(\boldsymbol{\sigma}\times\boldsymbol{m})] \qquad \text{Eq. 4-15}$$

In equation 4-15, the Gilbert damping torque is given by $\boldsymbol{T}_{Damp} = \alpha\left(\boldsymbol{m}\times\frac{\partial \boldsymbol{m}}{\partial t}\right)$. For certain spin state, the damping torque has the opposite direction to the T_{ST} as shown in Fig. 4-16 (b). If the current is selected carefully, the two torques can cancel each other. As a result, the magnetization may undergo a steady oscillation around the *x* axis. And when $T_{ST} = -T_{Damp}$, the equation 4-15 can be re-written as:

$$\frac{\partial \boldsymbol{m}}{\partial t} = -\mu_0\gamma\left(\boldsymbol{m}\times\boldsymbol{H}_{eff}\right) \quad \text{Eq. 4-16}$$

Here the effective field H_{eff} is the external magnetic field. The direction of this torque is perpendicular to the magnetization, driving the circular precession of the spin as shown by the dashed pathway in Fig. 4-16 (b). The amplitude of the oscillation is defined as the radius of the circular trajectory of the magnetic precession. The oscillation frequency is calculated as:

$$f \sim \frac{1}{2\pi}\left|\frac{\partial \boldsymbol{m}}{\partial t}\right| \sim \left|\boldsymbol{m}\times\boldsymbol{H}_{eff}\right| \quad \text{Eq. 4-17}$$

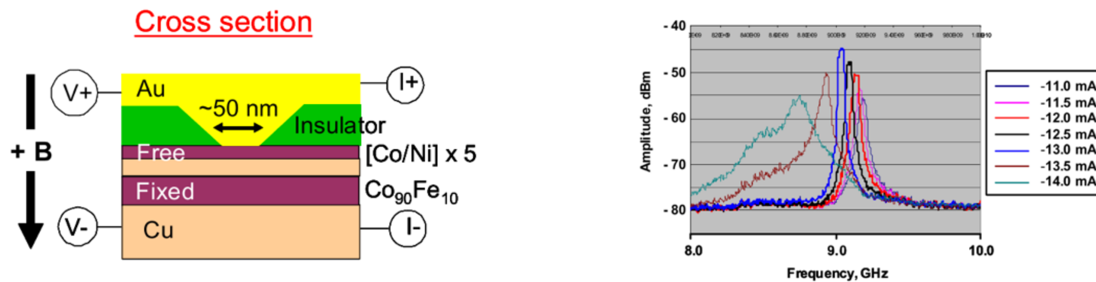

Figure 4-17. Radiation of a STNO with external bias field. Left: device illustration. Right: radiation signal with different applied current. Reference: [158].

In the conventional STNO, the oscillation amplitude and frequency can be tuned by changing the amplitude of the applied current and the external bias field. As shown in Fig. 4-17, Wickenden et al (2009) reported a 50 nm STNO and measured its radiation at a distance of 1 m.

However, a major drawback of conventional STNO is the requirement of an external applied magnetic field. This requirement prohibits its on-chip application due to physical sizes. More recently, researchers have suggested approaches to eliminate the bias field requirement as summarized in Fig. 4-18. Generally, the idea is to use a fixed layer that has a perpendicular polarization component. Houssameddine et al (2007) proposed using a fixed layer with perpendicular magnetic anisotropy.[159] Zhou et al (2008) simulated a STNO structure with the fixed layer having a tilted magnetization and demonstrated field-free magnetic oscillation.[107] Zhang et al (2012) simulated a STNO with combined in-plane and perpendicular polarizers.[160]

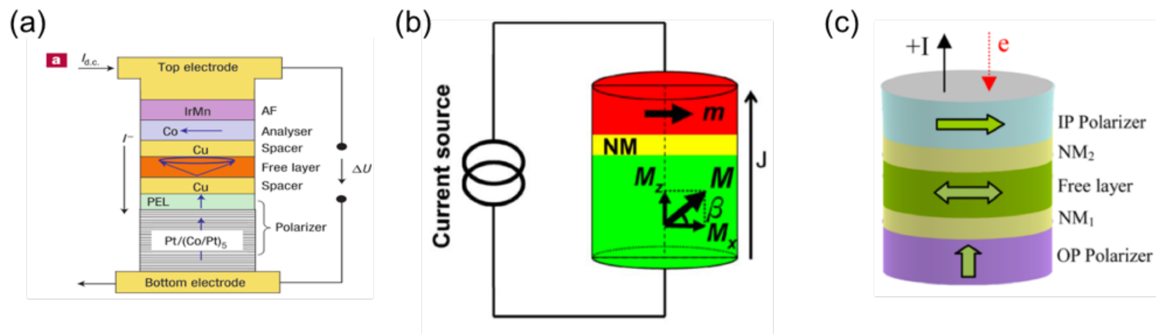

Figure 4-18. Different ways of achieving field-free STNO. (a) The fixed layer has perpendicular easy axis, reference: [159]. (b) The fixed layer has a canted magnetization, reference:s [107]. (c) The MTJ stack has two fixed layer with in-plane and perpendicular easy axis, respectively, reference: [160].

The use of a perpendicular polarizer eliminates the external bias field requirement as illustrated in the example device shown in Fig. 4-19. In Fig. 4-19 (a), the fixed layer has perpendicular polarization, therefore, when the current is applied to the MTJ stack, it is polarized as **σ**=(0,0,+1). Fig. 4-19 shows the vector diagram and it should be emphasized that the coordinates are different from that in Fig. 4-16. The effective field is also different from Fig. 4-16, which represents the isotropic in-plane anisotropy. In other words, the effective field is changing with the spin state and is always along the radial direction of the precession cone. As shown in Fig. 4-19 (b), without the application of external field, the T_{ST} and T_{Damp} have the chance to cancel with each other if the current is carefully selected.

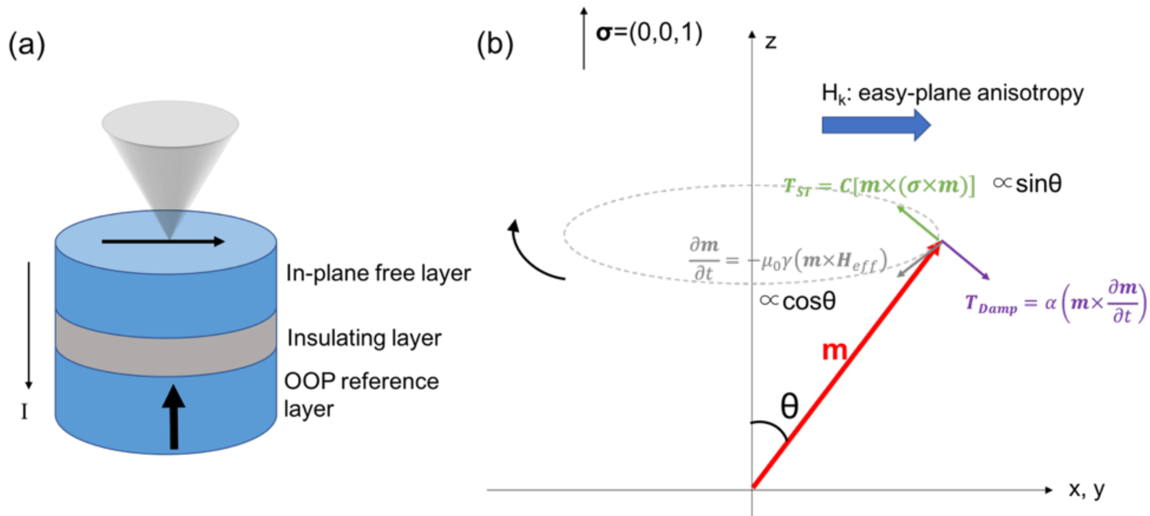

Figure 4-19. Device and vector analysis for the field-free STNO.

Although the field-free STNO can be achieved by applying a perpendicular polarizer, the STNO tunability is sacrificed. In conventional STNO, there are two inputs – external field and the applied current, and two outputs – oscillation frequency and amplitude. It is possible to cover all these two output combinations by varying the two inputs. However, in the field-free STNO design using perpendicular polarizer, there is only one input, i.e., the current. Both the oscillation

frequency and amplitude is affected by the input current. An obvious shortcoming of having one input and two outputs is that the two outputs are correlated with each other, therefore, it is hard to achieve an arbitrary combination of oscillation frequency and amplitude in the STNO.

The other drawback of the previous proposed STNO is that the degradation of the tunnel layer in the MTJ stack as the current constantly flowing through the thin oxide layer. As shown in Fig. 4-20, the breakdown of the tunnel oxide is always an issue for STT device, however, it is not an issue for SOT device. Therefore, it is preferred that using SOT in STNO for spin polarization. The goal of this work is to use strain to replace the external bias field, and use SOT to replace the STT for polarizing the spins.

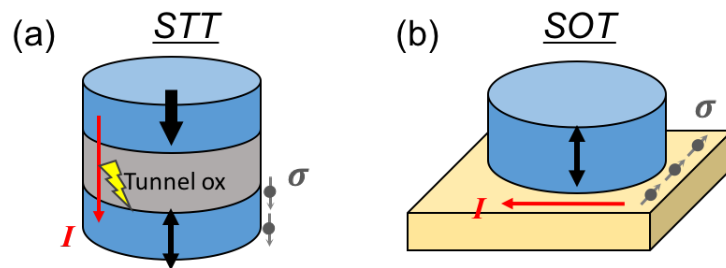

Figure 4-20. Comparison between STT-based and SOT based STNO.

4.4.2 Simulation setup

Figure 4-21(a) shows the simulated structure represented by the finite element model. Note this is the same structure that was shown in Section 4.3, and the only difference is the applied voltage here is -1.5 V. The magnetic element is a CoFeB disk with a 50 nm diameter and a 1.5 nm thickness. The SOT effect was considered as a constant spin polarization along *x* axis as $\hat{\boldsymbol{\sigma}}$ = (1,0,0). The CoFeB disk is attached to a 100 nm-thick $Pb[Zr_xTi_{1-x}]O_3$ (PZT) substrate poled along the *z* axis. Two 50 nm × 50 nm electrodes are placed on the PZT top surface and are 20 nm

away from the CoFeB edge in the *y* direction, while the bottom of the PZT is electrically grounded. The bottom and four sides of the PZT is mechanically fixed. Note the Gilbert damping factor in all the simulations presented in Section 4.4 is 0.5, i.e. artificially high to improve numerical stability. Fig. 4-21(b) shows the snapshot of the simulation.

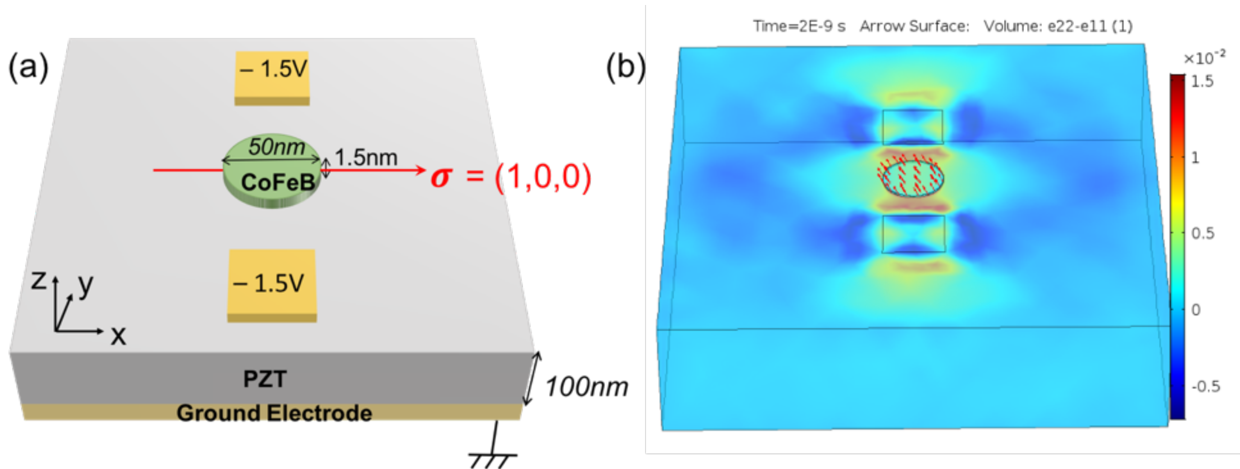

Figure 4-21. Simulation setup and the strain distribution for -1.5 V applied voltage.

Two models including the finite element model and the macrospin model are used in simulating the strain-mediated STNO. Fig. 4-22 shows the comparison of the simulation results using the two models. The two models have the same current input with current density 3.33×10^{7} A/cm^{2}. The applied voltage is -1.5 V inducing a biaxial strain $\varepsilon_{yy} - \varepsilon_{xx} = 5000$ ppm. This particular biaxial strain is used as input in the macrospin model. As shown in Fig. 4-22, the two models used in this section produce similar results. This is mainly because the magnetic disk is single-domain and the impact of ignoring the exchange anisotropy in the macrospin model is relatively insignificant. Therefore, for simplicity, all the following simulations in Section 4.4 are done using the macrospin model.

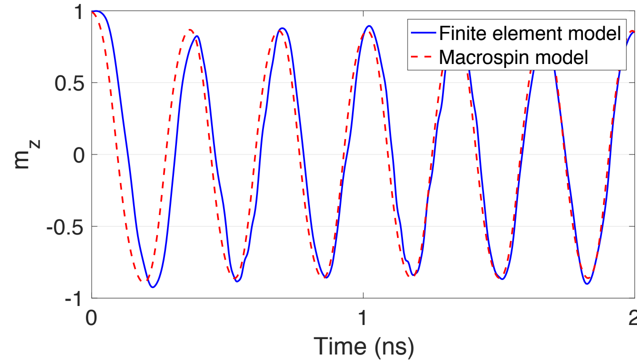

Figure 4-22. Comparison between the finite element model and the macrospin model.

4.4.3 Results and the role of strain

Figure 4-23 shows an example for steady magnetic oscillation achieved in the strain-mediated STNO. The magnetization starts from $m_z = 1$. The input strain is 5000 ppm along *y* axis, and current density is 2×10^7 A/cm^2. The definition of oscillation amplitude is shown in Fig. 4-23(a). Fig. 4-23(b) is the FFT analysis of the magnetization plot in (a) and the peak is oscillation frequency.

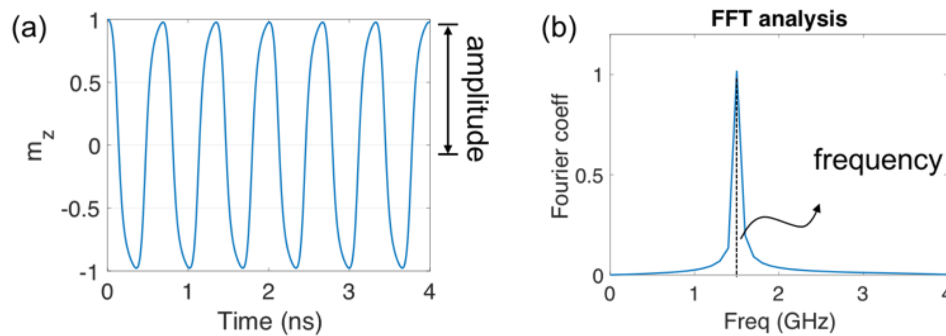

Figure 4-23. Simulation results of the strain-mediated STNO. (a) Perpendicular magnetization vs. time in a 4-ns simulation. (b) FFT of the plot in (a).

The working principle of the strain-mediated STNO is explained as follows. Fig. 4-24(a) shows the total effective magnetic field, which consists of the magnetoelastic field $\boldsymbol{H}_{ME} \sim m_y \hat{\boldsymbol{y}}$ and PMA field $\boldsymbol{H}_{PMA} \sim m_z \hat{\boldsymbol{z}}$. The summation of the two fields are almost radial in *yz*-plane. (Obviously it is not strictly radial everywhere in *yz*-plane because the magnitude of the two fields are only approximately equivalent.) Fig. 4-24(b) illustrates the 3D vector analysis. If one compares this with Fig. 4-19, it can be inferred that the total effective field behaves similar to an isotropic in-plane anisotropy. Note the coordinates are different, and the spin-transfer torque is now a spin-orbit torque. In other words, the strain-induced magnetoelastic field, together with the PMA field, behaves similar to an isotropic radial field in the oscillation. This results in the field-free steady magnetic oscillation.

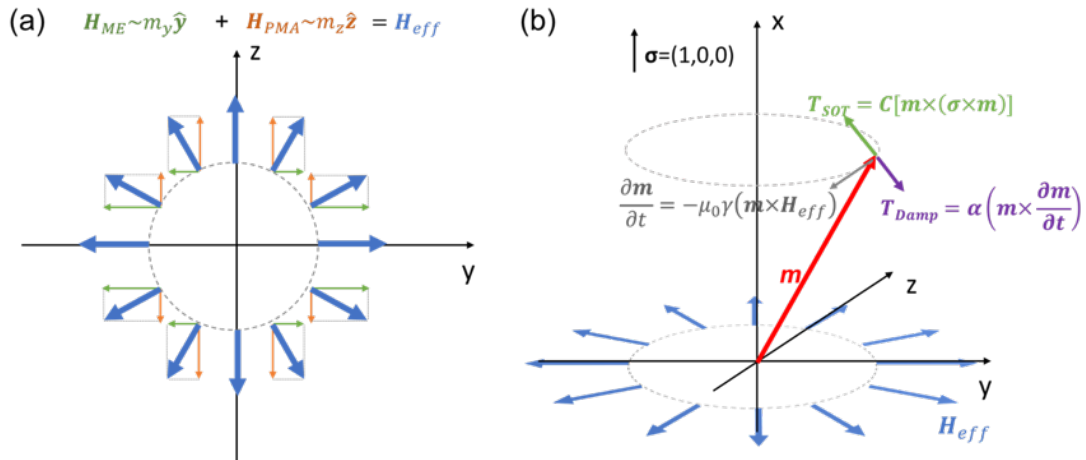

Figure 4-24. (a) Illustration of the total effective field in *yz*-plane. (b) 3D vector analysis showing how the spin-orbit torque cancels with the Gilbert damping torque.

The strain thus enables the field-free STNO steady oscillation. Furthermore, the strain can be easily tuned by varying the voltage applied to the piezoelectric substrate. One advantage of the strain-mediated STNO compared to previously proposed field-free STNO is that the existence of strain adds significantly increased tunability for the STNO. Because now we have two inputs

(strain and current) and two outputs (oscillation frequency and amplitude) again, which makes it possible to cover a wider range of oscillation behaviors by varying the two inputs. This will be further confirmed by a later parametric study.

Another advantage is the strain-mediated STNO is self-adjustable. Fig. 4-25 gives the reaction flow of the STNO system given a sudden current decrease. As shown in Fig. 4-25(a), when the current decreases, the T_{SOT} reacts first and decreases, as it is the only torque that is directly associated with the applied current. Then the damping torque becomes larger than the spin-orbit torque ($\boldsymbol{T}_{SOT} < \boldsymbol{T}_{Damp}$), therefore, the oscillation cone angle θ (as defined in Fig. 4-25) becomes larger. As a result, the spin-orbit toque increases as $\boldsymbol{T}_{SOT} \propto sin\theta$ while the damping torque decreases as $\boldsymbol{T}_{Damp} \propto cos\theta$. The system soon reaches a new equilibrium ($\boldsymbol{T}_{SOT} = \boldsymbol{T}_{Damp}$) and the magnetization achieves a new stable state. As shown in Fig. 4-25 (c), the new stable magnetic oscillation state has a larger amplitude. And the oscillation frequency $f \sim \frac{\partial \boldsymbol{m}}{\partial t} \propto cos\theta$ decreases. It is shown that the strain-mediated STNO is resistive to small input variation, which is very important for practical application as the thermal fluctuation exists.

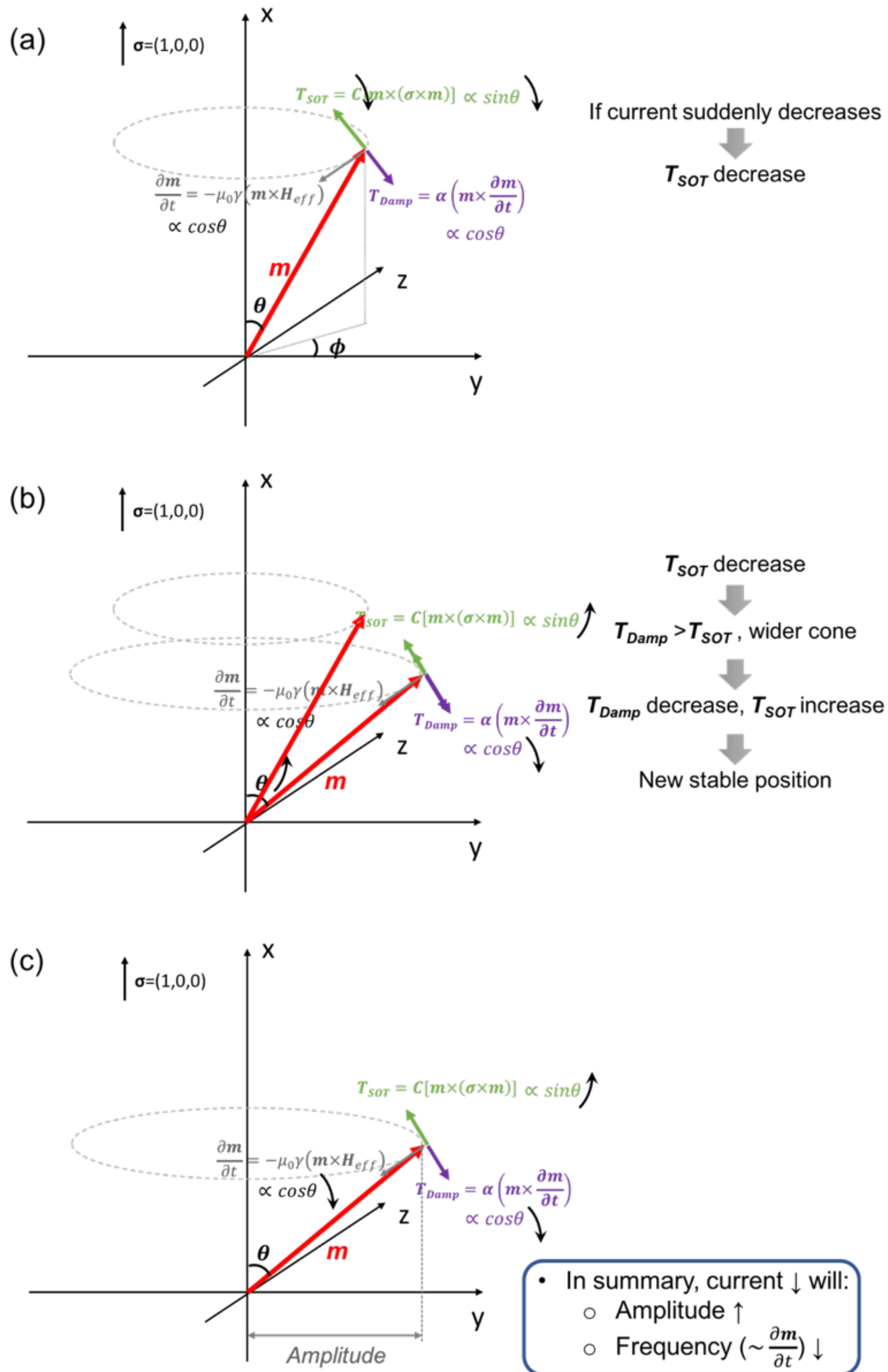

Figure 4-25. Self-adjustable property of the strain-mediated STNO.

A parametric study is conducted with the macrospin model using the applied strain and current as input. Note the strain is applied as a uniaxial tensile strain along y axis. The oscillation amplitude and frequency are illustrated in Fig. 4-26. Each small box represents a 5-ns macrospin simulation with magnetization initialized as pointing along $+z$ direction. The state is counted as 'steady oscillation' if the oscillation amplitude of m_z in the last 1ns is <1%. For all the steady oscillation cases, the oscillation amplitude and frequency, which are defined in Fig. 4-23, are plotted in Fig. 4-26(a) and (b), respectively. For other cases, either switching or non-switching or non-steady oscillation, are all represented as the 0 amplitude and 0 frequency, i.e. all dark blue boxes in the Fig. 4-26.

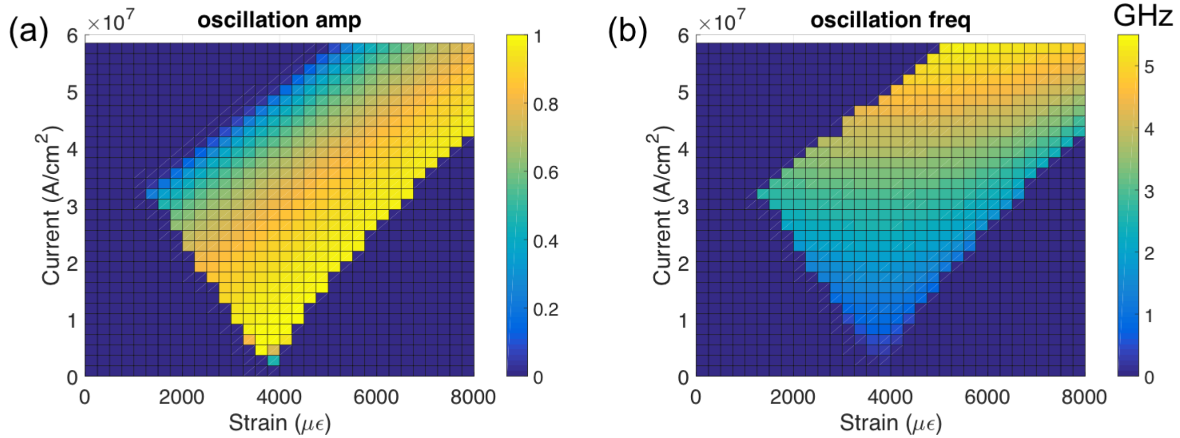

Figure 4-26. Phase diagram of the parametric study for the strain-mediated STNO with varying input strain and current. Gilbert damping is $\alpha = 0.5$.

From the parametric study, it can be seen that the oscillation amplitude can be tuned widely, almost covering the complete range 0~1. The oscillation frequency can be tuned from a few hundreds of megahertz to ~5 GHz. Interestingly, the amplitude and frequency are not completely dependent on each other. In contrast, the oscillation amplitude is more influenced by strain, while the frequency is more influenced by current.

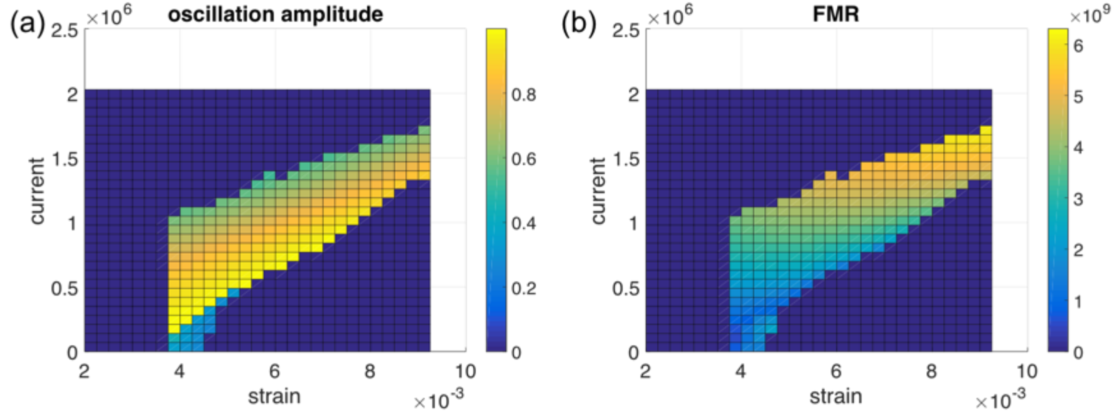

Figure 4-27. Phase diagram of the parametric study for the strain-mediated STNO with varying input strain and current. Gilbert damping is $\alpha = 0.01$.

Figure 4-27 shows the same parametric study but with real Gilbert damping $\alpha = 0.01$. Similar trends are observed in the amplitude and frequency plots. Some cases that do not follow the general trend in the lower left corner of the plot are mainly because the simulation time is not long enough to reach the final state, causing fake steady oscillation. It should be emphasized here that the required current for steady oscillation is one order of magnitude lower than in Fig. 4-26. This is because the oscillation happens when the spin-orbit torque from the current cancels with the Gilbert damping. Therefore, the required current to cancel smaller damping is lower.

4.4.4 Mathematical derivation

To better understand the working principle of the strain-mediated STNO, a simplified mathematical derivation is performed in this section. The LLG equation with damping-like SOT term is [50], [152], [153]:

$$\frac{\partial \boldsymbol{m}}{\partial t} = -\mu_0 \gamma \left(\boldsymbol{m} \times \boldsymbol{H}_{eff}\right) + \alpha \left(\boldsymbol{m} \times \frac{\partial \boldsymbol{m}}{\partial t}\right) + \frac{\gamma \hbar}{2e} \frac{J_C}{M_S t_F} \xi_{DL} \boldsymbol{m} \times (\widehat{\boldsymbol{\sigma}} \times \boldsymbol{m}) \qquad \text{Eq. 4-18}$$

where μ_0 the vacuum permittivity, γ the gyromagnetic ratio, $\hbar$ the reduced Planck constant, e the elementary charge, J_C the current density, $\hat{\boldsymbol{\sigma}}$ the polarized spin accumulation, α the Gilbert damping factor, t_F the thickness of the free magnetic layer, M_S the saturation magnetization, and ξ_{DL} is the damping-like spin Hall angle. The damping torque is $\boldsymbol{T}_{Damp} = \alpha\left(\boldsymbol{m}\times\frac{\partial \boldsymbol{m}}{\partial t}\right)$, and the SOT is $\boldsymbol{T}_{SOT} = \mu_0\gamma C[\boldsymbol{m}\times(\boldsymbol{\sigma}\times\boldsymbol{m})]$, where $C = \frac{\hbar}{2e}\frac{J_C}{\mu_0 M_S t_F}$. The spin Hall angle ξ_{DL} is assumed to be 1. The steady oscillation happens when spin-orbit torque cancels with damping torque, i.e., $\boldsymbol{T}_{SOT} = -\boldsymbol{T}_{Damp}$. Then the governing equation becomes:

$$\alpha\left(\boldsymbol{m}\times\frac{\partial \boldsymbol{m}}{\partial t}\right) = -\mu_0\gamma C[\boldsymbol{m}\times(\boldsymbol{\sigma}\times\boldsymbol{m})] \quad \text{Eq. 4-19}$$

The effective field consists of the magnetoelastic field and the PMA field:

$$\boldsymbol{H}_{eff} = \frac{2}{\mu_0 M_S} B_1 \varepsilon m_y \hat{\boldsymbol{y}} + K_{pma} m_z \hat{\boldsymbol{z}} \quad \text{Eq. 4-20}$$

where ε is the tensile strain along y axis, B_1 is the first order magnetoelastic coefficient, and K_{pma} is the PMA coefficient. For CoFeB simulated in the model, $B_1 = -2.77\times10^7$ N/m^2 and $K_{PMA} = -K_i/t_F$, where K_i = 1.3 mJ/m^2 and t_F is the thickness of the CoFeB.

We assume the magnetic oscillation is a perfect circular precession in *yz*-plane as shown in Fig. 4-25. Therefore, the magnetization can be written in cylindrical coordinate as:

$$m_x = cos\theta, m_y = sin\theta cos\phi, m_z = sin\theta sin\phi \quad \text{Eq. 4-21}$$

where θ and ϕ are defined in Fig. 4-25(a). Plug the equation 4-21 into equation 4-19, and take the amplitude on both sides, we can get:

$$\alpha\left|\frac{\partial \boldsymbol{m}}{\partial t}\right| = \mu_0\gamma C sin\theta \quad \text{Eq. 4-21}$$

At the same time, plugging equation 4-19 into 4-18 gives:

$$|\frac{\partial \boldsymbol{m}}{\partial t}| = \mu_0 \gamma |\boldsymbol{m} \times \boldsymbol{H}_{eff}| \quad \text{Eq. 4-22}$$

Plugging the effective field (equation 4-20) into equation 4-22, and plugging the calculated $|\frac{\partial \boldsymbol{m}}{\partial t}|$ into equation 4-21 result in:

$$cos\theta = \frac{1}{\frac{2}{\mu_0 M_S} B_1 \varepsilon \, cos^2\varphi + K_{pma} sin^2\varphi} \cdot \frac{C}{\alpha} \quad \text{Eq. 4-23}$$

Average this for a full precession loop:

$$< cos\theta >= \frac{1}{2\pi} \int_0^{2\pi} \frac{1}{\lambda_1 cos^2\varphi \, + \lambda_2 sin^2\varphi} d\varphi \cdot \frac{C}{\alpha} = \frac{C}{\alpha\sqrt{\lambda_1 \lambda_2}} \quad \text{Eq. 4-24}$$

where $\lambda_1 = \frac{2}{\mu_0 M_S} B_1 \varepsilon$ and $\lambda_2 = K_{pma}$. When $\lambda_1 = \lambda_2$, the strength of PMA and magnetoelastic field are equal and the total effective field is equivalent to an isotropic in-plane anisotropy, as discussed in Fig. 4-24. However, this condition is not critical for achieving steady magnetic oscillation. Generally we only require $\lambda_1 \approx \lambda_2$ and the precession trajectory is not a perfect circle as a compensation. In this case:

$$cos\theta \approx \frac{\mu_0 M_S}{2\alpha B_1} \frac{C}{\varepsilon} \quad \text{Eq. 4-25}$$

Then the amplitude of the oscillation can be written as a function of current and strain:

$$amp(C, \varepsilon) = sin\theta = sin\,(arccos(\frac{\mu_0 MS}{2\alpha B1} \frac{C}{\varepsilon})) \quad \text{Eq. 4-26}$$

And the frequency can also be written as a function of current and strain:

$$f(C, \varepsilon) = \frac{\omega}{2\pi} = \frac{1}{2\pi} |\frac{\partial \boldsymbol{m}}{\partial t}|_{proj} = \frac{\mu_0 \gamma}{2\pi} \frac{C}{\alpha} \sqrt{1 - \frac{C^2 \mu_0 M_S}{2\alpha^2 B_1 \varepsilon K_{PMA}}} \quad \text{Eq. 4-27}$$

The ‘proj’ means projection onto the *yz*-plane. Please note C is not current, but it is a coefficient including the current density as defined previously.

Then we compare the analytical solution (equation 4-26 and 4-27) with the numerical simulation results. Fig. 4-28 shows the comparison for constant current and varying strain in the phase diagram shown in Fig. 4-27. The blue circles in Fig. 4-28 (b) and (d) represents the macrospin model results for the slice indicated in Fig. 4-28 (a) and (c), respectively.

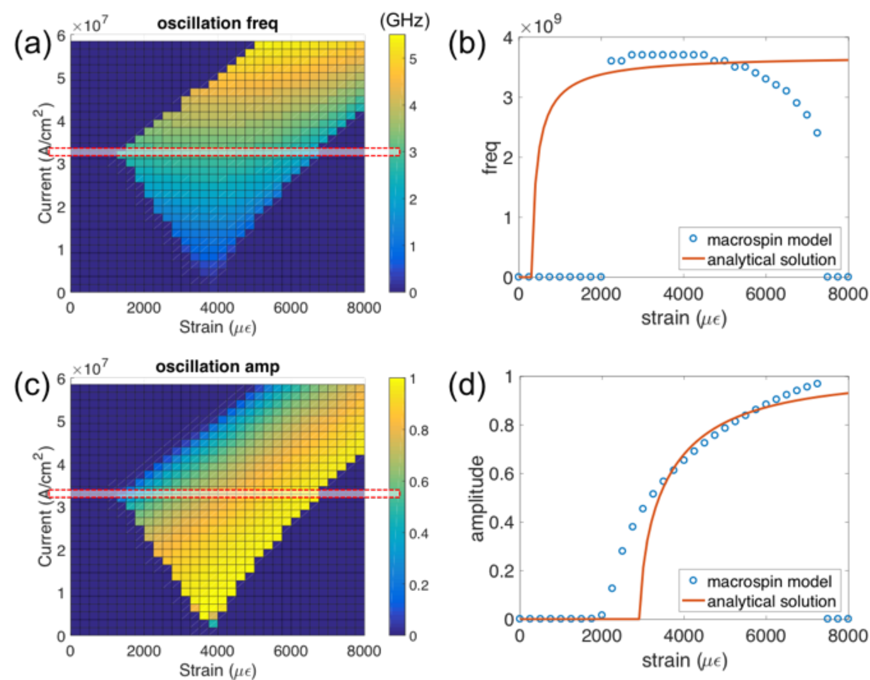

Figure 4-28. Comparison between the analytical solution and numerical simulation. A slice of the phase diagram with constant current and varying strain is examined.

A similar comparison is performed for the constant strain and varying current, as shown in Fig. 4-29. There is good agreement between the model results and the analytical solution.

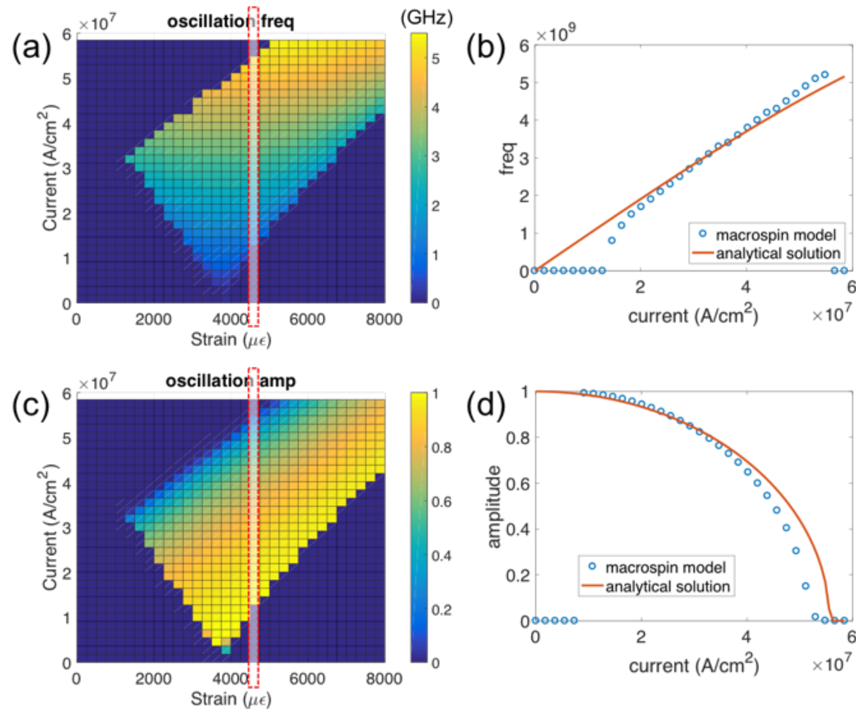

Figure 4-29. Comparison between the analytical solution and numerical simulation. A slice of the phase diagram with constant strain and varying current is examined.

4.4.5 Applications

The strain-mediated STNO can have various applications. Fig. 4-30 illustrates a potential design of using the strain-mediated STNO array as an antenna. A continuous heavy metal (e.g., Ta) is deposited on top of the piezoelectric substrate (e.g., PMN-PT). An in-plane current is applied to the Ta layer while the PMN-PT is strained by applying voltage to the bottom electrode. An array of magnetic nano-oscillator is patterned on Ta layer. Under a constant applied DC current and DC voltage, the magnetization of the oscillator array may oscillate steadily. With appropriate synchronization mechanism, the magnetic array may radiate electromagnetic waves through an oscillating magnetic dipole. The radiation frequency,

amplitude and cone direction could be tuned in this application by varying the applied strain and current.

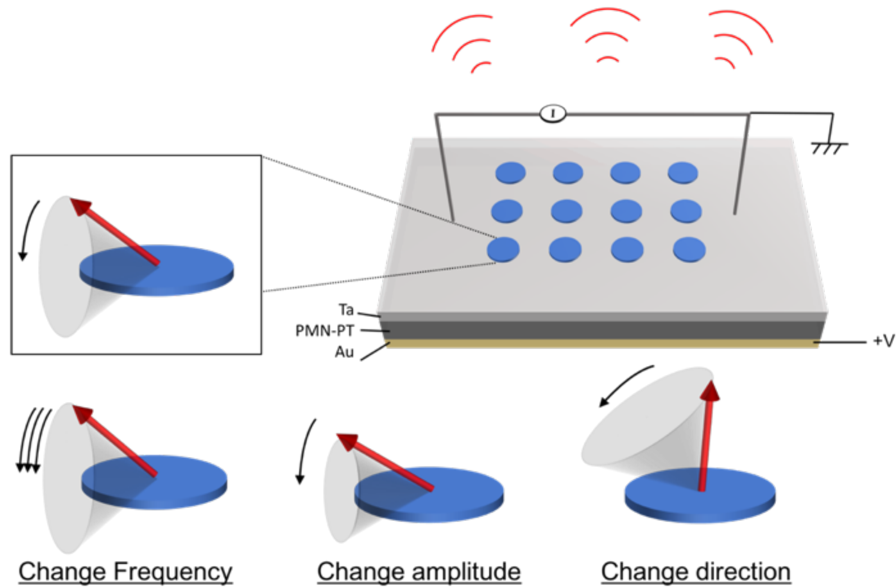

Figure 4-30. Using an array of strain-mediated STNO as a radiator.

Another potential application is illustrated in Fig. 4-31. All previous simulations in this section have temporally invariant current and strain input as shown in Fig. 4-31(a). And the induced magnetic oscillation has a single frequency component f_1 as shown in Fig. 4-31 (b) and (c). If we keep the strain input unchanged but apply an AC current input with frequency f_0 as shown in Fig. 4-31 (d), the induced magnetic oscillation can have multiple components: f_1, f_1+f_0, f_1-f_0, f_1+2f_0, f_1-2f_0 etc., as shown in the FFT plot in Fig. 4-31(f). This special property produces a strain-mediated STNO with potential application as a frequency mixer as illustrated in Fig. 4-31 (g).

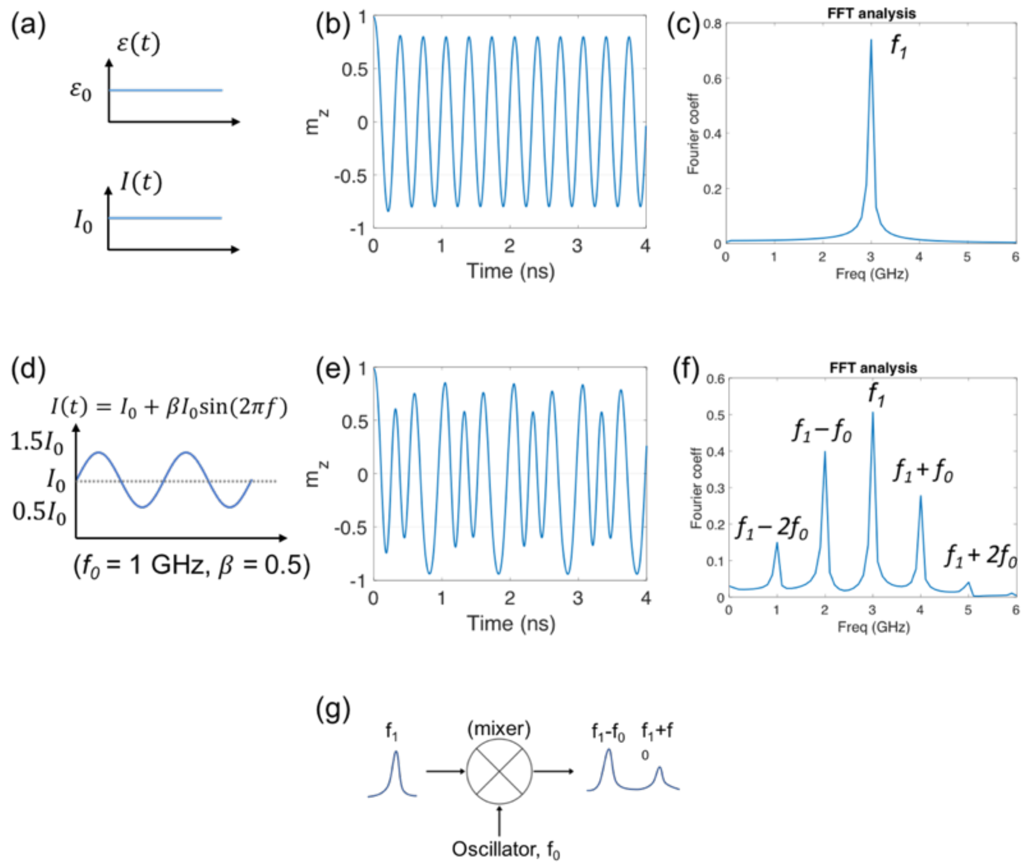

Figure 4-31. Using strain-mediated STNO as a frequency mixer.

By changing the amplitude of the AC current, the system can have more tunability. As demonstrated in Fig. 4-32, an AC current is applied at the same frequency. The amplitude of the AC current is different in Fig. 4-32 (a)(d)(g). The resulting magnetic oscillations have the same frequency components, however, the ratio between the frequency peaks are different, as highlighted in Fig. 4-32 (c)(f)(i).

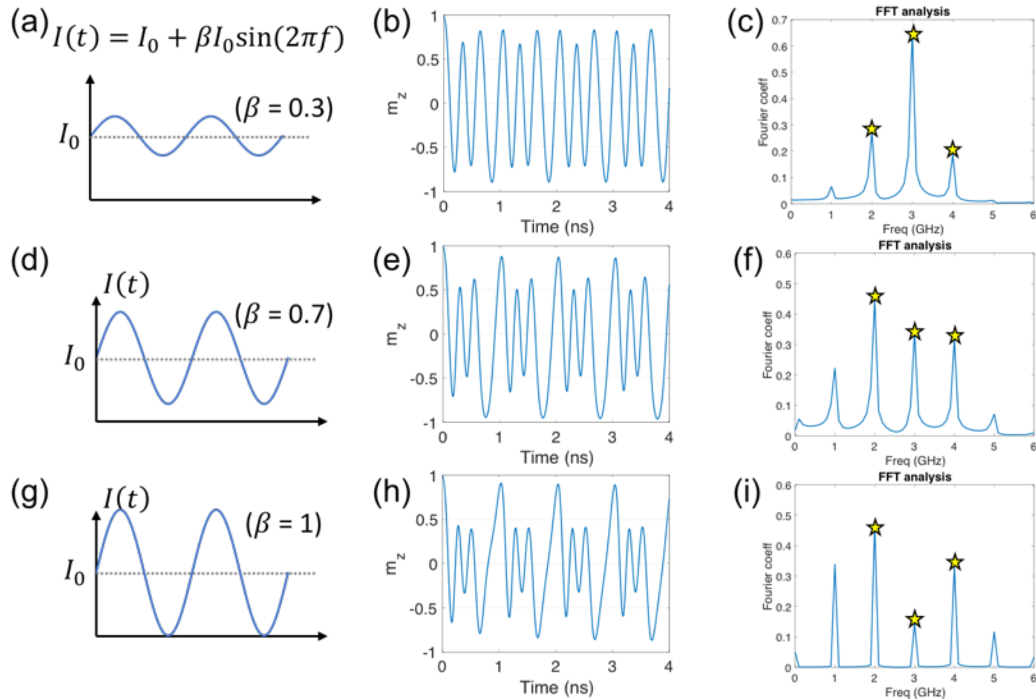

Figure 4-32. Magnetic oscillation with AC current input.

4.5 Deterministic directional perpendicular switching for memory application

The switching mechanism shown in Section 4.3 is deterministic but not directional. The final state depends on the initial state. The mechanism is interesting in a way that the magnetization always switch counterclockwise or clockwise every time the current/voltage is applied, however, it is not very useful as a memory device. In this section, we present a new deterministic perpendicular switching method using a hybrid strain + SOT control. The strain-induced magnetoelastic anisotropy breaks the lateral symmetry, and the resulting symmetry-breaking is controllable. A finite element model and a macrospin model are used to numerically simulate the strain-mediated SOT switching mechanism. The switching direction ('up' or 'down') is dictated by the voltage polarity (positive or negative) applied to the piezoelectric layer in the

magnetoelastic/heavy metal/piezoelectric heterostructure. The switching speed can be as fast as 10 GHz. More importantly, this control mechanism can be potentially implemented in a magnetic random-access memory system with small footprint, high endurance and high tunnel magnetoresistance (TMR) readout ratio.[161]

4.5.1 Background: perpendicular magnetic switching by SOT

Non-volatile magnetic random-access memory (MRAM) is of significant interest recently because it promises zero stand-by power and the key for MRAM device is deterministic magnetic switching. One of the most well developed magnetic switching mechanisms is through spin-transfer torque (STT)[48], [162]–[166]. However, STT-MRAM (magnetic random-access memory) is facing endurance issues because the high current density required for writing damages the thin insulating barrier[166]–[169]. For this reason, researchers have begun to investigate spin-orbit torque (SOT) approaches in heavy metal/ferromagnetic metal heterostructures [51], [167], [170]–[173]. The SOT switching mechanism offers higher endurance since the write current does not pass through the insulating barrier. Also, SOT is considered to be more energy efficient than STT and theoretically requires lower current density for switching[171]. For magnetic memory devices, memory bits with perpendicular magnetic anisotropy (PMA) are desirable because they have higher thermal stability and smaller footprint compared to in-plane memory bits[21], [22]. However, out-of-plane (OOP) switching in memory bits with PMA remains a challenge for SOT devices.

Deterministic OOP switching in SOT devices usually requires an external magnetic bias field[157], [170], [174]–[176], but the bias field requirement decreases energy efficiency and becomes challenging to integrate for on-chip applications. Field-free deterministic OOP

switching has been investigated using a variety of methods. Yu *et al* investigated a ferromagnetic wedge shape to induce a field-like torque which breaks the lateral symmetry[49]. Similarly, You *et al* studied other shape engineering to break the symmetry with a tilted magnetic anisotropy[177]. However, in these methods complex fabrication approaches limit the scalability. A more straightforward way is to replace the external field with an exchange-bias field from an adjacent antiferromagnetic layer [178], [179], or a dipole field from an nearby magnetically fixed layer[180]. However, all of these symmetry-breaking methods are non-controllable once the devices are built. To address this issue, researchers have recently developed an SOT device that uses an in-plane electric field to achieve controllable symmetry-breaking[181]. However, this field-free deterministic OOP switching still relies on an induced asymmetric anisotropy, similar to previously listed symmetry-breaking methods. Here, we demonstrate that symmetric/uniaxial anisotropies like strain-induced magnetoelastic anisotropy also can, surprisingly and counterintuitively, break the lateral symmetry and yield field-free switching in SOT devices.

In particular, we demonstrate that strain-induced magnetoelastic anisotropy can feasibly serve as the symmetry-breaking mechanism. The magnetoelastic anisotropy is induced in the magnetoelastic material (e.g., CoFeB) by locally straining an attached piezoelectric layer through externally applied voltage. The strain-induced magnetoelastic anisotropy is uniaxial since the piezo-strains are uniaxial in nature. This form of strain-mediated control represents the most energy efficient way to control magnetism in current nanoscale technologies[18]–[20], [36]. It should be noted that using only strain control to switch magnetization is non-deterministic and thus requires precise voltage pulse timing [19], [60], [62].

4.5.2 Simulated structure

Figure 4-33 shows the magnetoelastic/heavy metal/piezoelectric heterostructure simulated in the finite element model. The magnetic element is a CoFeB disk with a 50 nm diameter and a 1.5 nm thickness. Underneath the CoFeB disk, there is a canted thin (< 10 nm) heavy metal (e.g., Ta) strip and the SOT current is applied 45° counter-clockwise from the *–y* axis. The SOT current causes spin polarized electrons to accumulate at the magnetoelastic/heavy metal interface.

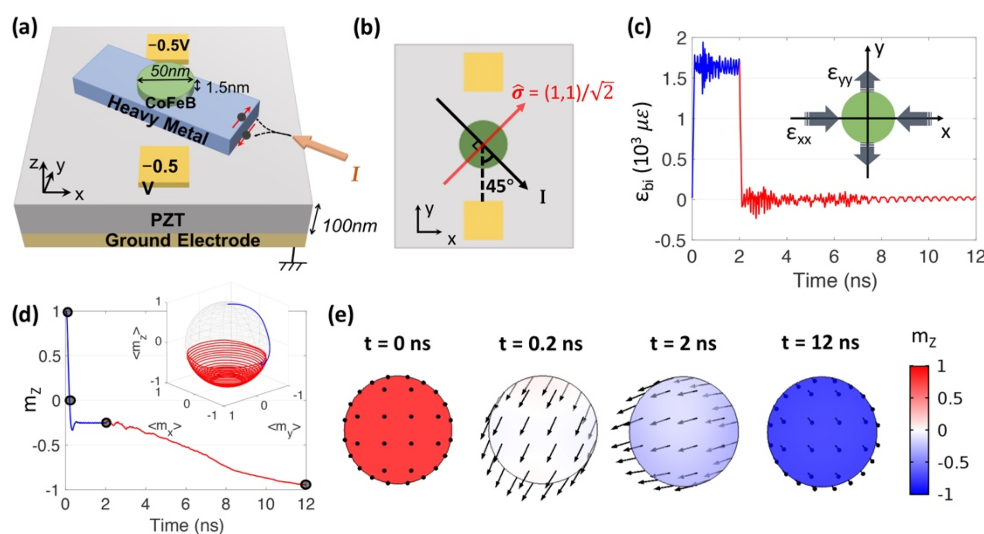

Figure 4-33. (a) Schematic illustration of the simulated structure. (b) The top view of the simulated structure. (c) Temporal change of biaxial strain induced by the −0.5 V applied voltage. (d) Temporal evolution of the perpendicular magnetization in the free CoFeB layer. (e) Vector diagrams of the magnetization distribution.

As shown in Fig. 4-33(b), the spin polarization is perpendicular to the applied current as $\hat{\boldsymbol{\sigma}} = (1,1)/\sqrt{2}$, which then exerts spin-orbit torque on the CoFeB magnetic moment[49], [50], [171]. The heavy metal strip is attached to a 100 nm-thick $Pb[Zr_xTi_{1-x}]O_3$ (PZT) substrate poled along the *z* axis. Two 50 nm × 50 nm electrodes are placed on PZT top surface and are 20 nm away

from the CoFeB edge along the y direction, while the bottom of the PZT is electrically grounded. The assumptions, boundary conditions, and material parameters are described in the Methods section. The CoFeB magnetization is initialized as 'up' (i.e., pointing to the $+z$ direction). At t = 0, a −0.5 V voltage is applied to the two top electrodes and a current with density of 5×10^7 A/cm^2 is applied to the heavy metal strip simultaneously. Both voltage/current inputs are removed at t = 2 ns.

4.5.3 Simulation results and analysis

Figure 4-33(c) shows the CoFeB disk's volume-averaged biaxial strain $\varepsilon_{bi} = \varepsilon_{yy} - \varepsilon_{xx}$ as a function of time during the application and removal of voltage/current identified by red and blue colors respectively. Due to shear lag effects, the vertical electrical field inside the PZT layer causes anisotropic in-plane strains[36], [46]. In this case, a −0.5 V voltage induces volume-averaged biaxial strain $\varepsilon_{bi} \approx 1600\ \mu\varepsilon$ inside the CoFeB disk. It is shown that the biaxial strain rises and oscillates at 1600 $\mu\varepsilon$ within the first 2 ns. Following voltage removal at 2 ns, the strain decays to 0 with small oscillations as the magnetization precesses to its new equilibrium position. The small oscillations are caused by the inverse magnetoelastic effect. The relatively long precession towards the new equilibrium state ($m_z = -1$) is related to the relatively low Gilbert damping of CoFeB ($\alpha = 0.01$).

Figure 4-33(d) shows the volume-averaged perpendicular magnetization m_z as a function of time while the inset shows the magnetization trajectory. The voltage/current application and removal are identified as the blue and red portions of the response, respectively. As can be seen, the magnetization stabilizes at 2 ns is down-canted (i.e., $m_z < 0$) before removal of the voltage/current. Therefore, upon removal of both voltage and current (t = 2 ns), the

magnetization preferably selects ‘down’ to its new equilibrium state (i.e., $m_z = -1$). Thus, during this voltage/current application and subsequent removal, the magnetization undergoes 180° OOP switching from ‘up’ to ‘down’.

To better understand the magnetic switching process, Fig. 4-33(e) provides magnetic vector diagrams at four representative time points corresponding to the four data points highlighted in Fig. 4-33(d). The arrows indicate in-plane magnetization direction and amplitude while color represents the perpendicular amplitude m_z which varies between −1 and +1. At t = 0, all spins are initialized as ‘up’, while at t = 0.2 ns the spins rotate to in-plane through 90° switching. The coherent switching observed is attributed to the relatively small CoFeB disk’s diameter compared to its single-domain limit[19], [63]. After t = 0.2 ns, the magnetization starts to cant down and remain in the –*z* space in the following process. At t = 2 ns, the magnetization stabilizes in a down-canted direction (see Fig. 4-33(d)) with $m_z = -0.23$ for this specific voltage/current combination. At t = 12 ns, the spins reach a new equilibrium state ($m_z = -1$). It can be inferred that removing the voltage/current at any time after 0.2 ns will result in deterministic magnetic switching from ‘up’ to ‘down’, which corresponds to a 5 GHz writing speed. Although the length of time for the voltage/current is relatively unimportant as long as the minimum time (i.e., 0.2 ns in this particular case) is reached, the simultaneous removal of voltage and current pulses is important. More specifically, the magnetization is likely to rotate back to in-plane and align with current (or strain) direction, if the current (or strain) pulse lasts longer than the other input. Increasing voltage or current magnitudes increases writing speed up to ~10 GHz (see Note 3 in Supplemental Information in next section for more simulation results of switching speed). It is worth noting that the piezoelectric response (RC ~ 10^{-13} s) and elastodynamic response (characteristic time of 10^{-12} s, as calculated from the mechanical wave

speed) are both faster than the characteristic magnetic response time ($10^{-10} \sim 10^{-9}$ s), which is related to the ferromagnetic resonance (FMR) of the system.[20] For simplicity, in the following results, we only focus on the m_z temporal evolution during the application of voltage/current during t = 0 ~ 2 ns.

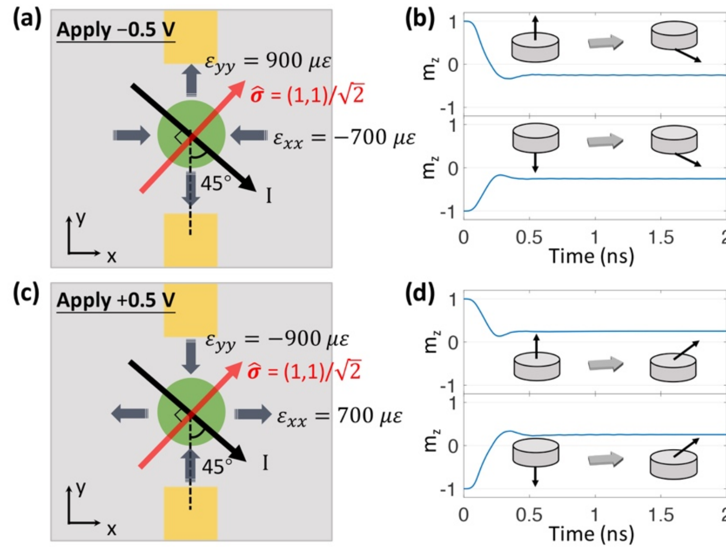

Figure 4-34. Finite element model results of strain-mediated SOT switching for different voltage polarities (positive or negative) and initial states (‘up’ or ‘down’).

Figure 4-34 provides more finite element simulation results to investigate the impact of voltage polarities (positive or negative) and initial states (‘up’ or ‘down’) on the final magnetic states. For all cases in Fig. 4-34, the current density and direction are the same as presented in Fig. 4-33. Fig. 4-34(a) illustrates in-plane principal tension and compression for the −0.5 V case, indicating the corresponding magnetoelastic field is along ±*y* axis (not shown here) since CoFeB is a positive magnetostrictive material. Note the field is bidirectional due to the uniaxial nature of the strains. Fig. 4-34(b) shows the volume-averaged m_z as a function of time for −0.5 V applied voltage for both ‘up’ and ‘down’ initialization. At t = 2 ns, the magnetization is down-canted as

$m_z = -0.23$, regardless of the initial state ('up' or 'down'). It can be inferred that the final magnetic states following voltage/current removal are 'down' ($m_z = -1$) for both cases.

If one reverses the current direction in Fig. 4-34(a) by 180°, which is not shown here, the final state is the same, i.e., pointing 'down'. This can be explained as follows. If one rotates the *x-y* coordinates with respect to *z* axis by 180°, the SOT current reverses direction while the voltage-induced strain remains the same due to its uniaxial nature. This means that the two cases (positive/negative applied current) are physically identical. Therefore, the final states for positive and negative applied current are the same. In contrast, reversing the voltage polarity reverses the final state. As shown in Fig. 4-34(c), for the +0.5 V case, the principal tension and compression directions is reoriented by 90° compared to −0.5 V case shown in Fig. 4-34(a), and the corresponding magnetoelastic field is now along ±*x* axis (not shown here). The switching results for the configuration in Fig. 4-34(c) are shown in Fig 4-34(d). The magnetic states at t = 2 ns are both up-canted with $m_z = +0.23$ regardless of the initial states. It can be inferred that the final magnetic states following voltage/current removal are 'up' ($m_z = +1$). These results presented in Fig. 4-34 clearly demonstrate that the switching direction (i.e., 'up' or 'down') is dictated by the voltage polarity (i.e., positive or negative) used to strain the PZT layer. More simulation results with varying initial states can be found in Note 2 in Section 4.5.5.

In addition to voltage polarity and initial state, there are three additional parameters (i.e., strain amplitude, current density, and relative orientation of strain/current) that influence the strain-mediated SOT switching. Parametric studies using the macrospin model are performed to investigate the influence these three parameters have on the strain-mediated SOT switching, and the results are presented in Fig. 4-35. In all the cases demonstrated in Fig. 4-35, the voltage is

kept negative and the magnetization is always initialized 'up' (i.e., $m_z = +1$). It is shown that the macrospin model provides reasonably accurate results when compared to the fully coupled finite element model (see Note 1 in Section 4.5.5 for the comparison between the two models)). Fig. 4-35(a) illustrates the principal strain directions and the definition of the relative orientation θ. From the previous finite element model results, the negative voltage induced strains are tensile along *y* direction and compressive along *x* direction. For simplicity, we set $\varepsilon_{xx} = 0$ in the macrospin model and the biaxial strain becomes $\varepsilon_{bi} = \varepsilon_{yy} - \varepsilon_{xx} = \varepsilon_{yy}$. In the parametric studies, the SOT current density is varied from 0 ~ 8×10^7 A/cm^2, the biaxial strain is varied from 0 ~ 4000 με, and θ is varied from 0 ~ 90°.

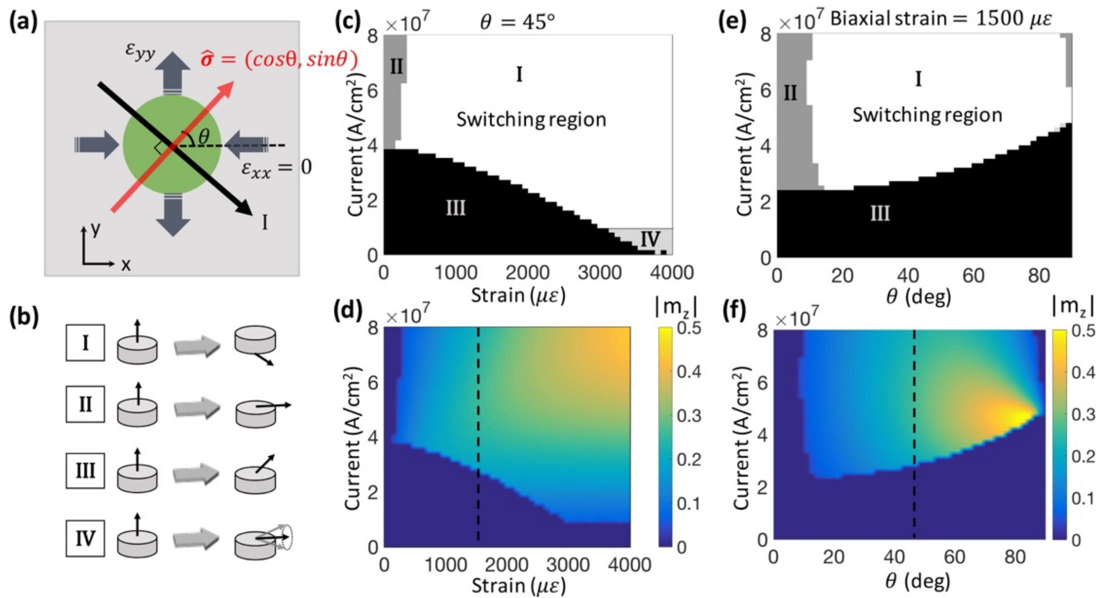

Figure 4-35. Switching phase diagrams for strain-mediated SOT switching.

Fig. 4-35(b) illustrates the four types of magnetic state identified at t = 2 ns using the criterion described in Note 6 in Section 4.5.5. The type I state represents successful switching with magnetization switching from 'up' to 'down'. The type II state refers to magnetization

switching 90° to in-plane where the applied SOT current is sufficiently large to hold the magnetization in-plane. The type III state occurs when the applied voltage and current are both relatively small producing magnetization rotation of less than 90°. Finally, the type IV state represents continued magnetic oscillation, which is beyond the scope of this work and is not discussed in detail.

In the first parametric study, which consists of 2,601 cases (i.e., a 51 × 51 grid), the biaxial strain and the current density are varied while the relative orientation is fixed as θ = 45°. The physical constraint to select the 51 × 51 grid is driven by available data representing the maximum plausible piezo-strain and maximum current density present in the literatures [51], [173], [182], [183]. Fig. 4-35(c) shows the switching phase diagram, and the four separate regions correspond to the four types of magnetic state shown in Fig. 4-35(b). The successful switching cases (region I) are further examined in Fig. 4-35(d). The m_z amplitude at t = 2 ns is illustrated in color for each case in region I, and the diagram is smoothed using linear interpolation. For other regions, the m_z values are all set to be zero. This does not mean the final m_z for those cases are actually zero, but instead, it only indicates that those cases are 'non-switching'. The switching initiates when the biaxial strain is as low as $\varepsilon_{bi} = \varepsilon_{yy} - \varepsilon_{xx} = 230\ \mu\varepsilon$. As the strain increases, the threshold current (i.e., the minimum current that enables switching) decreases. In other words, a tradeoff exists between the threshold strain and threshold current. In this case, the threshold current reaches a minimum of ~1×10^7 A/cm^2 at 3000 $\mu\varepsilon$ strain amplitude. Further strain increase does not continue to reduce the threshold current because oscillations begin to occur.

The second parametric study also consists of an additional 2,061 cases (i.e., a 51 × 51 grid) with fixed biaxial strain $\varepsilon_{bi} = \varepsilon_{yy} - \varepsilon_{xx} = 1500\ \mu\varepsilon$ while varying θ and current density. Fig. 4-35(e) shows the switching phase diagram for this parametric study. Only three types of magnetic states (type I, II, and III) are found, with the magnetic oscillation (type IV) being absent due to the relatively small strains investigated. Fig. 4-35(f) further examines all the successful switching cases (region I) and the m_z amplitude at t = 2 ns for each case is represented in the color map. The results show that switching is absent when the current is parallel (θ = 0°) or perpendicular (θ = 90°) to the magnetoelastic field (i.e., *y* axis). This feature will be explained in the next section using symmetry analysis. For Fig. 4-35(f), both the threshold current and m_z decrease as θ decreases. Smaller threshold currents represent more energy efficient switching process, while lower m_z values represent less reliable switching if thermal fluctuations are included. In other words, for a given voltage, a tradeoff exists between energy efficiency and the reliability of magnetization reversal (or write error). It is also interesting to note that the dashed cut-lines in Figs. 4-35(d) and 4-35(f) have similar profiles because they both represent switching behaviors as a function of current density for a fixed current direction θ = 45° and a fixed biaxial strain $\varepsilon_{bi} = 1500\ \mu\varepsilon$.

To understand the physics behind the deterministic switching, Fig. 4-36 presents symmetry analysis for three scenarios of strain-mediated SOT switching. In all the configurations shown in Fig. 4-36, the green sheet represents the magnetic element with PMA, and the grey sheet represents the heavy metal (e.g., Ta). The SOT current *I* is always applied along the –*x*, and the accumulated spin polarization is $\hat{\boldsymbol{\sigma}} = -\hat{y}$. Therefore, the damping-like spin-orbit field is $\boldsymbol{H}_{SO} \propto \boldsymbol{m}\times\hat{\boldsymbol{\sigma}} = \hat{y}\times\boldsymbol{m}$ and the spin-orbit torque is $\boldsymbol{\tau}_{SO} \propto \boldsymbol{H}_{SO}\times\boldsymbol{m}$. The magnetoelastic field is

generalized as a uniaxial field $\boldsymbol{H_{Uni}}$ and is represented by a bidirectional arrow [24], [46], [184], [185].

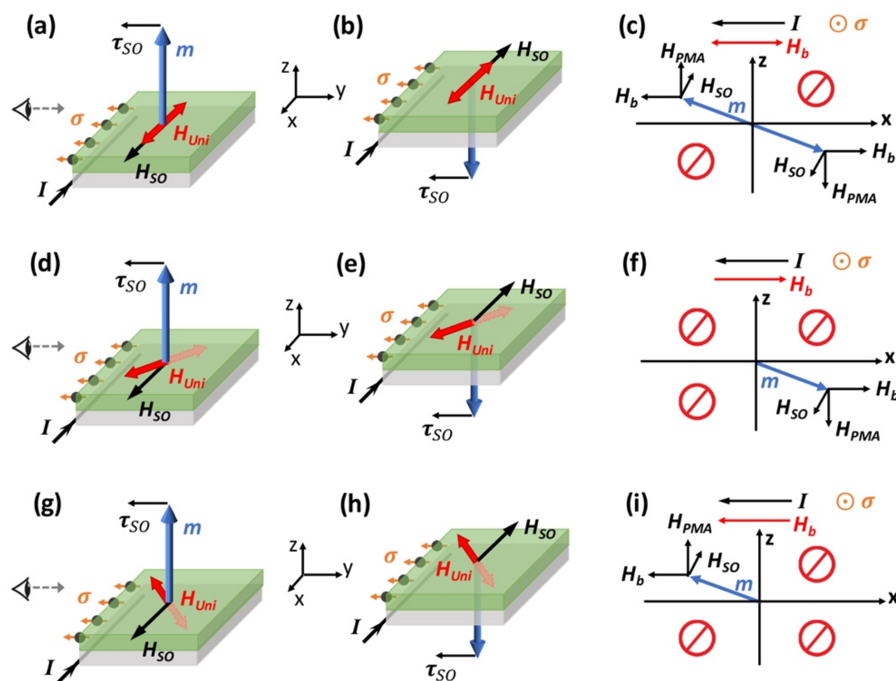

Figure 4-36. Symmetry analysis of strain-mediated SOT switching.

Figs. 4-36(a-c) show the symmetry analysis when the $\boldsymbol{H_{Uni}}$ is applied along the direction of the current *I*. In the beginning of the switching process, $\boldsymbol{\tau_{SO}}$ is the only driving torque. Due to the direction of $\boldsymbol{\tau_{SO}}$ relative to the $\boldsymbol{H_{Uni}}$, both directions/branches of $\boldsymbol{H_{Uni}}$ are equally effective. Therefore, applying $\boldsymbol{H_{Uni}}$ along the direction of current is equivalent to applying a bidirectional external bias field $\boldsymbol{H_b}$ along the current. As shown in Fig. 4-36(c), this results in two magnetic stable states in the second and the fourth quadrants in the *x-z* plane. Specifically, the branch of $\boldsymbol{H_{Uni}}$ that is parallel to the SOT current prefers an end-state canted 'up', while the branch of $\boldsymbol{H_{Uni}}$ that is anti-parallel to the SOT current prefers an opposite end-state, i.e. canted 'down'. The dependence of the switching direction on the external field direction agrees with experimental results shown in previous research[170], where opposite switching behaviors were observed

when using Pt as the heavy metal. Note Pt is known to exhibit the opposite SOT switching behavior in contrast to Ta used in our simulation[51]. In conclusion, when the uniaxial field is applied along the SOT current direction, the symmetry is not broken, and deterministic switching is not produced.

Figs. 4-36(d-f) show the symmetry analysis when $\boldsymbol{H_{Uni}}$ is applied 45° clockwise relative to current *I* in the *x-y* plane. One can easily recognize the configurations in Figs. 4-36(d) and (e) are the same as Fig. 4-34(a), where −0.5 V voltage is applied to the PZT top electrodes. The spin-orbit torque $\boldsymbol{\tau_{SO}}$ helps 'push' the magnetization towards a specific hemisphere in the beginning of the switching, and keeps the magnetization in that hemisphere during the following switching process. Therefore, the $\boldsymbol{H_{uni}}$ branch that lies in that hemisphere becomes effective. It turns out that the spin-orbit torque always pushes the magnetization into the same hemisphere regardless of the initial magnetic state as shown in Figs. 4-36(d) and (e). More specifically, because $\boldsymbol{\tau_{SO}}$ is along positive +*x* axis in both Figs. 4-36(d) and (e), the $\boldsymbol{H_{Uni}}$ branch with positive *x* component is effective. The effective branch of $\boldsymbol{H_{Uni}}$ is shown in red, while the dummy branch of $\boldsymbol{H_{Uni}}$ is shown in light pink. Note the field component that is perpendicular to the SOT current does not contribute to the symmetry breaking. Because the projection of $\boldsymbol{H_{Uni}}$ onto the SOT current is anti-parallel to the current, it is equivalent to applying an external bias field anti-parallel to the current, as shown in Fig. 4-36(f). Therefore, the symmetry is broken and only a down-canted state in the fourth quadrant is allowed, while the states in other quadrants are unstable/prohibited. This agrees with the simulation results presented in Fig. 4-34(b), which showed that final states are always down-canted regardless of initial states.

Figs. 4-36(g-i) show the symmetry analysis when $\boldsymbol{H_{Uni}}$ is applied 45° counter-clockwise relative to the current *I* in *x-y* plane. This configuration is the same as in Fig. 4-34(c), where +0.5 V voltage is applied to the PZT top electrodes. Similar to previous situation shown in Figs. 4-36(c-e), only one branch of $\boldsymbol{H_{Uni}}$ is effective during the switching process depending on the direction of $\boldsymbol{\tau_{SO}}$. However, the projection of the effective $\boldsymbol{H_{Uni}}$ onto the SOT current is now parallel to the current. Therefore, the effective $\boldsymbol{H_{Uni}}$ is equivalent to applying an external bias field parallel to the current, as shown in Fig. 4-36(i). The symmetry is also broken and the up-canted state is selected. This agrees with the simulation results presented in Fig. 4-34(d), i.e., final states are always up-canted regardless of initial states. In complement to the symmetry analysis presented in Fig. 4-36, the mirror symmetry analysis is provided in Appendix and mathematical derivations using divergence arguments is provided in Note 5 in Section 4.5.5.

4.5.4 Memory device design

Based on the strain-mediated SOT switching mechanism demonstrated above, we are able to design a magnetic memory system. Fig. 4-37 shows the proposed Magnetoelastic Spin-Orbit Torque Random Accessed Memory (MeSOT-RAM). The previous simulated structure is a representative one-bit memory example of the presented array architecture. Fig. 4-37(a) illustrates a representative 2 × 2 memory array architecture. Each memory bit has a perpendicular magnetic tunnel junction (pMTJ) stack whose free layer and reference layer are both CoFeB with PMA. As a result, the memory device has relatively small footprint hence high storage capacity. Random access is feasible because for certain choices of applied current/voltage, neither voltage nor current is sufficient to switch the pMTJ by itself.

Compared to normal SOT-RAM[186], [187], although the MeSOT-RAM requires an extra terminal to actuate the PZT, the removal of the transistor for each pMTJ for random access will largely reduce the device size. Therefore, the overall footprint is expected to be smaller than normal SOT-RAM. All bits are connected in rows by bitlines (BL) and in columns by platelines (PL), and the BL/PL are designed to tilt from each other. Fig. 4-37(b) shows the suggested materials in the MeSOT-RAM. Writing a bit requires concurrently applying voltage/current to the PL/BL, respectively. Applying +0.5V/−0.5V and a SOT current results in the magnetization of free layer switching deterministically up/down, respectively (i.e., writing '1' or '0'). Readout from this design is achieved by applying voltage across the wordline (WL) and BL and measuring the pMTJ's magnetoresistance, similar to reading in conventional MRAMs. High TMR readout ratio is promised because the symmetry-breaking by magnetoelastic anisotropy is in-situ controllable. In addition, the separate writing and reading pathways provide relatively high endurance and low write error rate.

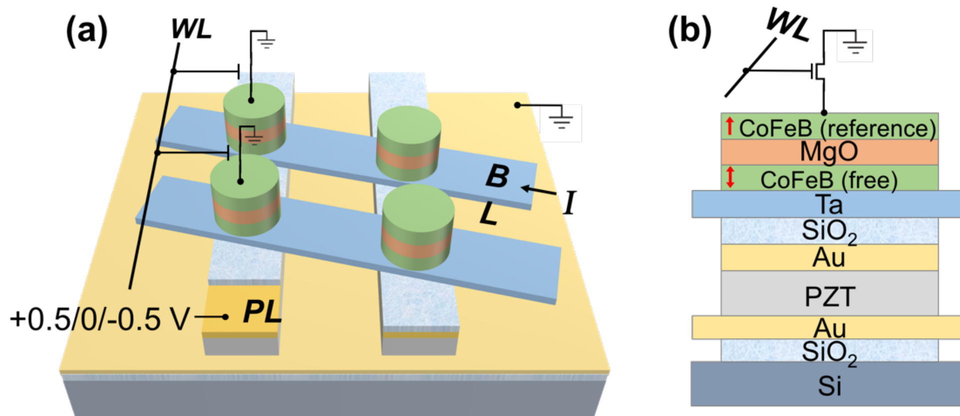

Figure 4-37. Schematics of MeSOT-RAM based on strain-mediated SOT switching mechanism.

4.5.5 Supplemental information

Note 1. Comparison of the finite element model and the macrospin model

Figure 4-38 compares the simulation results from finite element model and macrospin model for the structure shown in Fig. 4-33(a). The two simulations have same inputs: strain $\varepsilon_{yy} = 900\ \mu\varepsilon$ and $\varepsilon_{xx} = -700\ \mu\varepsilon$, current density 5×10^7 A/cm^2, and angle θ = 45°, θ is defined in Fig. 4-38(a). The shadowed region (t = 0 ~ 2 ns) represents the time in which the strain and current are applied. In this region, the two models produce very similar magnetization reorientation results. The main reason for this agreement is the magnetoelastic field $\boldsymbol{H}_{ME}$ dominates to orientation and both models have the same form for $\boldsymbol{H}_{ME}$. However, after the strain and current are removed (2 ~ 12ns period), the two lines become slightly different. This difference is associated with the internal rise in exchange anisotropy (due to slight variations in **m**) which the finite element model considers but is neglected in the macrospin model. Regardless, Fig. 4-38 shows the macrospin model is sufficiently accurate to simulate the strain-mediated SOT switching.

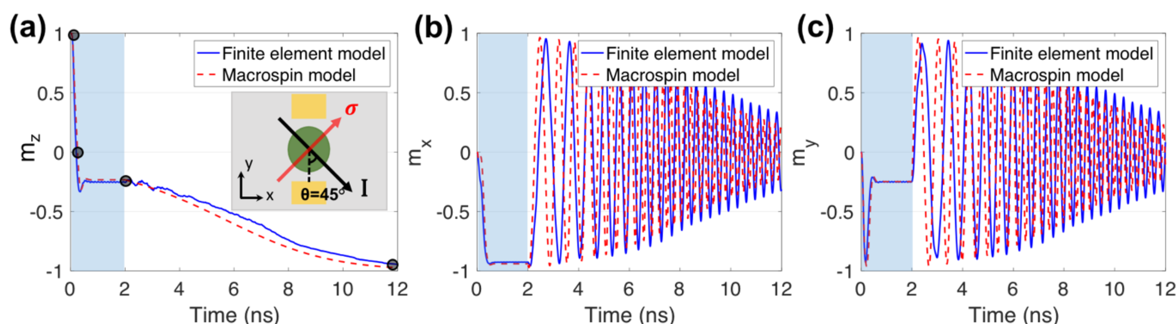

Figure 4-38. Simulation results of finite element model and macrospin model for the same structure shown in Fig. 4-33(a). (a)(b)(c) show the plot for m_z, m_x, m_y values, respectively.

Figure 4-39 presents the vector diagrams of the magnetization distribution at important time points t = 0, 0.2, 2, and 12 ns, which correspond to the highlighted points in Fig. 4-38(a), for both finite element model and macrospin model. It can be seen that both models predict similar results for selected time points. In Fig. 4-39(a) and (b), the arrows represent the in-plane magnetization amplitude and direction, while the colors represent the perpendicular magnetization m_z.

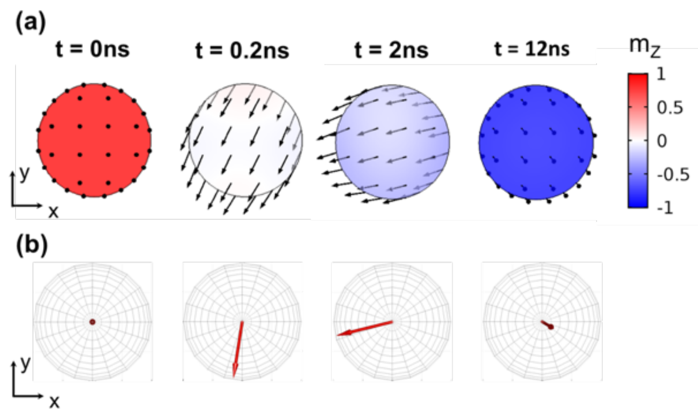

Figure 4-39. Vector diagram of finite element model and macrospin model.

Note 2. Impact of initial states

Figure 4-40 shows macrospin model results for different initial magnetic states. For all cases, a voltage of ±0.5V and a current density 5×10^7 A/cm^2 is applied for the geometry shown in Fig. 4-33(a). Different relative angles θ = 30°, 45°, 60° are compared. The initial state m_z is varied from −0.9 to +0.9. As shown in Fig. 4-40(a)(c)(e), the final state for +0.5V applied voltage is always canting upward regardless of the initial states. And Fig. 4-40(b)(d)(f) indicates that the final state for −0.5V applied voltage is always canting downward regardless of the initial states.

In summary, the initial state has no impact on the final state. This is in complementary to Fig. 4-34 to prove that the final state is not dependent on the initial state.

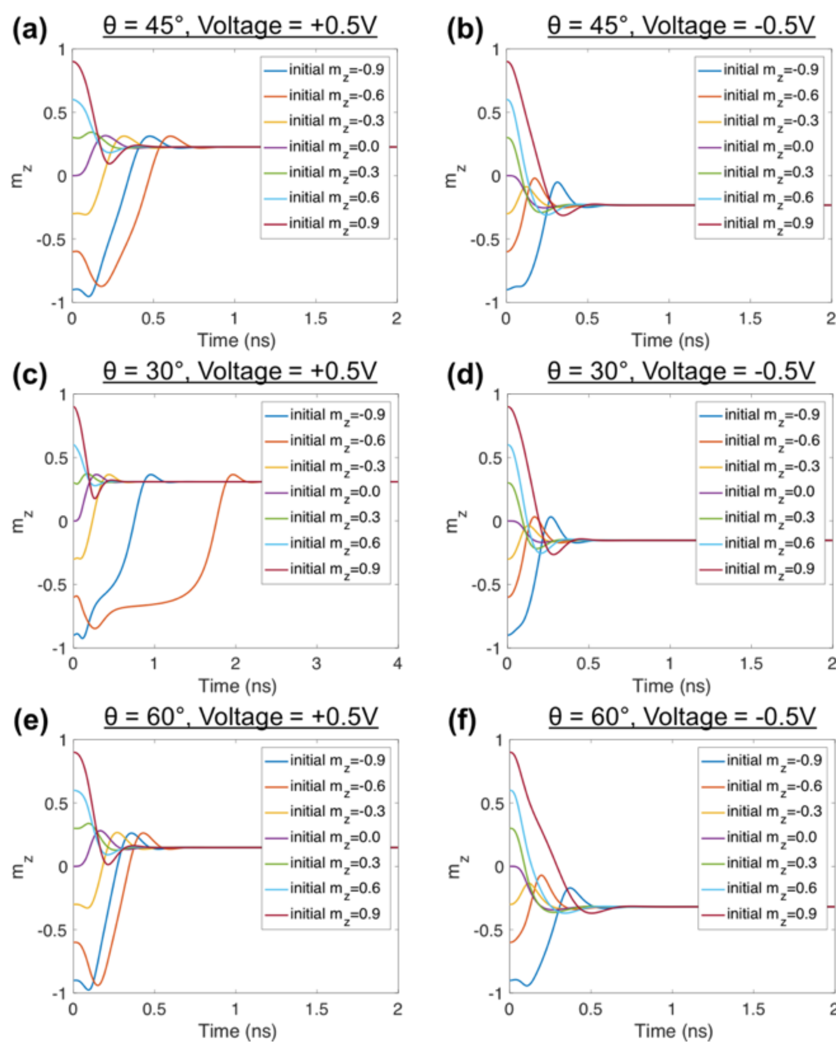

Figure 4-40. Temporal change of volume-averaged perpendicular magnetization m_z for different initial states and different relative angles under +0.5V and −0.5V applied voltages using the macrospin model.

Note 3. Switching speed

Figure 4-41 shows macrospin model results for the perpendicular component of magnetization m_z is plotted as a function of time. The simulated structure is shown in Fig. 4-

33(a). Each subplot in Fig. 4-41 has a different biaxial strain level (shown in the plot legends), while the current density is varied from 4 × 10^7 A/cm^2 to 1 × 10^8 A/cm^2 in each subplot. The dashed vertical lines in Fig. 4-41 (a)-(d) indicate the fastest switching case in each case studied. In every case, the fastest switching speed occurs when the applied current reaches the maximum value of 1 × 10^8 A/cm^2. As can be seen, increasing strain does not increase switching speed, but it does increase the amplitude of the switching, i.e. the amplitude of $|m_z|$ at t = 1 ns. The fastest switching speed of the strain-mediated SOT switching method is ~0.1 ns corresponding to an optimistic writing speed of ~10 GHz.

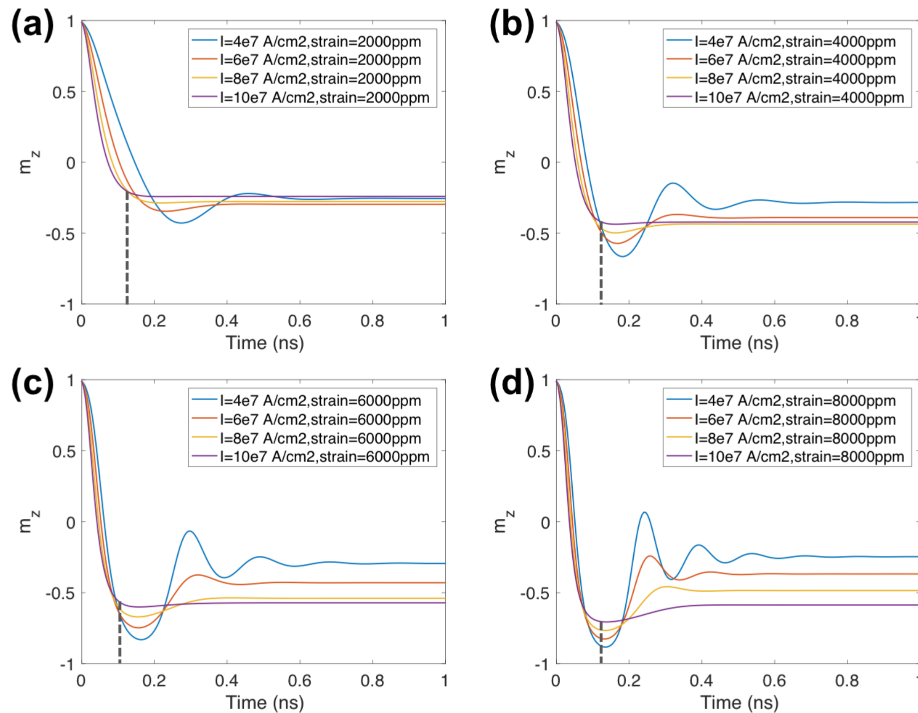

Figure 4-41. Macrospin results of varying current and voltage for fixed angle θ = 45°. The dashed vertical lines indicate the fastest switching case for each plot.

Note 4. Mirror symmetry analysis of symmetry breaking

Figure 4-42 provides an explanation of the mirror symmetry rules used in the manuscript. As shown in Fig. 4-42(a), for ordinary vectors such as velocity, any component that is perpendicular to the mirror reverse their direction in the mirror reflection. However, any vector component parallel to the mirror remains in their original direction after the mirror reflection. The opposite is true for a pseudovector (or axial vector) such as magnetic field or magnetization. As shown in Fig. 4-42(b), for these pseudovectors, any component perpendicular to the mirror remains in its original direction in the mirror reflection [54]. However, any pseudovector component parallel to the mirror reverses its direction in the mirror reflection. Mirror symmetry analysis is a useful tool to examine symmetry-breaking in SOT perpendicular switching, as presented in some previous publications [21,14].

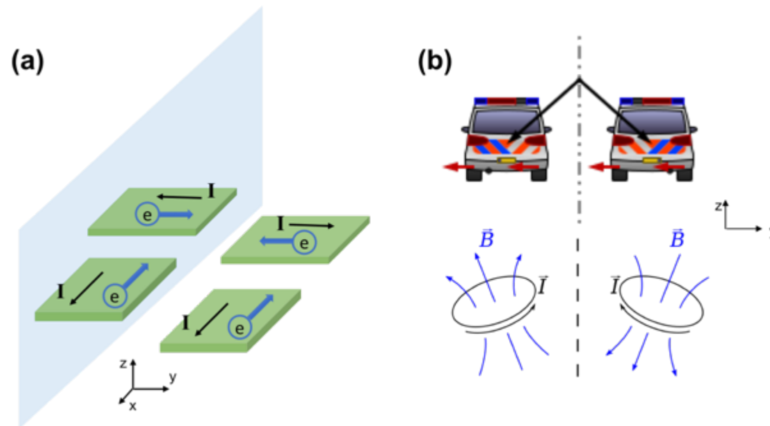

Figure 4-42. Mirror symmetry rules for (a) ordinary vector and (b) pseudovector/axial vector.

Figure 4-43 shows the mirror symmetry analysis for two situations: (a) applying pure SOT current; (b) applying SOT current combined with a magnetic bias field. Both scenarios consider a ferromagnetic layer with PMA (the green sheet). The blue parallelograms represent the mirror in the *x-z* plane. The SOT current is applied along the –*x* axis, therefore the induced electron polarization is along –*y* axis, i.e. $\hat{\boldsymbol{\sigma}} = -\hat{y}$. Therefore, the damping-like SOT field is $\boldsymbol{H}_{SOT-DL} \propto$

$\boldsymbol{m}\times\hat{\boldsymbol{\sigma}} = \hat{y}\times\boldsymbol{m}$. The current remains in its original direction in the mirror image because the velocity of an electron is ordinary vector. There are two pseudovectors in Fig. 4-43 (a): magnetization and the SOT field. Since both are parallel to the mirror plane, the two pseudovectors reverse their directions in the mirror image. The inputs in the real world and its mirror image remains the same, with both having the SOT current applied along –*x* axis. However, the two configurations produce opposite magnetization states. In other words, both "up" and "down" magnetization configurations exist with SOT current applied along –*x* axis. There is no preferable perpendicular direction, and the symmetry remains unbroken. Therefore, non-deterministic switching occurs.

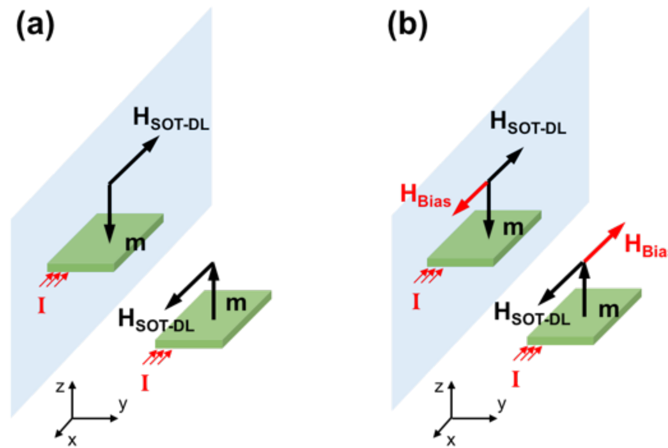

Figure 4-43. Mirror symmetry analysis with respect to *x-z* plane. (a) Pure SOT system. (b) Adding magnetic bias field to SOT system breaks in-plane symmetry.

In Fig. 4-43 (b), a bias field along –*x* axis is added to the system. Since the bias field is also an axial vector and is parallel to the mirror plane, it reverses its direction in the mirror image. The two configurations in the real world and mirror image now have different inputs: the currents are the same but the bias fields are in opposite directions. The bias field added to the SOT system breaks the symmetry. A unique m_z results based on the $\boldsymbol{H}_{Bias}$ and current direction

applied. In Fig. 4-43 (b), the bias field along *–x* axis prefers "up" while the bias field along *+x* axis prefers "down". This produces deterministic switching.

Note 5. Mathematical explanation for deterministic switching

As a complementary explanation to mirror symmetry analysis, we provide a mathematical approach to examine the stochastic nature of the switching process for different physical inputs (e.g., current and strain). The precessional magnetic dynamics are governed by the Landau-Lifshitz-Gilbert (LLG) equation with SOT terms [14,34,35]:

$$\frac{\partial \boldsymbol{m}}{\partial t} = -\mu_0\gamma\left(\boldsymbol{m}\times\boldsymbol{H}_{eff}\right) + \alpha\left(\boldsymbol{m}\times\frac{\partial \boldsymbol{m}}{\partial t}\right) - \frac{\gamma\hbar}{2e}\frac{J_C}{M_S t_F}\xi_{DL}\boldsymbol{m}\times(\boldsymbol{m}\times\widehat{\boldsymbol{\sigma}}) \qquad \text{Eq. 4-28}$$

As shown previously, the field-like torque does not influence the symmetry-breaking. Therefore, in this section, the field-like torque is neglected for simplification. The stable magnetization state is determined by solving the LLG equation with $\boldsymbol{\tau}_{tot} = 0$, then the equilibrium equation becomes:

$$\boldsymbol{\tau}_{tot} = 0 = -\mu_0\gamma\left(\boldsymbol{m}\times\boldsymbol{H}_{eff}\right) - \frac{\gamma\hbar}{2e}\frac{J_C}{M_S t_F}\xi_{DL}\boldsymbol{m}\times(\boldsymbol{m}\times\widehat{\boldsymbol{\sigma}}) \qquad \text{Eq. 4-29}$$

$\boldsymbol{H}_{eff}$ is the effective field and there are two dominating terms: $\boldsymbol{H}_{eff} \approx \boldsymbol{H}_{PMA} + \boldsymbol{H}_{ME}$, where $\boldsymbol{H}_{PMA}$ is the effective PMA field, and $\boldsymbol{H}_{ME}$ is the magnetoelastic field. The PMA field can be generalized using the following approach considering a phenomenological PMA coefficient [30,31]:

$$\boldsymbol{H}_{PMA} = -\frac{2}{\mu_0 M_S} K_{PMA} m_z \hat{\boldsymbol{z}} \qquad \text{Eq. 4-30}$$

For a certain magnetic materials and geometries, the PMA coefficient is a constant. For the positive magnetostrictive material CoFeB, both B_1 and B_2 are negative constants. Consider a simple case: $\varepsilon_{yy} > 0$, all other strains are zeros. Then the magnetoelastic field can be simplified as:

$$\boldsymbol{H}_{ME} = -\frac{2}{\mu_0 M_S} B_1 \varepsilon_{yy} m_y \hat{\boldsymbol{y}} \qquad \text{Eq. 4-31}$$

Plugging Eq. 4-30 and Eq. 4-31 into Eq. S4-29, we get the reduced equilibrium equation:

$$\boldsymbol{\tau}_{tot} = 0 = -\boldsymbol{m} \times (\mathrm{A} m_z \hat{\boldsymbol{z}} + \mathrm{B} m_y \hat{\boldsymbol{y}}) - \mathrm{C}[\boldsymbol{m} \times (\boldsymbol{m} \times \hat{\boldsymbol{\sigma}})] \qquad \text{Eq. 4-32}$$

where $A = -\frac{2\gamma}{M_S} K_{PMA}$, $B = -\frac{2\gamma}{M_S} B_1 \varepsilon_{yy}$, $C = \frac{\gamma\hbar}{2e}\frac{J_C}{M_S t_F}\xi_{DL}$ are three positive constants related to PMA, strain and current density, respectively. Consider a general in-plane polarization $\hat{\boldsymbol{\sigma}} = (\sigma_1, \sigma_2, 0)$. The equilibrium equation Eq. 4-32 can be expressed as:

$$\boldsymbol{\tau}_{tot} = \begin{pmatrix} -(A-B) m_y m_z + C(m_y^2 \sigma_1 + m_z^2 \sigma_1 - m_x m_y \sigma_2) \\ A m_x m_z + C(m_x^2 \sigma_2 + m_z^2 \sigma_2 - m_x m_y \sigma_1) \\ -B m_x m_y - C(m_x \sigma_1 + m_y \sigma_2) m_z \end{pmatrix} = \begin{pmatrix} 0 \\ 0 \\ 0 \end{pmatrix} \qquad \text{Eq. 4-33}$$

Under the constrain that:

$$m_1^2 + m_2^2 + m_3^2 = 1 \qquad \text{Eq. 4-34}$$

The magnetization state $\boldsymbol{m} = (m_x, m_y, m_z)$ represents the unknown to be solved. The governing equations Eq. 4-33 and Eq. 4-34 are homogeneous, which means if (m_{10}, m_{20}, m_{30}) is a solution,

then $(-m_{10}, -m_{20}, -m_{30})$ is also a solution. In other words, there can be more than one solution to the equilibrium equation. However, not every solution represents a stable magnetization state. As shown in Fig. 4-44, the equilibrium state can be classified as either stable or unstable. The two types can be differentiated by checking the divergence of total torque $\nabla \cdot \boldsymbol{\tau}_{tot}$. As shown in Fig. 4-44 (a) and (b), $\nabla \cdot \boldsymbol{\tau}_{tot} < 0$ and $\nabla \cdot \boldsymbol{\tau}_{tot} > 0$ indicate stable equilibrium state and unstable equilibrium state, respectively. The divergence for Eq. 4-33 is:

$$\nabla \cdot \boldsymbol{\tau}_{tot} = -2C(m_x\sigma_1 + m_y\sigma_2) \qquad \text{Eq. 4-35}$$

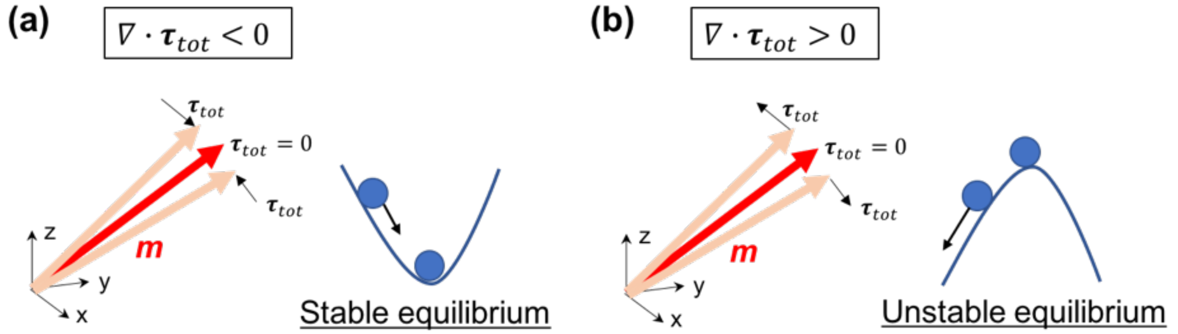

Figure 4-44. Illustration of divergence of total torque in stable and unstable equilibriums.

Case 1: consider only a SOT current is applied. For this case the equilibrium equation becomes:

$$\boldsymbol{\tau}_{tot} = \begin{pmatrix} -Am_y m_z + C(m_y^2\sigma_1 + m_z^2\sigma_1 - m_x m_y \sigma_2) \\ Am_x m_z + C(m_x^2\sigma_2 + m_z^2\sigma_2 - m_x m_y \sigma_1) \\ -C(m_x\sigma_1 + m_y\sigma_2)m_z \end{pmatrix} = \begin{pmatrix} 0 \\ 0 \\ 0 \end{pmatrix} \qquad \text{Eq. 4-36}$$

(i) If $m_z = 0$, one can solve for m_x and m_y by:

$$\begin{cases} m_y^2\sigma_1 - m_x m_y \sigma_2 = 0 \\ m_x^2\sigma_2 - m_x m_y \sigma_1 = 0 \\ m_x^2 + m_y^2 = 1 \\ \sigma_1^2 + \sigma_2^2 = 1 \end{cases} \qquad \text{Eq. 4-37}$$

The solution is simply $m_x = \sigma_1, m_y = \sigma_2$, or $m_x = -\sigma_1, m_y = -\sigma_2$, i.e. the magnetization follows the direction of electron polarization.

(ii) If $m_z \neq 0$, then there is a paired solution of pointing either up or down. Also from the 3rd line of Eq. 4-36, we get:

$$m_x\sigma_1 + m_y\sigma_2 = 0 \qquad \text{Eq. 4-38}$$

Therefore, the divergence of total torque is always zero:

$$\nabla \cdot \boldsymbol{\tau}_{tot} = -2C\left(m_x\sigma_1 + m_y\sigma_2\right) = 0 \qquad \text{Eq. 4-39}$$

This means that the two states (up or down) in each paired solution are both neutral equilibrium states. In conclusion, if SOT is the only input to the system, either the magnetization is forced to follow the electron polarization in-plane, or there are symmetric neutral equilibrium states out-of-plane, and deterministic switching is not produced.

Case 2: consider the current is applied along –*y* axis, which is parallel to the strain. The electron polarization has to be perpendicular to the strain (i.e., *x* axis), so let $\hat{\boldsymbol{\sigma}} = (1,0,0)$. The equilibrium equation becomes:

$$\boldsymbol{\tau}_{tot} = \begin{pmatrix} -(A-B)m_y m_z + C(m_y^2 + m_z^2) \\ A m_x m_z - C m_x m_y \\ -B m_x m_y - C m_x m_z \end{pmatrix} = \begin{pmatrix} 0 \\ 0 \\ 0 \end{pmatrix} \qquad \text{Eq. 4-40}$$

(i) If $m_x \neq 0$, then a closed form solution can be obtained by solving the 2nd and 3rd line of Eq. 4-40. The solution is $\boldsymbol{m}$ = (±1,0,0) with magnetization in-plane along the x axis.

(ii) If $m_x = 0$, symmetric solutions arise to Eq. 4-40. However, the divergence of total torque is always zero as:

$$\nabla \cdot \boldsymbol{\tau}_{tot} = -2Cm_x = 0 \qquad \text{Eq. 4-41}$$

This means the out-of-plane solution, if there is any, is always a neutral equilibrium state. In conclusion, if the system has strain and current inputs that are parallel to each other, then either magnetization follows the electron polarization in-plane, or there are symmetric equilibrium states out-of-plane. Therefore, deterministic switching is not produced.

Case 3: consider the situation when the current is canted from the strain. For example, let $\hat{\boldsymbol{\sigma}} = (1,1,0)/\sqrt{2}$. The equilibrium equation becomes:

$$\boldsymbol{\tau}_{tot} = \begin{pmatrix} -(A-B)m_y m_z + C(m_y^2 + m_z^2 - m_x m_y)/\sqrt{2} \\ A m_x m_z + C(m_x^2 + m_z^2 - m_x m_y)/\sqrt{2} \\ -B m_x m_y - C(m_x + m_y) m_z/\sqrt{2} \end{pmatrix} = \begin{pmatrix} 0 \\ 0 \\ 0 \end{pmatrix} \qquad \text{Eq. 4-42}$$

The divergence of the total torque is:

$$\nabla \cdot \boldsymbol{\tau}_{tot} = -\sqrt{2}C(m_x + m_y) \qquad \text{Eq. 4-43}$$

Obviously there is an absence of in-plane solutions because: if one let $m_z = 0$, then there is only trivial solution $\boldsymbol{m}$ = (0,0,0) to Eq. 4-42. However, this does not satisfy the uniformity equation 4-34. Therefore, no in-plane solution is possible for Eq. 4-42. In other words, the equilibrium state is always out-of-plane. Inferred from Eq. 4-43, in the paired solutions $\pm(m_{10}, m_{20}, m_{30})$, there is always one stable state and one unstable state, i.e. a specific direction (either up or down) is stable. Therefore, deterministic switching is produced.

Using this method, one can also arrive at the conclusion that applying bias field leads to deterministic switching. In conclusion, checking the divergence of the total torque is an equivalent method to mirror symmetry analysis, and both methods predict whether deterministic switching is possible.

Note 6. Criterion for switching phase diagrams

As shown in Fig. 4-45, there are four types of magnetization state after application of voltage/current. A criterion is provided to differentiate those behaviors in the macrospin code. The magnetization is initialized as 'up' (i.e., $m_z = +1$), then the temporal evolution of magnetization is performed for each combination of applied current, strain and angle between them. The perpendicular magnetization m_z after 2 ns voltage/current application is investigated. There are four types of possible magnetization states: (I) magnetization reverses its direction and stabilizes in the opposite phase; (II) magnetization experiences 90°switching and stabilizes in-plane; (III) magnetization experiences less than 90°switching and stabilizes in the original direction; or (IV) magnetization continuously oscillates across in-plane without stabilizing in any

preferred direction. If the variation of m_z between t = 2 ~ 3 ns is less than 5%, then the magnetization at 2ns is considered to be stabilized. Under the stabilized state, $m_z > 0.05$, $|m_z| < 0.05$ and $m_z < -0.05$ corresponds to type I, II, and III respectively. If the variation of m_z is greater than 5%, and m_z keeps changing its sign in the last 1ns, then it is classified as type IV. It is worth noting that the existence of type III does not conflict with the conclusion in Note 5 that in-plane equilibrium states do not exist for this combination strain/current. Mathematically there is absence of an exact "in-plane" solution (i.e., $m_z = 0$), however, any solution with $-0.05 < m_z < 0.05$ represents an absence of preferable perpendicular directions under thermal fluctuation. Therefore, we classify those solutions as "in-plane" solution.

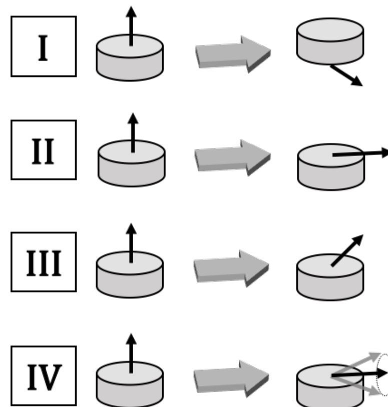

Figure 4-45. Four types of magnetization state after application of strain/current.

4.6 Chapter summary

In conclusion, a finite element model and a macrospin model are used to simulate hybrid SOT + strain control of a nanomagnetic structure with PMA. More specifically three interesting systems/applications are investigated:

(1) A deterministic but non-directional switching is achieved when the applied current is perpendicular to the uniaxial strain. With the same applied current and strain, the magnetization can switch from 'up' to 'down' and 'down' to 'up', depending on the initial state. The switching direction can be clockwise or counterclockwise depending on the current direction.

(2) A new spin-torque nano-oscillator is proposed using the hybrid SOT + strain control. The spin-orbit torque can cancel with the Gilbert damping and the total effective field (strain + PMA) is the driving field and keeps the magnetization oscillating steadily. The oscillation amplitude and frequency can be tuned within a large range by tuning the applied current and strain.

(3) A deterministic and directional perpendicular switching is achieved when the applied current has a skew angle with the uniaxial strain. The final magnetic state depends on the polarity of the applied voltage, but does not depend on the initial state. This symmetry-breaking mechanism is universally applicable to other uniaxial anisotropy. Using the uniaxial anisotropy to break the in-plane symmetry may open a new genre of field-free deterministic OOP switching in SOT devices and pave the way for next-generation non-volatile memory.

Chapter 5. Conclusion and outlook

In this thesis, we provide a comprehensive study of strain-mediated multiferroic control of perpendicular magnetization, which pave the way for using the strain-mediated multiferroics for non-volatile memory or other applications.

In Chapter 2, three multiferroic systems are simulated. First, strain-mediated perpendicular switching single magnetic nanodot is simulated and compared for CoFeB and Terfenol-D materials. Coherent and incoherent switching behaviors are observed in both CoFeB and Terfenol nanodots, with incoherent flipping associated with larger or faster applied switching voltages. The energy to flip a Terfenol-D memory element is an ultralow 22aJ, which proves the energy efficiency of the strain-mediated multiferroics. Second, the Bennett clocking process in an array of dipole coupled magnetic nanodots is simulated and compared for Ni, CoFeB and Terfenol-D material systems. The results show that the magnetic memory and logic can be implemented in the same device using strain-mediated multiferroics, which will be the crucial element for next generation in-memory computing devices. Third, we simulate a single magnetic nanodot with AC voltage input. It is found that when the frequency of the AC voltage input to the piezoelectric substrate matches the ferromagnetic resonance (FMR) of the magnetic nanodot, steady magnetic oscillation is achieved. Because the FMR is dependent on the voltage amplitude, the oscillation frequency can be easily tunable by tuning the amplitude of the AC voltage. With the thorough parametric study, we can design a purely mechanically driven magnetic nano-oscillator with steady perpendicular magnetic oscillation and broad frequency range.

In Chapter 3, we go through some of our experimental efforts in using strain-mediated multiferroics to control perpendicular magnetization. No obvious perpendicular magnetization change is observed in the device built on PMN-PT substrate. It is suggested that PMN-PT is not a good candidate for controlling perpendicular magnetization due to relatively small strain generated at the maximum applied field and competing in-plane and out-of-plane strain effects. In contrast, clear evidence of perpendicular magnetization modulation is observed in the device on PZT thin film. The perpendicular coercive field Hc of the CoFeB pillar can be modulated by about 20 Oe when 6 V is applied to the 200 nm thick PZT substrate. Theoretical calculation and micromagnetic simulation are done to confirm the Hc shift originates from the magnetoelastic energy due to the voltage induced strain. A simply optimization is performed and a new design is proposed in the end of the work, which has the potential to increase the Hc shift effect by 5 times.

In Chapter 4, we introduce a hybrid SOT + strain control mechanism. Various conditions are simulated with different combinations of the two inputs: SOT current and the voltage-induced strain. Interesting phenomena are observed in the simulation and are explained theoretically. Most importantly, a new deterministic and directional perpendicular magnetization switching mechanism is proposed using the hybrid strain-mediated SOT switching mechanism. Previous research has shown that an external bias field or other kinds of *asymmetric* anisotropies are needed to break the symmetry and allow deterministic perpendicular switching in SOT devices. Our work demonstrates for the first time that a *symmetric* anisotropy (i.e., strain-mediated magnetoelastic anisotropy) can also, surprisingly and unobviously, break symmetry in SOT devices in a specific design. This discovery is supported by both simulation results and theoretical interpretations from three different aspects (i.e., switching symmetry analysis, mirror

symmetry analysis, and mathematical interpretation). As a side note, this is also applicable to using other symmetric anisotropies to break symmetry in SOT devices, which opens new possibilities for deterministic perpendicular magnetization control for memory applications.

In the future endeavor, it is worth to try the optimized device design on PZT thin film proposed in Chapter 3. It is likely to achieve pure strain mediated perpendicular switching if the piezoelectric property of the 1 um PZT is similar to the 200 nm PZT, and if the coercive field of the magnetic film can be decreased to be less than 100 Oe. There are also more opportunities in using strain in other hybrid control systems (e.g., strain + SOT + dipole interaction) and in the devices beyond memory applications.

In closing, extensive efforts have been devoted to investigating the strain-mediated multiferroic control of perpendicular magnetization. However, there are still many obstacles to overcome before a workable memory device can be built based on strain-mediated multiferroics. In this thesis, I have tried to provide details in all the work beyond the scope of publications. I hope the readers could learn something extra than just reading through my journal publications, although it is said that no one except the author will read the dissertation. Should anyone have any questions, I am sure he/she is smart enough to find my contact information online and I am more than happy to address those confusions and help the successors.

References

[1] P. Hong, “Supplying the World’s Thirst for Data Storage,” Nov-2017. [Online]. Available: https://rctom.hbs.org/submission/supplying-the-worlds-thirst-for-data-storage/#. [Accessed: 24-Oct-2018].

[2] H. Lee, A. Lee, F. Ebrahimi, P. K. Amiri, and K. L. Wang, “Array-Level Analysis of Magneto-Electric Random-Access Memory for High-Performance Embedded Applications,” *IEEE Magn. Lett.*, vol. 8, 2017.

[3] “Write-limited sorts and joins for persistent memory.” [Online]. Available: https://blog.acolyer.org/2016/09/30/write-limited-sorts-and-joins-for-persistent-memory/. [Accessed: 06-Dec-2018].

[4] T. Perez, “Non-Volatile Memory: Emerging Technologies And Their Impacts on Memory Systems,” 2010.

[5] “Patent analysis for non-volatile memories,” 2014. [Online]. Available: https://www.electronicspecifier.com/around-the-industry/patent-analysis-for-non-volatile-memories. [Accessed: 24-Oct-2018].

[6] W. Zhao and G. Prenat, *Spintronics-based Computing*. 2015.

[7] W. H. Choi *et al.*, “A Magnetic Tunnel Junction based True Random Number Generator with conditional perturb and real-time output probability tracking,” *Int. Electron Devices Meet.*, vol. Februrary, p. 12.5.1-12.5.4, 2015.

[8] S. Sharmin, A. Jaiswal, and K. Roy, “Modeling and Design Space Exploration for Bit-Cells Based on Voltage-Assisted Switching of Magnetic Tunnel Junctions,” *IEEE Trans. Electron Devices*, vol. 63, no. 9, pp. 3493–3500, 2016.

[9] "MRAM (SOT-based memory)." [Online]. Available: http://nanospin.kaist.ac.kr/spin-orbit-torque-4/?ckattempt=1. [Accessed: 24-Oct-2018].

[10] Chris Edwards, "Switch to orbit mode boosts MRAM on 300mm wafers," 2018. [Online]. Available: http://www.techdesignforums.com/blog/2018/06/18/imec-sot-mram-300mm-vlsi/. [Accessed: 24-Oct-2018].

[11] S. Wang, H. Lee, F. Ebrahimi, P. Khalili Amiri, K. L. Wang, and P. Gupta, "Comparative Evaluation of Spin-Transfer-Torque and Magnetoelectric Random Access Memory," *IEEE J. Emerg. Sel. Top. Circuits Syst.*, vol. 6, no. 2, pp. 134–145, 2016.

[12] H. Palneedi, V. Annapureddy, S. Priya, and J. Ryu, "Status and Perspectives of Multiferroic Magnetoelectric Composite Materials and Applications," *Actuators*, vol. 5, no. 1, p. 9, 2016.

[13] J. Wang *et al.*, "Epitaxial BiFeO3 Multiferroic Thin Film Heterostructures," *Science (80-.).*, vol. 299, no. March, pp. 1719–1722, 2003.

[14] J. Ma, J. Hu, Z. Li, and C. W. Nan, "Recent progress in multiferroic magnetoelectric composites: From bulk to thin films," *Adv. Mater.*, vol. 23, no. 9, pp. 1062–1087, 2011.

[15] J. M. Hu *et al.*, "Purely electric-field-driven perpendicular magnetization reversal," *Nano Lett.*, vol. 15, pp. 616–622, 2015.

[16] A. K. Biswas, S. Bandyopadhyay, and J. Atulasimha, "Energy-efficient magnetoelastic non-volatile memory," *Appl. Phys. Lett.*, vol. 104, p. 232403, 2014.

[17] K. Roy, S. Bandyopadhyay, and J. Atulasimha, "Hybrid spintronics and straintronics: A magnetic technology for ultra low energy computing and signal processing," *Appl. Phys. Lett.*, vol. 99, p. 63108, 2011.

[18] Z. Zhao *et al.*, "Giant voltage manipulation of MgO-based magnetic tunnel junctions via

localized anisotropic strain: A potential pathway to ultra-energy-efficient memory technology," *Appl. Phys. Lett.*, vol. 109, p. 92403, 2016.

[19] Q. Wang *et al.*, "Strain-mediated 180 switching in CoFeB and Terfenol-D nanodots with perpendicular magnetic anisotropy," *Appl. Phys. Lett.*, vol. 110, no. 10, p. 102903, 2017.

[20] K. L. Wang, J. G. Alzate, and P. Khalili Amiri, "Low-power non-volatile spintronic memory: STT-RAM and beyond," *J. Phys. D. Appl. Phys.*, vol. 46, no. 7, p. 74003, 2013.

[21] N. Nishimura *et al.*, "Magnetic tunnel junction device with perpendicular magnetization films for high-density magnetic random access memory," *J. Appl. Phys.*, vol. 91, no. 8, pp. 5246–5249, 2002.

[22] S. Ikeda *et al.*, "A perpendicular-anisotropy CoFeB-MgO magnetic tunnel junction.," *Nat. Mater.*, vol. 9, no. 9, pp. 721–724, 2010.

[23] W. Kim *et al.*, "Extended scalability of perpendicular STT-MRAM towards sub-20nm MTJ node," *Int. Electron Devices Meet.*, pp. 24–1, 2011.

[24] R. C. O'handley, *Modern magnetic materials*. Wiley, 2000.

[25] G. Di Fratta, "The Newtonian potential and the demagnetizing factors of the general ellipsoid," *Proc. R. Soc. A*, vol. 472, no. 2190, p. 20160197, 2016.

[26] Z. Xiao, R. Lo Conte, C. Chen, C. Liang, and A. Sepulveda, "Bi-directional coupling in strain-mediated multiferroic heterostructures with magnetic domains and domain wall motion," *Sci. Rep.*, vol. 8, no. 1, p. 5207, 2018.

[27] "Electron Beam Source for Electron Beam Deposition." [Online]. Available: https://www.jeol.co.jp/en/science/eb.html. [Accessed: 31-Oct-2018].

[28] "File:DCplasmaSputtering.jpg - Wikimedia Commons." [Online]. Available: https://commons.wikimedia.org/wiki/File:DCplasmaSputtering.jpg. [Accessed: 31-Oct-

2018].

[29] C. Wang and T. Suga, "Investigation of fluorine containing plasma activation for room-temperature bonding of Si-based materials," *Microelectron. Reliab.*, vol. 52, no. 2, pp. 347–351, 2012.

[30] Wikipedia contributors, "Magneto-optic Kerr effect," *Wikipedia, The Free Encyclopedia.* [Online]. Available: https://en.wikipedia.org/w/index.php?title=Magneto-optic_Kerr_effect&oldid=856350761. [Accessed: 03-Nov-2018].

[31] Wikipedia contributors, "Vibrating-sample magnetometer," *Wikipedia, The Free Encyclopedia.* [Online]. Available: https://en.wikipedia.org/w/index.php?title=Vibrating-sample_magnetometer&oldid=837065713. [Accessed: 03-Nov-2018].

[32] M. Gradhand *et al.*, "First-principle calculations of the Berry curvature of Bloch states for charge and spin transport of electrons," *J. Phys. Condens. Matter*, vol. 24, no. 21, p. 213202, 2012.

[33] "Ferroelectrics & Ferroelectric materials." [Online]. Available: http://www.globalsino.com/EM/page3544.html. [Accessed: 04-Nov-2018].

[34] M. G. Cain, J. Tesař, and M. van Veghel, *Characterisation of Ferroelectric Bulk Materials and Thin Films*. Springer Netherlands, 2014.

[35] Wikipedia contributors, "Strain gauge," *Wikipedia, The Free Encyclopedia.* [Online]. Available: https://en.wikipedia.org/w/index.php?title=Strain_gauge&oldid=854623915. [Accessed: 04-Nov-2018].

[36] J. Cui *et al.*, "A method to control magnetism in individual strain-mediated magnetoelectric islands," *Appl. Phys. Lett.*, vol. 103, no. 23, p. 232905, 2013.

[37] R. J. A. Steenwelle, "Characterization of piezo- and ferroelectric thin films by Scanning

Probe Techniques," *Master thesis, Univ. Twente*, 2007.

[38] D. Chiba, Y. Nakatani, F. Matsukura, and H. Ohno, "Simulation of magnetization switching by electric-field manipulation of magnetic anisotropy," *Appl. Phys. Lett.*, vol. 96, p. 192506, 2010.

[39] J. Atulasimha and S. Bandyopadhyay, "Bennett clocking of nanomagnetic logic using multiferroic single-domain nanomagnets," *Appl. Phys. Lett.*, vol. 97, no. 17, 2010.

[40] K. Roy, S. Bandyopadhyay, and J. Atulasimha, "Energy dissipation and switching delay in stress-induced switching of multiferroic nanomagnets in the presence of thermal fluctuations," *J. Appl. Phys.*, vol. 112, p. 23914, 2012.

[41] N. M. Aimon, J. Liao, and C. A. Ross, "Simulation of inhomogeneous magnetoelastic anisotropy in ferroelectric/ferromagnetic nanocomposites," *Appl. Phys. Lett.*, vol. 101, p. 232901, 2012.

[42] Y. Yahagi, B. Harteneck, S. Cabrini, and H. Schmidt, "Controlling nanomagnet magnetization dynamics via magnetoelastic coupling," *Phys. Rev. B - Condens. Matter Mater. Phys.*, vol. 90, p. 140405, 2014.

[43] I. Gilbert *et al.*, "Magnetic microscopy and simulation of strain-mediated control of magnetization in PMN-PT/Ni nanostructures," *Appl. Phys. Lett.*, vol. 109, no. 16, p. 162404, 2016.

[44] A. C. Chavez, W. Y. Sun, J. Atulasimha, K. L. Wang, and G. P. Carman, "Voltage induced artificial ferromagnetic-antiferromagnetic ordering in synthetic multiferroics," *J. Appl. Phys.*, vol. 122, p. 224102, 2017.

[45] C.-Y. Liang *et al.*, "Modeling of magnetoelastic nanostructures with a fully coupled mechanical-micromagnetic model.," *Nanotechnology*, vol. 25, no. 43, p. 435701, 2014.

[46] C. Y. Liang *et al.*, “Electrical control of a single magnetoelastic domain structure on a clamped piezoelectric thin film - Analysis,” *J. Appl. Phys.*, vol. 116, no. 12, p. 123909, 2014.

[47] A. Brataas, A. D. Kent, and H. Ohno, “Current-induced torques in magnetic materials.,” *Nat. Mater.*, vol. 11, no. 5, pp. 372–81, 2012.

[48] Z. Diao *et al.*, “Spin-transfer torque switching in magnetic tunnel junctions and spin-transfer torque random access memory,” *J. Phys. Condens. Matter*, vol. 19, no. 16, p. 165209, 2007.

[49] G. Yu *et al.*, “Switching of perpendicular magnetization by spin-orbit torques in the absence of external magnetic fields.,” *Nat. Nanotechnol.*, vol. 9, no. May, p. 548, 2014.

[50] S. Fukami, T. Anekawa, C. Zhang, and H. Ohno, “A spin–orbit torque switching scheme with collinear magnetic easy axis and current configuration,” *Nat. Nanotechnol.*, vol. 11, no. March, pp. 621–625, 2016.

[51] L. Liu, C.-F. Pai, Y. Li, H. W. Tseng, D. C. Ralph, and R. A. Buhrman, “Spin-Torque Switching with the Giant Spin Hall Effect of Tantalum,” *Science (80-.).*, vol. 336, pp. 555–558, 2012.

[52] W. Eerenstein, N. D. Mathur, J. F. Scott, and J. F, “Scott: Multiferroic and magnetoelectric materials,” *Nature*, vol. 442759, no. August, pp. 759–765, 2006.

[53] R. Ramesh and N. A. Spaldin, “Multiferroics: progress and prospects in thin films,” *Nat. Mater.*, vol. 6, no. 1, pp. 21–29, 2007.

[54] W.-G. Wang, M. Li, S. Hageman, and C. L. Chien, “Electric-field-assisted switching in magnetic tunnel junctions,” *Nat. Mater.*, vol. 11, no. 1, pp. 64–68, 2011.

[55] T. Maruyama *et al.*, “Large voltage-induced magnetic anisotropy change in a few atomic

layers of iron.," *Nat. Nanotechnol.*, vol. 4, no. 3, pp. 158–161, 2009.

[56] J. J. Yang *et al.*, "Electric field manipulation of magnetization at room temperature in multiferroic CoFe[sub 2]O[sub 4]/Pb(Mg[sub 1/3]Nb[sub 2/3])[sub 0.7]Ti[sub 0.3]O[sub 3] heterostructures," *Appl. Phys. Lett.*, vol. 94, no. 21, p. 212504, 2009.

[57] T. Wu *et al.*, "Electrical control of reversible and permanent magnetization reorientation for magnetoelectric memory devices," *Appl. Phys. Lett.*, vol. 98, no. 26, pp. 15–18, 2011.

[58] J. J. Wang, J. M. Hu, J. Ma, J. X. Zhang, L. Q. Chen, and C. W. Nan, "Full 180° magnetization reversal with electric fields.," *Sci. Rep.*, vol. 4, p. 7507, 2014.

[59] R. C. Peng, J. J. Wang, J. M. Hu, L. Q. Chen, and C. W. Nan, "Electric-field-driven magnetization reversal in square-shaped nanomagnet-based multiferroic heterostructure," *Appl. Phys. Lett.*, vol. 106, no. 14, p. 142901, 2015.

[60] X. Li *et al.*, "Strain-mediated 180° perpendicular magnetization switching of a single domain multiferroic structure," *J. Appl. Phys.*, vol. 118, no. 1, p. 14101, 2015.

[61] M. Yi, B.-X. Xu, and Z. Shen, "180° magnetization switching in nanocylinders by a mechanical strain," *Extrem. Mech. Lett.*, vol. 3, pp. 66–71, 2015.

[62] R.-C. Peng, J.-M. Hu, K. Momeni, J.-J. Wang, L.-Q. Chen, and C.-W. Nan, "Fast 180° magnetization switching in a strain-mediated multiferroic heterostructure driven by a voltage," *Sci. Rep.*, vol. 6, no. February, p. 27561, 2016.

[63] M. M. Al-Rashid, S. Bandyopadhyay, and J. Atulasimha, "Dynamic Error in Strain-Induced Magnetization Reversal of Nanomagnets Due to Incoherent Switching and Formation of Metastable States: A Size-Dependent Study," *IEEE Trans. Electron Devices*, vol. 63, no. 8, pp. 3307–3313, 2016.

[64] N. Nishimura *et al.*, "Magnetic tunnel junction device with perpendicular magnetization

films for high-density magnetic random access memory," *J. Appl. Phys.*, vol. 91, no. 8, pp. 5246–5249, 2002.

[65] K. Roy, S. Bandyopadhyay, and J. Atulasimha, "Energy dissipation and switching delay in stress-induced switching of multiferroic nanomagnets in the presence of thermal fluctuations," *J. Appl. Phys.*, vol. 112, no. 2, p. 23914, 2012.

[66] M. S. Fashami, K. Munira, S. Bandyopadhyay, A. W. Ghosh, and J. Atulasimha, "Switching of dipole coupled multiferroic nanomagnets in the presence of thermal noise: Reliability of nanomagnetic logic," *IEEE Trans. Nanotechnol.*, vol. 12, no. 6, pp. 1206–1212, 2013.

[67] G. Nader, E. Silva, and J. Adamowski, "Effective damping value of piezoelectric transducers determined by experimental techniques and numerical analysis," *ABCM Symp. Ser. Mechatronics*, vol. 1, pp. 271–279, 2004.

[68] K. S. Kim *et al.*, "Magnetic and Structural Properties of FeCoB Thin Films," *IEEE Trans. Magn.*, vol. 37, no. 4, pp. 2302–2304, 2001.

[69] H. Sato *et al.*, "CoFeB Thickness Dependence of Thermal Stability Factor in CoFeB/MgO Perpendicular Magnetic Tunnel Junctions," *IEEE Magn. Lett.*, vol. 3, p. 3000204, 2012.

[70] D. Wang, C. Nordman, Z. Qian, J. M. Daughton, and J. Myers, "Magnetostriction effect of amorphous CoFeB thin films and application in spin-dependent tunnel junctions," *J. Appl. Phys.*, vol. 97, p. 10C906, 2005.

[71] D. B. Gopman, J. W. Lau, K. P. Mohanchandra, K. Wetzlar, and G. P. Carman, "Determination of the exchange constant of Tb0.3Dy0.7Fe2 by broadband ferromagnetic resonance spectroscopy," *Phys. Rev. B*, vol. 93, no. 6, p. 64425, 2016.

[72] G. Dewar, "Effect of the large magnetostriction of Terfenol-D on microwave

transmission," *J. Appl. Phys.*, vol. 81, no. 8, pp. 5713–5715, 1997.

[73] Y. C. Shu, M. P. Lin, and K. C. Wu, "Micromagnetic modeling of magnetostrictive materials under intrinsic stress," *Mech. Mater.*, vol. 36, no. 10, pp. 975–997, 2004.

[74] A. Speliotis and D. Niarchos, "Magnetostrictive properties of amorphous and crystalline TbDyFe thin films," *Sensors Actuators, A Phys.*, vol. 106, no. 1–3, pp. 298–301, 2003.

[75] E. Quandt, "Multitarget sputtering of high magnetostrictive Tb-Dy-Fe films," *J. Appl. Phys.*, vol. 75, no. 10, pp. 5653–5655, 1994.

[76] U. Parlak, M. E. Aköz, S. Tokdemir Öztürk, and M. Erkovan, "Thickness Dependent Magnetic Properties of Polycrystalline Nickel Thin Films," *Acta Phys. Pol. A*, vol. 127, no. 4, pp. 995–997, 2015.

[77] T. Lafont *et al.*, "Magnetostrictive – piezoelectric composite structures for energy harvesting," *J. Micromechanics Microengineering*, vol. 22, no. 9, p. 94009, 2015.

[78] M. S. Fashami, K. Roy, J. Atulasimha, and S. Bandyopadhyay, "Magnetization dynamics, Bennett clocking and associated energy dissipation in multiferroic logic.," *Nanotechnology*, vol. 22, p. 155201, 2011.

[79] A. Imre *et al.*, "<title>Field-coupled nanomagnets for logic applications</title>," vol. 5838, no. 574, pp. 162–170, 2005.

[80] T. D. M and T. D. M., "The Promise of Nanomagnetics and Spintronics for Future Logic and Universal Memory," *Proc. IEEE*, vol. 98, no. 12, p. 2155, 2010.

[81] C. H. Bennett, "The Thermodynamics of Computation--a Review," vol. 21, no. 12, pp. 905–940, 1982.

[82] S. Bandyopadhyay, B. Das, and a E. Miller, "Supercomputing with spin-polarized single electrons in a quantum coupled architecture," *Nanotechnology*, vol. 5, pp. 113–133, 1994.

[83] I. Amlani, A. O. Orlov, G. Toth, G. H. Bernstein, C. S. Lent, and G. L. Snider, "Digital Logic Gate Using Quantum-Dot Cellular Automata," *Science (80-.).*, vol. 284, no. 5412, pp. 289–291, 1999.

[84] G. H. Bernstein *et al.*, "Magnetic QCA systems," *Microelectronics J.*, vol. 36, no. 7, pp. 619–624, 2005.

[85] A. Imre, G. Csaba, L. Ji, A. Orlov, G. H. Bernstein, and W. Porod, "Majority logic gate for magnetic quantum-dot cellular automata," *Science (80-.).*, vol. 311, no. January, pp. 205–209, 2006.

[86] R. P. Cowburn and M. E. Welland, "Room Temperature Magnetic Quantum Cellular Automata," *Science (80-.).*, vol. 287, no. February, pp. 1466–1469, 2000.

[87] M. T. Alam, M. J. Siddiq, G. H. Bernstein, M. Niemier, W. Porod, and X. S. Hu, "On-chip clocking for nanomagnet logic devices," *IEEE Trans. Nanotechnol.*, vol. 9, no. 3, pp. 348–351, 2010.

[88] D. Bhowmik, L. You, and S. Salahuddin, "Spin Hall effect clocking of nanomagnetic logic without a magnetic field," *Nat. Nanotechnol.*, vol. 9, no. 1, pp. 59–63, 2013.

[89] N. D'Souza, J. Atulasimha, and S. Bandyopadhyay, "Four-state nanomagnetic logic using multiferroics," *J. Phys. D Appl. Phys*, vol. 44, pp. 265001–7, 2011.

[90] M. S. Fashami, J. Atulasimha, and S. Bandyopadhyay, "Magnetization Dynamics, Throughput and Energy Dissipation in a Universal Multiferroic Nanomagnetic Logic Gate with Fan-in and Fan-out," *Nanotechnology*, vol. 23, p. 105201, 2012.

[91] M. Al-rashid, J. Atulasimha, and S. Bandyopadhyay, "Geometry Effects in Switching of Nanomagnets with Strain: Reliability, Energy Dissipation and Clock Speed in Dipole-Coupled Nanomagnetic Logic," 2014.

[92] K. Munira *et al.*, “Reducing error rates in straintronic multiferroic dipole-coupled nanomagnetic logic by pulse shaping,” *arXiv Prepr. arXiv …*, vol. 26, no. 24, p. 1405.4000, 2014.

[93] N. D’Souza, M. S. Fashami, S. Bandyopadhyay, and J. Atulasimha, “Experimental Clocking of Nanomagnets with Strain for Ultralow Power Boolean Logic,” 2016.

[94] M. T. Niemier *et al.*, “Clocking structures and power analysis for nanomagnet-based logic devices,” *Low Power Electron. Des. (ISLPED), 2007 ACM/IEEE Int. Symp.*, pp. 26–31, 2007.

[95] P. Li *et al.*, “Switching behavior of lithographically fabricated nanomagnets for logic applications,” *J. Appl. Phys.*, vol. 111, no. 7, pp. 2013–2016, 2012.

[96] G. Csaba, A. Imre, G. H. Bernstein, W. Porod, and V. Metlushko, “Nanocomputing by Field-Coupled Nanomagnets,” vol. 1, no. 4, pp. 209–213, 2002.

[97] G. Bochi *et al.*, “Perpendicular magnetic anisotropy, domains, and misfit strain in epitaxial Ni/Cu 1− x Ni x/Cu/Si (001) thin films,” *Phys. Rev. B*, vol. 52, no. 10, p. 7311, 1995.

[98] A. Arevalo and I. G. Foulds, “Parametric Study of Polyimide – Lead Zirconate Titanate Thin Film Cantilivers for Transducer Applications,” *2013 COMSOL Conf. Rotterdam, Holl.*, 2013.

[99] A. Mourachkine, O. V. Yazyev, C. Ducati, and J. P. Ansermet, “Template nanowires for spintronics applications: Nanomagnet microwave resonators functioning in zero applied magnetic field,” *Nano Lett.*, vol. 8, no. 11, pp. 3683–3687, 2008.

[100] S. I. Kiselev *et al.*, “Microwave oscillations of a nanomagnet driven by a spin-polarized current,” *Nature*, vol. 425, no. 6956, pp. 380–383, 2003.

[101] F. Badets, L. Lagae, S. Cornelissen, T. Devolder, and C. Chappert, “Injection locked CMOS buffer dedicated to nanomagnetic based voltage controlled oscillator,” *Proc. 15th IEEE Int. Conf. Electron. Circuits Syst. ICECS 2008*, pp. 190–193, 2008.

[102] P. M. Braganca, B. A. Gurney, B. A. Wilson, J. A. Katine, S. Maat, and J. R. Childress, “Nanoscale magnetic field detection using a spin torque oscillator,” *Nanotechnology*, vol. 21, no. 23, p. 235202, 2010.

[103] J. Torrejon *et al.*, “Neuromorphic computing with nanoscale spintronic oscillators,” *Nat. Publ. Gr.*, vol. 547, no. 7664, pp. 428–431, 2017.

[104] Z. Zeng *et al.*, “Ultralow-current-density and bias-field-free spin-transfer nano-oscillator,” *Sci. Rep.*, vol. 3, pp. 1–5, 2013.

[105] Y. Zhou, H. Zhang, Y. Liu, and J. Åkerman, “Macrospin and micromagnetic studies of tilted polarizer spin-torque nano-oscillators,” *J. Appl. Phys.*, vol. 112, no. 6, 2012.

[106] M. D’Aquino, C. Serpico, R. Bonin, G. Bertotti, and I. D. Mayergoyz, “Micromagnetic analysis of injection locking in spin-transfer nano-oscillators,” *Phys. Rev. B - Condens. Matter Mater. Phys.*, vol. 82, no. 6, pp. 1–11, 2010.

[107] Y. Zhou, C. L. Zha, S. Bonetti, J. Persson, and J. Åkerman, “Spin-torque oscillator with tilted fixed layer magnetization,” *Appl. Phys. Lett.*, vol. 92, p. 262508, 2008.

[108] C. H. Sim, M. Moneck, T. Liew, and J. G. Zhu, “Frequency-tunable perpendicular spin torque oscillator,” *J. Appl. Phys.*, vol. 111, no. 7, pp. 1–4, 2012.

[109] S. Cherepov *et al.*, “Electric-field-induced spin wave generation using multiferroic magnetoelectric cells,” *Appl. Phys. Lett.*, vol. 104, p. 82403, 2014.

[110] C. Chen, A. Barra, A. Mal, G. Carman, and A. Sepulveda, “Voltage induced mechanical / spin wave propagation over long distances,” *Appl. Phys. Lett.*, vol. 110, p. 72401, 2017.

[111] D. Labanowski, A. Jung, and S. Salahuddin, “Power absorption in acoustically driven ferromagnetic resonance,” *Appl. Phys. Lett.*, vol. 108, p. 22905, 2016.

[112] X. Li *et al.*, “Spin wave generation by surface acoustic waves Spin wave generation by surface acoustic waves,” *J. Appl. Phys.*, vol. 122, p. 43904, 2017.

[113] G. Yu, H. Zhang, Y. Li, J. Li, D. Zhang, and N. Sun, “Resonance of magnetization excited by voltage in magnetoelectric heterostructures,” *Mater. Res. Express*, vol. 5, p. 45021, 2018.

[114] C. Kittel, “On the theory of ferromagnetic resonance absorption,” *Phys. Rev.*, vol. 73, no. 2, p. 155, 1948.

[115] M. T. Bootsmann, S. Dokupil, E. Quandt, T. Ivanov, N. C. Abedinov, and M. Löhndorf, “Switching of magnetostrictive micro-dot arrays by mechanical strain,” *IEEE Trans. Magn.*, vol. 41, no. 10, pp. 3505–3507, 2005.

[116] B. Özkaya, S. R. Saranu, S. Mohanan, and U. Herr, “Effects of uniaxial stress on the magnetic properties of thin films and GMR sensors prepared on polyimide substrates,” *Phys. Status Solidi Appl. Mater. Sci.*, vol. 205, no. 8, pp. 1876–1879, 2008.

[117] J. G. Wan, J. M. Liu, G. H. Wang, and C. W. Nan, “Electric-field-induced magnetization in Pb(Zr,Ti)O3/Terfenol-D composite structures,” *Appl. Phys. Lett.*, vol. 88, no. 18, p. 182502, 2006.

[118] M. Weiler *et al.*, “Voltage controlled inversion of magnetic anisotropy in a ferromagnetic thin film at room temperature,” *New J. Phys.*, vol. 11, no. 1, p. 13021, 2009.

[119] M. Liu *et al.*, “Giant electric field tuning of magnetic properties in multiferroic ferrite/ferroelectric heterostructures,” *Adv. Funct. Mater.*, vol. 19, no. 11, pp. 1826–1831, 2009.

[120] T. Wu *et al.*, "Giant electric-field-induced reversible and permanent magnetization reorientation on magnetoelectric Ni/(011) [Pb (Mg1/3Nb2/3) O3](1-x)-[PbTiO3]xheterostructure," *Appl. Phys. Lett.*, vol. 98, no. 1, p. 12504, 2011.

[121] S. Zhang *et al.*, "Electric-field control of nonvolatile magnetization in Co 40Fe 40B 20/Pb(Mg 1/3Nb 2/3) 0.7Ti 0.3O 3 structure at room temperature," *Phys. Rev. Lett.*, vol. 108, no. 13, p. 137203, 2012.

[122] M. Buzzi *et al.*, "Single domain spin manipulation by electric fields in strain coupled artificial multiferroic nanostructures," *Phys. Rev. Lett.*, vol. 111, no. 2, p. 27204, 2013.

[123] P. Li *et al.*, "Electric Field Manipulation of Magnetization Rotation and Tunneling Magnetoresistance of Magnetic Tunnel Junctions at Room Temperature.," *Adv. Mater.*, vol. 26, pp. 4320–4325, 2014.

[124] R. N. Torah, S. P. Beeby, and N. M. White, "Experimental investigation into the effect of substrate clamping on the piezoelectric behaviour of thick-film PZT elements," *J. Phys. D. Appl. Phys.*, vol. 37, no. 7, pp. 1074–1078, 2004.

[125] K. Lefki and G. J. M. Dormans, "Measurement of piezoelectric coefficients of ferroelectric thin films," *J. Appl. Phys.*, vol. 76, p. 1764, 1994.

[126] Y. C. Zhou, Z. Y. Yang, and X. J. Zheng, "Residual stress in PZT thin films prepared by pulsed laser deposition," *Surf. Coatings Technol.*, vol. 162, pp. 202–211, 2003.

[127] T.-K. Chung, S. Keller, and G. P. Carman, "Electric-field-induced reversible magnetic single-domain evolution in a magnetoelectric thin film," *Appl. Phys. Lett.*, vol. 94, p. 132501, 2009.

[128] J. Cui *et al.*, "Generation of localized strain in a thin film piezoelectric to control individual magnetoelectric heterostructures," *Appl. Phys. Lett.*, vol. 107, p. 92903, 2015.

[129] J. H. Kim, K. S. Ryu, J. W. Jeong, and S. C. Shin, “Large converse magnetoelectric coupling effect at room temperature in CoPd/PMN-PT (001) heterostructure,” *Appl. Phys. Lett.*, vol. 97, p. 252508, 2010.

[130] Y. T. Yang *et al.*, “Electric-field-assisted magnetization switching in FePd/Pb(Mg1/3Nb2/3)O3-PbTiO3heterostructure at room temperature,” *J. Appl. Phys.*, vol. 114, p. 144902, 2013.

[131] Y. T. Yang *et al.*, “Electric field control of magnetic properties in CoPt/Pb(Mg1/3Nb2/3)O3-PbTiO3heterostructure at room temperature,” *Appl. Phys. Lett.*, vol. 103, p. 82404, 2013.

[132] N. Lei *et al.*, “Magnetization reversal assisted by the inverse piezoelectric effect in Co-Fe-B/ferroelectric multilayers,” *Phys. Rev. B*, vol. 84, p. 12404, 2011.

[133] G. Yu *et al.*, “Strain-induced modulation of perpendicular magnetic anisotropy in Ta / CoFeB / MgO structures investigated by ferromagnetic resonance Strain-induced modulation of perpendicular magnetic anisotropy in Ta / CoFeB / MgO structures investigated by ferromagnet,” vol. 72402, no. 2015, 2015.

[134] J. P. Domann, W. Y. Sun, L. T. Schelhas, and G. P. Carman, “Strain-mediated multiferroic control of spontaneous exchange bias in Ni-NiO heterostructures,” *J. Appl. Phys.*, vol. 120, p. 143904, 2016.

[135] J. Cui *et al.*, “A method to control magnetism in individual strain-mediated magnetoelectric islands A method to control magnetism in individual strain-mediated magnetoelectric islands,” vol. 232905, no. 2013, 2017.

[136] K. R. Williams, K. Gupta, and M. Wasilik, “Etch rates for micromachining processing - part II,” *J. Microelectromechanical Syst.*, vol. 12, no. 6, p. 761, 2003.

[137] R. H. T. Wilke *et al.*, “Sputter deposition of PZT piezoelectric films on thin glass substrates for adjustable x-ray optics,” *Appl. Opt.*, vol. 52, no. 14, p. 3412, 2013.

[138] Z. Ma *et al.*, “Effect of 90° domain movement on the piezoelectric response of patterned PbZr0.2Ti0.8O3/SrTiO3/Si heterostructures,” *Appl. Phys. Lett.*, vol. 87, p. 72907, 2005.

[139] M. Endo, S. Kanai, S. Ikeda, F. Matsukura, and H. Ohno, “Electric-field effects on thickness dependent magnetic anisotropy of sputtered MgO/Co40Fe40B20/Ta structures,” *Appl. Phys. Lett.*, vol. 96, p. 212503, 2010.

[140] M. Liu, J. Lou, S. Li, and N. X. Sun, “E-field control of exchange bias and deterministic magnetization switching in AFM/FM/FE multiferroic heterostructures,” *Adv. Funct. Mater.*, vol. 21, no. 13, pp. 2593–2598, 2011.

[141] R. Lo Conte *et al.*, “Influence of Nonuniform Micron-Scale Strain Distributions on the Electrical Reorientation of Magnetic Microstructures in a Composite Multiferroic Heterostructure,” *Nano Lett.*, vol. 18, no. 3, pp. 1952–1961, 2018.

[142] V. Nagarajan *et al.*, “Dynamics of ferroelastic domains in ferroelectric thin films,” *Nat. Mater.*, vol. 2, pp. 43–47, 2003.

[143] A. K. Biswas, S. Bandyopadhyay, and J. Atulasimha, “Acoustically assisted spin-transfer-torque switching of nanomagnets: An energy-efficient hybrid writing scheme for non-volatile memory,” *Appl. Phys. Lett.*, vol. 103, no. 23, p. 232401, 2013.

[144] A. Khan, D. E. Nikonov, S. Manipatruni, T. Ghani, and I. A. Young, “Voltage induced magnetostrictive switching of nanomagnets: Strain assisted strain transfer torque random access memory,” *Appl. Phys. Lett.*, vol. 104, p. 262407, 2014.

[145] J. G. Alzate *et al.*, “Voltage-induced switching of nanoscale magnetic tunnel junctions,” *Tech. Dig. - Int. Electron Devices Meet. IEDM*, pp. 681–684, 2012.

[146] R. Dorrance *et al.*, “Diode-MTJ crossbar memory cell using voltage-induced unipolar switching for high-density MRAM,” *IEEE Electron Device Lett.*, vol. 34, no. 6, pp. 753–755, 2013.

[147] W. Kang, Y. Ran, W. Lv, Y. Zhang, W. Zhao, and S. Member, “High-Speed, Low-Power, Magnetic Non-Volatile Flip-Flop With Voltage-Controlled, MagneticMagnetic Anisotropy Assistance,” *IEEE Magn. Lett.*, vol. 7, pp. 1–5, 2016.

[148] H. Yoda *et al.*, “Voltage-control spintronics memory (VoCSM) having potentials of ultra-low energy-consumption and high-density,” *Tech. Dig. - Int. Electron Devices Meet. IEDM*, p. 27.6.1-27.6.4, 2017.

[149] A. Van Den Brink *et al.*, “Spin-Hall-assisted magnetic random access memory,” *Appl. Phys. Lett.*, vol. 104, p. 12403, 2014.

[150] Z. Wang, W. Zhao, and E. Deng, “Perpendicular-anisotropy magnetic tunnel junction switched by spin-Hall-assisted spin- transfer torque,” *J. Phys. D Appl. Phys*, vol. 48, p. 65001, 2015.

[151] N. Sato, F. Xue, R. M. White, C. Bi, and S. X. Wang, “Two-terminal spin – orbit torque magnetoresistive random access memory,” *Nat. Electron.*, vol. 1, no. September, pp. 508–511, 2018.

[152] J. Park, G. E. Rowlands, O. J. Lee, D. C. Ralph, and R. A. Buhrman, “Macrospin modeling of sub-ns pulse switching of perpendicularly magnetized free layer via spin-orbit torques for cryogenic memory applications,” *Appl. Phys. Lett.*, vol. 105, no. 10, p. 102404, 2014.

[153] G. Finocchio, M. Carpentieri, E. Martinez, and B. Azzerboni, “Switching of a single ferromagnetic layer driven by spin Hall effect,” *Appl. Phys. Lett.*, vol. 102, no. 21, p.

212410, 2013.

[154] Z. Wang, W. Zhao, E. Deng, J. Klein, and C. Chappert, “Perpendicular-anisotropy magnetic tunnel junction switched by spin-Hall-assisted spin-transfer torque,” *J. Phys. D. Appl. Phys.*, vol. 48, p. 65001, 2015.

[155] S. Iihama, Q. Ma, T. Kubota, S. Mizukami, Y. Ando, and T. Miyazaki, “Damping of Magnetization Precession in Perpendicularly Magnetized CoFeB Alloy Thin Films,” *Appl. Phys. Express*, vol. 5, p. 83001, 2012.

[156] T. Devolder *et al.*, “Damping of CoxFe80-xB20 ultrathin films with perpendicular magnetic anisotropy,” *Appl. Phys. Lett.*, vol. 102, p. 22407, 2013.

[157] Y. Fan *et al.*, “Magnetization switching through giant spin-orbit torque in a magnetically doped topological insulator heterostructure.,” *Nat. Mater.*, vol. 13, no. 7, p. 699, 2014.

[158] A. E. Wickenden *et al.*, “Spin Torque Nano Oscillators as Potential Terahertz (THz) Communications Devices,” *Army Res. Lab.*, no. April, 2009.

[159] D. Houssameddine *et al.*, “Spin-torque oscillator using a perpendicular polarizer and a planar free layer.,” *Nat. Mater.*, vol. 6, no. 6, pp. 441–447, 2007.

[160] H. Zhang, Z. Hou, J. Zhang, Z. Zhang, and Y. Liu, “Precession frequency and fast switching dependence on the in-plane and out-of-plane dual spin-torque polarizers,” *Appl. Phys. Lett.*, vol. 100, p. 142409, 2012.

[161] Q. Wang, J. Domann, G. Yu, A. Barra, K. L. Wang, and G. P. Carman, “Strain-Mediated Spin-Orbit-Torque Switching for Magnetic Memory,” *Phys. Rev. Appl.*, vol. 10, p. 34052, 2018.

[162] J. C. Slonczewski, “Current-driven excitation of magnetic multilayers,” *J. Magn. Magn. Mater.*, vol. 159, p. L1, 1996.

[163] L. Berger, “Emission of spin waves by a magnetic multilayer traversed by a current,” *Phys. Rev. B*, vol. 54, no. 13, pp. 9353–9358, 1996.

[164] J. A. Katine, F. J. Albert, and R. A. Buhrman, “Current-Driven Magnetization Reversal and Spin-Wave Excitations in Co/Cu/Co Pillars,” *Phys. Rev. Lett.*, vol. 84, no. 14, pp. 3149–3152, 2000.

[165] D. C. Ralph and M. D. Stiles, “Spin transfer torques,” *J. Magn. Magn. Mater.*, vol. 320, pp. 1190–1216, 2008.

[166] Y. Huai, “Spin-Transfer Torque MRAM (STT-MRAM): Challenges and Prospects,” *AAPPS Bull.*, vol. 18, no. 6, pp. 33–40, 2008.

[167] M. Cubukcu *et al.*, “Spin-orbit torque magnetization switching of a three-terminal perpendicular magnetic tunnel junction,” *Appl. Phys. Lett.*, vol. 104, no. 4, p. 42406, 2014.

[168] H. Yoda, T. Kishi, T. Nagase, M. Yoshikawa, and K. Nishiyama, “High efficient spin transfer torque writing on perpendicular magnetic tunnel junctions for high density MRAMs,” *Curr. Appl. Phys.*, vol. 10, no. 1, pp. e87–e89, 2010.

[169] J. A. Katine and E. E. Fullerton, “Device implications of spin-transfer torques,” *J. Magn. Magn. Mater.*, vol. 320, pp. 1217–1226, 2008.

[170] I. M. Miron *et al.*, “Perpendicular switching of a single ferromagnetic layer induced by in-plane current injection.,” *Nature*, vol. 476, no. 7359, pp. 189–193, 2011.

[171] L. Liu, O. J. Lee, T. J. Gudmundsen, D. C. Ralph, and R. A. Buhrman, “Current-induced switching of perpendicularly magnetized magnetic layers using spin torque from the spin hall effect,” *Phys. Rev. Lett.*, vol. 109, no. 9, p. 96602, 2012.

[172] C. O. Avci *et al.*, “Magnetization switching of an MgO / Co / Pt layer by in-plane current injection Magnetization switching of an MgO / Co / Pt layer by in-plane current

injection," *Appl. Phys. Lett.*, vol. 100, p. 212404, 2012.

[173] S. Fukami, T. Anekawa, C. Zhang, and H. Ohno, "A spin-orbit torque switching scheme with collinear magnetic easy axis and current configuration," *Nat. Nanotechnol.*, vol. 11, no. March, pp. 621–625, 2016.

[174] X. Qiu *et al.*, "Spin–orbit-torque engineering via oxygen manipulation," *Nat. Nanotechnol.*, vol. 10, no. 4, pp. 333–338, 2015.

[175] K. Lee *et al.*, "Threshold current for switching of a perpendicular magnetic layer induced by spin Hall effect," *Appl. Phys. Lett.*, vol. 102, p. 112410, 2013.

[176] K. Garello *et al.*, "Ultrafast magnetization switching by spin-orbit torques," *Appl. Phys. Lett.*, vol. 105, p. 212402, 2014.

[177] L. You *et al.*, "Switching of perpendicularly polarized nanomagnets with spin orbit torque without an external magnetic field by engineering a tilted anisotropy," *Proc. Natl. Acad. Sci.*, vol. 112, no. 33, pp. 10310–10315, 2015.

[178] Y.-W. Oh *et al.*, "Field-free switching of perpendicular magnetization through spin-orbit torque in antiferromagnet/ferromagnet/oxide structures.," *Nat. Nanotechnol.*, vol. 11, no. 10, pp. 878–884, 2016.

[179] A. van den Brink *et al.*, "Field-free magnetization reversal by spin-Hall effect and exchange bias," *Nat. Commun.*, vol. 7, p. 10854, 2016.

[180] J. Chen, D. Zhang, Z. Zhao, M. Li, and J. Wang, "Field-free spin-orbit torque switching of composite perpendicular CoFeB / Gd / CoFeB layers utilized for three-terminal magnetic tunnel junctions," *Appl. Phys. Lett.*, vol. 111, p. 12402, 2017.

[181] K. Cai *et al.*, "Electric field control of deterministic current-induced magnetization switching in a hybrid ferromagnetic/ferroelectric structure," *Nat. Mater.*, vol. 16, p. 712,

2017.

[182] X. Ren, “Large electric-field-induced strain in ferroelectric crystals by point-defect-mediated reversible domain switching,” *Nat. Mater.*, vol. 3, pp. 91–94, 2004.

[183] S. Park, T. R. Shrout, S. Park, and T. R. Shrout, “Ultrahigh strain and piezoelectric behavior in relaxor based ferroelectric single crystals Ultrahigh strain and piezoelectric behavior in relaxor based ferroelectric single crystals,” *J. Appl. Phys.*, vol. 82, p. 1804, 1997.

[184] A. K. Biswas, S. Bandyopadhyay, and J. Atulasimha, “Highly reliable low-energy writing of bits in non-volatile multiferroic memory based on 180-degree magnetization switching with voltage-generated stress,” *arXiv Prepr.*, vol. 1407.2140, 2014.

[185] K. Roy, “Ultra-low-energy straintronics using multiferroic composites,” *Proc. SPIE*, vol. 9167, p. 91670U, 2014.

[186] E. Eken *et al.*, “Spin-Hall Assisted STT-RAM Design and Discussion,” *Syst. Lev. Interconnect Predict.*, 2016.

[187] Y. Kim, S. Member, X. Fong, K. Kwon, M. Chen, and K. Roy, “Multilevel Spin-Orbit Torque MRAMs,” *IEEE Trans. Electron Devices*, vol. 62, no. 2, pp. 561–568, 2015.

The end and a new start.